Boundary Layer Flow Separation Control by Synthetic Jet Actuators

by

Mohammad Jafari

A thesis submitted to the University of Huddersfield in partial fulfilment of the requirements for the degree of Doctor of Philosophy

Department of Engineering and Technology
School of Computing and Engineering

University of Huddersfield

March 2020

Declaration

No portion of the work in the thesis has been submitted in support of an application for another degree or qualification of this or any other university or other institute of learning.

Copyright Statement

Abstract

In this research the effectiveness of synthetic jet actuators (SJAs) for the boundary layer flow separation control over a circular hump model at chord Reynolds number in range of 10^5 with speed in range of 10 m/s in turbulent regime is studied both experimentally and numerically. A low speed closed circuit wind tunnel with velocity range of 0-25 m/s, as well as a circular hump model have been designed and manufactured to enable the research. Improvement of the performance of synthetic jet actuators is achieved by geometrical optimization of SJAs through a series of Hot-Wire Anemometry (HWA) experiments in quiescent conditions (no cross flow). The influence of different geometrical and operational parameters including actuator position, the ratio of the peak exit jet velocity of actuators to the free stream velocity of cross flow (VR), actuation frequency and waveform on the flow separation control are investigated by both Hot-Wire Anemometry (HWA) and Particle Image Velocimetry (PIV) techniques. The results revealed that the best location of SJAs to attain the best performance is somewhere upstream and close to the separation point. Improvement of aerodynamic performance of active flow control has been achieved by optimization of both geometrical and operational parameters of active flow control.

The results show that the best performance of synthetic jet actuators in control of flow separation over the hump model occurs at optimum value of velocity ratio of 1.85 with 42.6 and 44.2% reduction of the length of recirculation region by using sine and square wave excitation of SJAs, respectively. This achievement is a unique improvement in control of flow separation. The Unsteady Reynolds-Averaged Navier-Stokes (URANS) simulations are utilized to numerically investigate boundary layer flow separation over a hump model and its active control. The OpenFoam software is used to numerically simulate and analyze the flow by K-Omega SST model. The SJAs have been fully simulated in this study by considering both cavity and membrane oscillations. Also, Merging and Stitching techniques have been utilized to generate the computational grid for actuated case which were very useful to greatly reduce the computational costs. The three-dimensional Computational Fluid Dynamics (CFD) simulations of unactuated case, as well as the simulation of interaction of vortical structures generated by synthetic jet actuators with cross flow revealed more information about the flow physics of separation phenomenon and its control and suggest some ideas (e.g. geometrical optimization of SJAs) to improve the aerodynamic performance of active flow control. The full simulation of synthetic jet actuators and their interaction with cross flow, alongside utilization of Merging and Stitching techniques for mesh generation is arguably the first attempt of this kind. For completeness, the accuracy of URANS technique as well as the effectiveness of synthetic jet actuators have been evaluated by comparison of numerical predictions with experimental data. The instantaneous and time-averaged results are in reasonable agreement with experimental results and depict the successful performance of SJAs to delay flow separation by interaction of vortical structures with separated shear flow. Although, the predictions of separation flows in fluid dynamics field always is challenging, but the comparison of numerical results with experimental data shows that the K-Omega SST model can be used as a good strategy for prediction of flow separation and its control.

Acknowledgments

I would like to express my deepest appreciations to Prof. Artur Jaworski for supervision of this research. His advice, support, patience and his detailed knowledge of aerodynamics field were elemental factors to accomplish this research.

Many thanks go to Dr. Ahmed Hamood for his support, creative ideas and help during the hump model and wind tunnel manufacturing and assembly processes.

My special gratitude extends to the team of technicians led by Mr. Richard Bailley for creative attitudes during planning and manufacturing of the hump model and the hump model mounting in the test section of the wind tunnel as well as the wind tunnel assembly process. Contributions from Mr. Robert Powis, Mr. Philip Holdsworth, Mr. Steven Goldstein and Mr. Ben Lear were fundamental for the research.

Finally, I acknowledge 3M Buckley Innovation Centre of University of Huddersfield and specially Dr. Steve Andrew for their support of the research project and devoting two computational nodes with 48 cores for computations and post-processing of the data of the numerical part of the research.

Table of Contents

Title Page	1
Declaration	2
Copyright Statement	2
Abstract	3
Acknowledgements	4
Table of Content	5
Nomenclature	8
Abbreviations	10
List of Figures	11
List of Tables	23
Chapter 1- Introduction	24
1.1- Importance and Applications of Flow Separation Control	24
1.2- Aim and Objectives of the Current Research	26
1.3- Summary	28
Chapter 2- Literature Review	29
2.1- Flow Separation and Reattachment	29
2.2- History, Theory and Mechanism of Synthetic Jet Actuators	34
2.3- Effective Design Parameters	38
2.3.1- Geometrical Parameters	38
2.3.2- Operational Parameters	43
2.3.3- Non-Dimensional Parameters	46
2.4- Interaction of Synthetic Jet Actuators with Uniform Cross Flow	49
2.5- Summary	62
Chapter 3- Experimental and Numerical Methodologies	63
3.1- Experimental Methodology	63
3.1.1- Wind Tunnel	63
3.1.2- Wind Tunnel Power Considerations	66
3.1.3- Hump Model and Mounting System	73
3.1.4- Actuator Array and Driving Circuitry System	77
3.1.5- Constant Temperature Anemometry System	80
3.1.5.1- Principles of Operation	80
3.1.5.2- Experimental Setup and Data Acquisition	81
3.1.5.3- Data Post Processing	83
3.1.5.4- Calibration Process	85
3.1.6- Particle Image Velocimetry (PIV) Technique	86
3.1.6.1- Principles of Operation	86
3.1.6.2- Experimental Setup and Data Acquisition	87
3.1.6.3- Data Post Processing	90
3.1.6.4- Calibration Process	91
3.1.7- Flow Seeding Technique	92

3.2- Numerical Methodology 95
3.2.1- Geometry and Computational Grid 95
3.2.1.1- Computational Grid of Unactuated Case 99
3.2.1.2- Computational Grid of Actuated Case 101
3.2.2- K-Omega Shear Stress Transport (SST) Turbulence Model 103
3.2.3- Initial and Boundary Conditions 104
3.2.4- Numerical Method 106
3.3- Summary 107
Chapter 4- Results 108
4.1- Wind Tunnel Flow Quality Measurements 108
4.2- Characteristics of Single Actuator in Quiescent Flow Conditions 110
4.3- Flow Separation over the Hump Model- Unactuated Case 113
4.3.1- Measurements of Flow Features by HWA Technique- Unactuated Case 114
4.3.2- Measurements of Flow Features by PIV Technique- Unactuated Case 119
4.4- Flow Separation and its control over the Hump Model- Actuated Case 127
4.4.1- Measurements of Flow Features by HWA Technique- Actuated Case 127
4.4.2- Measurements of Flow Features by PIV Technique- Actuated Case 129
4.5- Numerical Results 178
4.5.1- Unsteady State – Unactuated Case 178
4.5.2- Unsteady State – Actuated Case 183
4.5.2.1- Single SJA in Quiescent Conditions (No Cross-Flow) 183
4.5.2.2- Interaction of Synthetic Jet Actuators with a Uniform Cross-Flow 188
4.6- Summary 196
Chapter 5- Discussion 197
5.1- Wind Tunnel Flow Quality 197
5.2- Characteristics of Single Actuator in Quiescent Flow Conditions 198
5.3- Flow Separation over the Hump Model- Unactuated Case 200
5.3.1- Measurements of Flow Features by HWA Technique- Unactuated Case 200
5.3.2- Criteria of Identification of Reattachment and Separation Points Location in PIV Studies 202
5.3.3- Measurements of Flow Features by PIV Technique- Unactuated Case 204
5.4- Flow Separation and its control over the Hump Model- Actuated Case 205
5.4.1- Measurements of Flow Features by HWA Technique- Actuated Case 206
5.4.2- Measurements of Flow Features by PIV Technique- Actuated Case 207
5.5- Flow Separation and its control over the Hump Model by Numerical Simulations 216
5.5.1 Unsteady State – Unactuated Case 217
5.5.2 Unsteady State –Actuated Case 219
5.5.2.1- Single SJA in Quiescent Conditions 219
5.5.2.2- Interaction of Synthetic Jet Actuators with Uniform Cross-Flow 221
5.6- Summary 223

Chapter 6- Conclusions 224
References 228
Appendix A- Software Testing using Cylindrical Bar 242
Appendix B- MATLAB program to help the HWA data processing 244
Appendix C- Additional Hot Wire Anemometry (HWA) Results 246
Appendix D- Additional Particle Image Velocimetry (PIV) Results 252

Nomenclature

A	Actuator orifice area (m^2)
A_w	Wire surface (m^2)
a_{00} , a_{01}, a_{02} , a_{03}, a_{04}	Probe calibration constants
b	Wing span (m)
C	Hump/wing chord (m), Capacitance (nF)
C_D	Drag coefficient
C_f	Skin friction coefficient
C_L	Lift coefficient
C_p	Pressure coefficient
C_μ	Momentum coefficient
D	Diameter of cavity (m)
d	Orifice diameter (m)
F	Force (N)
F^+	Dimensionless frequency
$\hat{F}$	Mapping Function
f	Frequency (Hz)
f_H	Helmholtz frequency (Hz)
H	Height of cavity (m)
h	Hump height (m), Depth of orifice (m)
h_{eff}	Effective depth of orifice (m)
I	Current (A)
k	Turbulent Kinetic Energy $(m/s)^2$
L	Stroke length
l	Turbulence Length Scale (m)
Ma	Mach number
n	Number of actuators
p	Pressure(N/m^2)
Q	Convective heat transfer (J)
Re	Reynolds number

St	Strouhal number
SR	Sampling rate (Hz)
T	Period of cycle (s)
T_0	Ambient Temperature (K)
T_w	Wire temperature (K)
t	time (s)
U_{inst}	Instantaneous velocity (m/s)
U_0	Average of the instantaneous velocity of the orifice (m/s)
U	Free stream velocity (m/s)
U_j	Synthetic jet velocity (m/s)
U_{max}	Maximum velocity (m/s)
U_{sound}	Velocity of sound (m/s)
u, v, w	Velocity components (m/s)
V	Velocity (m/s)
V_{cavity}	Volume of the cavity (m^3)
V_{p-p}	Peak to peak voltage (V)
VR	Velocity ratio
x, y, z	Cartesian coordinate (m)
Δ	Laplace Operator
θ	Phase angle (Degree)
ν	Kinematic viscosity (m^2/s)
ν_t	Turbulence Viscosity (m^2/s)
ρ	Density (kg/m^3)
ϕ	Angular Position of Actuator
ω	Turbulence Specific Dissipation Rate (1/s)

Abbreviations

APG: Adverse-Pressure Gradient
BDSJ: Bi-Directional Synthetic Jet
CFD: Computational Fluid Dynamics
CFJ: Co-Flow Jet
CTA: Constant Temperature Anemometer
DES: Detached Eddy Simulation
DDES: Delayed Detached Eddy Simulation
DNS: Direct Numerical Simulation
FFT: Fast- Fourier Transform
FUN2D: Full Unstructured Navier-Stokes 2-Dimensional
HWA: Hot Wire Anemometery
IDDES: Improved Delayed Detached Eddy Simulation
ILES: Implicit Large-Eddy Simulation
IPMC: Polymer Metal Composite
LES: Large-Eddy Simulation
LSB: Laminar Separation Bubble
MVGs: Micro-Vortex Generators
PIV: Particle Image Velocimetry
PSD: Power Spectral Density
RANS: Reynolds-Averaged Navier-Stokes
RASB: Recessed Angled Span-wise Blowing
RFD: Radial Field Diaphragms
RMS: Root Mean Square
SJA: Synthetic Jet Actuator
SMA: Shape Memory Alloy
STJ: Steady-Straight Jet
STL: Stereolithography
stddev: Standard Deviation
TLNS3D: Thin-Layer Navier-Stokes 3-Dimensional
TTL: Transistor-Transistor Logic
URANS: Unsteady Reynolds-Averaged Navier-Stokes
VGJ: Steady-Angled Jet

List of Figures

Fig.1.1. Flow visualization with no control (left) and with flow control (right) (Prandtl (1904)). 25

Fig.2.1. Pressure based (a) and geometrical based (b) flow separation with A and B as separation points (Sturm et al (2012)). 29

Fig.2.2. Velocity profile before (a), while (b) and after (c) separation of boundary layer (Sturm et al (2012)). 30

Fig.2.3. Surface pressure distribution with laminar separation bubble (Shah et al (2015). 32

Fig.2.4. Illustration of laminar separation bubble (Shah et al (2015)). 32

Fig.2.5. Axial filaments of dye, water tunnel, 2 in./sec, bubble (bottom), spiral (top) burst types (Lambourne and Bryer (1961)). 33

Fig.2.6. Schematic of components for generation of SJ (Bazdidi Tehrani et al (2016)). 35

Fig.2.7. The exploded view (left) and assembled view (right) of diaphragm actuator (Koopmans and Hoeijmakers (2014)). 35

Fig.2.8. Four stages of synthetic jet (Polsenberg et al (2005)). 36

Fig.2.9. Well-spaced orifices case, in terms of the diaphragm displacement level, the actual orifice spacing and non-dimensional spacing given by the orifice spacing divided by the orifice diameter (Watson et al (2003)). 41

Fig.2.10. Maximum jet velocity changes between normal and high temperatures. (a) d=2 mm, (b) f=200 Hz, Eri et al (2018). 42

Fig.2.11. Profile of changes of maximum velocity and maximum momentum, peak pressure ratio and suction air mass between the SJAcon and SJAau (f=200 Hz, d=2 mm, T=800 K), Eri et al (2018). 42

Fig.2.12. (a) Radial velocity profile and (b) profile of radial rms velocity for bigger diameter (D= 2mm) orifice at location, y/D= 1.5 for different excitation conditions and carrier frequency of 475 Hz (Qayoum et al (2010)). 46

Fig.2.13. Mean and fluctuating pressures representing the effects of excitation frequency (left) and evolution of the pressure fluctuations at the fundamental frequency downstream of the $x/c = 0.64$ slot (right), cμ=0.13% and M∞ = 0.25; Re = 16 million (Seifert & Pack (2002). 47

Fig.2.14. Contours of overall separation control effect for active actuator (Ishtiaq et al (2016)). 50

Fig 2.15. Dye visualization of vortex structures generated by synthetic jets on a laminar boundary layer: (a) hairpin vortices; (b) stretched and tilted vortex rings; and (c) distorted vortex rings (modified by Zhou (2010), from Zhong et al, 2005). 51

Fig.2.16. (a) VR– L and (b) Re_L – VR parameter space of the different vortical structures seen due to the interaction between a synthetic jet and a boundary layer (Jabbal and Zhong (2008)). 51
Fig.2.17. Iso-surfaces of vortex structures colored by stream-wise velocity for the time-averaged unactuated case, time-averaged actuated case and phase-averaged (phase angle of 180^o) actuated cases (Salunkhea et al (2016)). 53
Fig.2.18. Change of (a) C_L and (b) C_D versus Attack Angle, actuated and unactuated (baseline) cases (Tang et al (2014)). 54
Fig.2.19. Flow separation control using optimal set of parameters for the SJA (Koopmans and Hoeijmakers (2014)). 54
Fig.2.20. Pressure profiles over a hump for different actuator locations for baseline case and cases near the optimal position (Takao (2006)). 55
Fig.2.21. Unactuated computational results versus experimental data (left) and mean pressures of the controlled flow using suction (c_μ= -0.077%) and periodic excitation (c_μ= 0.095%) at F^+ =1.6 (Right) and M_∞ = 0.25; Re = 16 million (Viken et al (2003)). 56
Fig.2.22. Total pressure field, view in flow direction. From left: reference conditions - unactuated, no phase shift of the synthetic jet, and phase shift of amplitude modulation of the synthetic jet (Pick et al (2013)). 56
Fig.2.23. Velocity field, view in flow direction. From left: reference conditions-unactuated, no phase shift of the synthetic jet, and phase shift of amplitude modulation of the synthetic jet (Pick et al (2013)). 57
Fig.2.24. Instantaneous stream-wise vorticity contours. (a) Baseline; (b) steady suction; (c) oscillatory jet (You et al (2005). 58
Fig.2.25. Skin friction coefficient predicted by the LES, ____, baseline case; ----- steady suction; ...., oscillatory jet, o, experiment (Greenblatt et al (2004 and 2005)). 59
Fig.2.26. Oil flow visualization for baseline case (left), VGT mode (middle) and STJ mode (right) (Koklu (2015)). 62
Fig.3.1. Top view of the closed loop wind tunnel at the University of Huddersfield. 65
Fig.3.2. Fan pressure-volume curve (Woodcock & Wilson Ltd). 73
Fig.3.3. Hump model without removable parts (left) and insert of pressure taps (right). 75
Fig.3.4. 2D schematic of the insert of pressure taps (side view), dimensions are in mm. 75
Fig.3.5. 2D schematic of synthetic jet array. 75
Fig.3.6. Schematic of an individual SJA with 3 orifices. 76
Fig.3.7. 2D schematic of insert shaft support. 76

Fig.3.8. The hump model contains actuator array and the pressure taps insert (left), and its position in the test section (right). 77
Fig.3.9. Synthetic jet actuators supported by clamping pieces. 78
Fig.3.10. PDm200 connection diagram (PiezoDrive Ltd, (2017)). 79
Fig.3.11. Hump model in the test section contains actuators array connected to driving circuitry system. 80
Fig.3.12. CTA principle diagram (Jorgensen (2002)). 81
Fig.3.13. Typical CTA measuring chain (Jorgensen (2002)). 82
Fig.3.14. Traverse system mounted on the test section sidewall supporting HWA probe. PIV laser sheet delivery system is shown at the top. 83
Fig.3.15. Calibration curve fit, coefficients and mean square error. 86
Fig.3.16. General schematic of experimental setup for PIV. 87
Fig.3.17. Schematic of experimental setup of PIV system. 88
Fig.3.18 The schematic of basic PIV timing system (adapted from Adrian, R.J. & Westerweel, J (2011)). 89
Fig.3.19. The schematic of the seeder. 93
Fig.3.20. The general schematic of experimental setup. 94
Fig.3.21. Background Mesh, first stage of mesh generation in snappyHexMesh process. 96
Fig.3.22. A slice of the whole geometry contains one cavity and 3 orifices. 97
Fig.3.23. (a) Computational domain and mesh in the X-Y plane, (b) Closer view of inlet and near wall region and (c) Closer view of region contains hump apex and hump trailing edge. 100
Fig.3.24. (a) Computational Grid in X-Y plane for actuated case and (b) Closer view of computational grid showing slaveMesh stitched to masterMesh by stitching three corresponding patches, X-Y plane. 102
Fig.4.1. Measurement planes and coordinate system. 109
Fig.4.2. (a) Velocity profiles in planes Z=150 mm, (b) Z=0 mm and (c) Z=-150 mm; (d) velocity and turbulence intensity in plane Z=0 mm and X=550 mm, $U_\infty = 7\ m/s$. 109
Fig.4.3. Velocity boundary layer profile in plane Z= 150 mm at X= 550 mm, $U_\infty = 7\ m/s$. 110
Fig.4.4. Frequency response of single SJA with orifice diameter of 1 mm at Vp-p of 23 Volt. 110
Fig.4.5. Profile of orifice outlet velocity versus actuation voltage at Frequency of 960 Hz for orifice diameter of 1 mm. 111
Fig.4.6. Profile of time history of exit jet velocity at y= 0.5 mm above the orifice with actuation voltage of 22Vp-p at Frequency of 960 Hz. 111
Fig.4.7. Profile of time history of exit jet velocity at y= 1.5 mm above the orifice with actuation voltage of 22Vp-p at Frequency of 960 Hz. 112

Fig.4.8. Profile of peak velocity of exit jet versus height above the orifice outlet with actuation voltage of 22Vp-p at Frequency of 960 Hz. 112
Fig.4.9. Power spectrum density estimate of exit jet velocity at Y = 0.5 mm above the orifice outlet with actuation voltage of 22Vp-p at Frequency of 960 Hz, $U_\infty = 7\ m/s$. 113
Fig.4.10. Power spectrum density estimate of exit jet velocity at Y = 15.5 mm above the orifice outlet with actuation voltage of 22Vp-p at Frequency of 960, $U_\infty = 7\ m/s$. 113
Fig 4.11. Locations of HWA measurements lines in the wake region. 114
Fig.4.12. Velocity profiles in the wake region for 3 free stream velocities in plane Z =0 at X = 600 mm. 115
Fig.4.13. RMS Velocity profiles in the wake region for free stream velocity of 7m/s in plane Z = 0. 115
Fig.4.14. Velocity profiles in the wake region for 3 free stream velocities in plane Z = 0 at X = 590 mm. 116
Fig.4.15. Trajectory of Max RMS velocity in the wake region in plane Z = 0, $U_\infty = 7\ m/s$. 116
Fig.4.16. Power spectral density profiles in and out of the wake region in plane Z = 0 at X = 570 mm, $U_\infty = 7\ m/s$. 117
Fig.4.17. Power spectral density profiles in and out of the wake region in plane Z = 0 at X = 580 mm, $U_\infty = 7\ m/s$. 117
Fig.4.18. Power spectral density profiles in and out of the wake region in plane Z = 0 at X = 590 mm, $U_\infty = 7\ m/s$. 118
Fig.4.19. Power spectral density profiles in and out of the wake region in plane Z =0 at X = 600 mm, $U_\infty = 7\ m/s$. 118
Fig.4.20. (a , b) Instantaneous velocity vector and magnitude fields in the wake region- unactuated case, $U_\infty = 7\ m/s$. 120
Fig.4.20. (c , d) Instantaneous velocity vector and magnitude fields in the wake region- unactuated case, $U_\infty = 7\ m/s$. 121
Fig.4.20. (e , f) Instantaneous velocity vector and magnitude fields in the wake region- unactuated case, $U_\infty = 7\ m/s$. 122
Fig.4.20. (g , h) Instantaneous velocity vector and magnitude fields in the wake region- unactuated case, $U_\infty = 7\ m/s$. 123
Fig.4.21. (a , b) Average velocity vector and magnitude fields, unactuated case. 124
Fig.4.21. (c , d) Average velocity vector and magnitude fields, closer view near the reattachment point with smaller display grid factor, Regions A and B of Fig.4.21(a , b) - unactuated case, $U_\infty = 7\ m/s$. 125
Fig.4.22. Streamlines profile - unactuated case, $U_\infty = 7\ m/s$. 126
Fig.4.23. Vorticity Contour in the wake region- unactuated case, $U_\infty = 7\ m/s$. 126

Fig.4.24. RMS Velocity profile in the wake region- unactuated case, $U_\infty = 7\ m/s$. 127
Fig.4.25. RMS Velocity profiles for angular positions of SJAs in plane Z=0, Sine Wave, VR=1.50, Fr=960 Hz, $U_\infty = 7\ m/s$. 128
Fig.4.26. RMS Velocity profiles for different waveforms in plane Z= 0, Sine Wave, VR=1.50, Fr=960 Hz, $\phi = 9.5°$, $U_\infty = 7\ m/s$. 129
Fig.4.27. (a , b) Instantaneous velocity vector and magnitude fields in the wake region- actuated case, Sine wave, VR=1.5, Angular position: $\phi = 0°$, $U_\infty = 7\ m/s$. 131
Fig.4.27. (c , d) Instantaneous velocity vector and magnitude fields in the wake region- actuated case, Sine wave, VR=1.5, Angular position: $\phi = 0°$, $U_\infty = 7\ m/s$. 132
Fig.4.27. (e, f) Instantaneous velocity vector and magnitude fields in the wake region- actuated case, Sine wave, VR=1.5, Angular position: $\phi = 0°$, $U_\infty = 7\ m/s$. 133
Fig.4.28. (a , b) Average velocity vector and magnitude fields in the wake region- actuated case, Sine wave, VR=1.5, Angular position: $\phi = 0°$, $U_\infty = 7\ m/s$. 134
Fig.4.29. Streamlines profile, actuated case, Sine wave, VR=1.5, Angular position: $\phi = 0°$, $U_\infty = 7\ m/s$. 135
Fig.4.30. Vorticity contour, actuated case, Sine wave, VR=1.5, Angular position: $\phi = 0°$, $U_\infty = 7\ m/s$. 135
Fig.4.31. RMS Velocity contour actuated case, Sine wave, VR=1.5, Angular position: $\phi = 0°$, $U_\infty = 7\ m/s$. 136
Fig.4.32. (a , b) Instantaneous velocity vector and magnitude fields in the wake region- actuated case, Sine wave, VR=1.5, Angular position: $\phi = 9.50°$, $U_\infty = 7\ m/s$. 137
Fig.4.32. (c , d) Instantaneous velocity vector and magnitude fields in the wake region- actuated case, Sine wave, VR=1.5, Angular position: $\phi = 9.50°$, $U_\infty = 7\ m/s$. 138
Fig.4.32. (e, f) Instantaneous velocity vector and magnitude fields in the wake region- actuated case, Sine wave, VR=1.5, Angular position: $\phi = 9.50°$, $U_\infty = 7\ m/s$. 139
Fig 4.33. (a , b) Average velocity vector and magnitude fields in the wake region- actuated case, Sine wave, VR=1.5, Angular position: $\phi = 9.50°$, $U_\infty = 7\ m/s$. 140
Fig.4.34. Streamlines profile, actuated case, Sine wave, VR=1.5, Angular position: $\phi = 9.50°$, $U_\infty = 7\ m/s$. 141
Fig.4.35. Vorticity contour, actuated case, Sine wave, VR=1.5, Angular position: $\phi = 9.50°$, $U_\infty = 7\ m/s$. 141

Fig.4.36. RMS Velocity contour actuated case, Sine wave, VR=1.5, Angular position: $\phi = 9.50°, U_\infty = 7\ m/s$. 142
Fig.4.37. (a , b) Instantaneous velocity vector and magnitude fields in the wake region- actuated case, Sine wave, VR=1.5, Angular position: $\phi = 15°, U_\infty = 7\ m/s$. 143
Fig.4.37. (c , d) Instantaneous velocity vector and magnitude fields in the wake region- actuated case, Sine wave, VR=1.5, Angular position: $\phi = 15°, U_\infty = 7\ m/s$. 144
Fig.4.37. (e , f) Instantaneous velocity vector and magnitude fields in the wake region- actuated case, Sine wave, VR=1.5, Angular position: $\phi = 15°, U_\infty = 7\ m/s$. 145
Fig.4.38. (a , b) Average velocity vector and magnitude fields in the wake region- actuated case, Sine wave, VR=1.5, Angular position: $\phi = 15°, U_\infty = 7\ m/s$. 146
Fig.4.39. Streamlines profile, actuated case, Sine wave, VR=1.5, Angular position: $\phi = 15°, U_\infty = 7\ m/s$. 147
Fig.4.40. Vorticity contour, actuated case, Sine wave, VR=1.5, Angular position: $\phi = 15°, U_\infty = 7\ m/s$. 147
Fig.4.41. RMS Velocity contour actuated case, Sine wave, VR=1.5, Angular position: $\phi = 15°, U_\infty = 7\ m/s$. 148
Fig.4.42. (a , b) Instantaneous velocity vector and magnitude fields in the wake region- actuated case, Sine wave, VR=1.15, Angular position: $\phi = 15°, U_\infty = 7\ m/s$. 149
Fig.4.42. (c , d) Instantaneous velocity vector and magnitude fields in the wake region- actuated case, Sine wave, VR=1.15, Angular position: $\phi = 15°, U_\infty = 7\ m/s$. 150
Fig.4.42. (e , f) Instantaneous velocity vector and magnitude fields in the wake region- actuated case, Sine wave, VR=1.15, Angular position: $\phi = 15°, U_\infty = 7\ m/s$. 151
Fig.4.43. (a , b) Average velocity vector and magnitude fields in the wake region- actuated case, Sine wave, VR=1.15, Angular position: $\phi = 15°, U_\infty = 7\ m/s$. 152
Fig.4.44. Streamlines profile, actuated case, Sine wave, VR=1.15, Angular position: $\phi = 15°, U_\infty = 7\ m/s$. 153
Fig.4.45. Vorticity contour, actuated case, Sine wave, VR=1.15, Angular position: $\phi = 15°, U_\infty = 7\ m/s$. 153
Fig.4.46. RMS velocity contour, actuated case, Sine wave, VR=1.15, Angular position: $\phi = 15°, U_\infty = 7\ m/s$. 154

Fig.4.47. (a, b) Instantaneous velocity vector and magnitude fields in the wake region- actuated case, Sine wave, VR=1.85, Angular position: $\phi = 15°$, $U_\infty = 7\ m/s$. 155
Fig.4.47. (c, d) Instantaneous velocity vector and magnitude fields in the wake region- actuated case, Sine wave, VR=1.85, Angular position: $\phi = 15°$, $U_\infty = 7\ m/s$. 156
Fig.4.47. (e, f) Instantaneous velocity vector and magnitude fields in the wake region- actuated case, Sine wave, VR=1.85, Angular position: $\phi = 15°$, $U_\infty = 7\ m/s$. 157
Fig.4.48. (a , b) Average velocity vector and magnitude fields in the wake region- actuated case, Sine wave, VR=1.85, Angular position: $\phi = 15°$, $U_\infty = 7\ m/s$. 158
Fig.4.49. Streamlines profile, actuated case, Sine wave, VR=1.85, Angular position: $\phi = 15°$, $U_\infty = 7\ m/s$. 159
Fig.4.50. Vorticity contour, actuated case, Sine wave, VR=1.85, Angular position: $\phi = 15°$, $U_\infty = 7\ m/s$. 159
Fig.4.51. RMS velocity contour, actuated case, Sine wave, VR=1.85, Angular position: $\phi = 15°$. 160
Fig.4.52. RMS velocity contour, actuated case, Sine wave, VR=2.2, Angular position: $\phi = 15°$, $U_\infty = 7\ m/s$. 160
Fig.4.53. (a , b) Instantaneous velocity vector and magnitude fields in the wake region- actuated case, Sine wave, VR=2.2, Angular position: $\phi = 15°$, $U_\infty = 7\ m/s$. 161
Fig.4.53. (c , d) Instantaneous velocity vector and magnitude fields in the wake region- actuated case, Sine wave, VR=2.2, Angular position: $\phi = 15°$, $U_\infty = 7\ m/s$. 162
Fig.4.53. (e , f) Instantaneous velocity vector and magnitude fields in the wake region- actuated case, Sine wave, VR=2.2, Angular position: $\phi = 15°$, $U_\infty = 7\ m/s$. 163
Fig.4.54. (a , b) Average velocity vector and magnitude fields in the wake region- actuated case, Sine wave, VR=2.2, Angular position: $\phi = 15°$, $U_\infty = 7\ m/s$. 164
Fig.4.55. Streamlines profile, actuated case, Sine wave, VR=2.2, Angular position: $\phi = 15°$, $U_\infty = 7\ m/s$. 165
Fig.4.56. Vorticity contour, actuated case, Sine wave, VR=2.2, Angular position: $\phi = 15°$, $U_\infty = 7\ m/s$. 165
Fig.4.57. (a , b) Instantaneous velocity vector and magnitude fields in the wake region- actuated case, Square wave, VR=1.85, Angular position: $\phi = 15°$, $U_\infty = 7\ m/s$. 167

Fig.4.57. (c , d) Instantaneous velocity vector and magnitude fields in the wake region- actuated case, Square wave, VR=1.85, Angular position: $\phi = 15°$, $U_\infty = 7\ m/s$. 168
Fig.4.57. (e , f) Instantaneous velocity vector and magnitude fields in the wake region- actuated case, Square wave, VR=1.85, Angular position: $\phi = 15°$, $U_\infty = 7\ m/s$. 169
Fig.4.58. (a , b) Average velocity vector and magnitude fields in the wake region- actuated case, Square wave, VR=1.85, Angular position: $\phi = 15°$, $U_\infty = 7\ m/s$. 170
Fig.4.59. Streamlines profile, actuated case, Square wave, VR=1.85, Angular position: $\phi = 15°, U_\infty = 7\ m/s$. 171
Fig.4.60. Vorticity contour, actuated case, Square wave, VR=1.85, Angular position: $\phi = 15°, U_\infty = 7\ m/s$. 171
Fig.4.61. RMS velocity contour, actuated case, Square wave, VR=1.85, Angular position: $\phi = 15°, U_\infty = 7\ m/s$. 172
Fig.4.62. (a , b) Instantaneous velocity vector and magnitude fields in the wake region- actuated case, Square wave, VR=2.2, Angular position: $\phi = 15°, U_\infty = 7\ m/s$. 173
Fig.4.62. (c , d) Instantaneous velocity vector and magnitude fields in the wake region- actuated case, Square wave, VR=2.2, Angular position: $\phi = 15°, U_\infty = 7\ m/s$. 174
Fig.4.62. (e , f) Instantaneous velocity vector and magnitude fields in the wake region- actuated case, Square wave, VR=2.2, Angular position: $\phi = 15°, U_\infty = 7\ m/s$. 175
Fig.4.63. (a , b) Average velocity vector and magnitude fields in the wake region- actuated case, Square wave, VR=2.2, Angular position: $\phi = 15°, U_\infty = 7\ m/s$. 176
Fig.4.64. Streamlines profile, actuated case, Square wave, VR=2.2, Angular position: $\phi = 15°, U_\infty = 7\ m/s$. 177
Fig.4.65. Vorticity contour, actuated case, Square wave, VR=2.2, Angular position: $\phi = 15°, U_\infty = 7\ m/s$. 177
Fig.4.66. RMS velocity contour, actuated case, Square wave, VR=2.2, Angular position: $\phi = 15°, U_\infty = 7\ m/s$. 178
Fig.4.67. Average turbulent kinetic energy at X =0.3 m, $U_\infty = 7m/s$. 179
Fig.4.68. Velocity profile in the boundary layer at X =0.3 m, $U_\infty = 7m/s$. 179
Fig.4.69. Turbulent kinetic energy contour, unactuated case, $U_\infty = 7m/s$. 180
Fig.4.70. Velocity contour, unactuated case, $U_\infty = 7m/s$. 180
Fig.4.71. Pressure contour, unactuated case, $U_\infty = 7m/s$. 180
Fig.4.72. (a) Velocity field, unactuated case, $U_\infty = 7m/s$, and (b) Closer view of the wake region. 181

Fig.4.73. Streamlines profiles, unactuated case, $U_\infty = 7m/s$. 182
Fig.4.74. Surface pressure profile, unactuated case, $U_\infty = 7m/s$. 182
Fig.4.75. Standard deviation of surface pressure profile, unactuated case, $U_\infty = 7m/s$. 182
Fig.4.76. Minimum wall shear stress profile, unactuated case, $U_\infty = 7m/s$. 183
Fig.4.77. History of velocity component in y-direction. 184
Fig.4.78. Pressure contour of single actuator, blowing phase, quiescent flow condition, Z-Y plane. 184
Fig.4.79. Velocity contour of single actuator, blowing phase, quiescent conditions, Z-Y plane. 185
Fig.4.80. (a) Velocity profile, blowing phase, quiescent conditions, X-Y plane and (b) Closer view of generated vortex ring at the orifice outlet. 186
Fig.4.81. Velocity profile, blowing phase, quiescent conditions, Z-Y plane. 187
Fig.4.82. Vorticity contour of single actuator, blowing phase, log scale, quiescent conditions, Z-Y plane. 187
Fig.4.83. Vorticity magnitude profile in Z-Y plane along line Z =0.0006 m, blowing phase. 188
Fig.4.84. (a). Instantaneous velocity field, Time=0.05 s, actuated case, $\phi = 9.5°, U_\infty = 7\ m/s$, and (b) Closer view of the wake region. 189
Fig.4.85. (a). Instantaneous velocity field, Time=0.075 s, actuated case, $\phi = 9.5°, U_\infty = 7\ m/s$, and (b) Closer view of the wake region. 190
Fig.4.86. (a). Instantaneous velocity field, Time=0.15 s, actuated case, $\phi = 9.5°, U_\infty = 7\ m/s$, and (b) Closer view of the wake region. 191
Fig.4.87. (a). Instantaneous velocity field, Time=0.20 s, actuated case, $\phi = 9.5°, U_\infty = 7\ m/s$, and (b) Closer view of the wake region. 192
Fig.4.88. (a). Time averaged velocity field, actuated case, $\phi = 9.5°, U_\infty = 7\ m/s$, and (b) Closer view of the wake region. 193
Fig.4.89. Time averaged velocity contour, actuated case, $\phi = 9.5°, U_\infty = 7\ m/s$. 194
Fig.4.90. Time averaged pressure contour, actuated case, $\phi = 9.5°, U_\infty = 7\ m/s$. 194
Fig.4.91. Time averaged wall shear stress profile on the hump surface contains actuators, $\phi = 9.5°, U_\infty = 7\ m/s$. 195
Fig.4.92. Time averaged vorticity profile on the hump surface contains actuators, $\phi = 9.5°, U_\infty = 7\ m/s$. 195
Fig.4.93. Time averaged wall shear stress -stddev profile on the hump surface and the floor of the test section (downstream of actuators) , $\phi = 9.5°, U_\infty = 7\ m/s$. 196
Fig.5.1. Identification of reattachment point by velocity vector field. 203
Fig.5.2. Identification of separation point by velocity vector field. 203

Fig.5.3. SJAs angular position influence on the separation point location, VR=1.5, Sine Wave, $U_\infty = 7\ m/s$. 210
Fig.5.4. SJAs angular position influence on the reattachment point location, VR=1.5, Sine Wave, $U_\infty = 7\ m/s$. 211
Fig.5.5. SJAs angular position influence on the reduction of recirculation region length, VR=1.5, Sine Wave, $U_\infty = 7\ m/s$. 211
Fig.5.6. Prediction of boundary layer thickness- numerical data versus experimental data, $U_\infty = 7\ m/s$. 217
Fig.A.1. The cylindrical bar in the test section. 242
Fig.A.2. Velocity and RMS V profile behind the cylindrical bar, $U_\infty = 14.25\ m/s$. 243
Fig.A.3. Power spectral density profile, y = 40 mm, $U_\infty = 14.25\ m/s$. 243
Fig.C.1. RMS Velocity profiles in the wake region for free stream velocity of 9m/s in plane Z = 0. 246
Fig.C.2. Trajectory of Max RMS velocity in the wake region for free stream velocity of 9 m/s in plane Z = 0. 246
Fig.C.3. Power spectral density profiles in and out of the wake region in plane Z =0 at X = 570mm, $U_\infty = 9\ m/s$. 247
Fig C.4. Power spectral density profiles in and out of the wake region in plane Z =0 at X = 580mm, $U_\infty = 9\ m/s$. 247
Fig.C.5. Power spectral density profiles in and out of the wake region in plane Z =0 at X = 590mm, $U_\infty = 9\ m/s$. 248
Fig.C.6. Power spectral density profiles in and out of the wake region in plane Z =0 at X = 600mm, $U_\infty = 9\ m/s$. 248
Fig.C.7. RMS Velocity profiles in the wake region for free stream velocity of 12 m/s in plane Z = 0. 249
Fig.C.8. Trajectory of Max RMS velocity in the wake region for free stream velocity of 12 m/s in plane Z = 0. 249
Fig.C.9. Power spectral density profiles in and out of the wake region in plane Z =0 at X = 570mm, $U_\infty = 12\ m/s$. 250
Fig.C.10. Power spectral density profiles in and out of the wake region in plane Z =0 at X = 580mm, $U_\infty = 12\ m/s$. 250
Fig.C.11. Power spectral density profiles in and out of the wake region in plane Z =0 at X = 590mm, $U_\infty = 12\ m/s$. 251
Fig.C.12. Power spectral density profiles in and out of the wake region in plane Z =0 at X = 600mm, $U_\infty = 12\ m/s$. 251
Fig.D.1. (a , b) Instantaneous velocity vector and magnitude fields in the wake region- actuated case, Sine wave, VR=1.5, Angular position: $\phi = 5°$, $U_\infty = 7\ m/s$. 252

Fig.D.1. (c , d) Instantaneous velocity vector and magnitude fields in the wake region- actuated case, Sine wave, VR=1.5, Angular position: $\phi = 5°$, $U_\infty = 7\ m/s$. 253
Fig.D.1. (e , f) Instantaneous velocity vector and magnitude fields in the wake region- actuated case, Sine wave, VR=1.5, Angular position: $\phi = 5°$, $U_\infty = 7\ m/s$. 254
Fig.D.2. (a , b) Average velocity vector and magnitude fields in the wake region- actuated case, Sine wave, VR=1.5, Angular position: $\phi = 5°$, $U_\infty = 7\ m/s$. 255
Fig.D.3. Streamlines profile, actuated case, Sine wave, VR=1.5, Angular position: $\phi = 5°$, $U_\infty = 7\ m/s$. 256
Fig.D.4. Vorticity contour, actuated case, Sine wave, VR=1.5, Angular position: $\phi = 5°$, $U_\infty = 7\ m/s$. 256
Fig.D.5. RMS Velocity contour actuated case, Sine wave, VR=1.5, Angular position: $\phi = 5°$, $U_\infty = 7\ m/s$. 257
Fig.D.6. (a , b) Instantaneous velocity vector and magnitude fields in the wake region- actuated case, Sine wave, VR=1.5, Angular position: $\phi = 12.5°$, $U_\infty = 7\ m/s$. 258
Fig D.6. (c , d) Instantaneous velocity vector and magnitude fields in the wake region- actuated case, Sine wave, VR=1.5, Angular position: $\phi = 12.5°$, $U_\infty = 7\ m/s$. 259
Fig.D.6. (e , f) Instantaneous velocity vector and magnitude fields in the wake region- actuated case, Sine wave, VR=1.5, Angular position: $\phi = 12.5°$, $U_\infty = 7\ m/s$. 260
Fig.D.7. (a , b) Average velocity vector and magnitude fields in the wake region- actuated case, Sine wave, VR=1.5, Angular position: $\phi = 12.5°$, $U_\infty = 7\ m/s$. 261
Fig.D.8. Streamlines profile, actuated case, Sine wave, VR=1.5, Angular position: $\phi = 12.5°$, $U_\infty = 7\ m/s$. 262
Fig D.9. Vorticity contour, actuated case, Sine wave, VR=1.5, Angular position: $\phi = 12.5°$, $U_\infty = 7\ m/s$. 262
Fig.D.10. RMS Velocity contour actuated case, Sine wave, VR=1.5, Angular position: $\phi = 12.5°$, $U_\infty = 7\ m/s$. 263
Fig.D.11. RMS Velocity contour actuated case, Sine wave, VR=1.5, Angular position: $\phi = 17.5°$, $U_\infty = 7\ m/s$. 263
Fig.D.12. (a , b) Instantaneous velocity vector and magnitude fields in the wake region- actuated case, Sine wave, VR=1.5, Angular position: $\phi = 17.5°$, $U_\infty = 7\ m/s$. 264

Fig.D.12. (c , d) Instantaneous velocity vector and magnitude fields in the wake region- actuated case, Sine wave, VR=1.5, Angular position: $\phi = 17.5°, U_\infty = 7\ m/s$. 265
Fig.D.12. (e , f) Instantaneous velocity vector and magnitude fields in the wake region- actuated case, Sine wave, VR=1.5, Angular position: $\phi = 17.5°, U_\infty = 7\ m/s$. 266
Fig.D.13. (a , b) Average velocity vector and magnitude fields in the wake region- actuated case, Sine wave, VR=1.5, Angular position: $\phi = 17.5°, U_\infty = 7\ m/s$. 267
Fig.D.14. Streamlines profile, actuated case, Sine wave, VR=1.5, Angular position: $\phi = 17.5°, U_\infty = 7\ m/s$. 268
Fig.D.15. Vorticity contour, actuated case, Sine wave, VR=1.5, Angular position: $\phi = 17.5°, U_\infty = 7\ m/s$. 268
Fig.D.16. (a , b) Instantaneous velocity vector and magnitude fields in the wake region- actuated case, Sine wave, VR=1.5, Angular position: $\phi = 20°, U_\infty = 7\ m/s$. 269
Fig.D.16. (c , d) Instantaneous velocity vector and magnitude fields in the wake region- actuated case, Sine wave, VR=1.5, Angular position: $\phi = 20°, U_\infty = 7\ m/s$. 270
Fig.D.16. (e , f) Instantaneous velocity vector and magnitude fields in the wake region- actuated case, Sine wave, VR=1.5, Angular position: $\phi = 20°, U_\infty = 7\ m/s$. 271
Fig.D.17. (a , b) Average velocity vector and magnitude fields in the wake region- actuated case, Sine wave, VR=1.5, Angular position: $\phi = 20°, U_\infty = 7\ m/s$. 272
Fig.D.18. Streamlines profile, actuated case, Sine wave, VR=1.5, Angular position: $\phi = 20°, U_\infty = 7\ m/s$. 273
Fig.D.19. Vorticity contour, actuated case, Sine wave, VR=1.5, Angular position: $\phi = 20°, U_\infty = 7\ m/s$. 273
Fig.D.20. RMS Velocity contour actuated case, Sine wave, VR=1.5, Angular position: $\phi = 20°, U_\infty = 7\ m/s$. 274
Fig.D.21. RMS Velocity contour actuated case, Sine wave, VR=1.5, Angular position: $\phi = 25°, U_\infty = 7\ m/s$. 274
Fig.D.22. (a , b) Instantaneous velocity vector and magnitude fields in the wake region- actuated case, Sine wave, VR=1.5, Angular position: $\phi = 25°, U_\infty = 7\ m/s$. 275
Fig.D.22. (c , d) Instantaneous velocity vector and magnitude fields in the wake region- actuated case, Sine wave, VR=1.5, Angular position: $\phi = 25°, U_\infty = 7\ m/s$. 276

Fig.D.22. (e , f) Instantaneous velocity vector and magnitude fields in the wake region- actuated case, Sine wave, VR=1.5, Angular position: $\phi = 25°$, $U_\infty = 7\ m/s$. 277
Fig.D.23. (a , b) Average velocity vector and magnitude fields in the wake region- actuated case, Sine wave, VR=1.5, Angular position: $\phi = 25°$. 278
Fig.D.24. Streamlines profile, actuated case, Sine wave, VR=1.5, Angular position: $\phi = 25°$, $U_\infty = 7\ m/s$. 279
Fig.D.25. Vorticity contour, actuated case, Sine wave, VR=1.5, Angular position: $\phi = 25°$, $U_\infty = 7\ m/s$. 279
Fig.D.26. (a , b) Instantaneous velocity vector and magnitude fields in the wake region- actuated case, Square wave, VR=1.5, Angular position: $\phi = 15°$, $U_\infty = 7\ m/s$. 280
Fig.D.26. (c , d) Instantaneous velocity vector and magnitude fields in the wake region- actuated case, Square wave, VR=1.5, Angular position: $\phi = 15°$, $U_\infty = 7\ m/s$. 281
Fig.D.26. (e , f) Instantaneous velocity vector and magnitude fields in the wake region- actuated case, Square wave, VR=1.5, Angular position: $\phi = 15°$, $U_\infty = 7\ m/s$. 282
Fig.D.27. (a , b) Average velocity vector and magnitude fields in the wake region- actuated case, Square wave, VR=1.5, Angular position: $\phi = 15°$, $U_\infty = 7\ m/s$. 283
Fig.D.28. Streamlines profile, actuated case, Square wave, VR=1.5, Angular position: $\phi = 15°$, $U_\infty = 7\ m/s$. 284
Fig.D.29. Vorticity contour, actuated case, Square wave, VR=1.5, Angular position: $\phi = 15°$, $U_\infty = 7\ m/s$. 284
Fig.D.30. RMS velocity contour, actuated case, Square wave, VR=1.5, Angular position: $\phi = 15°$, $U_\infty = 7\ m/s$. 285

List of Tables

Table 3.1 Losses of Wind Tunnel Components. 72
Table 3.2 Structured Mesh Specifications-Unactuated Case. 99
Table 3.3 Mesh Specifications- Actuated Case. 101
Table 3.4 Constants of $\boldsymbol{k-\omega}$ Shear SST Model Equations. 104
Table 3.5 Boundary conditions relevant to the computational domain shown in Fig.3.22. 106
Table 5.1 Influence of Velocity Ratio VR on the Wake Region Features-Sine Wave. 214
Table 5.2 Influence of Velocity Ratio VR on the Wake Region Features-Square Wave. 216

Chapter 1- Introduction

1.1- Importance and Applications of Flow Separation Control

Shear layer flows are fundamental to many areas of fluid mechanics. They are found anywhere, where the flow experiences high velocity gradients, such as flows around aerodynamics or bluff bodies. Understanding their physics as well as trying to control such flows may have many practical applications including drag reduction in land, air and marine transportation, enhancing heat transfer in industrial devices e.g. heat exchangers or avoiding undesirable structural frequencies in mechanical and civil engineering . Consequently, the research about reattachment of separated flow partially or completely to the surface or delaying the onset of flow separation by control of the natural instabilities alongside increasing the safety level and system performance has a great influence in industries especially in aeronautical and aerospace applications.

Prandtl (1904) was the first researcher who reported influencing of the boundary layer successfully in order to change the aerodynamic performance. This is named flow control. Flatt (1961) proposed a definition for boundary layer control:

"Boundary layer control includes any mechanism or process through which the boundary layer of a fluid flow is caused to behave differently than it normally would were the flow developing naturally along a smooth straight surface."

Flow control can be categorized into two classes: passive flow control and active flow control. The use of vortex generators to affect the separation of turbulent boundary layer is an example of active flow control, (Gallas et al (2004)) or the air flow through the slots between the flap or slat and the main wing of aircraft (Gad-el-Hak (2000)). In case of active flow control, some kind of actuators are applied to interact with the fluid flow. Then, sensors in combination with a feedback loop define the actuation level (Tian et al (2006)).

Passive micro-vortex generators (MVGs) (Schubauer and Spangenberg (1960)) have been used successfully in both low-speed (Jenkins et al (2002) and Lin et al (1990)) and high-speed (McCormick (1992)) applications to control the boundary layer. Lin (2002) carried out a comprehensive review of researches relevant to vortex generator that used MVGs to control the separation of boundary-layer. During passive flow control, auxiliary power is not required and this is the benefit of this method in comparison with the active flow control method and flow control is achieved by geometrical modifications to change the level of mixing or turbulence in the flow.

Active flow control itself is classified into two methods: mechanical and pneumatic. In the first one, moving components interact with the flow field directly, e.g. use of adjustable flaps and slats on aircraft wings. Active pneumatic control involves either suction or blowing or both to inject or remove momentum in or from the flow respectively in order to change the shear or boundary layer momentum and vorticity content. During active flow control, additional energy is required to change the fluid flow in order to generate the favorable effects.Tangential blowing of fluid with high momentum changes the profile of velocity in the boundary layer in such a way that it withstands more against flow separation. The blowing can be performed in a steady method or in a periodic method. The mass flow required for flow control is reduced by the periodic method and large stream-wise vortical structures are produced by mixing of the low momentum boundary layer with free stream fluid possessing higher momentum. Combinations of these methods are also possible. A common combination is shifting periodically between blowing and suction in a way that net mass flux is zero.

Prandtl performed a series of experiments in the water tunnel to delay flow separation in the flow over a circular cylinder, flow separation was delayed by suction through a slot. This can be observed in images of flow visualization, as shown in Fig.1.1. Regular flow separation by the vortical structures behind the circular cylinder can be seen clearly, separation delay achieved by suction through a slot on the upper side of the circular cylinder at about the two o'clock position.

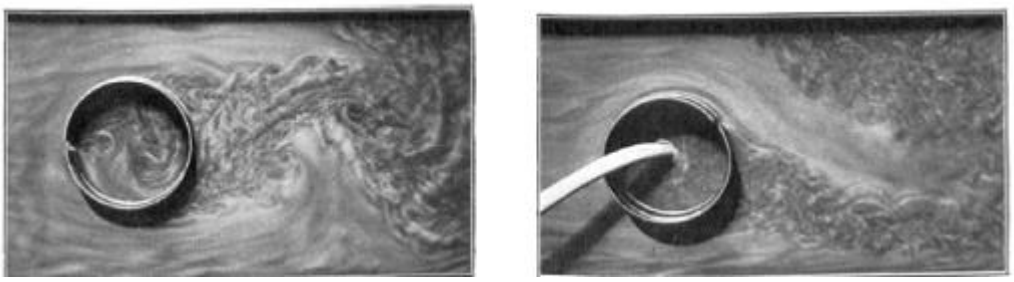

Fig.1.1. Flow visualization with no control (left) and with flow control (right) (Prandtl (1904)).

Active flow separation control has different applications in industries such as the drag reduction of the generic land vehicle (Aubrun et al (2010)), aerodynamic improvement of micro-aerial vehicles (Ugrina and Flatau (2005)) or bluff body shape of a helicopter fuselage (Potsdam and Le Pape (2008)) and flow separation control on turbine (Rivir et al

(2004) and Tesař et al (2008)) and compressor blades (Evans et al (2008)) to enhance their efficiency. Investigation of control of flow separation on flaps and slats of high-lift multi-element wing sections to enhance the aerodynamic performance at landing and take-off has been done by the Boeing company (Shmilovich and Yadlin (2009) and DeSalvo et al (2010)). Aerodynamic performance of airplane wings can be decreased considerably by flow separation. The flow separates because there is no enough momentum in the boundary layer to affect the adverse pressure gradient along the surface of airfoil . Control of flow separation influences the flow actively as flow separation is delayed and the performance of airfoil is enhanced (Koopmans and Hoeijmakers (2014)).

1.2- Aim and Objectives of the Current Research

Significant researches are published regarding fluid flow separation and its control, but the number of publications regarding flow separation control over hump models by utilization of synthetic jet actuators is limited. This research adds to the findings of this limited body of research, but also tries to answer some of discrepancies reported by other researchers, e.g. the deficiency of flow physics in vicinity of reattachment point of separated flow over circular hump model reported by Azzawi (2016) who previously worked on flow separation control under supervision of Prof. Jaworski. In addition, different ranges of actuation frequencies as well as actuation voltage (or velocity ratio) are reported by researches as the optimum values to achieve the best performance of active flow control. The effect of these parameters will be discussed in Chapter 2 in detail.

As mentioned above, the researches regarding flow separation and its control over hump model and specifically the circular hump is limited and the impact of important geometrical and operational parameters either is not studied, e.g. the influence of location of actuators, or is investigated in a limited range, e.g. considering velocity ratios (VR) just below value of 1.5 as well as considering a limited number of waveforms. In addition, the synthetic jet actuators are rarely fully simulated by Computational Fluid Dynamics (CFD) tools by researchers due to the excessive computational cost and the SJA is mainly considered in two dimensions and without simulation of cavity and membrane oscillations. Moreover, interaction of Vortical structure produced by synthetic jet actuators with cross flow rarely has been studied in three dimensions and the researches don't give information about flow in span-wise direction. In this research, it is tried to cover these deficiencies both experimentally and numerically.

In this thesis, an array of synthetic jet actuators is used to produce vortical structures in the boundary layer to interact with the quasi-periodic structures that are responsible for instabilities of fluid flow

in order to reattach the boundary layer completely or partially by delaying the onset of separation over a convex hump model by either reducing the recirculation width and reattachment point behind the hump, or changing the dominant frequency in the power spectral density of the vortex shedding.

The overall aim of this thesis study is to draw conclusions about the fluid dynamical mechanisms behind this method of flow actuation by using different measurement techniques including Particle Image Velocimetry (PIV), Hot Wire Anemometry (HWA) and suitable data processing techniques. In addition, a comprehensive numerical analysis is carried out to investigate some flow characteristics that cannot be studied experimentally due to limitations of the experimental equipment.

As a result of analysis of research gaps identified above, the following objective have been formulated:

1. Design, manufacture, and test a low speed closed circuit wind tunnel to enable the research
2. Design, manufacture and test a hump model to use in the current study
3. Optimize the geometrical and operational parameters that have greatest effect on the performance of synthetic jet actuators
4. Investigate and identify the onset of flow separation location, size of separation bubble, reattachment point location and shear layer vorticity over the existing model without actuation (baseline case), at chord Reynolds number in range of 10^5 in turbulent regime
5. Identification of the dominant frequency of the vortex shedding at the chosen baseline configuration and attempt to alter the structures that are responsible for instabilities of boundary layer by interaction of synthetic jet actuators with these structures
6. Investigate the effectiveness of synthetic jet actuators in reduction of instabilities by changing the actuation parameters, including angular position of synthetic jet actuators, the ratio of the peak exit jet velocity of actuators to the free stream velocity of cross flow (VR), actuation frequency and waveform
7. Use CFD modelling to compare with the experimental results and identify the flow mechanism behind SJA control, which cannot be easily found by experiments due to their limitations.

In Chapter 2, the physics of flow separation phenomenon and flow reattachment will be reviewed. The history, theory and the mechanism of synthetic jet actuators as well as the impacts of factors including geometrical and operational parameters on the performance of

synthetic jet actuators are reviewed and discussed. Finally, the interaction of synthetic jet actuators with the cross flow is discussed by review of selected experimental and numerical researches.

In Chapter 3, the design and manufacturing processes of the low speed closed circuit wind tunnel and the hump model are explained. The geometry of actuator array and the required driving circuit, including function generator and amplifier to drive the piezo-electric diaphragms, will be described. Then, the experimental setups of Hot wire Anemometry (HWA) and Particle Image Velocimetry Technique (PIV) will be explained in detail. In addition, the relevant calibration procedures for both techniques and suitable data post processing methods will be described. Finally, the methodology of numerical simulations will be illustrated.

In Chapter 4, the results of measurements of the wind tunnel flow quality will be presented. Then, the results of Hot Wire Anemometry (HWA) technique for quiescent flow conditions will be illustrated. The predictions of flow features by Hot Wire Anemometry (HWA) and Particle Image Velocimetry (PIV) techniques for both unactuated (baseline) case and actuated case will be shown. Finally, the predictions by numerical analysis for all quiescent flow conditions, unactuated (baseline) case and actuated case will be presented.

In Chapter 5, the presented experimental and numerical results are discussed in detail. In Chapter 6, the main conclusions of the research is drawn and some recommendations for supplementary research will be given. In Appendix A, more details about the test of hot wire system performance, data acquisition software as well as sample size and sampling rate of data is provided. In Appendix B, MATLAB programs to help the Hot Wire Anemometry (HWA) data processing is shown.In Appendices C, D and E, additional results of Hot Wire Anemometry (HWA) experiments, Particle Image Velocimetry (PIV) tests as well as numerical simulations will be shown.

1.3- Summary

An introduction to the applications and importance of flow separation control was provided. Also, the background of the current study, the research gaps, aim and objectives of the current research as well as the structure of the thesis were provided. In Chapter 2, the physics of flow separation phenomenon, theory and mechanism of SJAs as well as their interactions with cross flow will be reviewed and discussed.

Chapter 2- Literature Review

In this chapter, a broad range of studies regarding flow separation phenomenon, history, theory and mechanism of synthetic jet actuators, effective parameters on their performance as well as their interaction with uniform cross flow and active flow control are reviewed comprehensively and unanswered and ambiguous areas that require more investigation will be recognized.

2.1- Flow Separation and Reattachment

Bluff bodies are ever-present aerodynamic shapes, their characteristic periodic vortex shedding characteristics are features that if understood well enough, could be influenced to greatly reduce drag in road vehicles, or structural weight and cost in buildings due to the reduced wind loads. When flow separation happens on a surface, the velocity boundary layer will be detached from the surface, leading to unsteady flow conditions (Chang (1961), Schlichting et al (2006) and Bohl et al (2008)). Boundary layer detached from the surface of solid due to adverse pressure gradient. Fig.2.1 shows two types of flow separation: The pressure based flow separation, Fig.2.1(a), as a result of adverse pressure gradient happening at shapes without sharp edges e.g., airfoil and geometrically-based flow separation due to geometrical irregularity e.g., wall of house, as presented in Fig.2.1(b) (Sturm et al (2012)).

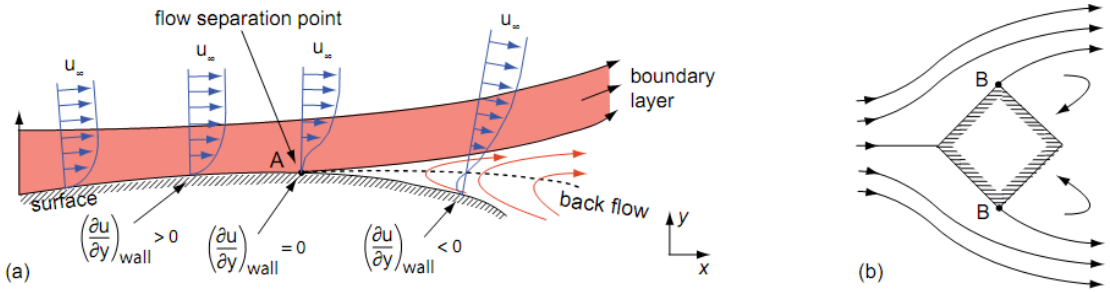

Fig.2.1. Pressure based (a) and geometrical based (b) flow separation with A and B as separation points (Sturm et al (2012)).

While a fluid particle arrives at the front of profile of airfoil, its direction is changed and consequently accelerated up to a peak velocity. Then fluid is decelerated from the maximum velocity down to the trailing edge because of increasing of static pressure, it is supposed that the fluid particles have a constant total energy and energy conversion occurs from static pressure energy to kinetic energy and in a reverse direction from kinetic energy

to static pressure energy. If we consider the effects of friction, then an amount of the total energy is wasted leading to a smaller values of kinetic energy. Consequently, at certain flow conditions, there will be not sufficient kinetic energy of the fluid particles to conquer the enhancing static pressure at the airfoil's rear. Velocity of fluid particles in the boundary layer very close to the surface experiencing the maximum friction drops about to zero. The boundary-layer flow is separated from the surface and eddies and vortices are formed and hence drag increases, specially pressure drag (Gad-el-Hak (2000), Sturm et al (2012), Ishtiaq et al (2016) and Genc et al (2012)).

Physics behind this phenomenon can be explained mathematically via the governing Navier Stocks equations for stationary case:

$$\frac{\partial \vec{V}}{\partial t} + (\vec{V}.\vec{\nabla}).\vec{V} = -\frac{1}{\rho}\vec{\nabla}p + \nu\Delta\vec{V} + \frac{1}{\rho}\vec{F} \qquad (2.1)$$

which ρ and ν are density and kinematic viscosity respectively, $\vec{V} = (u, v, w)$ is velocity field vector, $\vec{\nabla}p$ is pressure gradient, $\nu\Delta\vec{V}$ shows the friction effect and $\Delta = \frac{\partial^2}{\partial x^2} + \frac{\partial^2}{\partial y^2} + \frac{\partial^2}{\partial z^2}$ is the Laplace operator and $\vec{F}$ is the amount of external force per volume, (Stocker (2007)). In steady state case, by considering the surface at $y = 0$, and without external force, the equation (1) is reduced to the following equation:

$$0 = -\frac{1}{\rho}\frac{\partial p}{\partial x} + \nu\frac{\partial^2 u}{\partial y^2} \qquad (2.2)$$

The velocity profiles can be achieved in 3 cases: $\frac{\partial p}{\partial x} < 0, \frac{\partial p}{\partial x} = 0$ and $\frac{\partial p}{\partial x} > 0$ as shown in Fig.2.2.

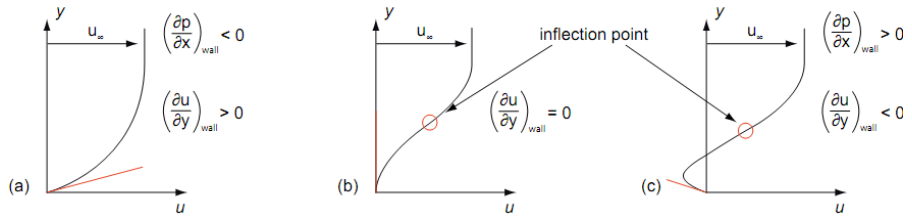

Fig.2.2. Velocity profile before (a), while (b) and after (c) separation of boundary layer (Sturm et al (2012)).

For the favorable gradient case (Fig 2.2(a)) there is no point of inflection and the profile is very rounded and consequently, fluid flow separation cannot occur and laminar profile is very resistant against transition to turbulence region. When we have a zero pressure gradient (Fig 2.2(b)), the point of inflection is at the wall and in this case, the separation again cannot occur. In an adverse pressure gradient (Fig 2.2(c)), point of inflection occurs in the boundary layer and its distance from the wall increases as the strength of adverse pressure gradient increases.

For a mild pressure gradient, a critical condition occurs where the wall shear becomes zero ($\frac{\partial \mathrm{u}}{\partial \mathrm{y}} = 0$) (Genc et al (2012)). This point is considered as the separation point, because reverse flow is created by any stronger gradients. Boundary layer thickness increases significantly and the main flow peeled away, or separated from the surface (White (2004)). The volume contains slowly recirculating air in between the reattachment point and separation point is named Laminar Separation Bubble or Turbulent Reattachment Bubble (Mayle (1991)).

The mechanism of laminar separation bubbles was first studied by Jones (1934) and also investigated deeper by Gaster (1963). They studied experimentally the stability behavior of the separation bubble. Horton (1968), developed an original semi-empirical bubble model in 1968 which has been broadly used in similar studies. Further studies in the characterization of laminar separation bubble have been done by McGregor (1954), Woodward (1970) and Young and Horton (1996). Broader studies on LSB and low Reynolds aerodynamics were carried out by Tani (1964), Lissaman (1983) and Carmichael (1981). Laminar separation bubbles can be categorized as short and long bubbles. The location and size of the bubble can't be given precisely because it is a function of different parameters in real flow conditions such as airfoil shape, roughness, angle of attack, freestream disturbances and Reynold number (Shah et al (2015), Genc et al (2012), Tani (1964) and Swift (2009)). The laminar separation bubble moves forward and shrinks in stream-wise extent by increasing of attack angle, which are categorized as short bubbles (Tani (1964)). Within this type of bubble, a small region of constant pressure can be detected, which leads to plateau in the profile of pressure distribution, as shown in Fig.2.3. The curve of the pressure distribution is recovered due to reattachment.

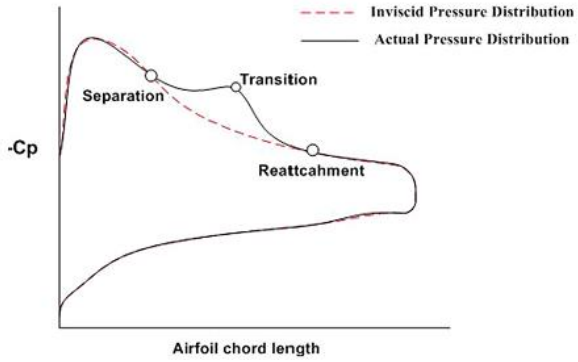

Fig.2.3. Surface pressure distribution with laminar separation bubble (Shah et al (2015)).

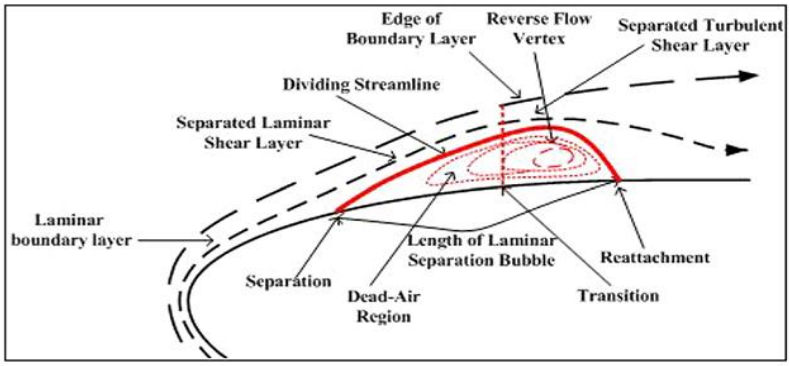

Fig.2.4. Illustration of laminar separation bubble (Shah et al (2015)).

When the attack angle enhances more, the separation point gets closer to the leading edge, and at a specific attack angle, the flow can no longer reattach to the surface of airfoil within a short distance. This phenomenon is named burst or breakdown of bubble (Genc et al (2012)). Flow separation doesn't occur completely due to occurrence of the breakdown phenomenon. The separated flow travels above the airfoil and it is reattched down-stream. The flow region under the detached flow circulates slowly and is called long bubble or dead-air region, as shown in Fig.2.4.

Tan & Auld (1992) studied the fluid flow over a Wortman FX67-150K airfoil at different Reynold numbers turbulence levels. They reported that short separation bubbles formed at moderate pressure gradient, and when pressure gradient is increased, the short separation bubble burst, leading to long separation bubble. They found that the flow will be reattached quickly after the transition for the short separation bubble case, while reattachment of the flow couldn't occur quickly for the long separation bubble case.

Separation and reattachment phenomena are also present in three dimensional flows (e.g. flow over swept wing). However, there is an additional complication of the presence of leading edge vortex which may burst (so called vortex breakdown) and which leads to a sudden change of structure of the leading edge vortex.

The two main geometric factors that are effective on the location of the vortex burst over a wing surface are the angle of attack and the angle of sweep of the wing. The vortex burst location moves towards the wing apex by increasing the angle of attack, whereas an increase in the sweep angle will cause the burst location moves toward the trailing edge of the wing and possibly into the wake. Lambourne and Bryer (1961), studied the bursting of leading edge vortices for very low speeds of flow (about 2 in. per sec) were made in water using a flat plate delta having 65^{o} sweep and beveled to 16^{o} on the underside, they categorized two distinct types of burst including spiral and bubble, they observed the behavior of dye introduced as a filament ahead of the apex of the model so that it was injected into one or both of the vortices and travelled close to the axis of the laminar vortex as shown in Fig.2.5.

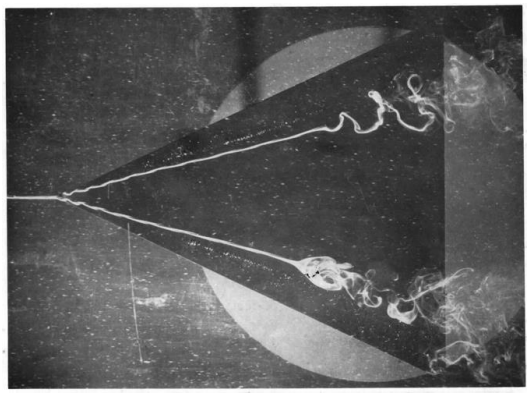

Fig.2.5. Axial filaments of dye, water tunnel, 2 in./sec, bubble (bottom), spiral (top) burst types (Lambourne and Bryer (1961)).

Sarpkaya (1971) carried out a research on stationary and travelling vortex breakdowns and identified three types of burst including bubble type (highly axisymmetric), spiral type (highly asymmetric) and a double helix form between bubble and spiral types. Bubble type is originated from high swirl velocities while spiral type is induced by lower velocities. Johari et al (1995) used Recessed Angled Span-wise Blowing (RASB) technique by mixing between blowing normal to the lifting surface and tangential to it and they discovered that RASB, with the jet of air

travelling from inboard to outboard, applied downstream of the natural burst location could delay the onset of burst phenomenon by up to 15% of the chord length. Jaworski (1996) carried out a considerable number of velocity and pressure measurements in the post-burst region of a delta wing. Phase locking techniques have been used in his measurements to identify the presence of the spiral instability in the flow.

Helin and Watry (1994) used a jet of air from the trailing edge of a delta wing (trailing edge blowing technique) to change the flow above the wing, they discovered that the presence of a trailing edge jet could shift the burst downstream by up to 18% of the chord. Shih and Ding (1996), showed the burst delay can occur in the presence of a trailing edge jet.

2.2. History, Theory and Mechanism of Synthetic Jet Actuators

Synthetic jet actuators have been used by many researchers successfully to remove or delay the fluid flow separation in a broad range of applications. In this section, history and principles of operation of this technology is investigated.

Synthetic jet technology has been tested as an excellent and promising means of active flow control in aeronautical and aerospace applications, including flow separation control (Zhong et al (2007), Amitay et al (2001), Amitay and Glezer (2002), Honohan et al (2000), Seifert and Pack (1999), Smith et al (1998), Wang et al (2007), Amitay et al (2004) and Wang et al (2014)), turbulence control (Rathnasingham and Breuer (2003)) and mixing control/ enhancement (Pavlova et al (2008) and Liu et al (2008)), vectoring (Xia and Luo (2007)), improvement of heat (Vukasinovic and Glezer (2003)) and mass transfer (Tesa (2009)), and increase of propulsion (Polsenberg et al (2005)).

The main purpose of the synthetic jets is production of a non-zero momentum flux with a zero net mass flux. Synthetic jets utilize the ambient fluid as the working fluid and they do not require a complex piping system (Bazdidi-Tehrani et al (2016)).

A typical synthetic jet, as shown in Fig 2.6, including an oscillating actuator connected to a semi-closed cavity that has a slot or orifice. The actuator of synthetic jet can be a diaphragm (Vukasinovic and Glezer (2003)), a speaker (Jin et al (2014) and McCormick (2000)), or mechanical piston (Iuso et al (2005) and Crook (2001)). An oscillatory flow is produced by changing the cavity volume at a specific frequency.

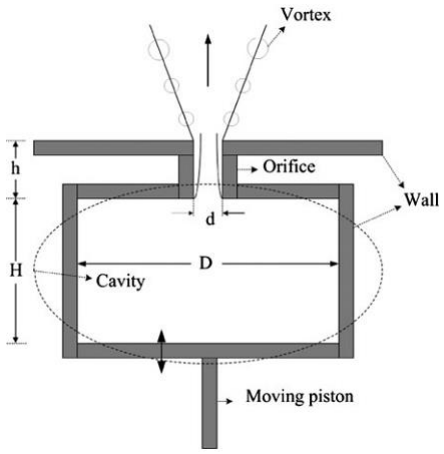

Fig.2.6. Schematic of components for generation of SJ (Bazdidi-Tehrani et al (2016)).

The exploded view and assembled view of the diaphragm actuator is shown in Fig.2.7. The piezo diaphragm is a bimorph sound component with part number P412013T-JB manufactured by APC International, Ltd (Koopmans and Hoeijmakers (2014)).

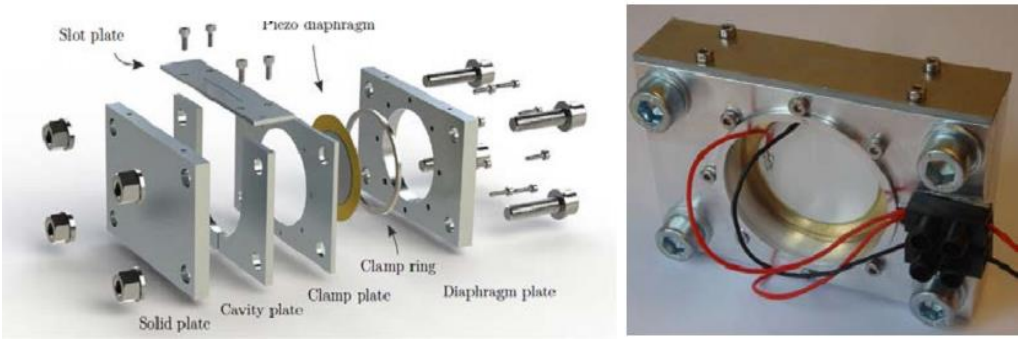

Fig.2.7. The exploded view (left) and assembled (right) view of diaphragm actuator (Koopmans and Hoeijmakers (2014)).

Fig.2.8 shows the four stages of generation of a vortex ring by a synthetic jet. Fluid is drawn into the chamber from around the orifice during the membrane's down-stroke. During the membrane up-stroke, fluid is ejected through the orifice, producing a vortex ring.

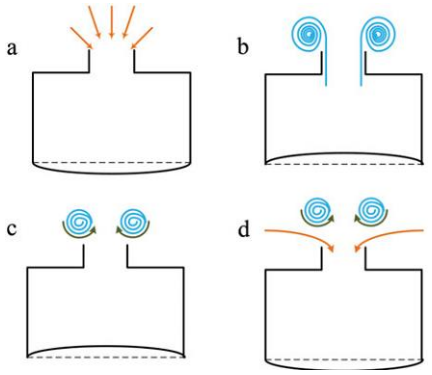

Fig.2.8. Four stages of synthetic jet (Polsenberg et al (2005)).

Vortex rings are produced in each cycle, and by repetition of cycles, a sequence of vortices is generated. The vortices spread away from the orifice under their own self-induced velocity. The synthetic jet drags the low momentum fluid in the boundary layer during down-stroke, and during the up-stroke the fluid adds momentum to the boundary layer. The main criterion for the formation of a synthetic jet flow is that a vortex ring produced during the phase of blowing has adequate distance from the orifice exit, therefore it is not drawn into the cavity during the phase of suction (Bazdidi-Tehrani et al (2016)).

The criterion for formation of synthetic jets has been discussed in a numerical and experimental work by Holman et al (2005). They computed the criterion of formation of two dimensional axisymmetric synthetic jets based on dimensionless numbers such as the Stokes number, Strouhal number and Reynolds number.

The oscillation of the diaphragm produces consecutive vortex structures that spread away from the orifice, forming a so-called synthetic jet. SJA can be performed easily in array to attain better flow control impacts due to its zero-net-mass-flux nature and compactness. This characteristic, together with others such as lack of piping systems (Bazdidi-Tehrani et al (2008)), having minimum movable parts (Polsenberg et el (2005)), makes SJA a better flow-control device in comparison to other traditional techniques. As for the flow separation control utilizing SJs, it is generally understood through three processes. First, additional momentum is injected into the ambient freestream flow by SJs directly, and the retarding boundary layer would be reenergized. This process is alike to steady blowing and has a restricted impact within a range of several diameters of orifice. (Tang et el (2014)). Second, the outer high-momentum flow into the boundary layer is brought by the

consecutive vortex structures generated by a SJA (Zhong et al (2007)). This is the same working mechanism of vortex generators and this also has a limited impact in control of flow separation. Third, the instability of the separated shear flow or separation bubble is influenced by the oscillation of SJs at specific frequencies and the large scale flow structures associated with the separated shear flow are broken into small-scale ones (Seifert and Pack (1999), Mittal et al (2005) and Hong (2006)).

Breaking of uncontrolled large scale flow structures into small-scale structures is helpful to re-attach the separated flow. The generation of synthetic jets considerably deforms the flow structures of the separated shear layer, also the high-momentum flow from upper layers is transferred into the near-wall region (Tang et el (2014)). After turning on the array of SJA, the flow separation is attenuated and the near-wall flow is reenergized and delays the flow separation.

The actuator has an important role in performance of the synthetic jets. The actuator of synthetic jet can be a diaphragm, a speaker, or mechanical piston. Tensi et al. (2002) used actuator of mechanical piston type with a slot opening on a cylindrical surface. It was revealed that the separation line was pushed back downstream significantly when the actuator was active.

Gilarranz and Rediniotis (2001) utilized piston actuator in their study, in the smoke visualization experiments, they applied the slot exit actuator on the top surface of NACA0015 aerofoil while attack angle was changed. At 20^{o} angle of attack and with the actuators inactive, the separation occurred at the leading edge, while the separation line had been pushed back downstream about 70 % of chord length when the actuators were active.

Piezo-electric diaphragms are being used widely in low voltage sound devices such as cellphones, buzzers and speakers and their displacement is large enough for use in effective synthetic jet actuators and they have many benefits than other actuators including having low mass, small size and being cheap (Koopmans and Hoeijmakers (2014)), high bandwidth, low-power requirements and broadband output from DC to AC in the several Kilo-Hertz range (Cattafesta and Sheplak (2011)).

2.3- Effective Design Parameters

However, the application of synthetic jet actuators is very effective to control the boundary layer flow separation, but the design of such technology is hard due to the complicated physics involved alongside high computational cost of fluid flow simulation. Optimization of geometry of synthetic jet actuators and operational parameters can give us a better understanding of the dimensionless parameters which determine the formation and development of vortex rollup and improvement of rollup strength. In the next sections, the effective parameters on performance of synthetic jet actuators including geometrical and operational parameters alongside non-dimensional parameter will be investigated.

2.3.1- Geometrical Parameters

The geometrical parameters including orifice shape, cavity shape and location of actuators are broadly investigated by researchers to optimize the performance of synthetic jet actuators. The formation of the vortical structures that form the synthetic jet is affected by the geometry of orifice. Kim et al (2012), studied the generation and evolution of synthetic jets exiting from circular and rectangular outlets in the direction normal to the surface. They found that circular exits have better performance than rectangular exits in terms of flow control ability and sustainable vortical structures. Also, they carried out some comparative studies according to the hole gap and the hole diameter to find an optimum shape of multiple serial circular exits, results showed that the hole gap had more considerable impact on characteristics of flow then the hole diameter.

Azzawi (2016) studied the effects of geometrical parameters on the effectiveness of synthetic jet actuators by considering three orifice diameters of 1.2 mm, 2.5 mm and 5 mm, and three cavity heights of 3mm, 3.5mm and 5.5 mm with a maximum cavity diameter of 32 mm. Results showed that the peak jet velocity was decreased by increasing the cavity height. He carried out some comparative studies on single, double and multiple orifice actuators to study the benefits of multiple orifice actuators over one orifice actuator to attain higher level of circulation, an optimum spacing of 10 mm was found to decrease the loss or cancellation of the vortex rings. Also, a higher vortex ring circulation (200%) and consequently, a larger amount of fluid and momentum transformation to the cross flow was achieved by using a three-orifice actuator.

Vasile and Amitay (2012), Amitay and Glezer (2002), Mossi and Bryant (2004), Kim and Garry (2006), Yang (2009) and Oyarzun and Cattafesta (2010) have used rectangular orifices in their studies. Vasile and Amitay (2012) have studied flow control for a finite and for a swept-back wing experimentally. They carried out Stereoscopic PIV measurements in a rectangular domain to better understand fluid flow structures around the synthetic jet. They considered 3 blowing ratios of 0.8, 1.2 and 2, and observed that the flow field becomes highly three dimensional in the adjacent of synthetic jet orifice and it is influenced by stream-wise structures which are connected to the finite span of the jet (edge vortices). Kim and Garry (2006) investigated the effect of changing the orifice aspect ratio and also the cavity depth by designing a modular SJA with a rectangular orifice. They changed the ratio of the length-to-width of the slots without maintaining a uniform orifice area, and consequently it is hard to evaluate the real effect of aspect ratio for equivalent designs. They found that for rectangular slots, the more uniform velocity distribution was achieved for aspect ratios less 10. Also, they observed that the jet output was increased by decreasing the cavity depth.

Yang (2009) designed a dual-diaphragm synthetic jet actuator to analyze the produced flow experimentally via PIV measurements. The results of these experiments are then compared with results of numerical simulations. He found that the jet output is increased by decreasing cavity depth and slot width, and the velocity magnitude could be controlled via adjustment of voltage magnitude. Smyk (2018) investigated, the effectiveness of synthetic jet actuators in 3 cases including one diaphragm, two diaphragms and damped chamber diaphragm. The actuators were utilized close to characteristic frequency, and the characteristic velocity as a function of the input power were evaluated. In case of using synthetic jets actuator with two diaphragms the value of momentum flux was increased around 79.62% and kinetic energy and energetic efficiency values were enhanced around 140.72% and 140.72%, respectively in comparison to actuator with one un-damped diaphragm by the same power input value.

Oyarzun and Cattafesta (2010) optimized orifice and cavity dimensions for a piezo disk with determined limitations. The optimized result has been manufactured and tested experimentally to verify the numerical simulation. Good agreement between the model and experimental data was achieved, the only deviation of agreement found for very small values of both the cavity and orifice heights. Based on the comparison between the model and experiments, a

nonlinear limitation was extended in terms of the height of cavity and orifice that was utilized in the optimization. They observed that for a given diaphragm, there is a single resonant peak in the frequency response for a range of Helmholtz frequencies, while actuator response had two resonant peaks outside of this range.

Feero et al (2014) investigated the effects of cavity shape on the jet performance by using cylindrical, conical and contraction cavities, while geometric similarity was maintained between cavities, they showed that the maximum momentum flux is achieved by applying cylindrical cavity and decreased from the conical to contraction cavity. They also considered the fluidic efficiency and found that noticeably less power was consumed by the contraction cavity at the resonant peak, and the maximum efficiency is attained at the resonance due to the lower Helmholtz frequency. However, Utturkar et al (2003) had investigated the sensitivity of synthetic jets to the design of the cavity in a numerical study. They reported that the jet exit flow was not greatly affected by different designs of cavity and the changes were relatively limited.

Greco et al (2013) have studied flow features in the near field of single and twin synthetic jets experimentally. They evaluated the influence of jets interaction by varying the jet axis distances with values of 1.1, 3 and 5-nozzle diameters. They found that twin circular synthetic jets at jet axis distances equivalent to 3 and 5 diameters have the same behavior with respect to the single circular synthetic jets, while a double vortex ring structure observed at jet axis distances equal to 1.1 diameters. This led to a different velocity distribution in the jet core, a lower jet width and higher axial velocities.

Jin et al (2014) showed that the change in orifice shapes and the cavity can enhance the value of maximum velocity, however this does not signifies an enhancment in Reynolds number or mass flow rate necessarily. Nani and Smith (2012) studied the efficiency of an axisymmetric synthetic jet actuator experimentally as a function of radius of curvature of the orifice inner edge in quiescent conditions. It was revealed that momentum flux downstream of the jet exit has not dependency to the orifice inner lip radius considerably, and therefore power consumption can be decreased by rounding the inner lip significantly.

Watson et al (2003) studied the synthetic jets from rectangular and dual-circular orifices, they investigated the effects of spacing between adjacent orifices and the level of excitation applied

to the diaphragm. They showed a rectangular orifice of a given exit plane area is more probable to generate a turbulent ring than the equivalent circular orifice due to a smoothing process which tries to create an axisymmetric ring from a non-axisymmetric slug of fluid. For well-spaced orifices two distinct rings are formed, one from each orifice, and propagate away from the plate with no interaction between them, as shown in Fig.2.9 (Watson et al (2003)).

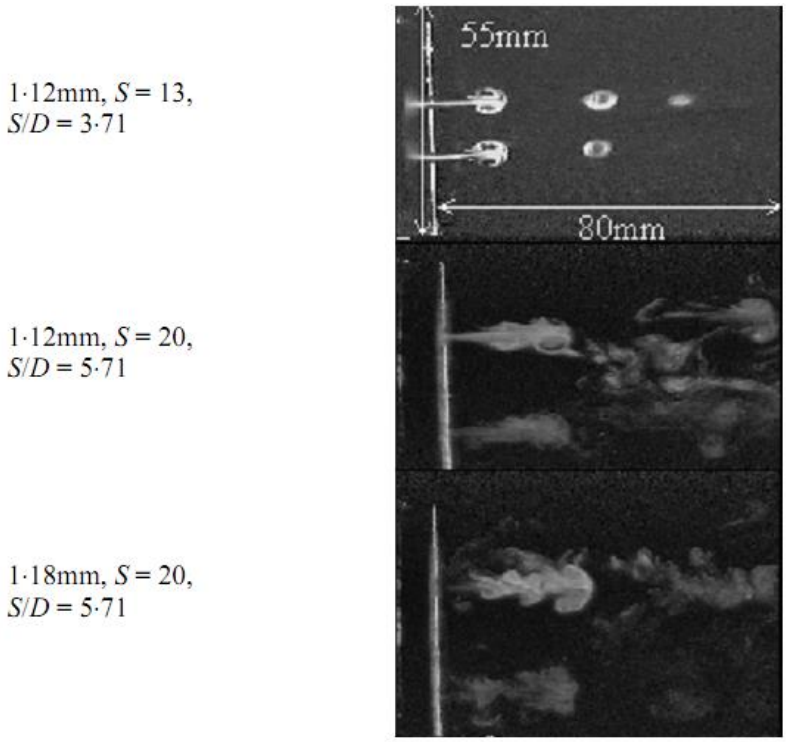

Fig.2.9. Well-spaced orifices case, in terms of the diaphragm displacement level, the actual orifice spacing and non-dimensional spacing given by the orifice spacing divided by the orifice diameter (Watson et al (2003)).

Kumar et al (2019) experimentally investigated a rectangular orifice synthetic jet at varying orifice aspect ratios and actuation frequencies, bifurcation of vortex rings in a synthetic jet of rectangular orifice was revealed using measurements of LIF imaging and Hot-film.

In a numerical study, Eri et al (2018) investigated the effect of the ambient temperature on the performance of piston type SJA as well as the impact of the auxiliary air inlet on performance of this type of SJA for high temperature conditions (T=800K). Also, the influence of the orifice diameter and the actuation frequency on jet momentum, mass flow and cylinder pressure were investigated for high and normal temperature conditions. They found that

ambient temperature had a considerable influence on the performance of SJA. By increasing the ambient temperature, the suction mass flow of the SJA is reduced and the jet velocity at outlet plane is increased to some extent, and consequently maximum jet momentum is decreased. Also, by increasing the orifice diameter and reducing actuation frequency, the reduction in SJA mass flow between high and normal temperatures is increased. At high temperature, the suction capacity of the SJA has been increased considerably by auxiliary air inlet, results are shown by Figs.2.10 and 2.11

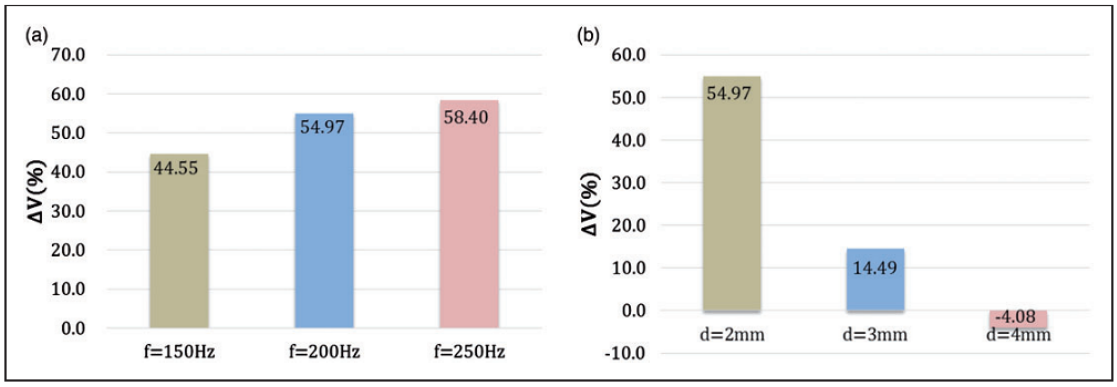

Fig.2.10. Maximum jet velocity changes between normal and high temperatures. (a) d=2 mm, (b) f=200 Hz, Eri et al (2018).

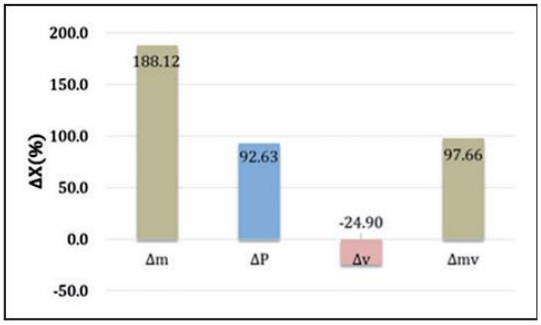

Fig.2.11. Profile of changes of maximum velocity and maximum momentum, peak pressure ratio and suction air mass between the SJAcon and SJAau (f=200 Hz, d=2 mm, T=800 K), Eri et al (2018).

Mu et al (2018) carried out a numerical analysis of unsteady synthetic jet by utilization of the 3-dimensional lattice Boltzmann method. The method predicted the expected flow feature in comparison with experimental data alongside supplying insight into the mechanism of suction and blowing strokes. Also, the anticipated zero-net mass-flux behavior was approved. It was observed that the suction flow is occurred along the periphery of the jet and the blowing flow along the centerline of the orifice.

The location of the SJA has a great importance to function flow separation control properly, for the sake of more effectiveness, it should be placed upstream of the location of separation. Seifert & Pack (2002) investigated the dependence on the actuator location and they found that an actuator should be positioned close to the separation point. Duvigneau et al (2006) found numerically the best location of the SJA at 23% of chord in order to enhance the time-averaged lift for a NACA0012 airfoil at a Reynolds number of 2×10^6 and an angle of attack of 18 degree.

2.3.2- Operational Parameters

The most important operational parameters that are influential on the synthetic jet formation and peak jet velocity are diaphragm type, waveform type, excitation frequency, excitation amplitude and amplitude modulation techniques.

Mallinson et al (1999), Smith et al. (1999) and Azzawi (2016) utilized piezoelectric diaphragm actuators in their research, since they are easy to build and could be operated over a broader range of frequency. However, a maximum peak to peak input voltage of no more than 15Vpp approximately is recommended by manufactures (Oyarzun and Cattafesta (2010)) but values of peak to peak voltages up to 200Vpp and 300Vpp have been used in some studies (Oyarzun and Cattafesta (2010), Gomes et al (2006) and Gressick et al (2008)) without failure of the piezo element.

A piezo element may be a so-called unimorphs, which means that it is made up from one active layer piezo material and one inactive layer (shim). The function of an element can be enhanced by using parallel polarized piezo material on both sides of inactive layer, resulting in a so-called bimorph (Koopmans and Hoeijmakers (2014)).

Mossi et al (2005) carried out a research on characterizing a synthetic jet using three classes of piezoelectric actuators as circular mechanical diaphragms including pre-stressed curved metallic Unimorph or Thunder, Bimorphs, and Radial Field Diaphragms, RFD. In case of the Thunder, they observed that the orifice shape, cavity volume and driving signal had a more considerable impact on the velocity as compared to voltage and frequency.

For the Bimorph, they found that all the parameters were important with the voltage being crucial. The RFD analysis revealed similar outcomes to the Bimorph. They observed that peak

velocity magnitude is different significantly with the different waveforms especially with a sine waveform which generates the weakest jet. Liang et al (2006), used Shape Memory Alloy (SMA) diaphragm, along with corresponding iron pads, electromagnetically driven to attain significant high jet velocities. However, beside the impressive level of jet output (190 m/s), the main drawbacks were the considerable power consumption (200W) and weight of SJA (1.36 kg). Morel-Fatio et al (2003) used 54 piezoelectric SJAs on the wings of a scaled-down model of Piper J-3 Cub aircraft. The model was tested at a Reynolds number above 10^5 in a wind tunnel. It was reported that the maximum lift coefficient improved 6% by applying the SJ actuation. The power consumption for all 54 actuators amazingly was only about 1W. Lee et al (2006), achieved greater displacement movements by utilizing Ionic Polymer Metal Composite (IPMC) diaphragms than achieved displacement via piezoelectric diaphragms, however, their drawback is supply of much lower levels of force and response time.

Amplitude and frequency are two inherent features of each waveform type that are influential on the peak displacement of the diaphragm and also the jet peak mean velocity respectively. Ohanian (2011) studied the effect of excitation parameter generated by square wave and sine wave and it was revealed that the generated peak jet velocity by square wave was higher than sine wave case by 20%.

Mane (2005) studied the effects of specific parameters on the function of the synthetic jet actuator utilizing jet velocity as the response variable by considering four types of actuators including Bimorph, Thunder, Lipca and RFD. Sine wave and sawtooth wave were applied as driving signal for all actuators, while square wave was applied only for RFD type. It was observed that driving signal had a considerable influence on velocity for all actuators. The sawtooth signal generated higher velocities then the sine signal. This result was attributed to the extra impulse supplied by the sawtooth signal. Two velocity peaks were produced by the sine signal with all actuators, the larger peak was attributed to blowing part of the synthetic jet cycle while the smaller peak was relevant to suction part. For RFD type, with a square signal, the synthetic jet generated velocities in similar scale as the sawtooth signal. Two velocity peaks with different magnitudes were formed due to the double impulse available in the square signal for both phases of blowing and suction. Although the square signal generated high velocities, dielectric breakdown at low frequencies and

consequently actuator damaging could be occurred by this type of waveform. The velocity enhanced as frequency was enhanced when a sine waveform used for frequency ranges for each actuator, while the velocity reached a constant value at about 10 Hz for actuators when sawtooth signal was applied.

The reason for observed behavior with the sawtooth signal was attributed to the choking condition seen in nozzle flows (John (1984)). Similar trend was observed by applying a square wave for the RFD type, choking at a low frequency of approximately 10 Hz (Mane (2005)).

Watson (2004) studied the effects of three waveform types including single sine, pulsed sine and dual sine on peak Jet to free-stream velocity ratios. The results revealed that the range of velocity ratios was from 0.11 to 0.64, in other word, for all cases the peak jet velocity was less than the free-stream velocity. The amplitude modulation excitation produced the maximum ratio of 0.64 at frequency 100 Hz with a peak-to-peak amplitude of 80V, while sine wave excitation produced a ratio of 0.63 at a considerably higher frequency 1200 Hz and peak-to-peak amplitude of 120V.

Qayoum et al (2010) investigated the effects of excitation voltage and modulation frequency on the characteristics of the synthetic jet. They considered several modulating frequencies including 10Hz, 25Hz, and 50Hz. The excitation voltages was in the range 5–50V. The jet penetration in the stream-wise direction enhanced by amplitude modulation. Same trend was observed for rms velocity fluctuations magnitude. Low frequency modulation resonated with the base (vortical) flow of the unmodulated jet and broadened the energy containing region of the power spectrum.

The radial distribution of the time-averaged and rms velocities for modulated and unmodulated jets have been compared as shown in Fig.2.12 (Qayoum et al (2010)). The amplitude modulation has not tangible effects on the time-averaged velocity while it has a great impact on the rms velocity profile specially in lower modulation frequencies. As it can be seen from Fig.2.12(b), the rms values greatly decrease by increasing frequency from 10Hz onwards to 50Hz.

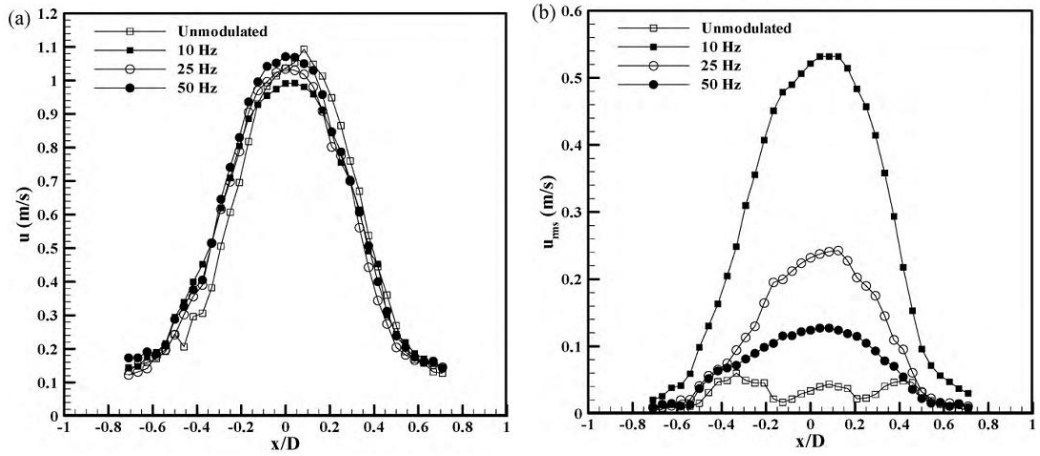

Fig.2.12.(a) Radial velocity profile and (b) profile of radial rms velocity for bigger diameter (D= 2mm) orifice at location, y/D= 1.5 for different excitation conditions and carrier frequency of 475 Hz (Qayoum et al (2010)).

2.3.3- Non-dimensional Parameters

For a SJA with a good performance, the internal dimensions of the actuator are influential. The fluid inside the cavity can behave as an acoustic spring and the fluid in the orifice as an acoustic mass. This mass-spring system possess a resonance frequency, which is named the Helmholtz frequency and is defined by (2-3), with U_{sound} the sound speed, A_{sj} the surface area of the orifices in the exit plane, h_{eff} the orifice effective depth and V_{cavity} the volume of cavity for inviscid, incompressible flow.

$$f_H = (U_{sound}/2\pi)(A_{sj}/h_{eff}V_{cavity})^{1/2} \quad (2\text{-}3)$$

For circular cavities, this value should be corrected by adding the end correction value similar to the effective mass in a mechanical spring-mass system, this value is $\frac{1}{7}$ times the radius of the orifice which must be added to the geometric orifice depth (Koopmans & Hoeijmakers (2014)). Researchers usually use the dimensionless form of frequency (Reduced frequency) which is defined as:

$$F^+ = fc/U \quad (2\text{-}4)$$

where f is the actuation frequency, c is the wing chord and U is the freestream velocity. Mittal et al (2005) used values of reduced frequency in range of (0.55–5.5) in their study, these values are slightly lower than the preferred F^+ values 3.6, 7.2 and 10.8 reported by

Tang et al (2014). Glezer and Amitay (2002) carried out a comprehensive review on interaction of SJs and separated flows, they proposed that the actuation frequency of synthetic jet should be at least bigger than the natural shedding frequency of airfoil about one order of magnitude for influential control of flow separation. While, Franck and Colonius (2012) found that low-frequency actuation at the order of a hump natural shedding frequency is more influential to delay flow separation than high-frequency actuation. Many researchers put much efforts to find the optimal forcing frequency, Seifert et al (1996), Nishri & Wygnanski (1998) and Amitay & Glezer (2002) reported that the best performance is approximately unity. The length of the vortical structures over the airfoil becomes about one-third to one-half of the chord length at this frequency.

In other study on a hump model tested in the NASA Langley 0.3-m Transonic Cryogenic Tunnel, Seifert & Pack (2002) investigated the effects of excitation frequency on the mean and fluctuating pressures at c_μ= 0.13% and M_∞ = 0.25; Re = 16 million. The model was equipped with 34 pressure taps in 1 row in stream wise direction and 27 pressure taps in 3 rows in span-wise direction. They found that the separated flow is most receptive to F^+=1.6, which is the most influential frequency for flow reattachment, while lower frequencies which are less influential in changing the mean flow persists to be amplified over the bubble and diminish at a lower rate downstream of reattachment as shown in Fig. 2.13. (Seifert & Pack (2002)).

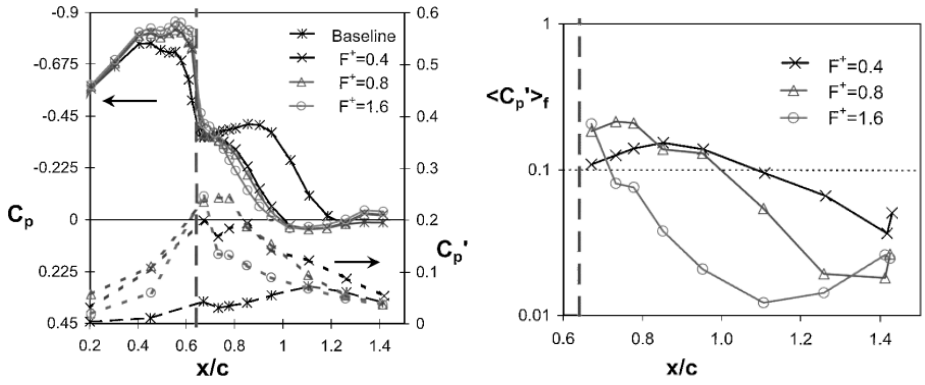

Fig.2.13. Mean and fluctuating pressures representing the effects of excitation frequency (left) and evolution of the pressure fluctuations at the fundamental frequency downstream of the $x/c = 0.64$ slot (right), c_μ=0.13% and M_∞ = 0.25; Re = 16 million (Seifert & Pack (2002)).

The stroke length is defined as the travelling distance of a fluid particle during the blowing phase as follows:

$$L_0 = \int_0^{T/2} U_{inst}(t)dt \tag{2-5}$$

where $U_{inst}(t)$ and T are instantaneous velocity and the period of cycle, respectively.

The Reynolds number is on of the most crucial non-dimensional flow factors for synthetic jets, which is defined as:

$$Re = \frac{U_0 d}{\nu} \tag{2-6}$$

where d is the diameter of the orifice, ν is the kinematic viscosity of the fluid and U_0 is the average of the instantaneous velocity of the orifice during the blowing phase.

Strouhal number is another important parameter in the analysis of a synthetic jet which represents the unsteady behavior of the synthetic jet flow and is defined as:

$$Sr = \frac{fd}{U} \tag{2-7}$$

which f, d and U are the frequency of vortex shedding, characteristic length and fluid velocity, respectively. Another important parameter that is broadly used by researchers is the ratio of synthetic jet velocity to the freestream velocity which is defined as:

$$VR = U_j/U \tag{2-8}$$

The ratio of unsteady force to viscous force is described by the Stokes number, the Stokes number is associated to the rollup of vortex rings from a SJA with a circular orifice which is defined as:

$$S = (2\pi f d^2/\nu)^{1/2} \tag{2-9}$$

In fact, it characterizes the entrainment capability of SJs. Zhou et al (2009) showed that the rollup of vortex rings happens when the Stokes number becomes more than 10. Smith and Swift (2003) compared the flow field of synthetic jets and continuous jets in the uniform

Reynolds number and large range of the dimensionless stroke length (L_o/d). Momentum coefficient, as another important parameter is defined as:

$$C_\mu = nAU_j^2/bcU^2 \tag{2-10}$$

(Tang et al (2014)), describing the ratio of ejected momentum by all the operating SJAs to the characteristic momentum of the freestream. b and c are wing span and wing chord respectively, and n is the number of actuators and A is the actuator orifice area. Unfortunately, definition of the momentum coefficient is not same in literature and we can find different definitions (Koopmans and Hoeijmakers (2014), Tian et al (2006), McCormick (2000), Oyarzun and Cattafesta (2010), Gressick et al (2008), Glezer et al (2005)). Most researchers just consider the time-dependent center line velocity at the exit plane of jet or just the maximum jet velocity at the centerline; spatial changes of the velocity are not considered. Most of the researchers have used momentum coefficients more than 10^{-4} (Chatlynne et al (2000), Amitay et al (2001) and Bazdidi-Tehrani et al (2008)). For synthetic jets with high-Reynolds-number, the Mach number is also used to show the ratio of maximum velocity of working fluid to local sound velocity.

$$Ma = \frac{U_{max}}{U_{sound}} \tag{2-11}$$

2.4- Interaction of Synthetic Jet Actuators with a Uniform Cross Flow

The actuation of the SJA array put effect on the structures of vortex in three approaches: firstly, the vortex structures shrink considerably after their interaction with the vortices generated by the array of SJA, secondly the congested, continuous vortex structures gradually are disconnected and finally the interaction between the SJs and the shear layer push down down the vortex trajectory towards the wing surface (Tang et al (2014)). Ishtiaq et al (2016) carried out a series of experiments including the PIV technique to investigate the impacts of the synthesized vortical structures on delaying of flow separation. They showed the quantitative flow separation delay in contours form as shown in Fig.2.14. The velocity ratio plot computed versus dimensionless stroke length L and frequency f gives diagonal curves.

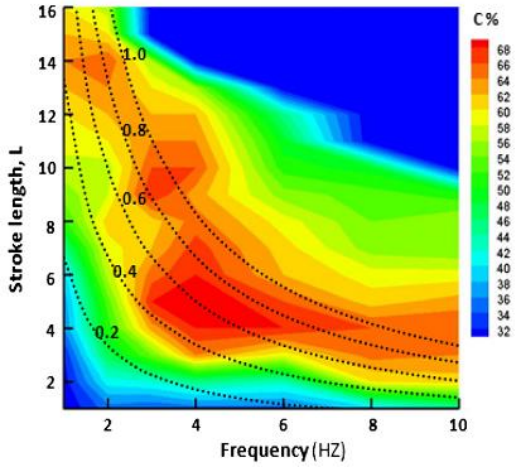

Fig.2.14. Contours of overall separation control effect for active actuator (Ishtiaq et al (2016)).

The maximum delay is achieved at stroke length between 4 to 6 and frequency 4 Hz. The important feature of SJAs is low power consumption to achieve the best control effect. Hence, it should be run at minimum practical stroke length to make sure lowest practical input energy. Jabbal and Zhong (2008) applied two qualitative visualization techniques including dye visualization of the synthetic jet structures together a stereoscopic imaging system to identify the vortical structures generated by the synthetic jet and analysis of the effect of synthetic jet structures along the wall utilizing a thermochromic liquid crystal-based convective heat transfer sensing system. They recognized three classes of vortical structures from the interaction of a synthetic jet with laminar cross flow including hairpin vortices, stretched vortex rings and tilted/distorted vortex rings, the same structures identified by Zhong et al (2005), as shown in Fig.2.15.

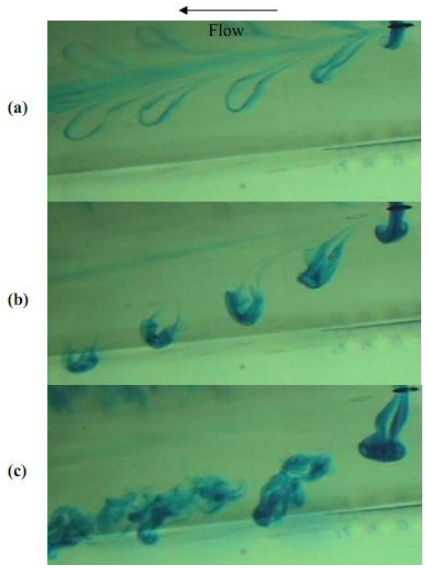

Fig.2.15. Dye visualization of vortex structures generated by synthetic jets on a laminar boundary layer: (a) hairpin vortices; (b) stretched and tilted vortex rings; and (c) distorted vortex rings (modified by Zhou (2010), from Zhong et al, (2005)).

The resident time in the near wall region and vorticity strength are two features that differ these structures from each other. As shown in Fig.2.16 (a), Strouhal number is the gradient of the VR– L graph, Fig 2.16 (b) shows the Re_L– VR graph with lines of constant St added.

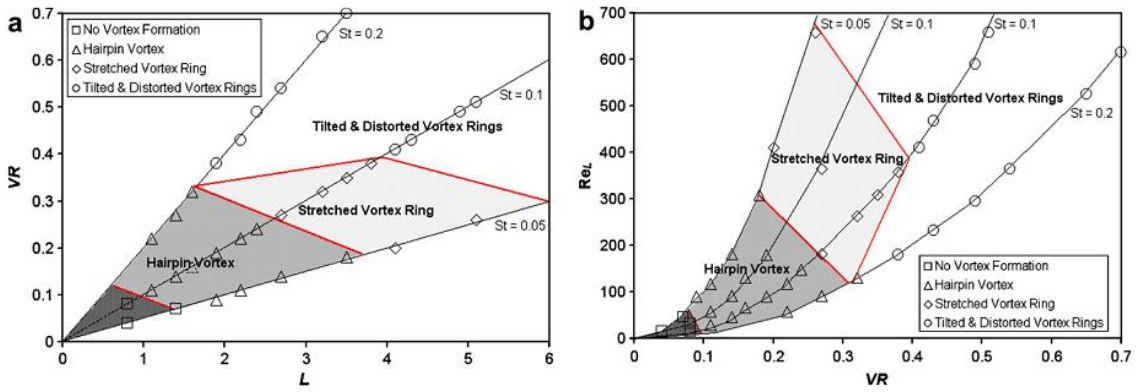

Fig.2.16. (a) VR– L and (b) Re_L– VR parameter space of the different vortical structures seen due to the interaction between a synthetic jet and a boundary layer (Jabbal and Zhong (2008)).

It can be observed that there is a lowest threshold in the stroke length of $L \approx 1$ and $VR \approx 0.1$, which is necessary for the formation of vortex in the boundary layer. Hairpin vortices and stretched vortex rings are formed below the velocity ratio of $VR \approx 0.4$, these vortical structures presumably are responsible for the separation delay. The intermediate range of

velocity ratio guarantees considerable resident time in the boundary layer. For higher values of velocity ratio, the resident time of tilted/distorted vortex rings in the boundary layer is short and consequently these vortical structures are not considered to be responsible for the delayed separation.

It is presumed that hairpin vortices are more effective compared to turbulent vortex rings in flow separation control because they remain near to the wall surface and therefore supply bigger effects on the boundary layer flow (Zhong and Jabbal (2007)).

Wood et al (2009) carried out PIV experiments over wing model NACA 4421 and they found that the coherency and power of counter-rotating vortical structures decreased and they lift off the wing surface as they spread downstream. It was revealed that the 2 dimensional vortices close to the jet orifice collapse to 3D flow structures as they convect downstream which enhances mixing and ineraction between the primary and boundary layer flows.

Salunkhea et al (2016) used a three-D Tomo-PIV system to capture the flow-field, a Laskin nozzle (Oil Droplet Generator 9307 from TSI) was utilized as seeder to produce the seeding particles with size of 1–2 μm. The three-D velocity vector field was obtained by utilizing three-D particle pattern cross-correlation of reconstitued particle distribution. A corrected median filter was applied to eliminate the spurious vectors in the vector field of velocity. Approximately 2% spurious velocity vectors were eliminated and then replaced via interpolation.

They illustrated 3D vortex structures colored by stream-wise velocity, with contours and velocity vectors, for the time-averaged unactuated case, time-averaged actuated case and different phase-locked actuated cases, as shown in Fig.2.17. The best performance was observed at the phase angle of 180^{o} as it is clear from the considerable decrease of large-scale vortex structures in the shear layer and the significant enhancement of the velocity of flow in the near-wall regions.

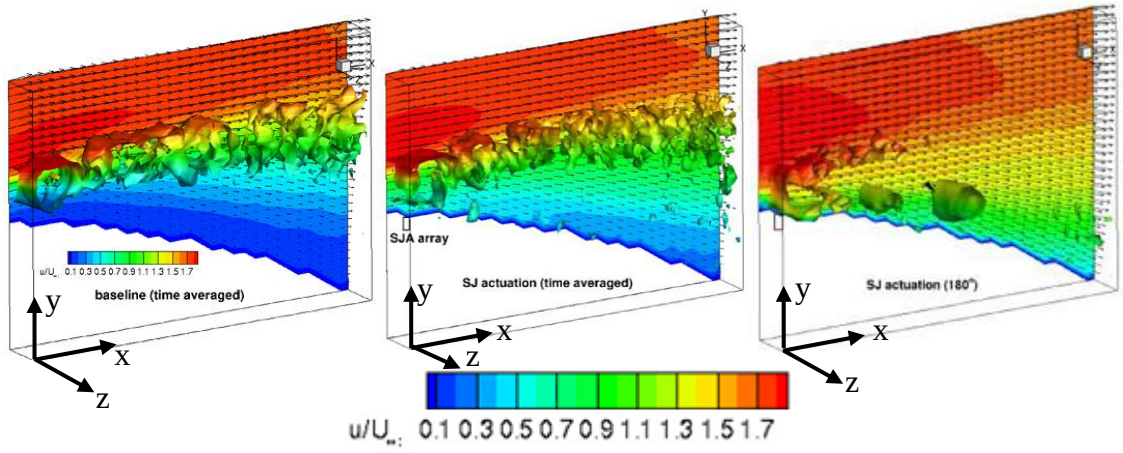

Fig.2.17. Iso-surfaces of vortex structures colored by streamwise velocity for the time-averaged unactuated case, time-averaged actuated case and phase-averaged (phase angle of 180^o) actuated cases (adapted from Salunkhea et al (2016)).

Considerable congestion of large-size vortical structures in the shear layer can be seen from the baseline case. A significant change in the flow field can be seen after turning on SJ array. By applying the synthetic jet actuators, the congested, continuous big vortex structures are collapsed and contracted considerably; the vortex trajectory is pushed down towards the wing surface; and the near-wall regions are reinforced to delay flow separation (Salunkhea et al (2016) and Tang et al (2014)).

Jin et al (2014) investigated the effect of synthetic jets experimentally on the icing process of a water droplet on a cold surface. The temperature of the surface on the icing process period was increased and the freezing time of the water droplet was prolonged by synthetic jet. Tian et al (2006) installed piezoelectric SJAs and unsteady pressure sensors on a NACA0025 airfoil model, realizing adaptive feedback control of flow separation at a chord Reynolds number of 10^5 and an angle of attack of 12^o. The full re-attachment of the separated flow attained by the feedback control. Ciuryla et al (2007) studied the flow and flight control on a Cessna 182 model by applying SJs at a chord Reynolds number of 10^5. Shear stress sensors were utilized for the feedback control. Maximum lift coefficient was improved by about 15% and the stall was delayed by 2^o. Tang et al (2014) studied the effectiveness of SJA arrays positioned at 23% and 43% of the chord from the leading edge of a low-speed wing model. The maximum enhance of the lift coefficient was achieved about 27.4% and the average decrease in the drag coefficient was achieved about 19.6%.

It was also revealed that upstream SJA array is more influential than its downstream counterpart as shown in Fig.2.18.

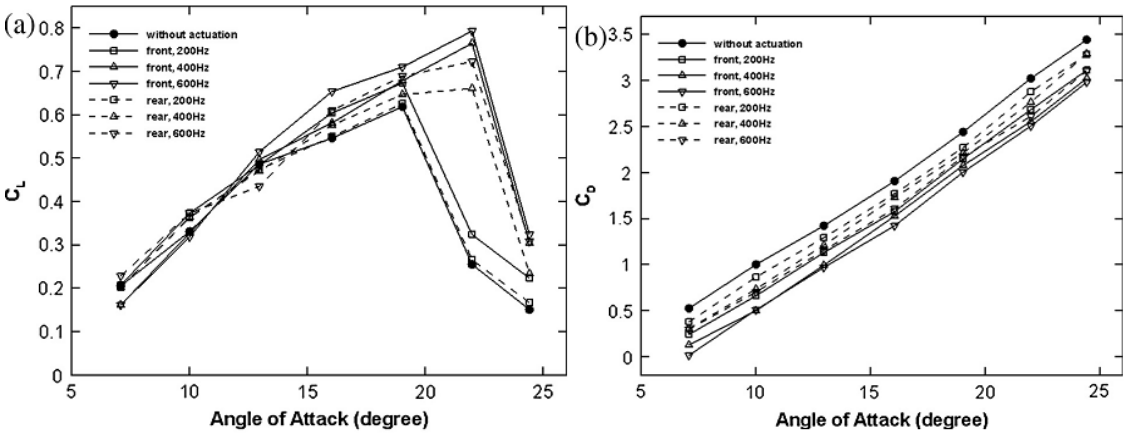

Fig.2.18. Change of (a) C_L and (b) C_D versus Attack Angle, actuated and unactuated (baseline) cases (Tang et al (2014)).

Koopmans and Hoeijmakers (2014) studied flow separation control using synthetic jet actuator experimentally for NACA0018 wing. They reported that the best combination of the highest practical jet velocity with the actuator and frequency of actuation is the dimensionless frequency F^+ of 5.9 (1300 Hz) and a momentum coefficient C_μ of 0.0014 (highest jet velocity 32.9 m/s and Velocity Ratio of 1.32). By applying these actuation factors, the lift coefficient was enhanced by 12% and the stall angle by 22%, as shown in Fig.2.19.

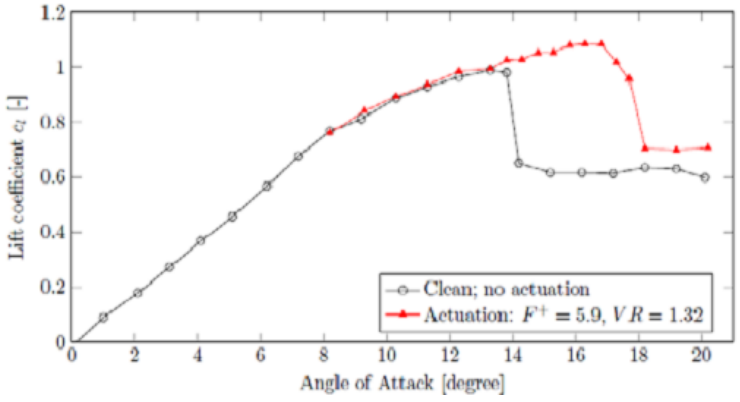

Fig.2.19. Flow separation control using optimal set of parameters for the SJA (Koopmans and Hoeijmakers (2014)).

Takao (2006) investigated the impacts of an oscillatory zero-net-mass-flux jet over a half-cylindrical hump in two dimensions using direct numerical simulation (DNS) to solve compressible, unsteady, laminar flows.

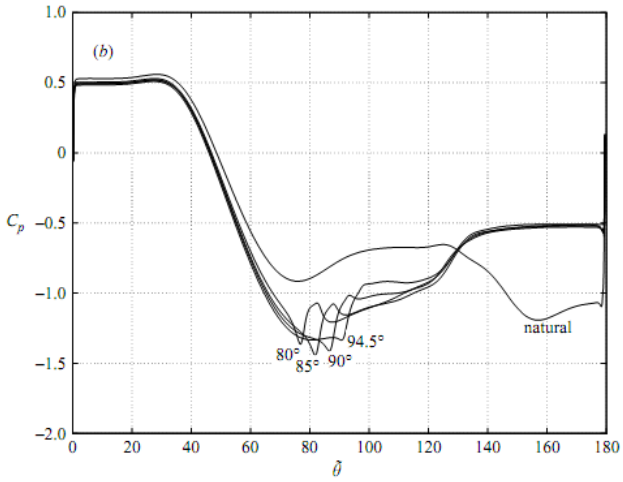

Fig.2.20. Pressure profiles over a hump for different actuator locations for baseline case and cases near the optimal position (Takao (2006)).

Between θ_{act}=80°-94.5° phase-locking occurred, and the pressure profiles became more favorable. The pressure jump was shifted to the actuator position, and the minimum pressure value was obtained when $\theta_{act} = 85°$, as shown in Fig.2.20.

Viken et al (2003) carried out a CFD investigation utilizing FUN2D (Full Unstructured Navier-Stokes 2-Dimensional), the structured TLNS3D (Thin-Layer Navier-Stokes 3-Dimensional) and structured CFL3D codes by applying the time-accurate Reynolds-Averaged Navier-Stokes (RANS) method to predict aerodynamic performance of the active flow control experimental database for a hump model. The excitation slot was located at the normalized stream-wise location of $X/C = 0.64$. Figure.2.21 depicts the calculated pressure coefficients versus the experimental data (Seifert, A. & Pack (2002)) for free stream Mach number of 0.25, and Re = 16 million for baseline case without actuation (Fig.2.21 a) and actuated suction and oscillatory cases (Fig 2.21 b). As it can be seen from Fig.2.21, the effects of actuation on mean Cp distributions in suction case of c_μ = -0.077% and the oscillatory case of $<c_\mu>$= 0.095% with F^+ = 1.6 are similar. The excitation frequency was assumed a perfect sine wave at the actuator boundary during the CFD computations while it was not perfect in the experiment (Seifert, A. & Pack (2002)). As the mass flow leaves the slot, two vortices are generated and transfer downstream and reenergize the boundary layer by higher momentum air transport into the lower layers of the boundary layer and decrease the separation bubble considerably.

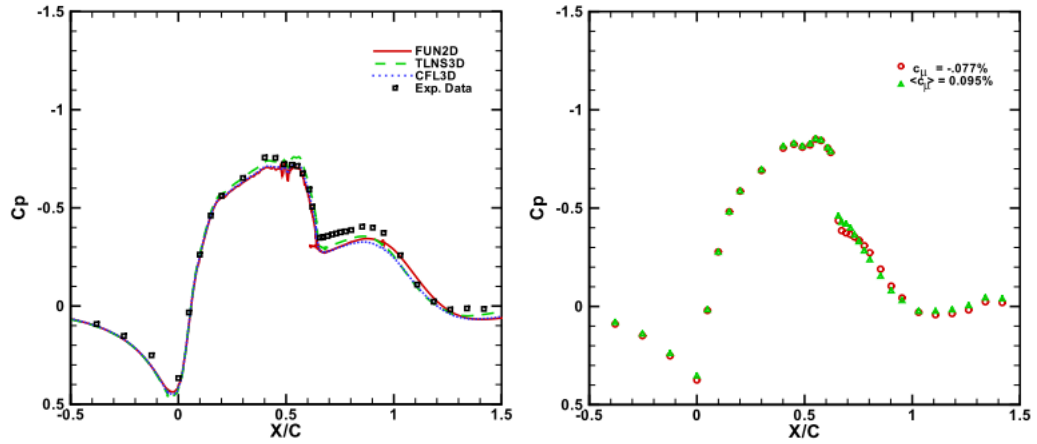

Fig.2.21. Unactuated CFD results versus experimental data (left) and mean pressures of the controlled flow using suction (c_μ= -0.077%) and periodic excitation (<c_μ>= 0.095%) at F^+ =1.6 (Right) and M_∞ = 0.25; Re = 16 million (Viken et al (2003)).

Pick et al (2013) studied the effect of modulated slotted synthetic jet bypass of hump model, they applied three experimental methods of measurement techniques including the pressure profile utilizing the Kiel total pressure probe, the velocity profile utilizing the HWA sensor and the visualization of the flow field utilizing the hot film and the thermos camera.

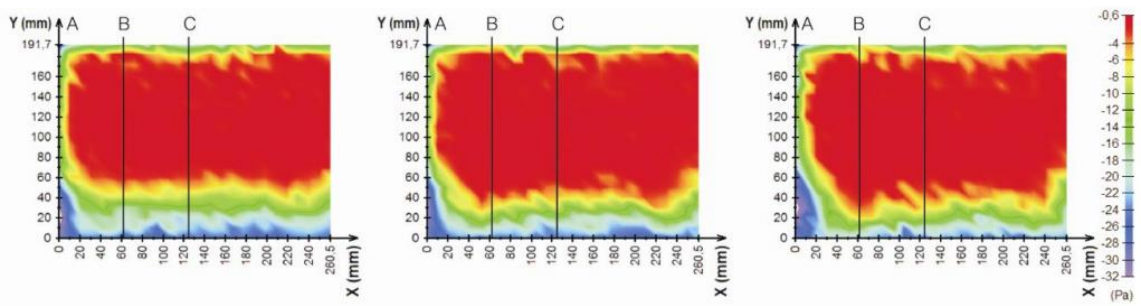

Fig.2.22. Total pressure field, view in flow direction. From left: reference conditions - unactuated, no phase shift of the synthetic jet, and phase shift of amplitude modulation of the synthetic jet (Pick et al (2013)).

(m/s)

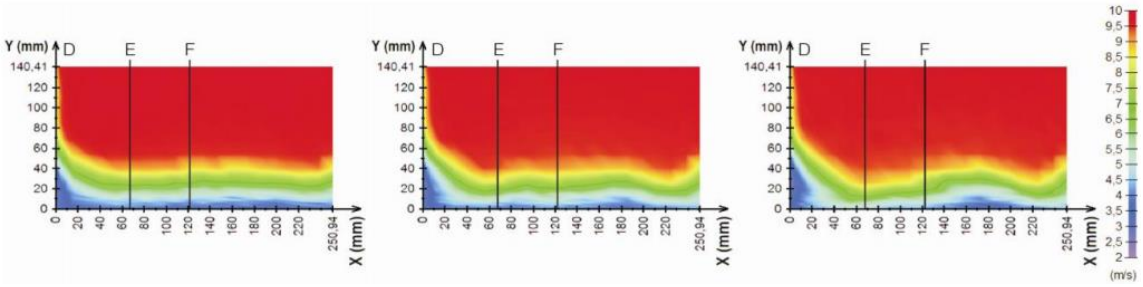

Fig.2.23. Velocity field, view in flow direction. From left: reference conditions-unactuated, no phase shift of the synthetic jet, and phase shift of amplitude modulation of the synthetic jet (Pick et al (2013)).

The positive effects of the opposite phase shift of the adjacent synthetic jet cells in the synthetic jet generator on reducing of the wake behind the model can be seen in Figs.2.22 and 2.23. The phase shift impacts the fluid flow around the model favorably in a way that it will support the generation of the longitudinal vortex structures similar to those being generated by vortex generators (Pick et al (2013)) and Souckova et al (2010)).

A wide range of numerical methods such as direct numerical simulation (DNS) (Postl et al (2004)), steady or unsteady Reynolds-averaged Navier-Stokes (RANS or URANS) simulations (Capizzano et al (2005), Morgan et al (2004) and Krishnan et al (2004)), large-eddy simulation (LES) with a constant Smagorin- sky model (Saric et al (2005)), detached eddy simulation (DES) (Krishnan et al (2004)) and implicit LES (ILES) (Morgan et al (2005)) have been applied to simulate separation of turbulent flow and its control over a hump model at $\mathrm{Re} = 9.36 \times 10^5$, where the Reynolds number is based on freestream velocity U and the hump chord C.

The DNS simulations of Postl et al (2004) were not good enough because of using unreal inflow boundary conditions and not adequate grid size and size of spanwise domain. ILES results of Morgan et al (2005) have better agreement with experimental results, whereas the applied Reynolds number in their study is only about one-fifth of the experimental Reynolds number. LES results of Saric et al (2005), with a constant Smagorinsky model give good predictions in the uncontrolled baseline and steady suction control cases, but these results show considerable divergence of mean velocity profiles from the experimental results of Greenblatt et al (2004 and 2005) in the oscillatory jet case. The

DES results of Krishnan et al (2004) were better in comparison with their RANS results, while there are considerable differences with experimental data of Seifert & Pack (2002).

You et al (2005) applied large-eddy simulation (LES) method with a dynamic subgrid-scale model and non-dissipative numerics to simulate the separation of turbulent flow and its control by synthetic jets over a wall mounted hump. Fig.2.24 shows the stream-wise vorticity contours with and without synthetic jet actuators, however, the authors have not provided a legend showing colors versus vorticity values.

As it can be seen in Fig.2.24 (a), small scale vortices between the separated shear layer and bottom wall are produced because of strong adverse pressure gradient near the cavity slot. Also, shear layer is weakened and separation bubble size is reduced due to removing mass flux through the cavity slot via steady suction, Fig.2.24(b). A periodic generation and convection of large-scale vortices can be seen in the oscillatory jet case as depicted in Fig. 2.24(c).

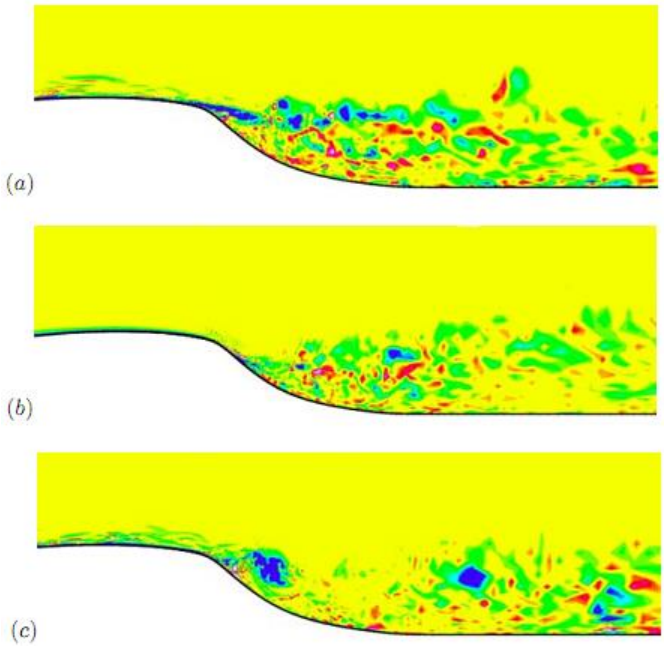

Fig.2.24. Instantaneous streamwise vorticity contours. (a) Baseline; (b) steady suction; (c) oscillatory jet, 20 contours in the range of ±35 (1/s) are plotted. (You et al (2005)).

The repetition of process of vortex roll-up and shedding is effective in separation bubble size reduction (You et al (2005).

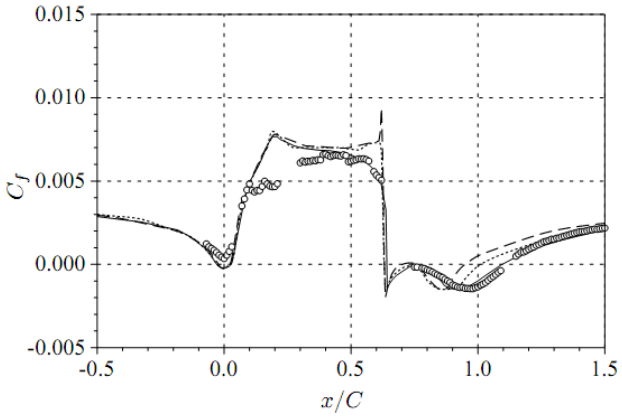

Fig.2.25. Skin friction coefficient predicted by the LES, ____, baseline case; ----- steady suction; ...., oscillatory jet; o, experimental data, (You et al (2005)).

You et al (2005) compared their results for the skin-friction coefficient C_f predicted by the LES for the uncontrolled and controlled cases and the experiment results of Greenblatt et al (2004 and 2005), the influence of steady suction and oscillatory jet on control of flow separation can be seen in Fig 2.25. The line $C_f = 0$ shows the frontier between separated and reattached flow. It is clear that the suction is more influential than the oscillatory jet to reduce the size of separation bubble, as shown in Figs.2.24 and 2.25.

Hybrid RANS/LES methods have been used by Saric et al (2008) and Jakirlic et al (2009), good comparisons carried out with experiments. Also, a seamless hybrid RANS-LES model based on transport equations for the subgrid stresses, using the elliptic-blending approach to account for the nonlocal kinematic blocking effect of the wall was developed by Fadai-Ghotbi et al (2010). Gritskevich et al (2012) suggested two modifications for hybrid CFD strategies including Delayed Detached Eddy Simulation (DDES) and DDES with Improved wall-modeling capability (IDDES) by fine-tuning of these methods to the k-ω SST background RANS model. Both modifications were tested on a range of attached and separated flows including wall-mounted hump, backward facing step developed channel, periodic hills, and hydrofoil with trailing edge separation.

Cappelli, D. and Mansour (2013) studied the flow separation over a hump model, benefits and drawbacks of RANS models including Spalart-Allmaras, $k-\varepsilon$, $k-\omega$ and $k-\omega-SST$ were evaluated by OpenFOAM software, however only unactuated case was considered and the slot flow control cases were not studied.

Fisher et al (2017) performed 2D unsteady RANS simulations for NASA 2D Hump" configuration to investigate potential advantages of varying the inflow and outflow directions of a Synthetic Jet, called the Bi-Directional Synthetic Jet (BDSJ) in comparison with the classical Synthetic Jet. Kara et al (2018) studied the potential use of a SWJ actuator to delay flow separation by performing a set of 2-DURANS simulations for the 2-D NASA hump model with an integrated SWJ actuator configuration to evaluate the function of the SWJ actuator in comparison with the baseline and experimental measurements.

In another numerical study, Tang and Agarwal (2018) investigated flow separation control over a NASA hump by considering a uniform blowing jet and a synthetic jet at Reynolds number $=1\times10^6$ based on hump chord and Mach number = 0.09 and by employing K-Omega SST and Spalart-Allmaras turbulence models. They found that for uniform blowing jet, and for jet velocities more than 85m/s, the separated flow is fully reattached to the surface and for the synthetic jet case, when the jet velocity is more than 49 m/s, the separated flow is reattached completely to the surface.

Kim and Kim (2019), numerically studied the installation conditions of fluidic oscillators embedded in a hump surface using three-dimensional Reynolds-averaged Navier–Stokes equations with a modified shear stress transport model to improve the flow separation over the hump. Aram and Shan (2019) investigated the synchronization of an array of sweeping exiting jets to improve flow control on a wall mounted hump by Improved Delayed Detached Eddy Simulation (IDDES) model.

Xu et al (2020) numerically studied the effect of Co-flow Jet (CFJ) active flow control on NASA hump model to investigate its performance to delay flow separation at low energy cost. The influence of the locations of CFJ suction and blowing was studied and experimental results of the unactuated case and actuated cases with steady injection and suction was utilized to evaluate the accuracy of numerical approach. They used the high fidelity in-house CFD code FASIP with the 2 dimensional unsteady Reynolds averaged Navier-Stokes (URANS) equations with one-equation Spalart-Allmaras model. The prediction of numerical simulations showed the effectiveness of using co-flow jet for the hump separation control. The flow was fully reattached with blowing location at 50% of hump chord and suction location at 70% hump chord at $C\mu=0.0077$ with the CFJ power

coefficient (Pc) of 0.0032 and the energy coefficient (CE) of 0.0034. The study revealed that that the optimum location for CFJ suction with the lowest energy consumption is at the location that the slope of the hump surface reaches to the minimum value. The validation of numerical analysis with experimental results showed good agreement with the experiment for both baseline and steady injection cases.

Active control of laminar flow separation over a two-dimensional hump with synthetic jets by study of the vortex dynamical mechanism was studied by J.J Wang et al (2014). The hydrogen bubble flow visualization and the two-dimensional PIV method were utilized to study the flow over the leeward side of the hump model. The successful suppression of the separation region was reported at various optimal actuating frequencies.

Koklu (2015) carried out a parametric experimental study on a long aluminum splitter plate with an APG ramp model with sweeping jet actuators to investigate the influence of synthetic jets in flow separation control. Surface flow visualization results of unactuated case and steady-straight jet mode (STJ) and steady-angled jet mode (VGJ), are shown in Fig.2.26. Travel of the oil mixture because of the blown jet is shown as darker areas close to the actuator exits. A stagnant oil flow area is seen between Stations 67 and 72 showing flow separation. Stagnant oil flow close to Station 64 is not observable probably due to the removing by flow driven oil, however separation of local flow has been occured. Thicker patterns of oil flow (low shear stress) were observed starting from Station 62, due to the thicker boundary layer (in STJ mode). Similar patterns of thick-oil flow were also seen for VGJ actuators. (Koklu (2015)).

Koklu (2018) also studied the unsteady and steady excitation of separated flow over the NASA hump model at subsonic speeds both numerically and experimentally. He observed that the unsteady excitation had better outcome in comparison to the steady one and its performance is a bit better than the sweeping jet actuators while the steady suction was observed to be the most successful, however his numerical analysis over predicted the separation bubbles.

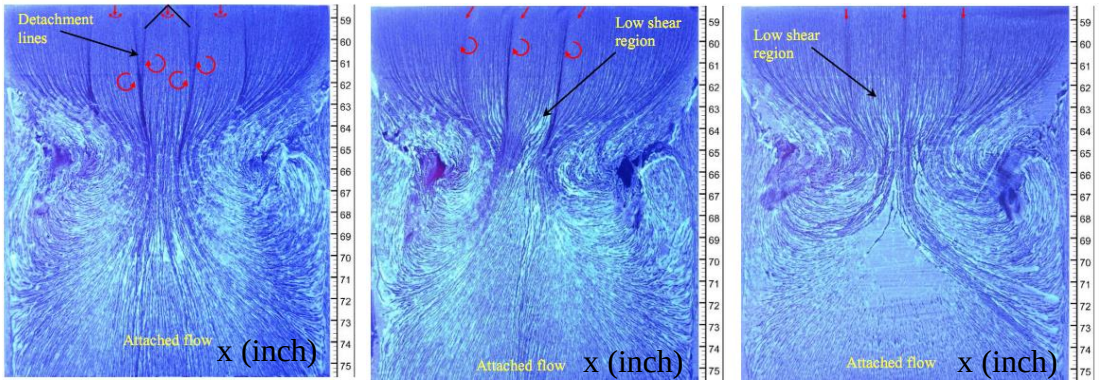

Fig.2.26. Oil flow visualization for baseline case (left), VGJ mode (middle) and STJ mode (right) (Koklu (2015)).

2.5- Summary

The physics of flow separation phenomenon and flow reattachment have been described. Also, the interaction of synthetic jet actuators with the cross flow is discussed by review of selected experimental and numerical researches. However, the research regarding flow separation and its control over the circular hump is limited and the influence of effective geometrical and operational parameters either is not investigated, e.g. the effect of angular position of actuators, or is studied in a narrow band, e.g. considering velocity ratios (VR) just below value of 1.5 as well as considering a limited number of waveforms. In addition, the SJAs is rarely fully simulated numerically by researchers due to the computational cost and the SJA is frequently considered in two dimensions and without considering the cavity and membrane. Also, interaction of cross flow with SJAs has been rarely considered in three dimensions and the researchers have not given information about flow in span-wise direction. This research attempts to fill these gaps both experimentally and numerically.

In Chapter 3, the experimental and numerical methodologies will be described. The experimental methodology section will cover the manufacturing processes of the wind tunnel and the hump model, In addition, the experimental setup of the project including the setup of Hot Wire Anemometry (HWA) technique as well as the setup of Particle Image Velocimetry (PIV) technique will be described in details. Also, the methodology of numerical analysis including geometry and computational grid generation process, initial and boundary conditions and numerical method will be explained.

Chapter 3- Experimental and Numerical Methodologies

In this chapter, both experimental and numerical methodologies are explained in details. The design and manufacturing processes of the low speed closed circuit wind tunnel and the hump model are described. Then, the experimental setups of Hot Wire Anemometry (HWA) and Particle Image Velocimetry (PIV) techniques will be explained. Also, the methodology of numerical simulations is described.

3.1- Experimental Methodology

In this section, in addition of the description of the wind tunnel and the hump model, the geometry of actuator array and the required driving circuitry system including function generator and amplifier to drive the piezo-electric diaphragms are described. Alongside the discretion of the setups of Hot Wire Anemometry (HWA) and Particle Image Velocimetry (PIV) techniques, the relevant calibration procedures for both techniques and suitable data post processing methods are explained.

3.1.1- Wind Tunnel

Since the end of the 19th century, wind tunnels are utilized to generate almost uniform air flows with low turbulence intensity. The benefit of wind tunnels is to test and evaluate the flow properties under controlled conditions in comparison with experiments in the open environment. Wind tunnels are generally manufactured in two types: closed loop wind tunnel and open circuit wind tunnel.

A low-speed closed loop wind tunnel with a velocity range of 0 – 25 m/s has been designed and manufactured to enable current studies. The wind tunnel was designed by the author using as a basis a blueprint of an old wind tunnel in University of Leeds (already decommissioned). This repeated the characteristic dimensions, but major changes had to be implemented to improve the flow quality and the range of wind speed. This was achieved by a newly designed settling chamber (to reduce the turbulence level and flow uniformity), a selection of the fan with better characteristics (to increase the range of wind speeds), change of the wind tunnel orientation (for a straightforward implementation of the measurement techniques, e.g. PIV) and improvements in the minor loses caused by

uneven connections between sections and suboptimal corner vanes. The wind tunnel parts were fabricated by an external company (BJ Stainless Fabrications Ltd, Leeds) and the assembly carried out by Huddersfield technician under the author's supervision. Additions of further features, e.g. traverse systems, laser optical paths and laser beam shielding were conducted by the author with occasional help from the workshop staff.

A 2 dimensional sketch of the wind tunnel (top view) is shown by Fig.3.1. The wind tunnel is constructed from several components that is described as follows: An Aerofoil axial fan (model 71JMv) with the design static pressure of 450 Pa and volume flow rate of 5 m^3/s is used to supply air flow through the wind tunnel (1). Neoprene rubber sections (2 & 18) are utilized to separate the fan vibrations from the rest of the wind tunnel. Rubber section (2) connects the fan to the first diffuser (3) that provides a transition between the circular outlet of the fan and the rectangular shape of the rest of the wind tunnel. Straight section (4) leads to the first corner (5). This has nine guide vanes, spaced 10 cm apart, and with 10 cm extended trailing edges which reduce the flow separation due to the turning of flow in the corner. Duct (6) with length of 400 mm is used to join the first corner (5) to the second corner (7). This has 11 guide vanes with the same extended trailing edges to straighten the flow before it enters the settling chamber (8). Settling chamber helps to straighten and make uniform the fluid flow, this section has a crucial role to remove the irregularities due to the fluid turning in guide vanes. The settling chamber with a cross section of 1000 mm × 1050 mm contains a layer of honeycomb (cell size of 9.5 mm and 100 mm thickness) to straighten the flow, and three mesh screens (1.04 mm aperture and 0.23 mm wire diameter) which are spaced 100 mm to help the creation of the flat velocity profile by adding local pressure drops across the three mesh layers. Mesh screens are capable to prevent separation or restore separated flow, the mechanics of the process is closely related to the mechanics of turbulent boundary layer separation. The mesh screen may avoid separation either by enhancing the normal velocity gradient in vicinity of diffuser wall, or by decreasing the pressure gradient along the wall or by a combination of both impacts (Schubauer & Spangenberg (1949)). The number of required mesh screens (preceding the contraction) has been determined using data from Bell and Mehta (1986). The contraction section (9) has the length of 1112 mm and contraction ratio of 4/1 is utilized to increase the air flow while suppressing the flow separation, flow fluctuations

and pressure losses. The test section (10) with dimensions of 1000 mm (length) × 500 mm (width) × 500 mm (height) which houses the hump model (11) is located downstream of the contraction. The wide-angle diffuser (12) downstream of the test section is used to decelerate the flow and to reduce the loss of kinetic energy of the fluid. To reduce flow separation, and help pressure recovery, the diffuser is equipped with three horizontal and three vertical splitting plates which are spaced ca. 170 – 250 mm (inlet to outlet, respectively). A "breather" with 0.05 hydraulic diameter of the test section (25 mm long gap) is introduced between the test section and diffuser to ensure atmospheric pressure in the test section. In addition, the breather is helpful to avoid flow pulsation in the test section and as well as the increase of flow temperature.

Diffuser (12) is connected to corner (13) which contains nine symmetric vanes with both leading and trailing edges extended by 10 cm. The cross section of this corner is reduced from 1000 mm × 1050 mm (inlet) to 1000 mm × 700 mm (outlet). Straight section (14) leads to the fourth corner section (15), which contains nine guide vanes similar to corner (5). The fourth corner is connected to the rectangular-to-circular transition duct (17) via a straight section (16).

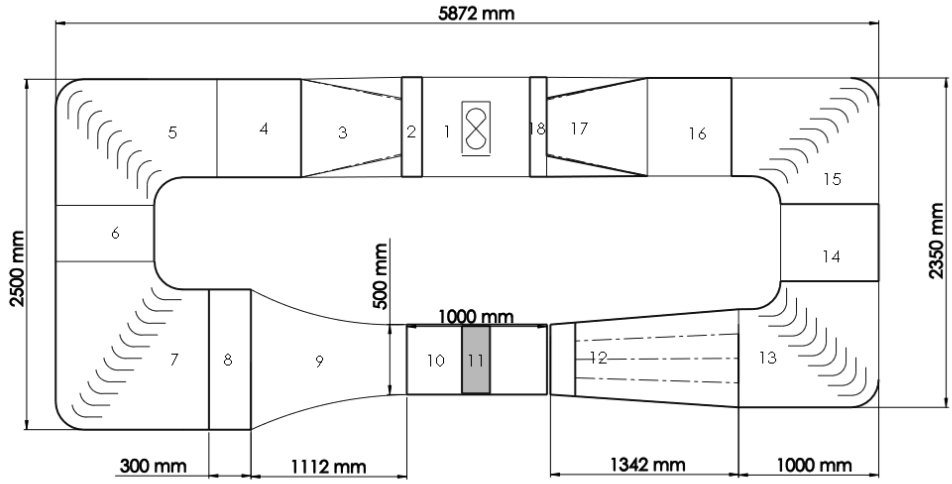

Fig.3.1. Top view of the closed loop wind tunnel at the University of Huddersfield.

3.1.2- Wind Tunnel Power Considerations

The local loss coefficient in each section is defined by the ratio of the pressure loss in the section to the dynamic pressure at the entrance to the section in a non-dimensional form.

$$K_l = \frac{\Delta H_l}{\frac{1}{2}\rho_l {V_l}^2} = \frac{\Delta H_l}{q_l} \tag{3.1}$$

where $K_l, \Delta H_l, \rho_l, V_l,$ and q_l are the local loss coefficient, total pressure loss, local density, local average velocity and dynamic pressure, respectively.

On the other hand, the time rate of energy loss in a component can be shown as a function of total pressure loss times the volume flow rate through the component as following:

$$\Delta E_l = A_l V_l \Delta H_l = A_l V_l K_l q_l \tag{3.2}$$

By substitution of ΔH_l from (3.1) into (3.2):

$$\Delta E_l = A_l V_l K_l q_l = K_l(\frac{1}{2}\dot{m}{V_l}^2) \tag{3.3}$$

The above equation states that the local loss coefficient can be expressed as the ratio of the rate of energy loss to the rate of flow of kinetic energy into the component. The net loss of the total pressure through all of the wind tunnel components can be obtained by dividing both sides of the (3.3) to the volume flow rate as follows:

$$\Delta P_{loss} = \sum K_l(\frac{1}{2}\rho {V_l}^2) \tag{3.4}$$

The velocities in each component of the wind tunnel can be related to the velocity of fluid through the test section by continuity equation as follows:

$$\Delta P_{loss} = \sum K_l(\frac{1}{2}\rho {V_{ts}}^2)(\frac{{A_{ts}}^2}{{A_l}^2}) = \frac{1}{2}\rho {V_{ts}}^2 K \tag{3.5}$$

where $K = \sum K_l(\frac{{A_{ts}}^2}{{A_l}^2})$ (3.6)

The total effective loss coefficient K can be obtained by calculation the local loss coefficient for each component of the wind tunnel.

Finally, the required fan power to recover the total pressure loss through all the wind tunnel components can be estimated by the following equation, where η_{fan} is the fan efficiency.

$$P_{loss} = \frac{1}{2}\rho A_{ts} {V_{ts}}^3 K/\eta_{fan} \tag{3.7}$$

Wattendorf (1938) divided a return wind tunnel into components and successively calculated the pressure losses in each component. Wallis (1983) applied the same method in more details and discussions. Here, the same approach is used for different components of the wind tunnel as follows:

Pressure Losses in Constant Area Section

For constant area sections, the pressure loss due to viscous effects is proportional to pipe length and can be expressed by the Darcy–Weisbach equation (3.8):

$$\Delta P_{loss\,/\rho} = fL/D_h \, \frac{1}{2}V^2 \tag{3.8}$$

By comparison the above equation with equation (3.5), the loss coefficient can be related to the Darcy friction factor f by

$$K_l = fL/D_h \tag{3.9}$$

where D_h is the hydraulic diameter of the section which is calculated as 4 times the flow area divided by the wetted perimeter of the section and L is the length of the section.

Diffuser Losses

The estimation of the diffuser loss parameter is a complex task. It depends on equivalent cone angle of the section and cross sectional shape. The total loss coefficient is the sum of wall friction and expansion loss as follows:

$$K_d = K_f + K_{ex} = \left(1 - \frac{1}{{A_r}^2}\right)\left(\frac{f}{8sin\theta}\right) + K_e(\theta)((A_r - 1)/A_r)^2 \tag{3.10}$$

where A_r , θ are diffuser area ratio and conical angle, respectively. In the above equation, it is assumed that the density and the friction coefficient are constant along with the one

dimensional treatment and the friction factor is calculated based on the entry Reynolds number (Barlow et al (1996)).

The friction factor is calculated by the Prandtl universal law of friction:

$$\frac{1}{\sqrt{f}} = 2\log_{10}(Re\sqrt{f}) - 0.8 \tag{3.11}$$

Here, we use the Iterative solution algorithm of Newton–Raphson method to calculate friction factor, equations (3.12) and (3.13) by Colebrook (1938) and White (1994) for Reynolds numbers greater than 100000 give a good approximation of friction factor for circular and non-circular ducts, respectively.

$$f = (1.8\log_{10}\left(\frac{Re_d}{6.9}\right))^{-2} \tag{3.12}$$

$$f = (1.8\log_{10}\left(\frac{0.64Re_{dh}}{6.9}\right))^{-2} \tag{3.13}$$

The parameter $K_e(\theta)$ greatly depends on the diffuser cross sectional shape, for the sake of calculation the diffuser is splitted into two parts: first part without splitting plates and second parts with splitting plates contains 16 parallel diffusers with equivalent cone angles of 7.295° and 1.71°, respectively. For diffuser with a square upstream-end cross section and $2\theta > 3°$ and $2\theta > 10°$, the expansion loss is calculated by equations (3.14) and (3.15), respectively (Eckert et al (1976)).

$$K_{ex-Rectangular} = 3.23334 \times 10^{-1} - (5.82939 \times 10^{-2} \times 2\theta) - (4.97151 \times 10^{-2} \times (2\theta^2)) + (1.99093 \times 10^{-2} \times (2\theta^3)) - (1.9863 \times 10^{-3} \times (2\theta^4)) + (2.06857 \times 10^{-5} \times (2\theta^5)) + (3.81387 \times 10^{-6} \times (2\theta^6)) \qquad 3° \leq 2\theta \leq 9° \tag{3.14}$$

$$K_{ex-Rectangular} = -1.36146 + 1.986460 \times 10^{-1}(2\theta) \qquad 10° \leq 2\theta \tag{3.15}$$

It should be noted that the pressure loss for individual diffusers and the total pressure loss for the whole diffusers are same in the parallel layout.

Corners Losses

It is assumed that the local corner loss coefficient is composed of two parts: local loss due to the flow rotation, which is accounted for about two-third of the loss and local loss due to the wall friction that is responsible for one-third of the loss. A good conservative estimation of local loss coefficient for 90-degree corner is given by

$$K_c = 0.1 + 4.55/(\log_{10} Re_c)^{2.58} \tag{3.16}$$

where Re_c is calculated based on the vane chord (Barlow et al (1996)).

Contraction or Nozzle Loss

Generally, the contraction or nozzle part consumes a small fraction of the drive power (approximately 3%), a good estimation of the contraction loss coefficient was proposed by Wattendorf (1938)

$$K_n = \frac{0.32 f_{av} L_n}{D_{ts}} \tag{3.17}$$

where f_{av} is calculated as the average of the values for contraction entrance and exit Reynolds numbers, L_n is the contraction length and D_{ts} is the hydraulic diameter at the exit of the contraction.

Honeycomb Losses

" A honeycomb is a guiding device through which the individual air filaments are rendered parallel" as stated by Prandtl (1933). The key parameters to compute the pressure loss coefficient of honeycomb are the screen porosity and the ratio of stream wise length to single cell hydraulic diameter.

Equation (3.18) is used to estimate the loss coefficient through the honeycomb ((Eckert et al (1976))

$$K_h = \lambda_h \left(\frac{L_h}{D_h} + 3\right)\left(\frac{1}{\beta_h}\right)^2 + \left(\frac{1}{\beta_h} - 1\right)^2 \tag{3.18}$$

where $\lambda_h = 0.375(\frac{\Delta}{D_h})^{0.4} Re_\Delta{}^{-0.1}$ for $Re_\Delta \leq 275$ and $\lambda_h = 0.214(\frac{\Delta}{D_h})^{0.4}$ for $Re_\Delta \geq 275$

and D_h , L_h and β_h are the hydraulic dimeter of honeycomb cell, honeycomb length in stream wise-direction and honeycomb porosity, respectively. The friction factor λ_h is calculated from Reynolds number based on honeycomb surface roughness.

Screens Losses

Mesh screens are utilized to control flow separation in wide-angle diffusers and turbulence for flow conditioning screens at the entrance of contraction part. The screen is characterized by two key parameters: The wire Reynold number and the screen porosity.

Equation (3.19) is utilized to evaluate the local loss coefficient of the screen (Eckert et al (1976)) as follows:

$$K_m = K_{mesh} K_{RN} \sigma_s + \left(\frac{\sigma_s}{\beta_s}\right)^2 \tag{3.19}$$

where

$$K_{RN} = 0.785\left(1 - \frac{Re_w}{354}\right) + 1.01 \quad for \ Re_{\mathrm{w}} \geq 400 \quad \text{and} \ K_{RN} = 1 \quad for \ Re_{\mathrm{w}} \geq 400 \tag{3.20}$$

σ_s represents the screen porosity, while β_s is the screen solidity and it is the complement of the screen porosity. Idel'chick (1966) suggests the mesh factor values of 2.1, 1.3 and 1.0 for silk thread, average circular metal wire and new metal wire, respectively.

Rectangular to Round Duct Losses

For the sake of loss coefficient for the rectangular to round part, it is treated such as contraction part and the friction factor is calculated as the average of the values for rectangular entrance and circular exit Reynolds numbers.

Round to Rectangular Duct Losses

This part is treated as a diffuser and equation (3.10) alongside equations (3-21) and (3-22) given by Eckert et al (1976) is used to calculate the loss coefficient as follows:

$$K_{ex-Circular} = 1.70925 \times 10^{-1} - (5.84932 \times 10^{-2} \times 2\theta) + \left(8.14936 \times 10^{-3} \times (2\theta^2)\right) + \left(1.34777 \times 10^{-4} \times (2\theta^3)\right) - \left(5.67258 \times 10^{-5} \times (2\theta^4)\right) - (4.15879 \times 10^{-7} \times (2\theta^5)) + (2.10219 \times 10^{-7} \times (2\theta^6)) \qquad 3° \leq 2\theta \leq 10° \tag{3.21}$$

$$K_{ex-Average} = (K_{ex-Circular} + K_{ex-Rectangular})/2 \tag{3.22}$$

The equivalent cone angel for round to rectangular part is 4.49° which is calculated by

$$\theta = tan^{-1}\left(\frac{\sqrt{A_e}-\sqrt{A_i}}{L\sqrt{\pi}}\right) \tag{3.23}$$

where A_e and A_i are the equivalent areas of exit and inlet of the part based on the hydraulic diameters and L is the length of component.

Model Losses

The losses due to the model are not considerable because of the small ratio of the projected area of the model with respect to the area of the test section. However, the blockage effect of the model was considered by the use of a hypothetical nozzle-diffuser to calculate the effect of the model on the pressure loss.

Table 3.1 Losses of Wind Tunnel Components.

Component	Local Loss Coefficient	Pressure Loss(Pascal)
Test section	0.02693	6.46213
Model	0.00470	1.12904
Diffuser (First Part)	0.04063	9.75176
Diffuser (with Splitting Plates)	0.00034	14.96684
Diffuser (without Splitting Plates)	0.31162	53.42428
First Corner (After Test Section)	0.16710	5.11544
Duct After First Corner	0.00796	0.24370
Second Corner	0.17068	5.22482
Duct After Second Corner	0.01194	0.36554
Rectangular to Round Duct	0.00446	0.13648
First Flange	0.00357	0.34168
Second Flange	0.00357	0.34168
Round to Rectangular Duct	0.07220	6.90931
Duct after Round to Rectangular Duct	0.00597	0.18277
Duct Before Third Corner	0.00597	0.18277
Third Corner	0.17068	5.22482
Duct After Third Corner	0.00995	0.30462
Fourth Corner	0.17068	5.22482
Settling Chamber	0.00528	0.07926
Contraction	0.01013	0.15202
Honeycomb	0.84865	12.72979
Mesh Screens	3.75720	56.35803
Total (with Splitting Plates)	4.24770	131.21308
Total (without Splitting Plates)	4.55897	169.67051

Table 3.1 depicts the summary of calculations relevant to the pressure loss for all components of the wind tunnel. However, the calculated total power from Eq.(3.7) to recover the calculated total pressure loss is 2.1kW, but by considering a safety factor in a conservative way, a 71JMv Aerofoil axial fan with duty shaft power of 3.84 kW, maximum rotational speed of 3000 rpm, actual duty of 5 m^3/s and static pressure of 450 Pa is utilized to supply air flow through the wind tunnel. Fig.3.2 depicts the fan "pressure-volume" curve and operating point of the fan (Woodcock & Wilson Ltd).

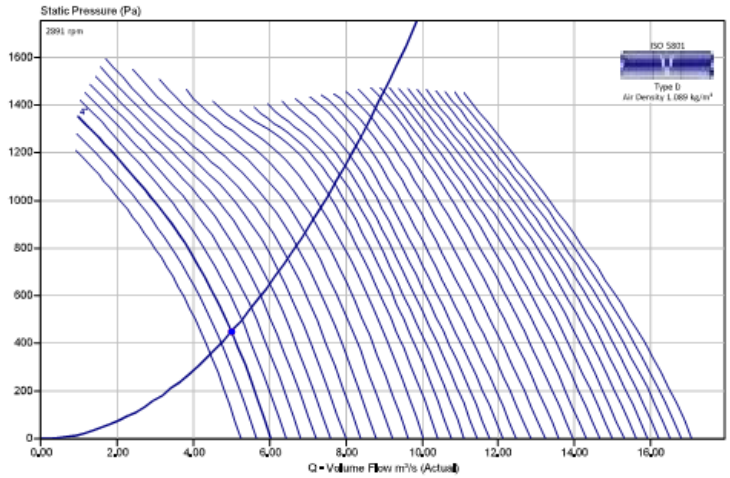

Fig.3.2. Fan pressure-volume curve (Woodcock & Wilson Ltd).

3.1.3- Hump Model and Mounting System

In this research, a hump model is used to investigate the effectiveness of an array of synthetic jet actuators on flow separation control. This model has been designed by the author following the model used by Azzawi (2016), and it was manufactured in the workshop of University of Huddersfield by technicians under supervision of the author. The array of SJAs was amended to achieve higher exit jet velocity. In addition, a removable part containing pressure taps was designed to enable the pressure measurements. The hump model has been manufactured from aluminum with hump chord of 200 mm, span length of 500 mm, the radius curvature of 181.7 mm and height of apex of 30 mm, while the circular profile of hump has been sustained with smooth external surface. Two removable parts has been designed to accommodate synthetic jet actuators and pressure taps in the hump model. The first one is used to accommodate 12 synthetic jet actuators to study the effectiveness of these actuators as active flow controller on the flow separation phenomenon and the second one is an insert contains pressure tap.

For the sake of pressure measurement on the hump surface, the model is equipped with one stream-wise row of pressure taps located downstream of the synthetic jet actuators. The hump model is modified in such a way that 19 taps of 1 mm diameter and 5 mm depth are made in the stream-wise direction. The pressure taps are spaced 5 mm. The Aluminum needles with internal diameter of 1mm has been used to connect the pressure taps to the pressure transducers by vinyl tubes. To have a good match between the needle tip and

insert surface, the needle was sticked out from the hole and then it was machined as much as the needle tip was flushed with the profile of the insert surface.

Also, the model is instrumented by dynamic pressure transducers to measure the pressure fluctuations with one of the ports connected to the reference pressure (P_∞) in the free stream at all times and the other port is connected to the output of an analog multiplexer, which measures pressure at different locations in test section. The tubes bundle is accommodated in the hollowed section under the hump surface. It should ne noted this pressure taps have been predicted for future projects and the pressure measurement are not presented in this research. The 3D models of the hump without removable parts and the pressure taps insert are shown by Fig.3.3, while 2 dimensional schematic of synthetic jet actuator array and an individual synthetic jet actuator with 3 orifices are shown by Figs.3.5 and 3.6, respectively.

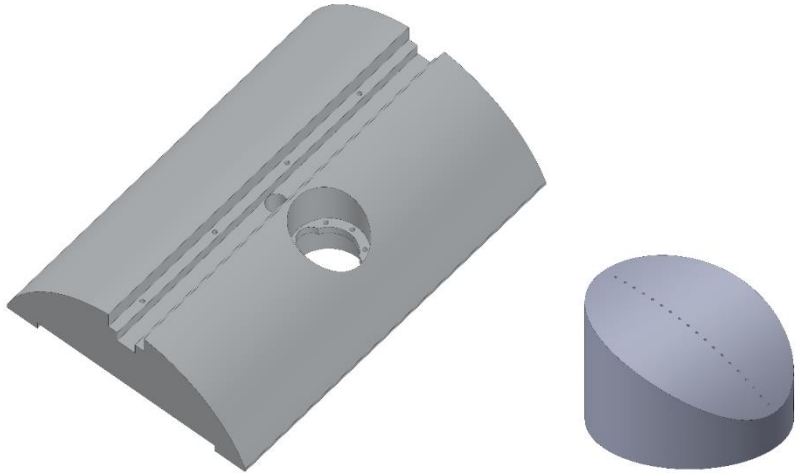

Fig.3.3. Hump model without removable parts (left) and insert of pressure taps (right).

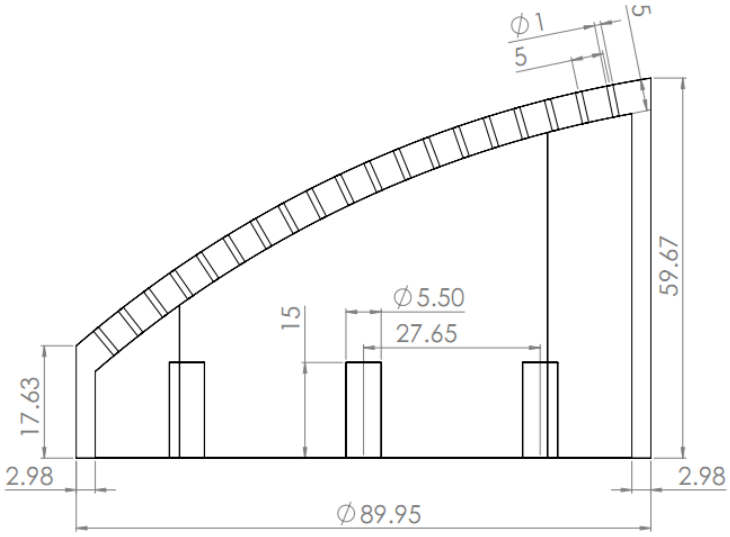

Fig.3.4. 2D schematic of the insert of pressure taps (side view), dimensions are in mm.

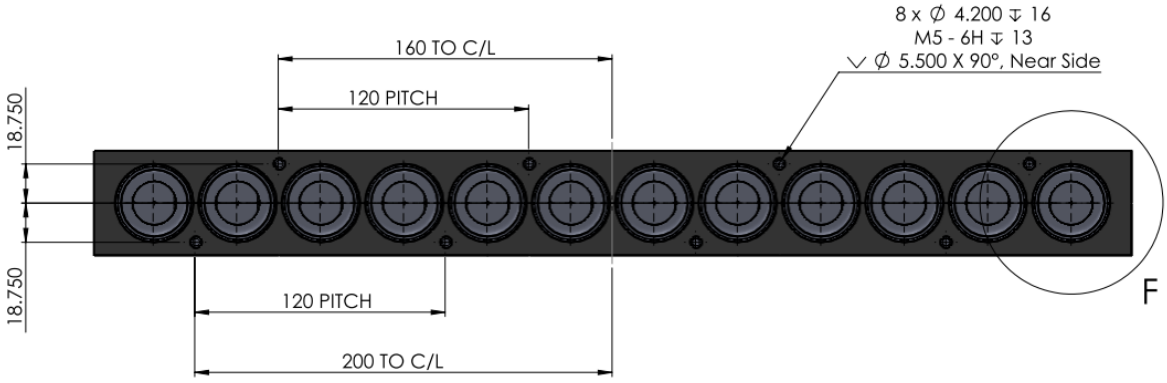

Fig.3.5. 2D schematic of synthetic jet array.

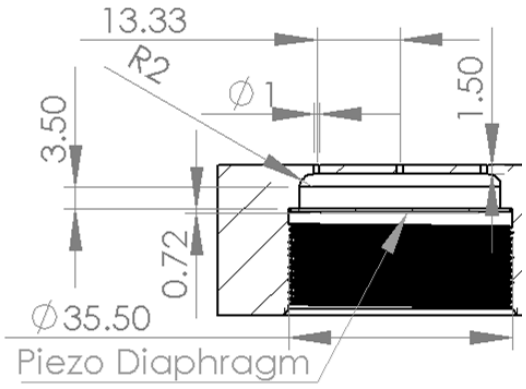

Fig.3.6. Schematic of an individual SJA with 3 orifices.

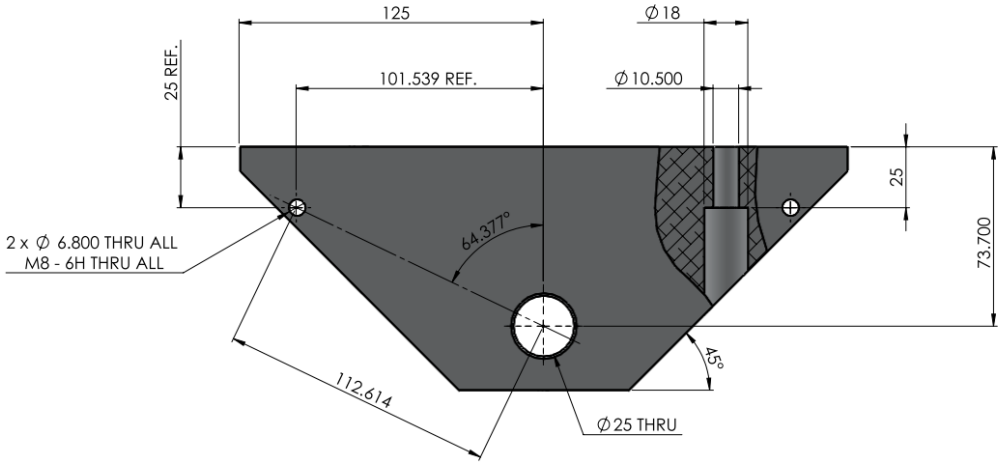

Fig.3.7. 2D schematic of insert shaft support.

Two inserts with semi triangular shape and with height of 100 mm, base length of 70mm and a thickness of 25mm as shown in Fig.3.7 is used to rotate the hump model as a whole. A pivot bar is placed in a hole of 25 mm diameter on rotating joint and this part is joined to the hump model by 8 mm holding brackets on both sides which make the hump capable to rotate into a radial slot around its centerline with a domain of (-32^o, 32^o) by loosening and tightening 2 M8 brackets fixed on two side wall plates, a 360^o digital inclinometer protractor is used to change the angular position of synthetic jet actuators. Centerline of hump model is perpendicular to the stream-wise direction at zero degree. Two side wall plates themselves are placed on a separate frame outside the wind tunnel which let the removable plates to be joined to the wind tunnel. These plates have radial slots parallel to the hump curvature and assist the hump to be rotated within these slots.

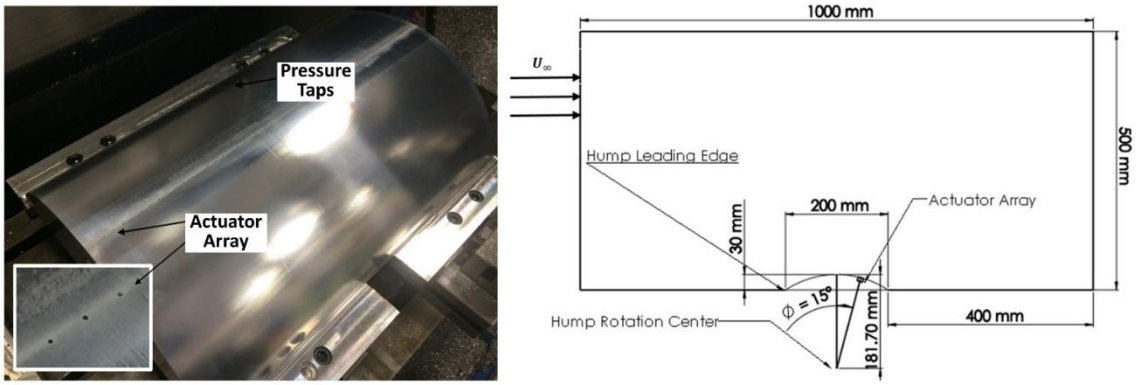

Fig.3.8. The hump model contains actuator array and the pressure taps insert (left), and its position in the test section (right).

3.1.4- Actuator Array and Driving Circuitry System

12 synthetic jet actuators are accommodated in the convex hump model by help of the first removable plate which is laid flush along the span center of hump surface. Each cavity contains 3 orifices which have been made by drilling radially in span-wise direction of hump model. Totally, 36 orifices have been drilled with a diastase of 10 mm between adjacent orifices of each cavity.

Synthetic jet actuators energize the boundary layer by adding momentum via air blowing and inhale the low momentum fluid in the boundary layer during air suction from the exterior region of orifices. In current research, piezoelectric diaphragms are used as actuators of synthetic jets, because they have some advantages than other actuators including small mass, small size, good frequency response and cost-effectiveness. A piezoelectric diaphragm consists of a membrane manufactured from a flexible material onto which a piezoelectric disc is bounded (Hong, G (2006)). The piezoelectric disc excites the membrane to extend and contract periodically by bending modes at a specified drive frequency leading to generation of a train of vortex rings which the net mass flux is zero.

A piezo-ceramic diaphragm of type FT-35T-2.6A1 is used as actuator in this research, the metal disk is made of brass with outer diameter of 35mm and thickness of 0.47 mm, and the ceramic disk has a diameter of 25 mm and a thickness of 0.25 mm which is bounded

by the metal disk. This diaphragm has a resonant frequency of 2.6± 0.5 kHz, a resonant impedance of 200 Ω and a static capacitance of 33±33% nF.

The piezo-ceramic diaphragms are held in place by help of a clamping piece from the same material of disc element with the depth of 10mm as shown in Fig.3.9.

Fig.3.9. Synthetic jet actuators supported by clamping pieces.

Azzawi, I.D.J, (2016) studied the performance of three clamping types including metal to metal, O-rings and Neoprene rubber to investigate which clamping type can supply a stronger seal. The diaphragm of each clamping was excited with a sine sweep over a frequency range of 10 Hz to 3 kHz, he found that the best uniformity of deformation was achieved by the metal to metal clamping compared to the other clamping methods and the maximum diaphragm displacement was achieved by applying the metal to metal clamping.

The driving circuitry consists of the function generator-TG1010A and 6 amplifiers- PDm-200 which are used to drive the piezo-electric diaphragms. The function generator-TG1010A can produce different types of waveforms between 0.1mHz and 10MHz with a resolution of 7 digits and an accuracy higher than 10ppm. Optional waveforms can be loaded via the digital interfaces and then applied in a similar method to the standard waveforms such as sine, square and pulse waveforms. Up to five optional waveforms of 1024 10-bit words can be stored in non-volatile memory. The PDm200 is a complete high-performance power supply and linear amplifier module to drive piezoelectric actuators with an output voltage of 100V, 150V and 200V switchable between unipolar and bipolar options. Up to +/-400V can be attained in the bridged configuration. The connection diagram is shown in Fig.3.10. It should be noted instead using Silicone Rubber Wire cables, the co-axial cables is used to connect the piezo-electric diaphragm to the PDm 200 amplifiers since they don't cause unstable vibrations in the diaphragms as Silicone Rubber Wire cables.

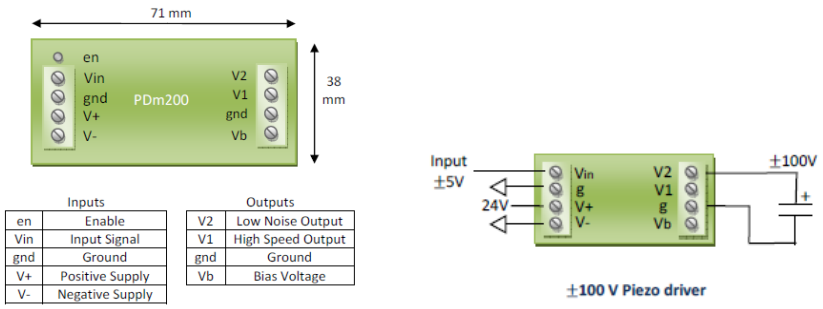

Fig.3.10. PDm200 connection diagram (PiezoDrive Ltd, (2017)).

The amplifier has an input voltage range of +/-10 V and a gain of 20. A power converter produces a bipolar or unipolar supply, while the voltage selector jumpers control the output voltage range. The load is connected directly to the high-speed output (V1) or through a filter (V2) which reduces the noise and bandwidth. At low frequencies, piezoelectric actuators can be estimated by a capacitance. The required current to drive actuator is proportional to the rate of change in voltage, the required current is approximately (PiezoDrive Ltd, (2017)):

$$I = C\ dV/dt \tag{3.24}$$

where I is the current, C is the capacitance, V is the voltage and t is the time. For a sine-wave, the maximum required current is:

$$I_{max} = \pm \pi V_{pp} C f \tag{3.25}$$

where V_{pp} is peak to peak voltage and f is frequency. For resonant frequency of 3.1kHz, static capacitance of 33±33% nF and peak to peak voltage of 100V, the required current to drive the actuator becomes 42.83 mA, on the other hand, the output RMS current of PDm200 amplifier is 102mA, therefore a PDm200 amplifier can provide the current up to two piezo electric actuators. Therefore, 6 amplifiers in bipolar mode are utilized to drive 12 synthetic jet actuators with a voltage range of ± 100 V.

The driving circuitry system including a power source, cooling fan and 6 amplifiers are connected to 12 synthetic jet actuators via connection wires as shown in Fig.3.11. However, the axial fan is utilised for the sake of heat transfer to cool the system, but the

PDm200 is protected against excessive temperature and current overload, the PDm200 will shut down when the heat-sink surpasses 70℃ (PiezoDrive Ltd, (2017)).

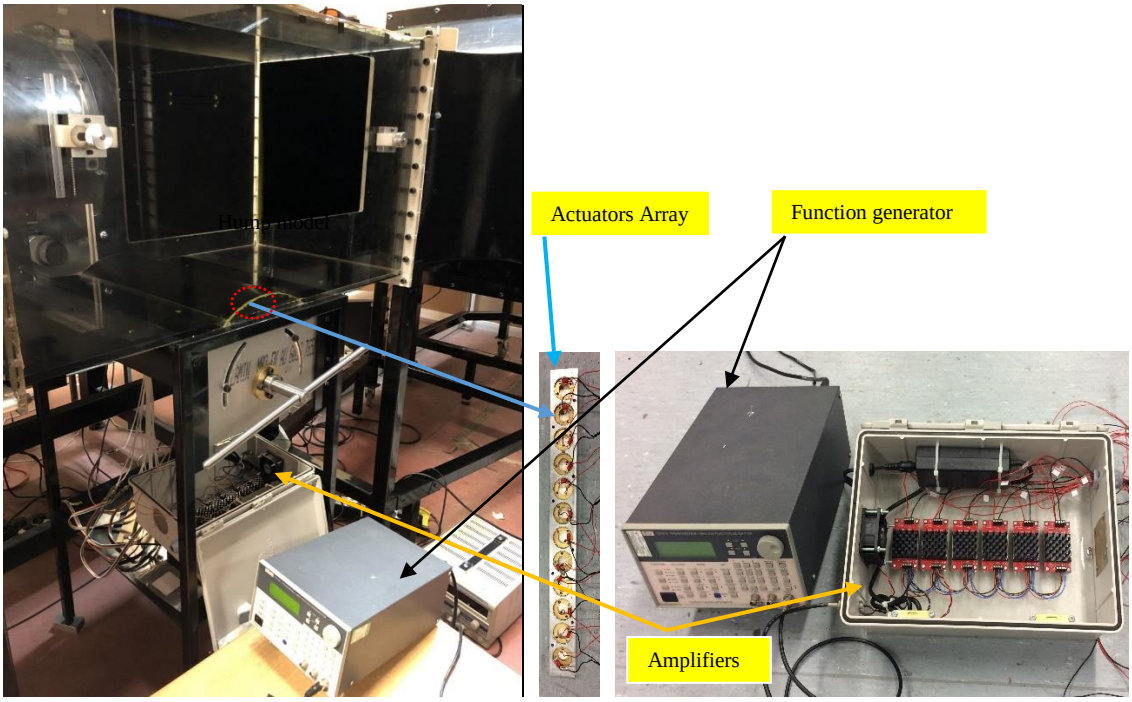

Fig.3.11. Hump model in the test section contains actuators array connected to driving circuitry system.

3.1.5- Constant Temperature Anemometry System

Constant Temperature Anemometry (CTA) is an appropriate measurement method well suited for the investigation of fine structures in turbulent flows. The CTA is used for many years in fluid mechanics as a relatively cheap and impressive technique to measure the rapid fluctuations in turbulent flows. In the next sections, principles of operation, experimental setup and data acquisition, post analysis of data and calibration process are presented.

3.1.5.1- Principles of Operation

A constant temperature anemometer consists of a bridge and amplifier circuit that controls a tiny wire or film sensor at constant temperature. The working principle of CTA is based on convective heat transfer from a heated sensor to the surrounding fluid; the heat transfer is primarily associated to the fluid velocity.

The hot wire is connected to one arm of a Wheatstone bridge against a variable resistor (Fig.3.12, Jorgensen (2002)), which defines the operating resistance, and therefore the hot wire operating temperature. When the bridge is in balance, there is no voltage difference across its diagonal. When fluid flow passes over the heated sensor, the bridge off-balance is sensed by amplifier and therefore the amplifier adjusts the voltage to the top of the bridge independent of cooling imposed by the fluid, keeping the bridge in balance. The bridge voltage shows the heat transfer and therefore it is a direct measure of the fluid velocity. The combination of high gain of the servo loop amplifier and the low thermal inertia of the sensor gives a very fast response to fluid flow fluctuations.

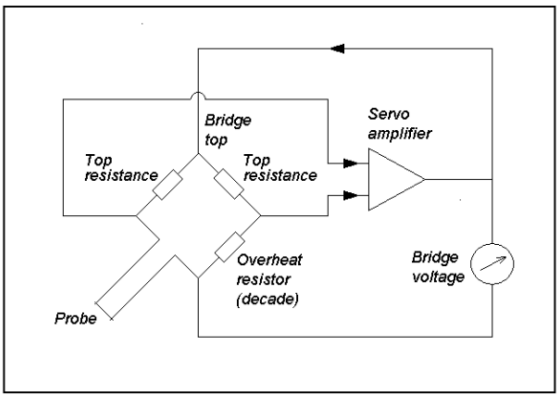

Fig.3.12. CTA principle diagram (Jorgensen (2002)).

CTA has some benefits over other flow measuring principles including high temporal resolution, which makes the CTA most suitable for measuring spectra, being easy to use, having analogue voltage, which information is not lost and being more affordable than Laser Doppler Anemometry (LDA) or Particle Image Velocimetry (PIV) systems (Jorgensen (2002)).

3.1.5.2- Experimental Setup and Data Acquisition

In this research, MiniCTA 54T42 system by Dantec is used to measure the fluid velocity. The system consists of a 55P11 probe with a single tungsten wire (5μm diameter and 250°C operational temperature), probe support, BNC cable with a length of 4m and 50 Ω probe cable to connect the probe to the bridge unit, A/D board, anemometer (1 to 4 channels) with built in signal conditioner. Prior to experiments, the single sensor probe is calibrated, the calibration process being performed in the wind-tunnel, where the

experiments are carried out with a Pitot-static tube as the velocity reference. The calibration produces a relationship between bridge voltage and a reference velocity.

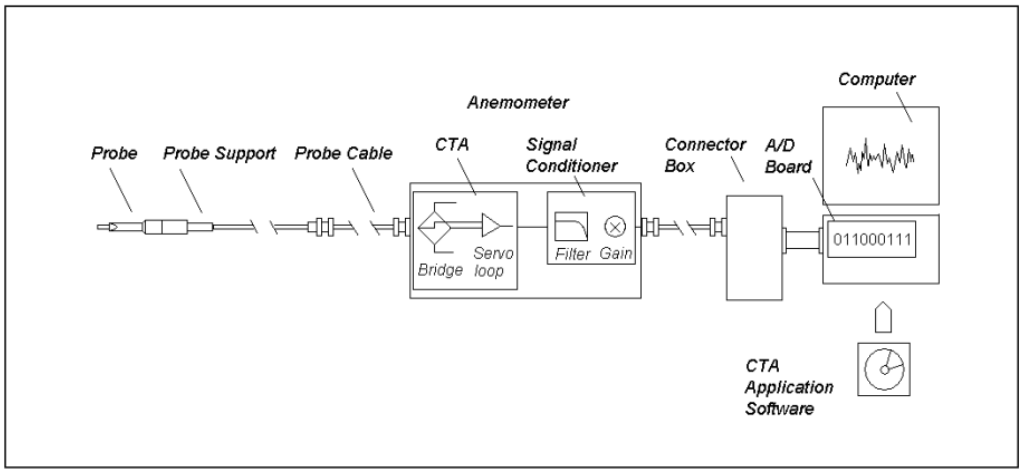

Fig.3.13. Typical CTA measuring chain (Jorgensen (2002)).

The typical Constant Temperature Anemometer measuring chain is shown in Fig.3.13 The entire ± 10Volt signal range is used for filtering and increasing the bridge voltage gain by settings provided by signal conditioners in the MiniCTA. The data acquisition by CTA system is carried out simultaneously with the signal applied to drive the 12 synthetic jet actuators, prior to amplification process to maintain ± 10Volt signal range. Based on Nyquist–Shannon sampling theorem, the sampling rate (SR) should be minimum two times the maximum frequency in the flow (Jorgensen (2002)):

$$SR = 2 \cdot f\ max \tag{3.26}$$

SR is decreased by the number of channels, n, in use:

$$SR(n) = 1/n \cdot 2 \cdot f\ max \tag{3.27}$$

If the sample size and sample rate of data acquisition are 128 kpt/channel and 10 kHz, respectively, therefore, the required time to acquire data becomes:

$$\frac{(sample\ size) \times 1024}{Sample\ rate, Hz} = \frac{(128) \times 1024}{10000} = 13.33\ s$$

The hot wire system performance, data acquisition software as well as the sample size and sampling rate of data are checked out by doing a test on a circular cylinder. The details of experiment can be found in Appendix A.

A controllable traverse system is used to move and control the probe in test section to measure flow velocity. This system is mounted at the wall of the test section as shown in Fig.3.14. It can be displaced in stream wise plane (x,y) and also perpendicular to this plane (z direction) with a domain of approximately (1m, 0.5m, 0.5m) and a resolution of 0.005mm.

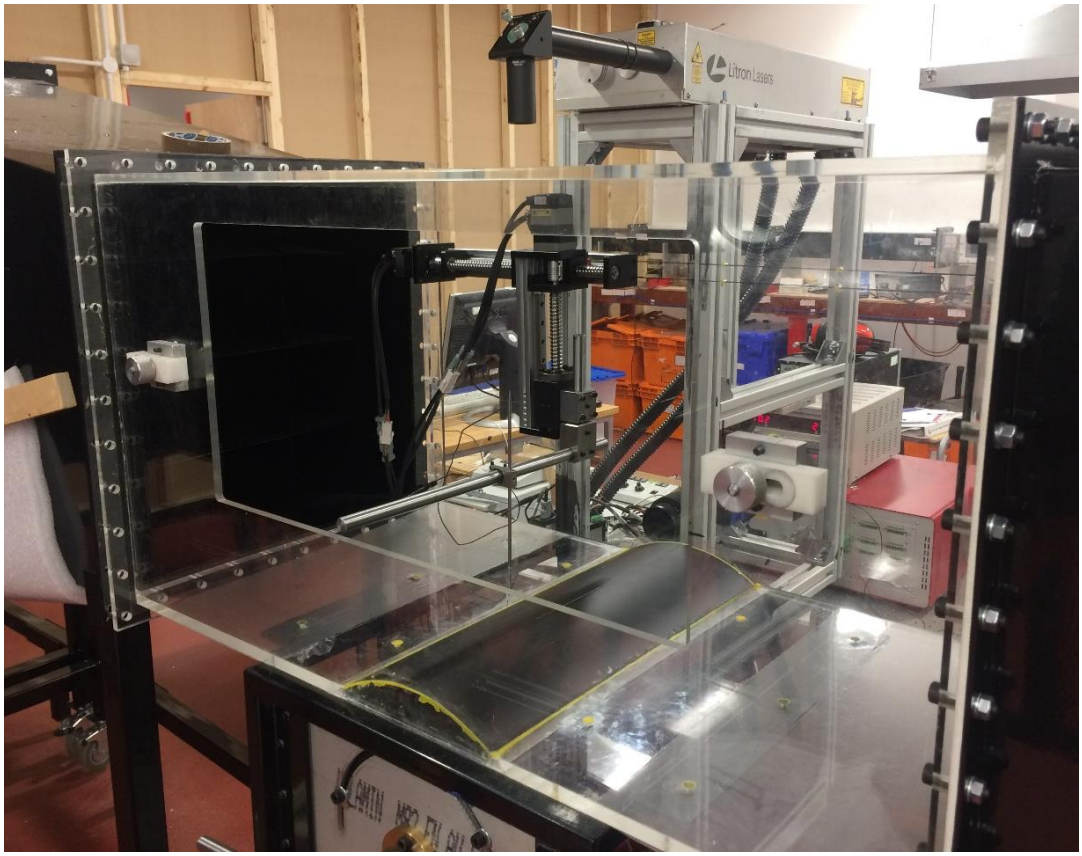

Fig.3.14. Traverse system mounted on the test section sidewall supporting HWA probe. PIV laser sheet delivery system is shown at the top.

3.1.5.3- Data Post Processing

The CTA system is used to determine the characteristics of wake flow behind the hump model by measuring the mean velocity, velocity fluctuation (RMS level) and the dominant frequency of fluctuations. Fast- Fourier Transform (FFT) is utilized to find the dominant

frequency of the velocity fluctuations. The FFT operation yields an output of amplitude or power of each trigonometric component as a function of their corresponding frequencies. The output is called Power Spectral Density (PSD) or frequency spectrum.

Welch's method (P.D. Welch (1967)) is used to estimate the power spectra by splitting up the time signal into successive overlapping segments, windowing of the overlapping segments, forming the periodogram for each segment, and averaging. However, 10 different windowing functions including Rectangular, Triangular, Hamming, Hann, Kaiser, Blackman, Balckmanharris, Gauss, Tukey and Taylor functions are tested in this research but noticeable difference is not observed between them. The Hamming window function is used to window the segments for all cases.

The dominant broadband of the velocity fluctuations is identified by the maximum amplitude in frequency spectra, which represents the magnitude of power for a specific broadband as a function of frequency. The region near to the frequency of zero in the frequency spectra is not considered because the output of CTA has a direct current bias. MATLAB programs are used to help the data processing (Appendix B).

However, it is not possible to get any information from the single sensor probe regarding the velocity direction of the fluid flow passing over it, but the direction is identifiable when the single sensor probe has been placed at the outlet of the orifice of actuator.

It is possible to define the direction of velocity due to the nature of flow field near to the jet exit plane, as Smith and Glezer (1998)) studied the formation and evolution of synthetic jets, while the jets leave the orifice with a very small area and as a result high velocity during blowing cycle, the fluid is drawn into the cavity from the whole area outside of the orifice during suction cycle leading to a considerable difference between the peak mean velocity during blowing cycle and velocity during suction cycle. The difference becomes more noticeable when the probe is removed against the actuator. This feature helps us to ascertain the velocity direction and consequently the diaphragm displacement without need to a displacement transducer alongside limitations of space to implement such facilities.

3.1.5.4- Calibration Process

Prior to experiments, the single sensor probe should be calibrated and the calibration process can be performed by two methods. In the first method, it can be carried out in a dedicated calibrator with a low-turbulent free jet, whose velocity is computed on basis of the pressure drop over its exit. In the second method, calibration can be performed in the wind-tunnel, where the experiments are going to carry out, with a pitot-static tube as the velocity reference. The second method is used to calibrate the single sensor probe in this research.

A calibration produces a relationship between bridge voltage and a reference velocity. The basic relationship between convective heat transfer Q and velocity V for a wire placed normal to the flow with the wire surface A_w, the heat transfer coefficient h and the wire over–temperature $T_w - T_0$ was proposed by King (1914):

$$Q = (T_w - T_0)A_w\, h = A + BV^n, n \approx 0.5 \tag{3.28}$$

where A and B are the calibration constants. The relation between the bridge voltage E and velocity V may be described as an exponential function or as a fourth order polynomial as follows (Bruun (1995)):

$$E^2 = A + BV^n \tag{3.29}$$

$$V = a_{00} + a_{01}E + a_{02}E^2 + a_{03}E^3 + a_{00}E^4 \tag{3.30}$$

where A, B , n and a_{00} , a_{01}, a_{02} , a_{03}, a_{04} are calibration constants. The velocity versus bridge voltage curve, the coefficients, and the mean square error as a measure of how well the curve fit the calibration points has been displayed by Fig.3.15 for 22 calibration points.

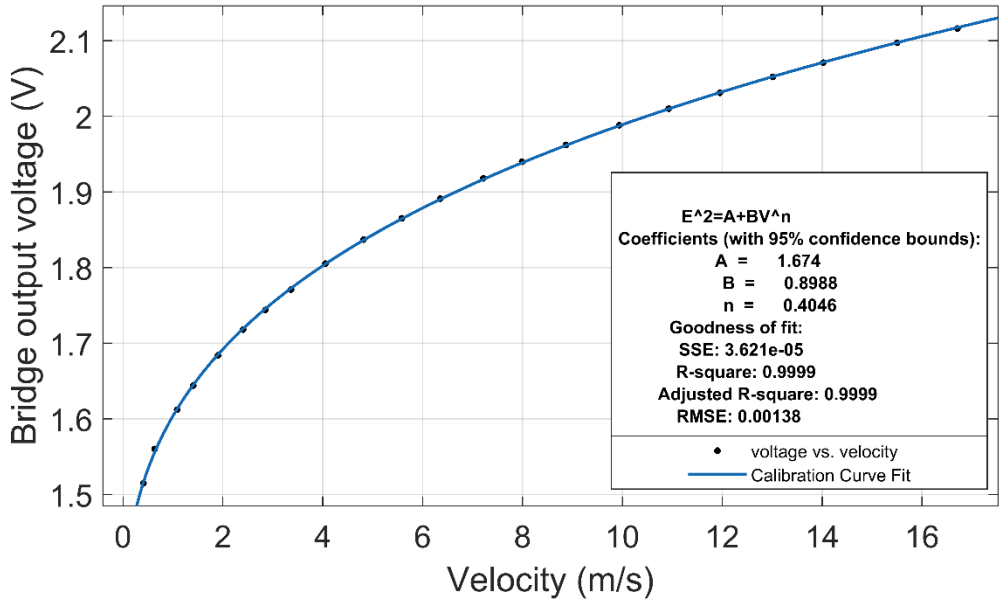

Fig.3.15. Calibration curve fit, coefficients and mean square error.

3.1.6- Particle Image Velocimetry (PIV) Technique

Particle Image Velocimetry or PIV, refers to a whole flow field technique used in fluid mechanics to determine the instantaneous fields of velocity vector by measuring the displacements of many fine particles which precisely follow the fluid motion. In the next sections, the principles of operation, experimental setup and data acquisition, post analysis of data, calibration process as well as the flow seeding technique will be explained.

3.1.6.1- Principles of Operation

The first basic work for a PIV theory was carried out theoretically by Adrian (1988), he described the expectation value of the auto-correlation function for a double-exposure continuous PIV image and used this description to make the general structure of principles for the experimental setup (Keane and Adrian 1990). The generalization of the theory carried out in the next studies by including multiple-exposure recordings (Keane and Adrian 1991) and analysis of cross-correlation (Keane and Adrian 1993). Main features of PIV technique are non-intrusive measurement, high velocity range (from zero to supersonic), high accuracy, capability of measurement of all 3 components of velocity and instantaneous velocity maps in a cross section of flow. Generally, a standard PIV system consists of monoscopic (single lens) camera, particle seeding, a double pulsed laser, light sheet forming optics, image

digitization hardware and a computer to save and analyze the acquired data. Fig.3.16 depicts the experimental arrangement for PIV recording. While flow is seeded by small tracer particles, a laser illuminates a light sheet twice within the flow with a specified time delay between pulses. Then the high-quality lens records the scattered light from the tracer on a one double frame or two single frames. After that the acquired data is digitized by the hardware and then the output is sent to the computer to store and analyze.

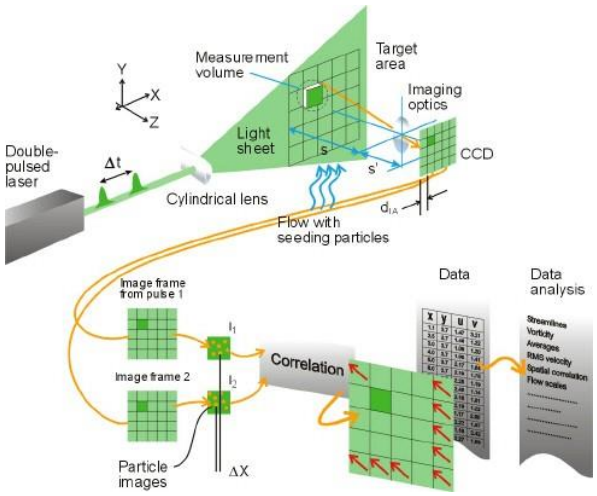

Fig.3.16. General schematic of experimental setup for PIV (Dantec LTD, (2020)).

3.1.6.2- Experimental Setup and Data Acquisition

In this research, a commercial PIV system by LaVision, which consists of a Nano-L-200-15 PIV pulsed Nd:Yag laser, ImagePro4M CCD camera with Sigma 105mm f/2.8 Macro – Nikon lens alongside a CNC-IMS8 controller (ISEL) as the traverse agent to move the camera, is used to acquire images. LaVison aerosol generator Sv-23113 is used to seed the flow with DEHS oil with 0.3 μm diameter of oil droplet and a life-time of 4 hours. The seeding of fluid is done from the diffuser inlet. While flow is seeded by small tracer particles, the laser beam is guided via black tube screwed to the end of laser head (as shown Fig. 3.13), then it is redirected in the vertical direction using NB1-K12 mirror with thickness of 6mm which is supported at a mirror mount connected to the other end of black tube. After that, this vertical laser beam is expanded via a cylindrical lens and is focused on the surface of hump model parallel to the stream wise plane (X-Y plane). Optical axis of camera is perpendicular to the side wall of the wind tunnel and the laser

sheet. A 532 nm band-pass filter in front of the CCD camera is used which allows only the scattering signal to be collected. While the laser illuminates the light sheet twice within the flow with a time delay of 50 μs between pulses, the scattered light from the particles is captured by camera operating at 5Hz to acquire 100 pairs of images in double-frame mode. Then, the acquired image-pairs are transferred to computer and data are processed by LaVision software (DaVis). Synchronization of the camera and laser pulses is controlled by a PTU (Programmable Timing Unit) with activation time of 0.342µs.

Prior to experiments and for the sake of maximum safety, matt black self-adhesive film and painted matt black aluminum sheets are utilized to cover all areas of the test section that are irrelevant to the area of interest to prevent any dangerous reflection from the internal walls of test section. In addition, laser interlock system is used to power off the laser upon opening the lab door by individuals. Also, the laser path between the laser head and the sheet optics is enclosed by black tubes which are screwed to the end of the laser head to prevent the escape of scattered light and reflections. The laser sheet after the lens, before it enters the wind tunnel is enclosed by an appropriate box.

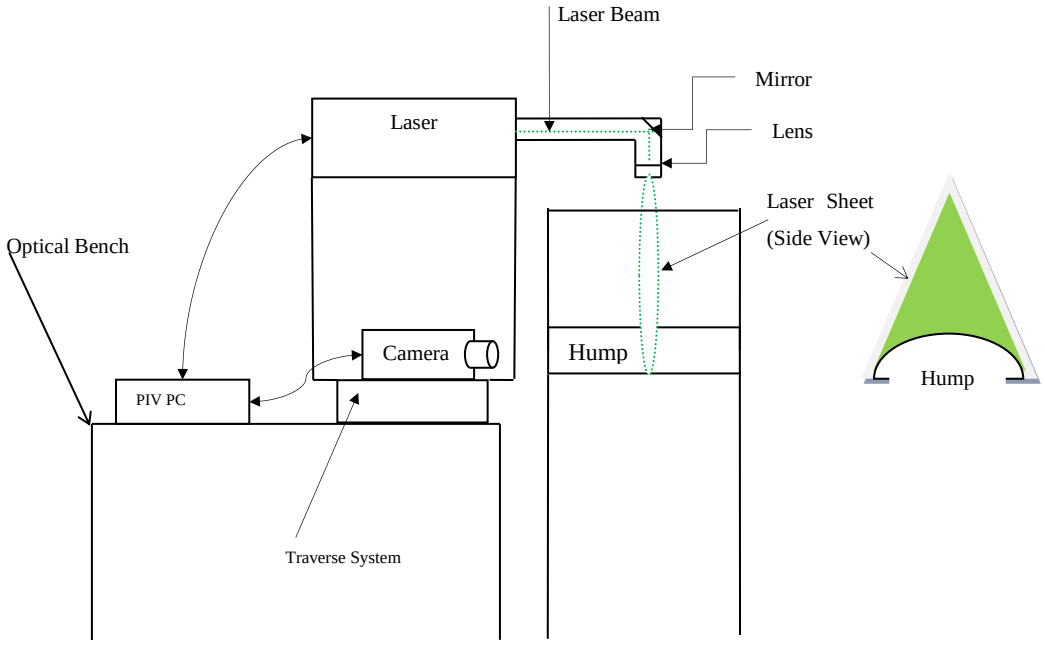

Fig.3.17. Schematic of experimental setup of PIV system.

The position of the laser sheet optics can be changed by and changing the mirror and lens positions; however, the laser power should be set on the low power values during laser sheet setting. The schematic of experimental setup is shown in Fig.3.17.

The schematic of basic PIV timing system is shown in Fig.3.18. At first, the PIV timing system receives an external trigger signal, then it sends a signal to the Nd:YAG lasers and the flash lamps of the lasers are initiated.

A short time later (generally 180µs), the Q-switches of the lasers receives the signals from the timing system and two laser light pulses are produced with a predetermined time delay and the recording of a frame pair with the digital camera is initiated by the timing system. Moreover, the surface of the hump model has been painted matt black to prevent any laser light reflection. The maximum frequency of Crystal oscillator of the laser is 10Hz, therefore the required minimum time to acquire a pair of image is 0.1 seconds.

The timing is set in a way that the first and second laser pulses occur in the first and second frames, respectively. The recording periods for the first and second frames are approximately 250 µs and 33ms, respectively, while the interframe time is very short (generally 0.2µs).

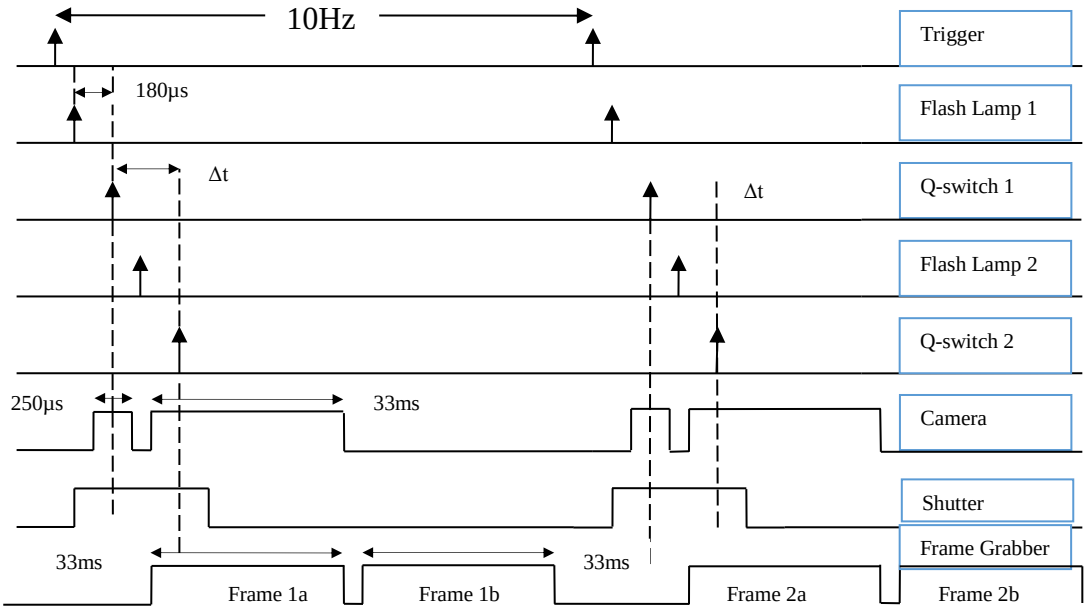

Fig.3.18. The schematic of basic PIV timing system (adapted from Adrian, R.J. & Westerweel, J (2011)).

When the acquired data in the first frame is transferred from the camera to the frame grabber, simultaneously the data is acquired in the second frame. After recording of the second frame, it also is transferred to the frame grabber.

All images can be acquired with the same recording period by the so-called frame straddling technique (Wernet (1991) and Lecordier et al (1994)). In this technique, the laser light pulses are coincided with the end of frame 1 and the starting of frame 2, respectively. The period time of recording generally is 33ms.

3.1.6.3- Data Post Processing

The acquired image-pairs are transferred to the computer and data are processed by LaVision software (DaVis). For the assessment of images via correlation technique, the whole image is divided in so-called interrogation windows. The correlation function performs operations on the intensities inside every interrogation window and passes through the whole PIV recording with a defined window shift. One velocity vector is given by the assessment for any interrogation window.

The evaluation of images is done iteratively via cross-correlation in multi pass mode by utilizing the standard FFT with initial and final interrogation window sizes of 64 pixel × 64 pixel (1 passes) and 32 pixel × 32 pixel (2 passes), respectively. During a multi-pass, the initial interrogation window size is divided by two in each step until the final interrogation window size is achieved.

Also, Gaussian weighting function is used for the interrogation windows by utilizing a round weighting factor (1:1) for initial interrogation window size of 64 pixel × 64 pixel with 50 percent overlap, which enhances the accuracy of the vector field computation as the outcome vector weights the local information higher than the pixel information further away and such represents the local shift better. However, the drawback is the higher calculation time. As in the current study, there is a high gradient in the wake region, the elliptical weighting factors (2:1) also is utilized for final interrogation window size of 32 pixel × 32 pixel with 50 percent overlap which enhances the accuracy of the vector field computation. Validation parameters are used in combination to fine-tune the processing

and to remove the spurious vectors. Peak validation is helpful to identify invalid vectors, but it is not able to produce an estimate of what the correct vector might be. Therefore, the invalidated vector will be replaced with zero, which in most cases can be absolutely far from the truth. Consequently, the peak validation is used in combination with a local neighborhood validation, which based on neighboring vectors is capable of producing a realistic estimate of what the spurious vector should have been. Individual vectors are compared to the local vectors in the neighborhood vector area by local neighborhood validation, replacement vectors are determined from a 3point × 3point neighborhood scheme.

If a spurious vector is identified, it is rejected and replaced by a vector, which is computed by local interpolation of the vectors available in the 3point × 3point area. Interpolation is done using median or moving average approach with specified iterations. Spurious vectors are detected via the value given to the Acceptance Factor. This factor gives a degree of freedom on velocity vector gradient in an effective manner inside the 3point × 3point area and if the calculated gradient is bigger than set, the central vector is eliminated. Whatever this factor is bigger; the velocity vector map is spatially rectified less. On the other hand, with lower values of factor, the vector map is smoothed at a level that eliminated all.

3.1.6.4- Calibration Process

Mathematical imaging models can be utilized to describe the transformation process of points from the object spaces to the image plane. All models have a number of variables and specifying the values of these variables in a particular image acquisition setup is referred to as Imaging Model Fit, because variables are fitted to provide the best match between corresponding coordinates in the object space and image plane.

For 2D imaging models, the calibration target is aligned with the light sheet (at location z=0) and a single image is enough to acquire. It is sufficient to define the pixel/mm scale without taking further distortions into account. Two points in the object space by insertion the calibration target in the object domain are identified with known distance in mm between them to calculate pixel / mm scaling.

Generally, it is not possible to illuminate the calibration target with a laser light source because a speckle pattern is produced due to the reflective surface of the calibration target which compromise the contrast of the calibration image, therefore the target is illuminated by a white light source.

3.1.7 - Flow Seeding Technique

In flow seeding technique, the visibility of particles that is their ability to form visible image under a certain illumination, should be considered as priority. It should be large adequately to reach the exposure levels that are at least 30-50% of the saturation level of the image recording medium. On the other hand, a good combination of enough laser power with particle having sufficient size and high refractive index should be maintained. In addition, PIV system doesn't work very well too far below the threshold at which the particles are vaporized by the laser energy. Therefore, improving visibility is best attained by improving the scattering of particles. To sustain the high fidelity tracking of the fluid, the size must be balanced against the need for small particle mass (Adrian, J.R and Westerwell, J (2011)).

Also, volume fraction (ratio of volume of particles to volume of unit volume of the fluid) can be controlled by utilizing small particles. When volume fraction is kept under .1%, based on Einstein's formula (Einstein 1906, 1911, Roscoe 1952) for a viscosity of a dilute suspension of uniform spheres, the added viscosity doesn't surpass 0.25% of the value without particles. Therefore, as an effective upper limit to keep the particles behavior such as flow, we should have approximately to 10 particles of diameter 20 μm in a cubic interrogation volume 500 μm on a side. In gaseous flow the mass fraction should not exceed 0.25% to prevent two phase flow effects which is corresponding to approximately to 10 particles of diameter 1 μm in a cubic interrogation volume 150 μm on a side (Adrian, J.R and Westerwell, J (2011)).

For the sake of flow seeding, different liquids such as Di-Ethyl-Hexyl-Sebacat (DEHS), dioctylpathalate, olive oil and vegetable olive have been applied successfully in a wide variety of researches. In this research, DEHS is used for the sake of smoke generation with utilization of a LaVision seeder (Sv-23113).

Generally, without considering of the source of smoke, it is crucial that smoke meets these criteria as following (Smits, A.J and Lim, T.T (2000)):

1. Particles must be able to track the flow field; therefore, they must be adequately small so that their motion reflects the flow motion.
2. The flow field under investigation must not be affected remarkably.
3. Particles must have high reflective properties.
4. It must be non-toxic.

The LaVision seeder generates a polydisperse aerosol by atomizing liquids into particles in the sub-micrometer range. In LaVision aerosol generator, four atomizer nozzles are integrated in the liquid vessel and concentration of particles is adjusted by setting the pressure reducer and/or by opening or closing the nozzles. Compressed air passes the atomizer nozzles and generates a high-velocity jet. As a consequence, the liquid in the reservoir bottle is broken up into droplets and suspended in the flow. Large droplets are separated by the liquid vessel leading to a particle size predominantly below 1µm.

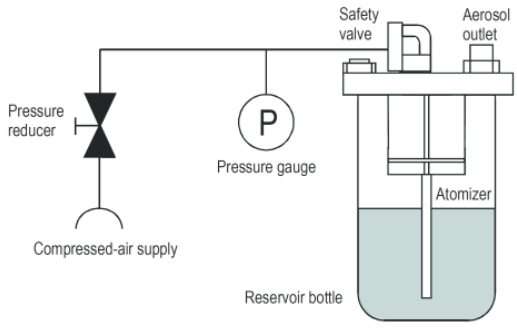

Fig.3.19. Schematic of the seeder.

A DEHS droplet with a 0.3 µm diameter has a life time of 4 hours; therefore, the large flow facilities such as wind tunnel are not permanently polluted. In addition, DEHS is a no soluble, odourless and colourless liquid which is appropriate for generation of steady aerosols. The advantages of using DEHS are spherical particle, long aerosol life times (also at high temperatures), lowest filter contamination due to the small particle sizes mainly below 1 µm and familiar optical properties.The general schematic of the experimental setup can be seen in Fig.3.20

Fig.3.20. The general schematic of experimental setup.

3.2- Numerical Methodology

In this section, the methodology of numerical analysis of the fluid flow over the hump model is described. The OpenFOAM (Open source Field Operation And Manipulation), an open source software for computational fluid dynamic is used for the sake of mesh generation to produce the computational grid, pre-processing and post-processing to prepare the simulation and to process the results of simulated cases. The geometry and computational grid generation process for both unactuated and actuated cases as well as the initial and boundary conditions of the problems and the employed numerical method is illustrated.

3.2.1- Geometry and Computational Grid

In this section, the process of mesh generation is discussed and the effects of important parameters on the quality of generated mesh is investigated. Grid generation is an essential part of numerical analysis and certain criteria must be satisfied to have a valid and accurate solution. Two powerful utilities of OpenFOAM software including blockMesh and snappyHexMesh tools are utilized to generate the mesh from complex geometries.

The snappyHexMesh utility is a powerful tool which generates three-dimensional mesh containing hexahedra and split-hexahedra from tri-surfaces or triangulated surface geometries automatically in Stereolithography (STL) format or Wavefront Object (OBJ) format.

The stages of mesh generation with snappyHexMesh tool are as following:

- Background mesh or base mesh generation
- Definition of the geometry
- Castellated mesh or Cartesian mesh generation
- Snapped mesh or body fitted mesh generation
- Boundary layer mesh generation (addition of layers near to the surfaces)
- Checkout of the mesh quality

In the first step, the blockMesh tool is used to generate the background mesh of hexahedral cells that covers the whole region of the test section contains the model within by external

boundary as shown in Fig.3.21. The background mesh defines a base level mesh density and the limits of the computational domains.

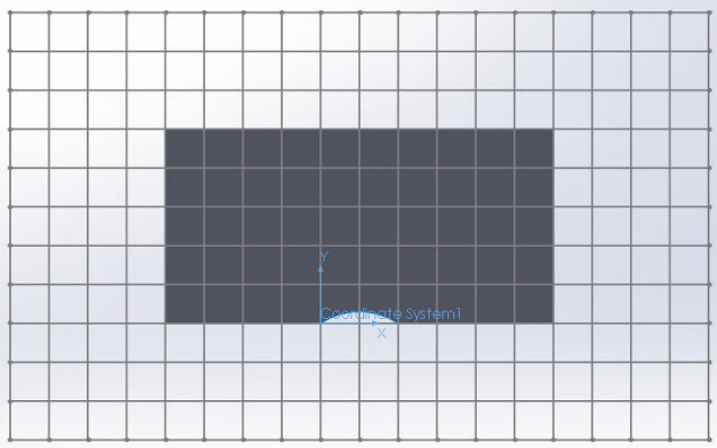

Fig.3.21. Background Mesh, first stage of mesh generation in snappyHexMesh process.

Three criteria must be considered when the background mesh is generated:

Firstly, the mesh must be composed entirely of hexes. Secondly, to speed up the convergence of snapping process, the cell aspect ratio should be around 1, at least near STL surfaces at which the subsequent snapping technique is exerted. Thirdly, at least one intersection of a cell edge with the tri-surface must be available.

In the next step, the made up geometry from multiple surfaces is defined. In this research, the surface geometries have been created in STL format made up by multiple surfaces rather than a single surface to generate the mesh. It has two advantages including the possibility of local refinement in each individual surface, e.g. surfaces relevant to tiny orifices or the cavities and more control on the mesh generation process. The refinement box also is defined in this stage.

In this numerical study, a slice (one-twelfth) of the whole geometry containing one cavity and 3 orifices for both un-actuated and actuated cases was considered.

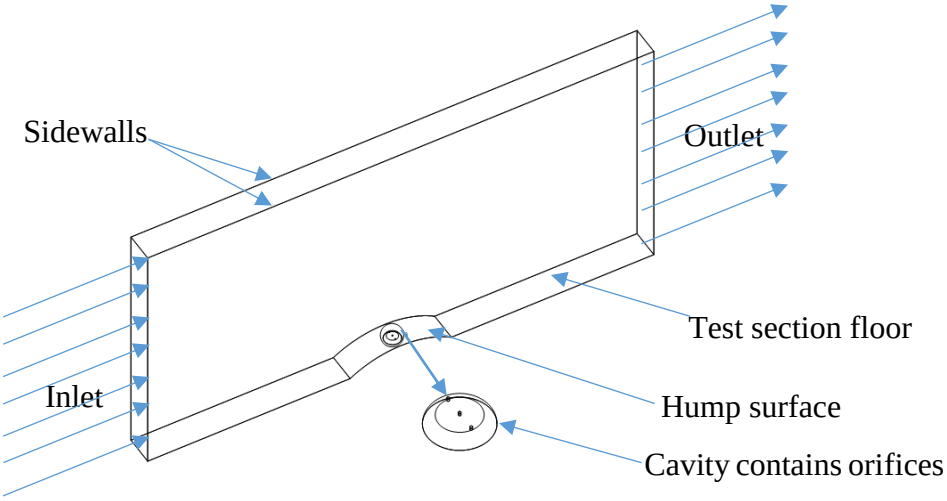

Fig.3.22. A slice of the whole geometry contains one cavity and 3 orifices.

In the third stage, the feature edge, surface and volume mesh refinement are defined and cell splitting is executed according to the specified settings in the castellatedMeshControls sub-dictionary of the snappyHexMesh dictionary. The most important parameters of castellatedMeshControls are nCellsBetweenLevels parameter to control the number of buffer layers of the cells between consecutive levels of refinement and resolveFeatureAngle parameter to control the local curvature refinement.

For the first parameter, we use typical value of 3 to control the transition between levels of cell refinement and having more gradual mesh and for the second one, we use the value of 80. Whatever the value of resolveFeatureAngle parameter is higher, the less feature is captured and the refinement in high curvature areas can't be added. Edge feature snapping also can be controlled by this parameter, the sharp angles in surface intersections couldn't be resolved by considering high value of this parameter.

The castellated mesh generation process is completed by specifying the refinement levels for feature edges and surfaces and refinement level for cells in relation to the surfaces of volume in distance mode. The generated mesh out of the boundaries of STL surfaces and inside the background mesh is removed by choosing an appropriate point located inside the STL surfaces with locationInMesh parameter. The cells that are more than 50% outside the bounding region containing the selected point are deleted and the kept internal mesh is ready for snapping process.

In the snapping stage, the jagged castellated surface from the mesh is removed by moving cell vertex points onto the surface geometry. The snapping process involves four stages as following (OpenFOAM(2017)):

1. Vertices in the castellated boundary are moved onto the STL surfaces.
2. The calculation for the relaxation of the internal mesh with the latest moved boundary vertices is carried out.
3. Responsible vertices for breaching the quality of mesh are identified.
4. Displacement of those vertices from their initial value at first stage is reduced and it is repeated from the second stage until mesh quality is satisfied.

Most important parameters to improve the quality of mesh are nSolveIter, nRelaxIter and nFeatureSnapIter parameters representing the number of mesh displacement relaxation iterations, the maximum number of snapping relaxation iterations and the number of feature edge snapping iterations, respectively. The values of 30, 5 and 15 have been set for these parameters, respectively. The quality of body fitted mesh can be improved by increasing the value of nSolveIter parameter, however the required time for calculations will be increased. The quality of edge features can be improved by increasing the value of nFeatureSnapIter parameter.

In the next step, additional layers of hexahedral cells aligned to the boundary surface are added to a specified set of boundary patches. This stage is optional and it is controlled by the settings in the addLayersControls sub-dictionary of the snappyHexMesh dictionary.

The generated mesh from previous stage is shrinked from the boundary and additional layers of cells are added in such a way that the mesh is projected back from the surface by a defined thickness in the direction normal to the surface. In the second stage of this process, the calculations for the relaxation of the internal mesh with the latest projected boundary vertices is carried out, the layers are added if the validation criteria is satisfied, otherwise the projected thickness is reduced and second stage is repeated until the validation criteria is satisfied, otherwise the layers shouldn’t be added.

3.2.1.1 Computational Grid of Unactuated Case

To reduce computational cost, the blockMesh tool is used to generate a structured mesh for unactuated case without considering the actuator. To size up the near-wall mesh in the computation, standard correlations for a fully turbulent boundary layer over a smooth flat plate under stream-wise zero pressure gradient are used, Calvert and Farrar (2008).

$$\delta/x = 0.37\, Re_x^{(-0.2)} \tag{3.31}$$

$$C = 0.058\, Re_x^{(-0.2)} \tag{3.32}$$

$$y^+ = yu_\tau/\nu \tag{3.33}$$

For a wall-resolved RANS simulation, the first cell height of the computational domain has to be of the same order of y^+= 1. Then, by considering the free stream velocity of 7 m/s at the inlet of the test section, the first cell height at the inlet should be considered 0.04 mm. The generated structured mesh in x-y plane is shown in Fig.3.23. The mesh specifications is summarized in Table 3.2.

Table 3.2 Structured Mesh Specifications-Unactuated Case.

Overall Number of HexaHedra Cells	Maximum Skewness	Average Non-orthogonality	Maximum-Non-orthogonality	Maximum Aspect Ratio
5530000	0.7	4.19 Degree	33.22 Degree	55.99

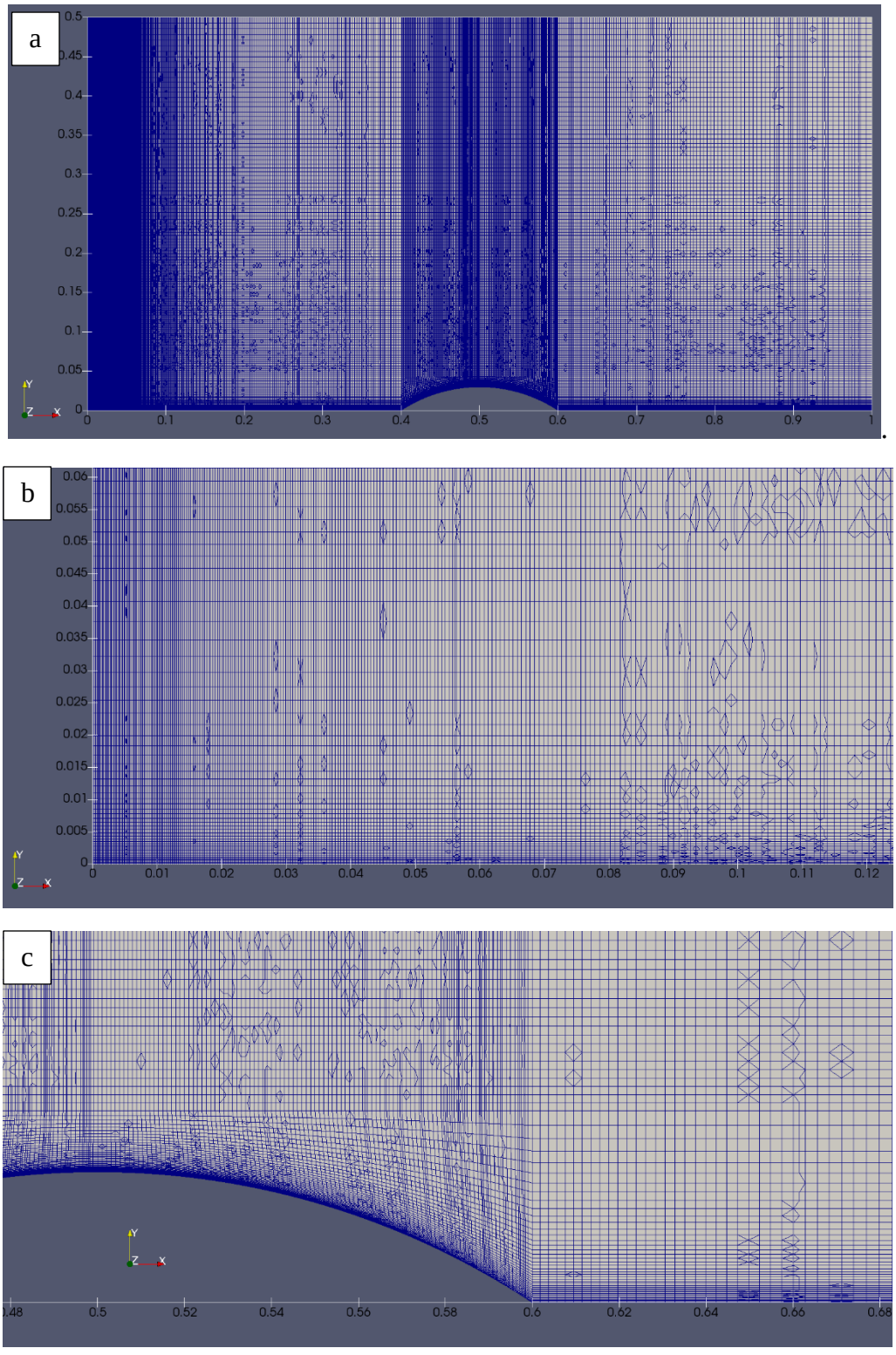

Fig.3.23. (a) Computational domain and mesh in the x-y plane, (b) Closer view of inlet and near wall region and (c) Closer view of region contains hump apex and hump trailing edge.

3.2.1.2- Computational Grid of Actuated Case

Due to the orifice size and the complexity of actuator geometry, it is preferred to get the best features of both blockMesh and snappyHexMesh tools by merging and stitching two separate meshes (so called masterMesh and slaveMesh) to produce the computational grid for actuated case. One benefit of this technique is the reduction of computational cost either by avoiding the refinement of cells in all directions during the refinement phase in case of using snappyHexMesh tool, or by avoiding giving the penalty to refine the computational blocks in neighborhood of orifice blocks in case of using blockMesh tool.

The procedure to generate the computational grid for actuated case is as follows:

1. Generation of computational grid (masterMesh) for the whole domain except the actuator mesh by blockMesh tool
2. Generation of computational grid (slaveMesh) for actuator by snappyHexMesh tool
3. Merging masterMesh and slaveMesh by mergeMesh tool
4. Stitching corresponding patches of masterMesh and slaveMesh by stitchMesh tool

Three pairs of corresponding patches are stitched to each other in three stages, consecutively. The mesh is designed with a cell size of 0.04 mm × 0.04 mm (X-Y plane) at the bottom left corner of the computational domain. This is expanded by exponential stretching with a ratio of 1.03 in Y direction and 1.08 in X direction. The cell size in span-wise direction for slaveMesh is 0.04 mm while for masterMesh it is 0.8 mm to reduce computational costs. The final computational grid of for actuated case as well as a closer view of slaveMesh which is stitched to the masterMesh are shown in X-Y plane by Fig.3 -24. The specifications of final mesh for actuated case are summarized in Table 3.3.

Table 3.3 Mesh Specifications- Actuated Case.

Overall Number of Cells	Hexahedra	Prisms	Tet-wedges	Polyhedra
13097910	12220822	169936	215	706937
Skewness	Average Non-orthogonality	Maximum-Non-orthogonality	Maximum Aspect Ratio	
3.7	9.49 Degree	43.39 Degree	373.07228	

It should be noted that the origin of coordinate system for actuated case was chosen at different point in comparison to unactuated case to make the process of mesh generation easier and less expensive by Merging and Stitching techniques. The X- coordinate of origin of computational domain for actuated case has been shifted 0.5 m to the right side in comparison to the unactuated case, ($X_{\text{Unactuated Case}} = X_{\text{Actuated Case}} + 0.5$ m).

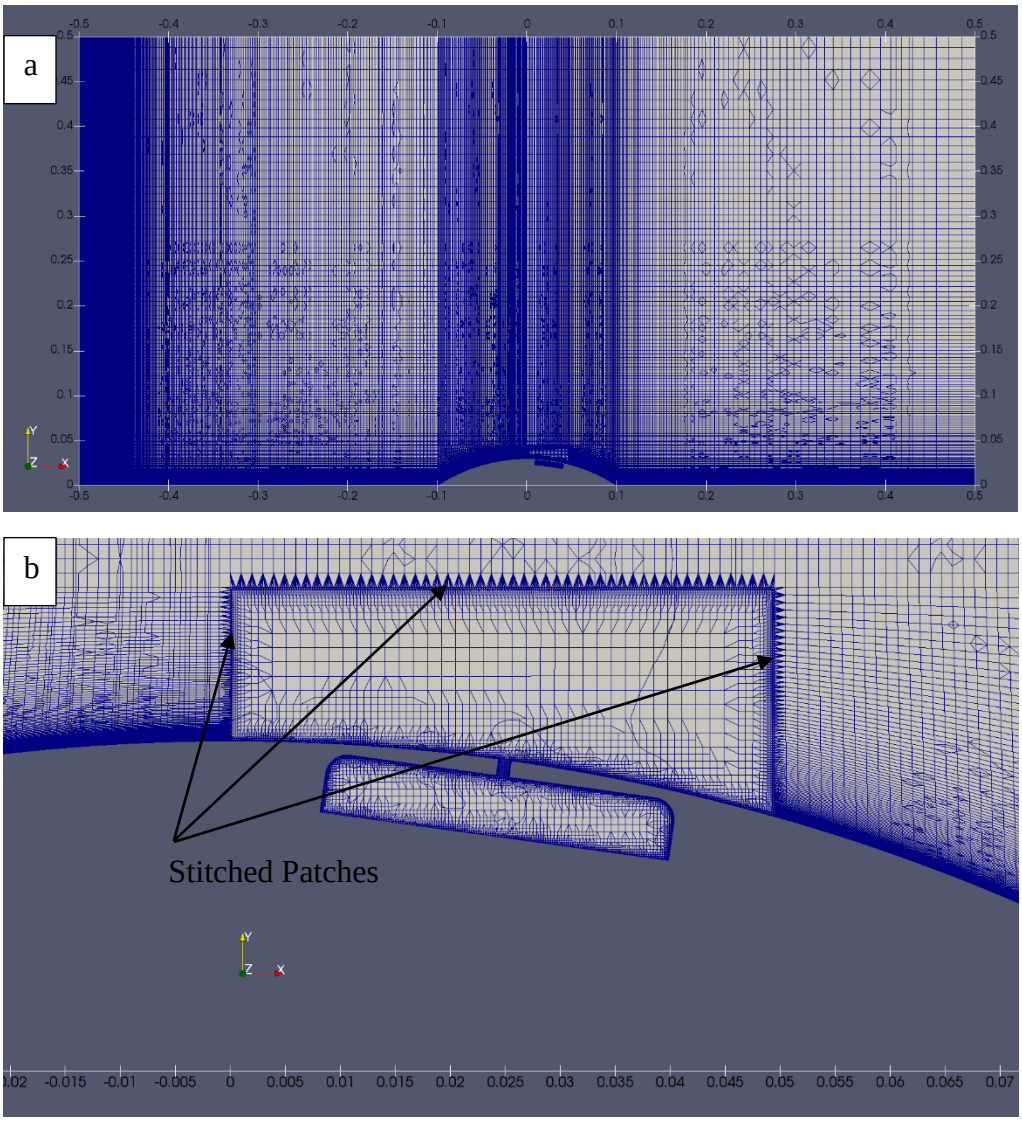

Fig.3.24. (a) Computational Grid in X-Y plane for actuated case and (b) Closer view of computational grid showing slaveMesh stitched to masterMesh by stitching three corresponding patches, X-Y plane.

It is worthwhile to mention that the overall number of generated cells either merely by snappyhexMesh tool or blockMesh tool (with minimum number of blocks for actuator to be able to define the structured mesh) are 26393697 and 24546457, respectively.

3.2.2- K-Omega Shear Stress Transport (SST) Turbulence Model

However, many turbulence models have been proposed by scientists so far to predict the flow behavior but each model has its own benefits and drawbacks based on the flow characteristics, the geometry and other involving parameters. In this research, the $\boldsymbol{k-\omega}$ Shear Stress Transport (SST) Model is used to predict the flow behavior in both actuated and un-actuated cases.

This model is implemented to overcome the drawbacks of the standard k-omega model due to the dependency on the freestream values of $\boldsymbol{k}$ and $\boldsymbol{\omega}$. Shear Stress Transport (SST) model is a combination of $\boldsymbol{k-\epsilon}$ and $\boldsymbol{k-\omega}$ models in such a way that $\boldsymbol{k-\epsilon}$ model is implemented for regions away from the walls and $\boldsymbol{k-\omega}$ model is used for near wall regions by a blending function.

This model is able to predict flow behavior for adverse pressure gradient conditions and flow separation. The turbulence specific dissipation rate equation is given by:

$$\frac{D}{Dt}(\rho\omega) = \nabla\cdot(\rho D_{\omega}\nabla\omega) + \frac{\rho\gamma G}{\nu} - \frac{2}{3}\rho\gamma\omega(\nabla\cdot u) - \rho\beta\omega^{2} - \rho(F_1-1)CD_{k\omega} + S_{\omega} \tag{3-31}$$

and the turbulence kinetic energy by:

$$\frac{D}{Dt}(\rho k) = \nabla\cdot(\rho D_{k}\nabla k) + \rho G - \frac{2}{3}\rho k(\nabla\cdot u) - \rho\beta^{*}\omega k + S_{k} \tag{3-32}$$

The turbulence viscosity is obtained using:

$$\nu_{t} = \frac{a_1 k}{max(a_1\omega, b_1 F_{23} S)} \tag{3-33}$$

The values of the constants of equations are given by Table 3.4.

Table 3.4 Constants of $\boldsymbol{k-\omega}$ Shear SST Model Equations.

a_1	b_1	c_1	β^*	α_{k1}	α_{k2}	$\alpha_{\omega1}$	$\alpha_{\omega2}$	β_1	β_2	γ_1	γ_2
0.31	1	10	0.09	0.85	1	0.5	0.856	0.075	0.0828	5/9	0.44

The relationship between turbulent kinetic energy, *k* and the turbulence intensity, *I*, is given by equation (3-34) as follows:

$$k = \frac{3}{2}(u_{avg}I)^2 \tag{3-34}$$

where u_{avg} is the mean flow velocity.

The turbulence intensity is defined as the ratio of the root-mean square of the velocity fluctuations to the mean flow velocity. For internal flows, such as flow in the wind tunnel, the turbulence intensity at the inlet generally depends on the upstream history of the flow. The measured turbulence intensity of the wind tunnel is around 0.66 percent. The turbulence length scale which describes the size of the large energy-containing eddies in a turbulent flow is set equal to the honeycomb pitch that is located in the settling chamber upstream of the contraction part.

The turbulence specific dissipation rate follows as:

$$\omega = k^{0.50}/{C_\mu}^{0.25}l \tag{3-35}$$

where l is the turbulence length scale .

3.2.3- Initial and Boundary Conditions

At inlet boundary, the turbulence quantities are defined while zeroGradient boundary condition is assumed at the outlet. The gradient of all quantities in span-wise direction are set to zero. Fixed velocity value of 7m/s is considered at the inlet and atmospheric pressure is assumed as at the outlet.

At all walls with no slip boundary conditions (hump surface and the floor of the test section), all turbulent quantities, except ω, are set to zero and ω satisfies equation (3-36) proposed by Menter (1992),

$$\omega = 10\frac{6\nu}{\beta_1(\Delta y)^2} \quad y = 0 \tag{3-36}$$

where Δy is the distance to the next point away from the wall.

Time varying boundary condition is assumed at the inlet of cavity as follows:

$$U(t) = U_0(Sin\ (2\pi f(t - t_0) + \emptyset)) \tag{3-37}$$

As in experiment, a function generator with an amplifier is used to excite the piezo electric diaphragms at the inlet of cavity with the Helmholtz frequency f of the cavity (960 Hz) and a known voltage Vpp of 23 Volt, then the amplitude U_0 in the above mentioned equation is unknown and it can't be determined by experiment, however the peak exit jet velocity at the orifice outlet is known. To have a successful interaction of vortical structures with the cross flow, the ratio of peak of exit jet to the free stream velocity of cross flow equivalent to 1.5 is used in experiment. Then, to find the amplitude U_0, the slaveMesh is used in quiescent flow conditions and the amplitude U_0 is changed by a trial and error procedure as long as the condition of exit jet at the orifice outlet is satisfied. Table 3.5 gives boundary conditions relevant to computational domain shown in Fig.3.22.

Table 3.5 Boundary conditions relevant to the computational domain shown in Fig.3.22.

Boundary Name	$k(m/s)^2$	$\omega(s^{-1})$	$\nu_t(m^2/s)$	$u(m/s)$	$p(Pa)$
Inlet	0.0032	99.3	0	(7,0,0)	Zero Gradient
Outlet	Zero Gradient	Zero Gradient	0	Zero Gradient	0
Sidewalls & Top	Zero Gradient	Zero Gradient	Zero Gradient	Zero Gradient	Zero Gradient
Test Section Floor and Hump Surface	0	7400000	0	No Slip	Zero Gradient
Internal Walls of Orifices	0	7400000	0	No Slip	Zero Gradient
Cavity Internal Wall	0	7400000	0	No Slip	Zero Gradient
Diaphragm	0	7400000	0	$0.0365\,Sin\,(2\pi \times 1000t) \times (1,1,0)$	Zero Gradient

3.2.4- Numerical Method

pisoFoam solver which is a transient solver for incompressible, turbulent flow by using the PISO algorithm is implemented in the current study.Geometric agglomerated algebraic multigrid solver (GAMG) and smoothSolver are used as the linear solvers for pressure and velocity fields, respectively. A fast solution on a mesh with a few number of cells is obtained by GAMG solver, then this solution is mapped onto a finer mesh and it is utilized as an initial guess to find a precise solution on the fine mesh. The GAMG uses Gauss-Seidel smoother while the smoothSolver utilizes symmetric Gauss-Seidel as the smoother.

First order implicit Euler scheme is utilized for time discretization for both unactuated and actuated cases. The divergence schemes are based on Gauss integration and the advected field is interpolated to the cell faces by selection of linearUpwind and limitedLinear

schemes for velocity and turbulence quantities, respectively. The time steps of $1.5 \times 10^{-5}s$ and $1 \times 10^{-6}s$ are used for unactuated and actuated cases, respectively. The maximum Courant number for unactuated case is 0.80153265 while this number for actuated case is fluctuating between 0.27 - 0.75 due to the time varying boundary condition of velocity at cavity inlet.The code is run on one of the nodes of HPC of University of Huddersfield with 24 cores, average required time for each iteration is 40 seconds and the computations for actuated case was performed for 3 months.

3.3- Summary

In this chapter, both experimental and numerical methodologies were explained. The process of manufacturing of the subsonic closed-circuit wind tunnel and the procedure of calculation of pressure losses in the wind tunnel to select the appropriate fan was explained. The wind tunnel was designed by the author using as a basis a blueprint of an old wind tunnel in University of Leeds. This repeated the characteristic dimensions, but major changes were implemented to improve the flow quality and the range of wind speed. Also, the hump model and the process of manufacturing as well as the actuator array and the required driving circuitry system to drive the piezo-electric diaphragm were described. The details of all experimental setups for measurement techniques including Constant Temperature Anemometry (CTA), Particle Image Velocimetry (PIV), techniques were explained. Also, the data acquisition procedure, calibration process and data post processing for both techniques were explained. The numerical methodology including geometry and computational grid generation, initial and boundary conditions as well as numerical method were described.

In Chapter 4, the results of experimental measurements including the measurements of flow quality of the wind tunnel and measurements of characteristics of single actuator in quiescent flow conditions by Hot Wire Anemometry (HWA) technique, measurements of flow separation over the hump model and its control by both Hot Wire Anemometry (HWA) and Particle Image Velocimetry (PIV) technique will be presented. Also, the results of numerical analysis for characteristics of single actuator in quiescent flow conditions and for flow separation over hump model for both unactuated and actuated cases will be shown.

Chapter 4- Results

In this chapter, the results of experimental studies including wind tunnel flow quality measurements, measurements of characteristics of single actuator in quiescent flow conditions and flow separation and its control over the hump model for both unactuated and actuated cases are presented. In addition, the results of numerical simulations including the simulation of single actuator in quiescent flow conditions and simulation of flow separation over hump model for both unactuated and actuated cases are shown.

4.1- Wind Tunnel Flow Quality Measurements

Prior to wind tunnel flow quality measurements, the hot wire system performance, data acquisition software as well as sample size and sampling rate of data were checked out by performing tests on a flow past circular cylinder (diameter D = 25 mm) placed horizontally in the test section. The wind tunnel speed was set at 14.25 m/s which yields the Reynolds number of ca. 24,000. The sample size of 131072 points with sampling rate of 10 kHz is used to acquire data. The vortex shedding frequency of 116.8 Hz behind the cylinder identified by dominant frequency from power spectral density estimate, yields a Strouhal number fD/U_∞ of 0.2049 which is close to the theoretical value of about 0.2. Therefore, the sample size of 131072 points with sampling rate of 10 kHz is used to acquire data for all HWA experiments in this research. More details regarding test on circular cylinder can be found in Appendix A.

The flow quality of the wind tunnel is evaluated by measuring the flow velocity and turbulence intensity in three 3 planes in span wise direction: Z=150 mm, 0 mm and -150 mm. Measurements are made along three lines in each plane which are located at X=110 mm, 270 mm and 550 mm as shown in Fig.4.1. The hot wire probe is moved from Y=0.25 mm above the floor of the test section to Y=499.75 mm (0.25 mm below the ceiling of the test section). Velocity profiles for lines located in planes Z=150, Z=0 and Z=-150 are shown in Fig.4.2 (a)-(c).

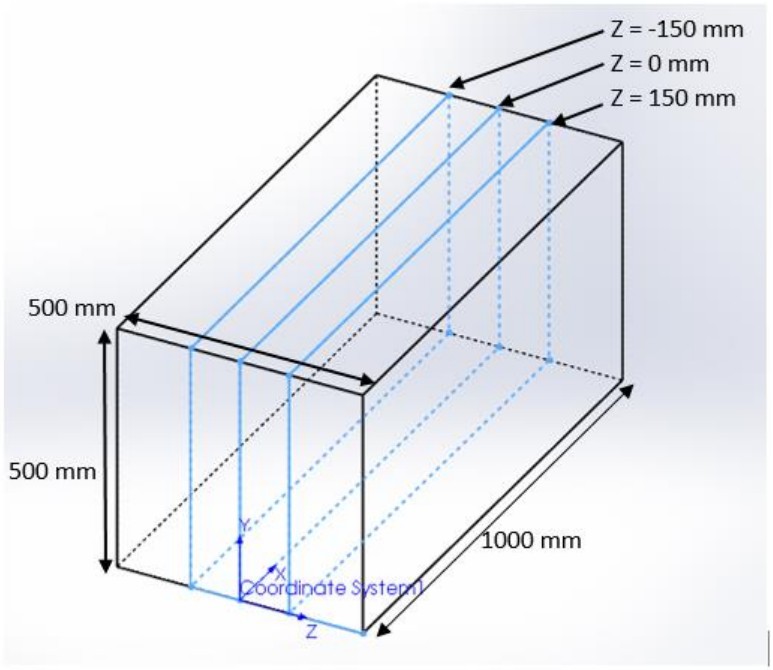

Fig.4.1. Measurement planes and coordinate system.

The measured turbulence intensity in plane Z=0 mm at X= 550 mm is shown in Fig. 4.2 (d). Fig. 4.3 shows the velocity profile in the boundary layer.

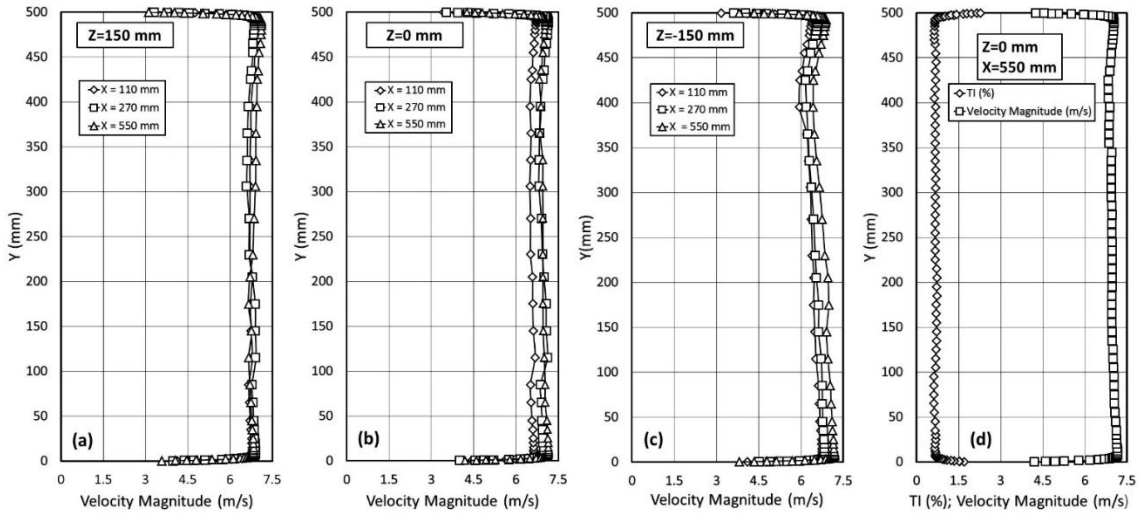

Fig.4.2. (a) Velocity profiles in planes Z=150 mm, (b) Z= 0 mm, (c) Z= -150 mm; and (d) velocity and turbulence intensity in plane Z= 0 mm and X= 550 mm, $U_\infty = 7\ m/s$.

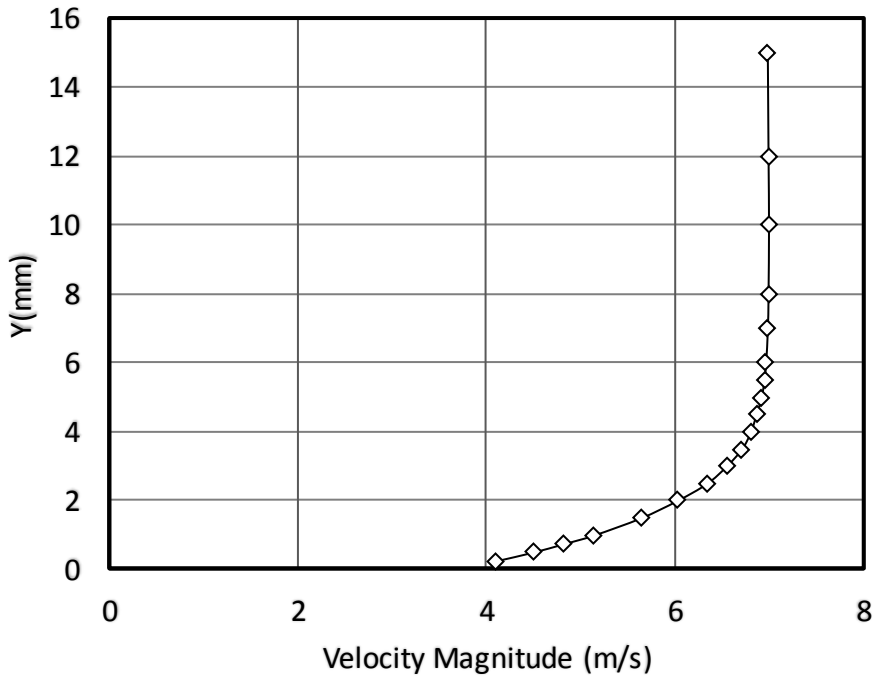

Fig.4.3. Velocity boundary layer profile in plane Z= 150 mm at X= 550 mm, $U_\infty = 7\ m/s$.

4.2- Characteristics of Single Actuator in Quiescent Flow Conditions

The typical frequency response of a synthetic jet actuator is shown by Fig.4.4. Fig.4.5 shows the peak exit jet velocity response of a synthetic jet actuator.

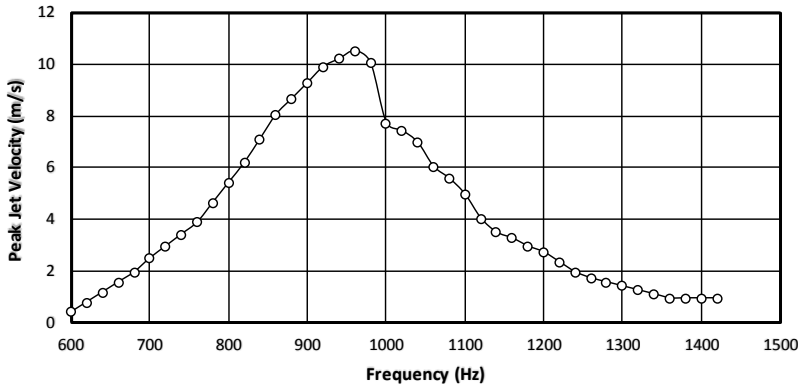

Fig.4.4. Frequency response of single SJA with orifice diameter of 1 mm at Vp-p of 23 Volt.

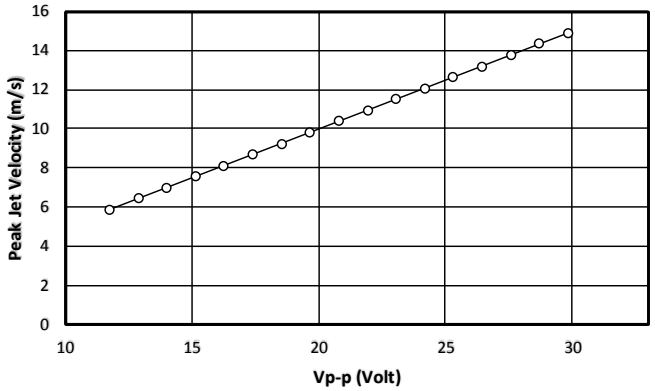

Fig.4.5. Profile of orifice outlet velocity versus actuation voltage at Frequency of 960 Hz for orifice diameter of 1 mm.

The profile of time history of exit jet velocity at height of 0.5 mm above the orifice is shown by Fig.4.6. The actuator is excited by the Helmholtz frequency of 960 Hz with actuation voltage of 22 V p-p. The Profile of time history of exit jet velocity at y= 1.5 mm above the orifice with actuation voltage of 22Vp-p at Frequency of 960 Hz is shown by Fig.4.7.The profile of peak velocity of exit jet for heights of $0.5\,mm \leq y \leq 15.5\,mm$ above orifice outlet is shown by Fig.4.8.

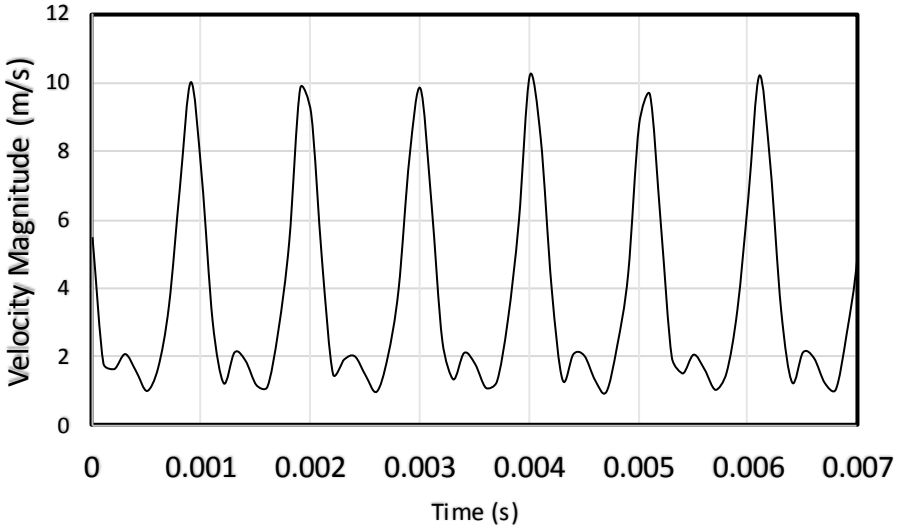

Fig.4.6. Profile of time history of exit jet velocity at y= 0.5 mm above the orifice with actuation voltage of 22Vp-p at Frequency of 960 Hz.

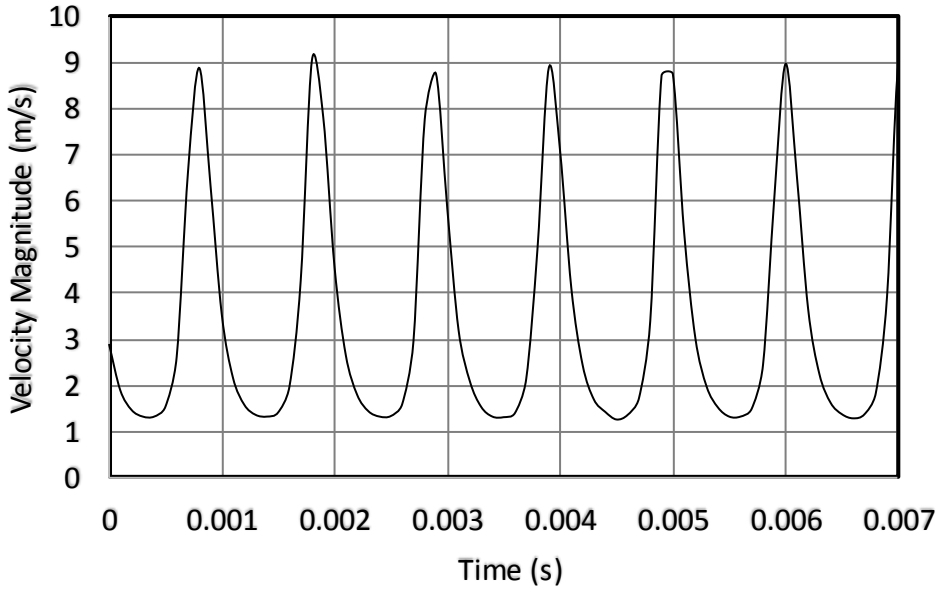

Fig.4.7. Profile of time history of exit jet velocity at y= 1.5 mm above the orifice with actuation voltage of 22Vp-p at Frequency of 960 Hz.

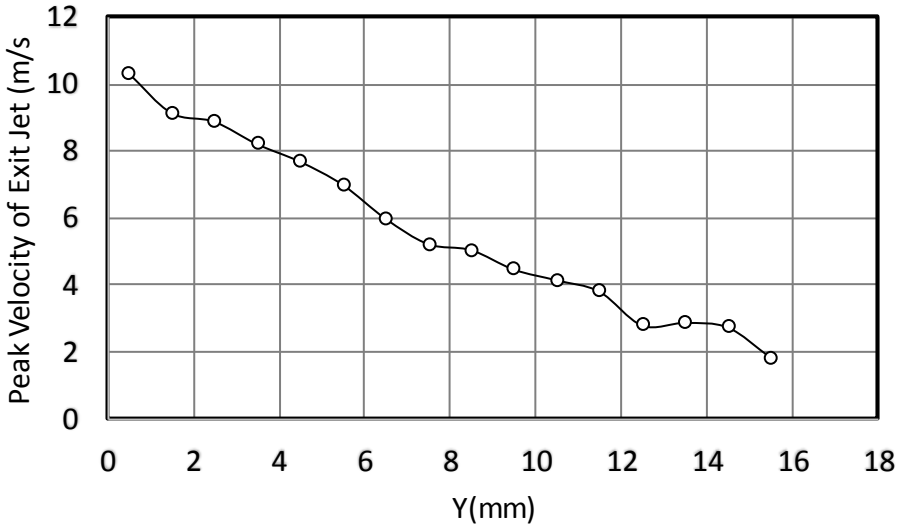

Fig 4.8. Profile of peak velocity of exit jet versus height above the orifice outlet with actuation voltage of 22Vp-p at Frequency of 960 Hz.

The power spectrum density profile of time history of exit jet velocity which is shown in Fig.4.6 has been obtained by Welch's method and it is shown by Fig.4.9. Fig.4.10 shows the power spectrum profile at height of Y =15.5 mm above the orifice.

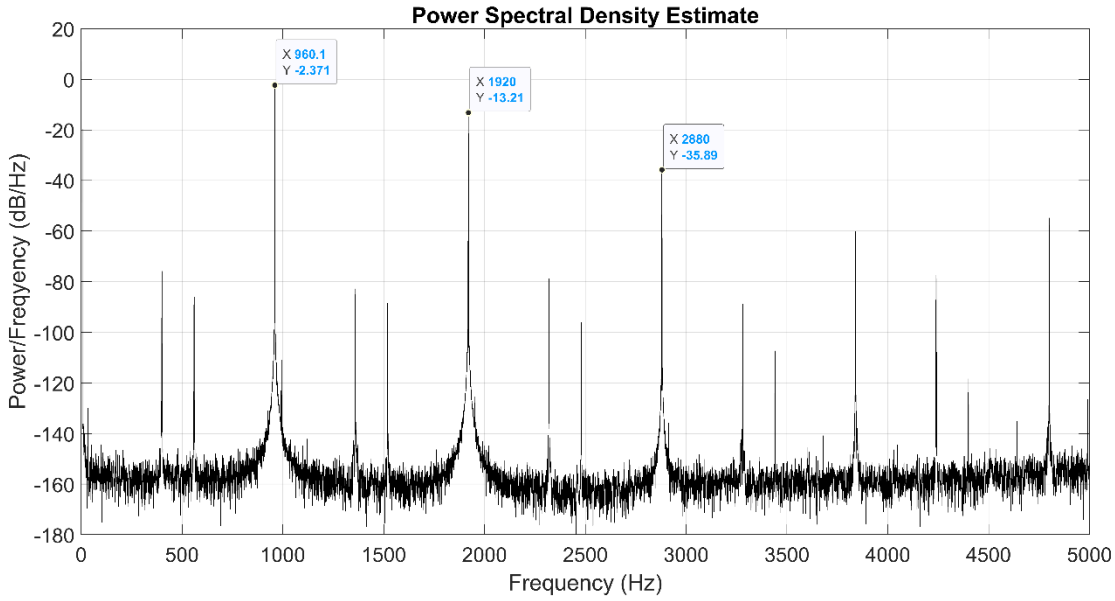

Fig.4.9. Power spectrum density estimate of exit jet velocity at Y = 0.5 mm above the orifice outlet with actuation voltage of 22Vp-p at Frequency of 960 Hz.

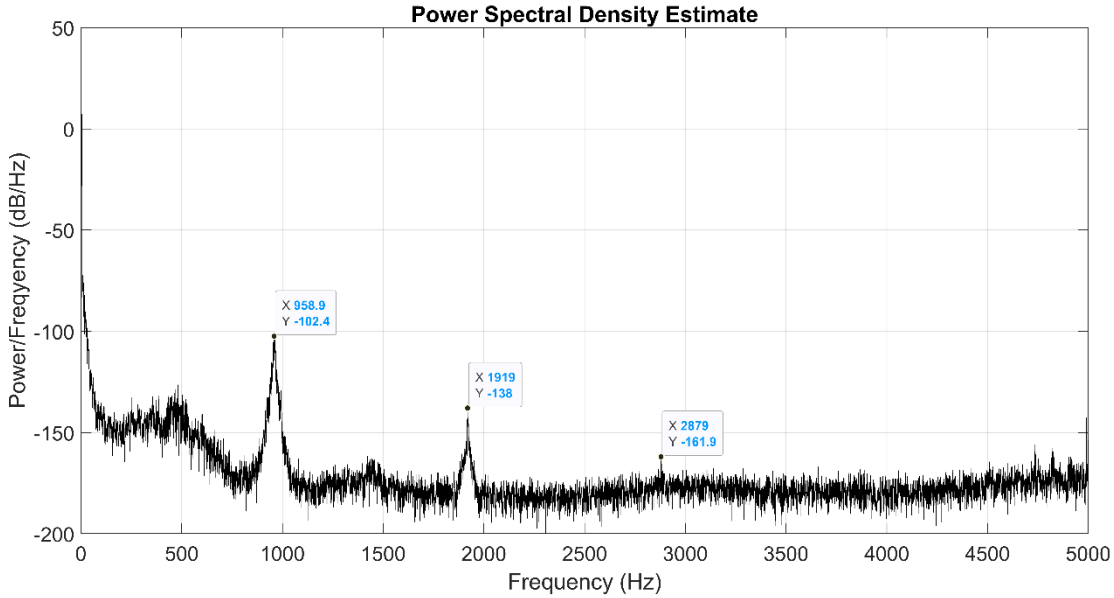

Fig.4.10. Power spectrum density estimate of exit jet velocity at Y = 15.5 mm above the orifice outlet with actuation voltage of 22Vp-p at Frequency of 960.

4.3- Flow Separation over the Hump Model- Unactuated Case

In this section, the results of flow measurements by HWA technique and PIV technique in and out of the wake region is presented.

4.3.1- Measurements of Flow Features by HWA Technique- Unactuated Case

The flow features in the wake region for unactuated cases have been studied for 3 free stream velocities of 7, 9 and 12 m/s, however the actuated cases all are performed for free stream velocity of 7m/s. The measurements are done in plane Z= 0 along 4 lines in the wake region which are located at X=570 mm, 580 mm, 590 mm and 600 mm as shown in Fig. 4.11.

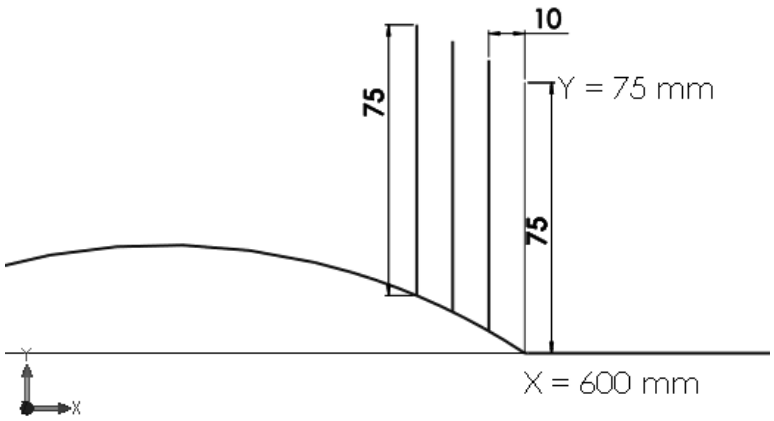

Fig.4.11. Locations of HWA measurements lines in the wake region.

For the measurement line located at hump trailing edge at X = 600 mm (hump trailing edge), the hot wire probe is traversed vertically from height of 0.25 mm above the hump surface to the height of 75 mm out of the wake region. The velocity profiles are shown in Fig. 4.12. For the measurement lines located at X = 590 mm, X = 580 mm and X = 570 mm, the hot wire probe is traversed vertically from height of 1 mm above the hump surface to the height of 75 mm out of the wake region. The RMS Velocity profiles in the wake region for free stream velocity of 7m/s in plane Z =0 at lines X= 570 mm, X = 580 mm, X = 590 as well as X = 600 mm is shown in Fig.4.13.

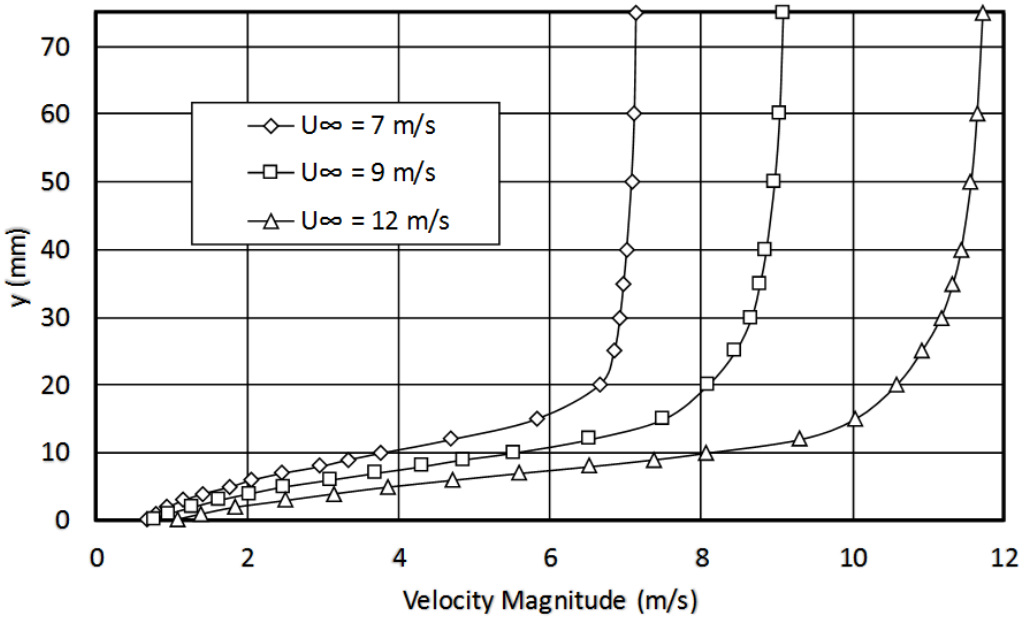

Fig.4.12. Velocity profiles in the wake region for 3 free stream velocities in plane Z = 0 at X = 600 mm.

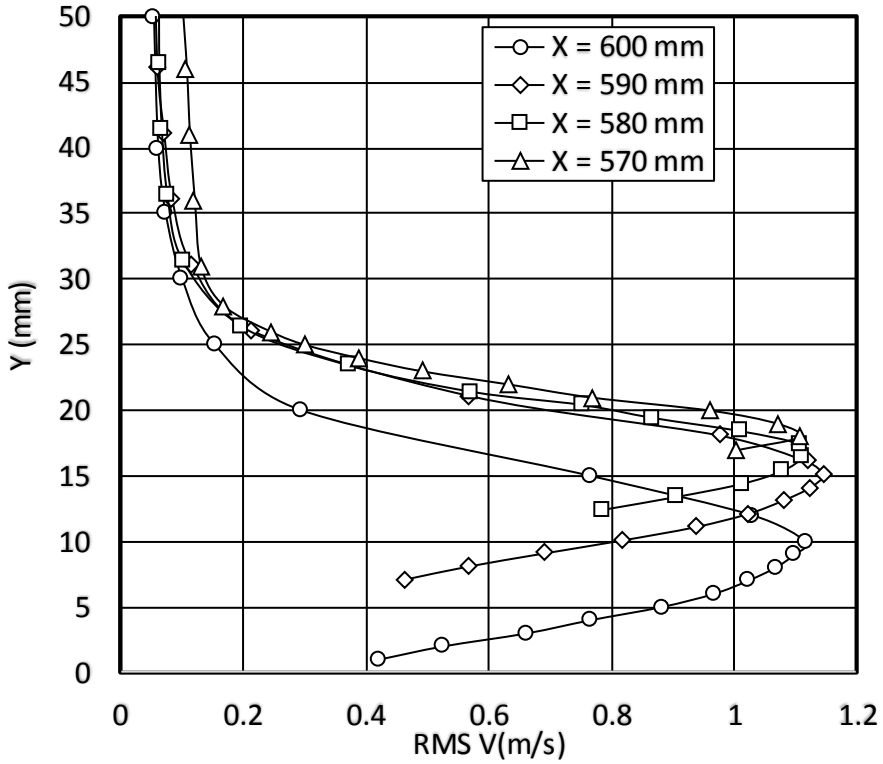

Fig.4.13. RMS Velocity profiles in the wake region for free stream velocity of 7m/s in plane Z = 0.

The velocity profiles for measurement line at X = 590 mm is shown in Fig 4.14. Fig4.15 shows the trajectory of maximum RMS velocity in the wake region. Figs. 4.16-19 show the profiles of the power spectral density estimate for 5 heights on the measurement line at X= 570-600 mm, respectively.

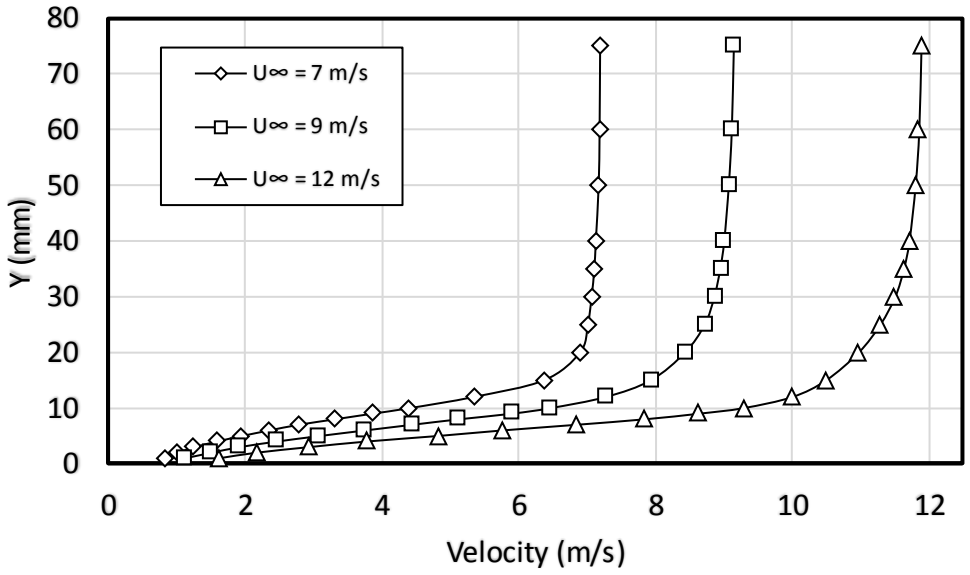

Fig.4.14. Velocity profiles in the wake region for 3 free stream velocities in plane Z = 0 at X = 590 mm.

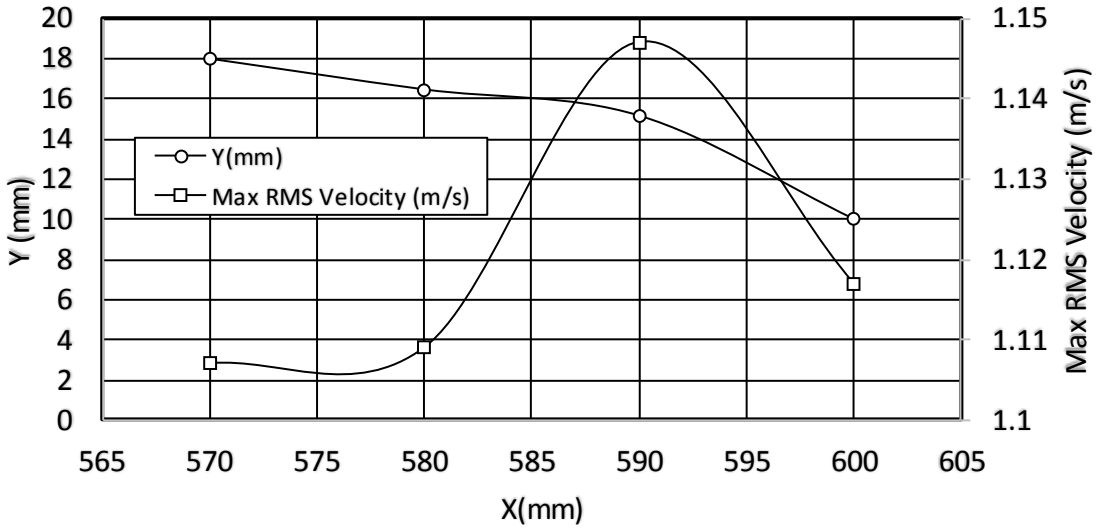

Fig.4.15. Trajectory of Max RMS velocity in the wake region in plane Z = 0, $U_\infty = 7\ m/s$.

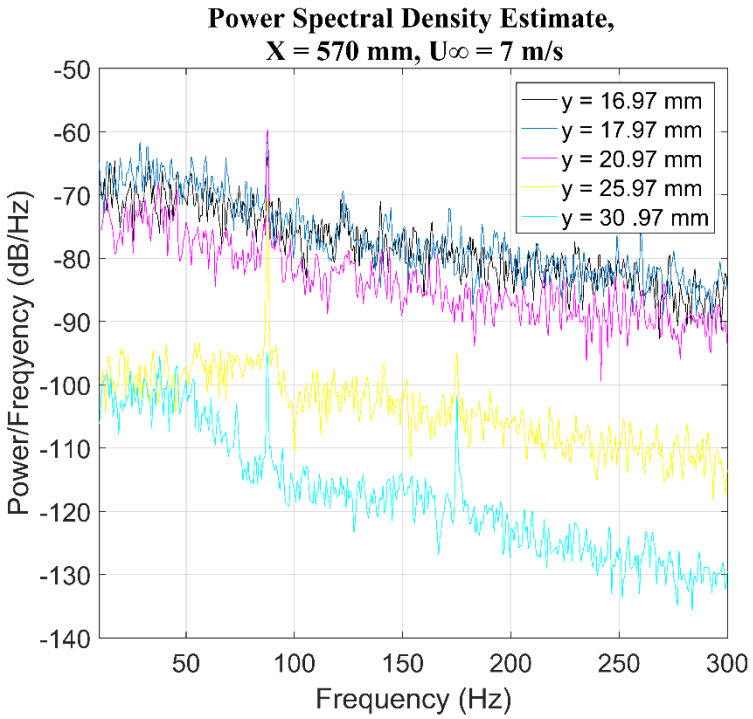

Fig.4.16. Power spectral density profiles in and out of the wake region in plane Z = 0 at X = 570 mm, $U_\infty = 7\ m/s$.

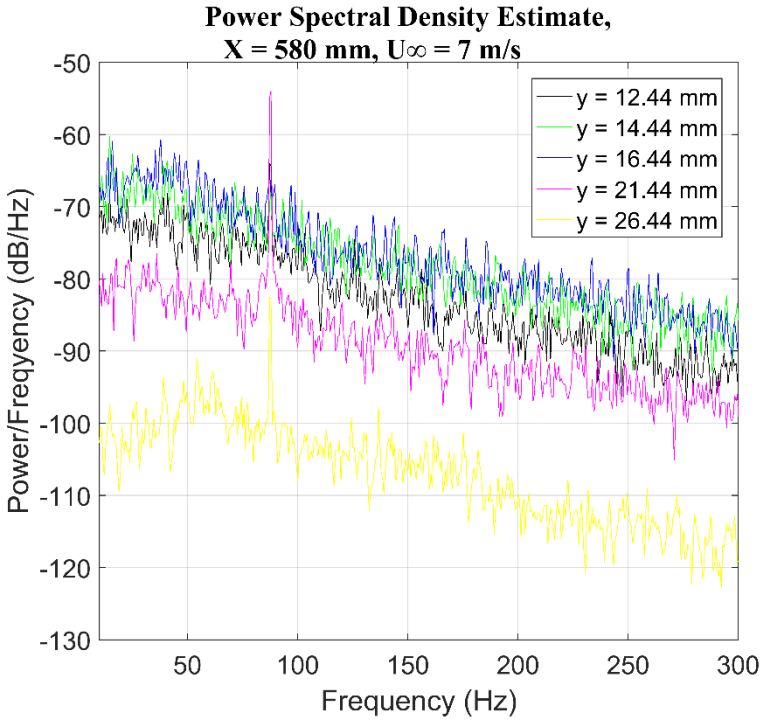

Fig.4.17. Power spectral density profiles in and out of the wake region in plane Z = 0 at X = 580 mm, $U_\infty = 7\ m/s$.

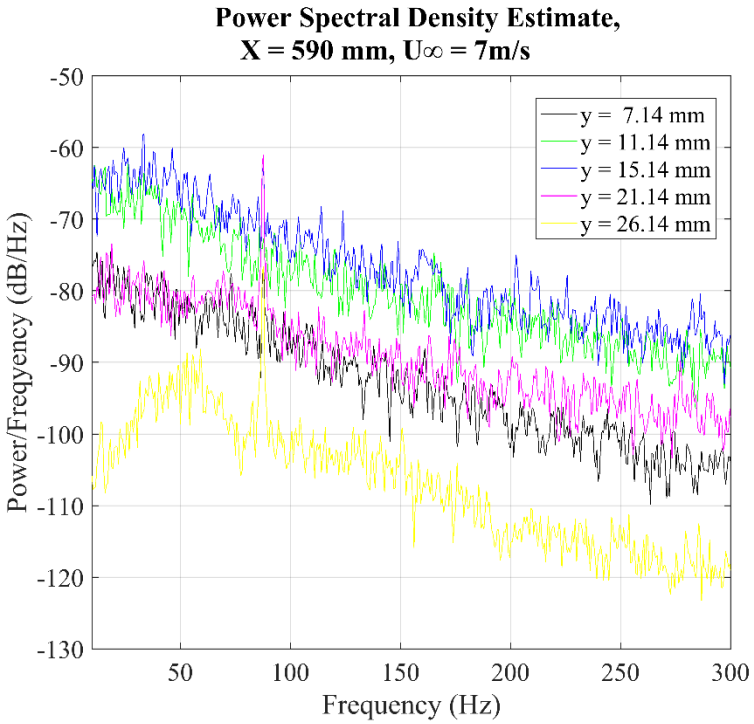

Fig.4.18. Power spectral density profiles in and out of the wake region in plane Z = 0 at X = 590 mm, $U_\infty = 7\ m/s$.

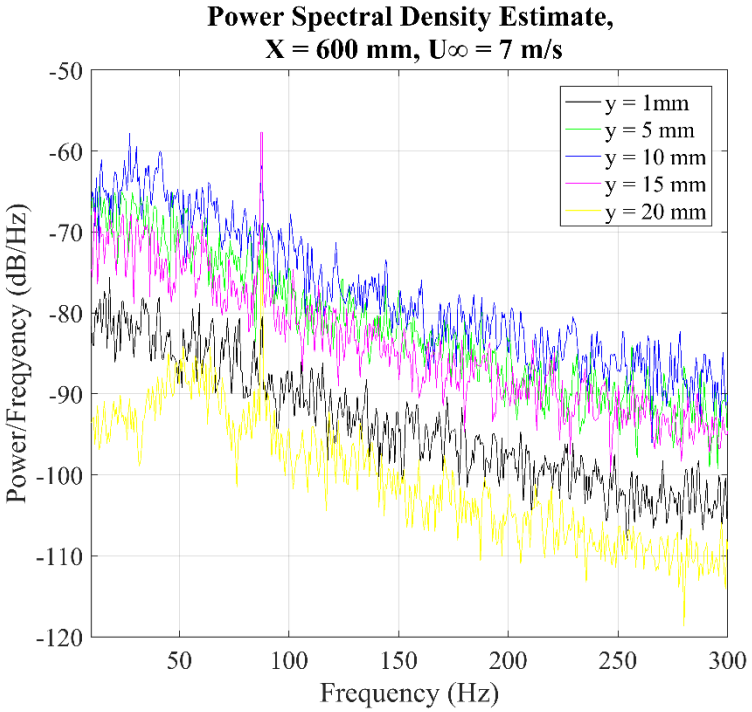

Fig.4.19. Power spectral density profiles in and out of the wake region in plane Z = 0 at X = 600 mm, $U_\infty = 7\ m/s$.

Additional results regarding free stream velocities of 9 and 12 m/s can be found in Appendix C.

4.3.2- Measurements of Flow Features by PIV Technique-Unactuated Case

In this section the results of experiments by Particle Image Velocimetry (PIV) technique for unactuated case is presented. For PIV measurements, 100 images in double frame mode are acquired for each case. Four selected samples of instantaneous velocity vector fields for unactuated case in the wake region is shown in Fig 4.20. The velocity vectors are shown by Figs 4.20 (a, c, e and g) and corresponding velocity magnitude are shown by Figs 4.20 (b, d, f and h). The average of velocity vector and magnitude fields, the streamlines, the vorticity contour as well as RMS velocity profiles are shown in Figs.4. 21-24, respectively.

This Space Intentionally Left Blank.

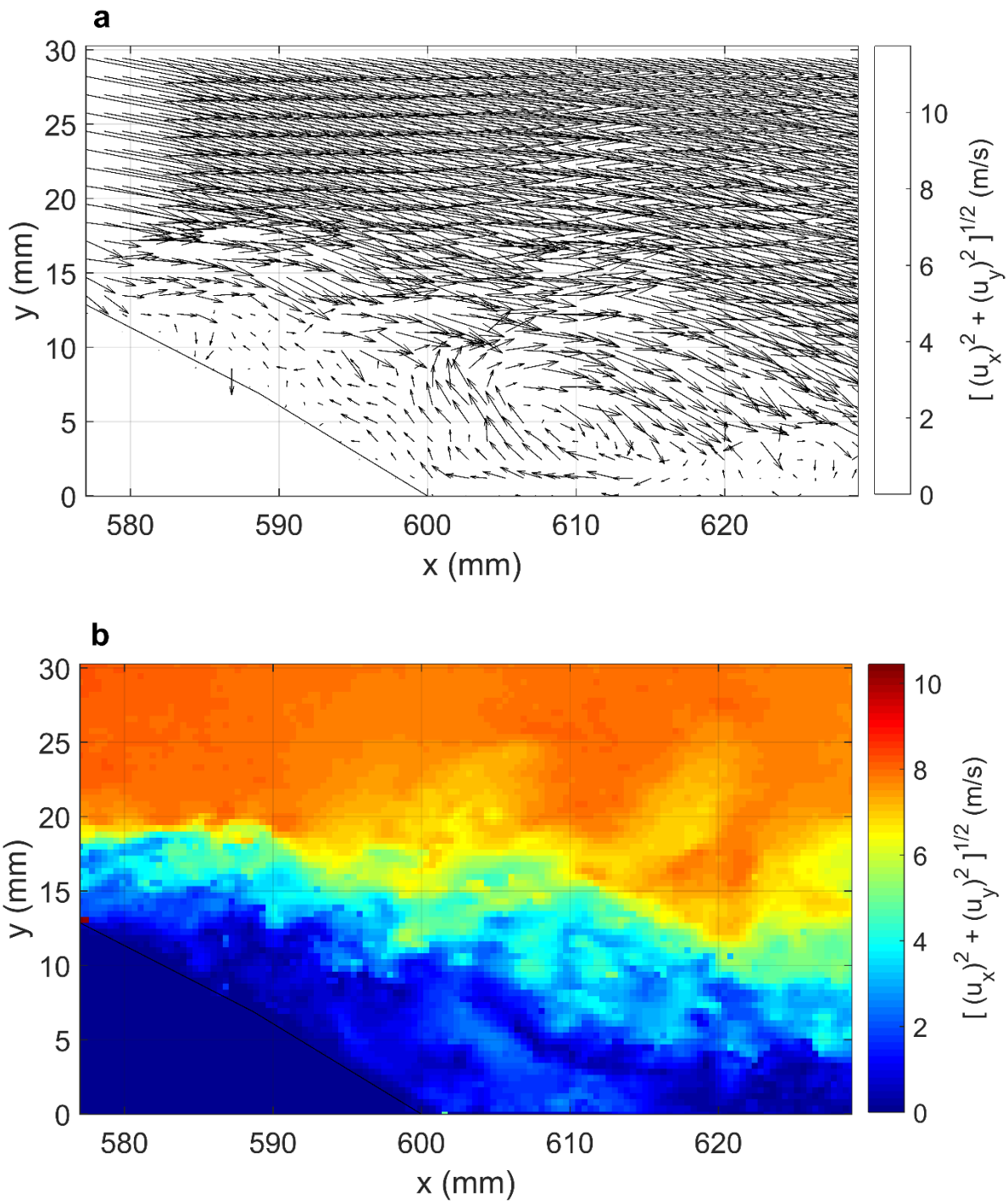

Fig.4.20. (a , b) Instantaneous velocity vector and magnitude fields in the wake region-unactuated case, $U_\infty = 7\ m/s$.

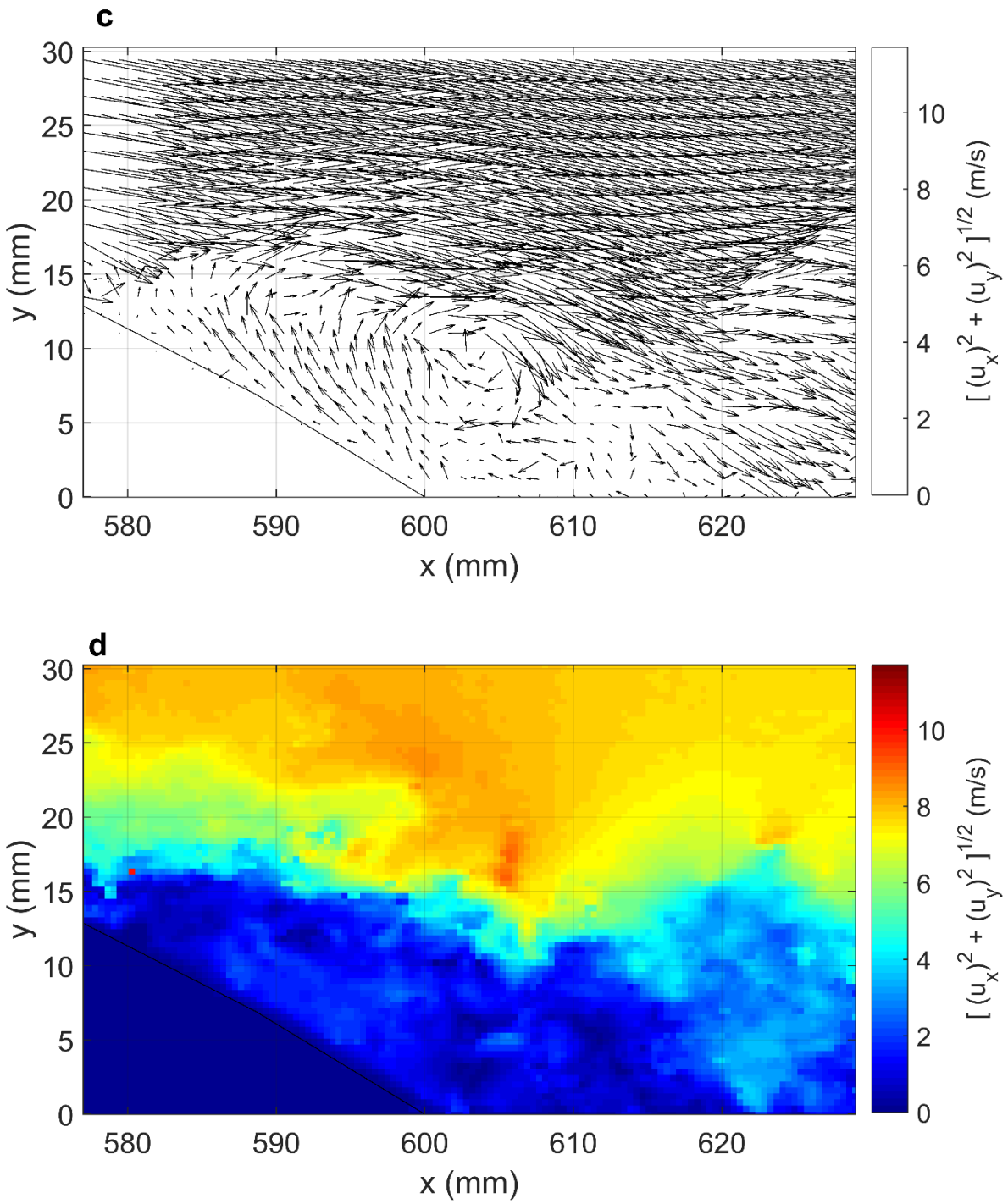

Fig.4.20. (c , d) Instantaneous velocity vector and magnitude fields in the wake region-unactuated case, $U_\infty = 7\ m/s$.

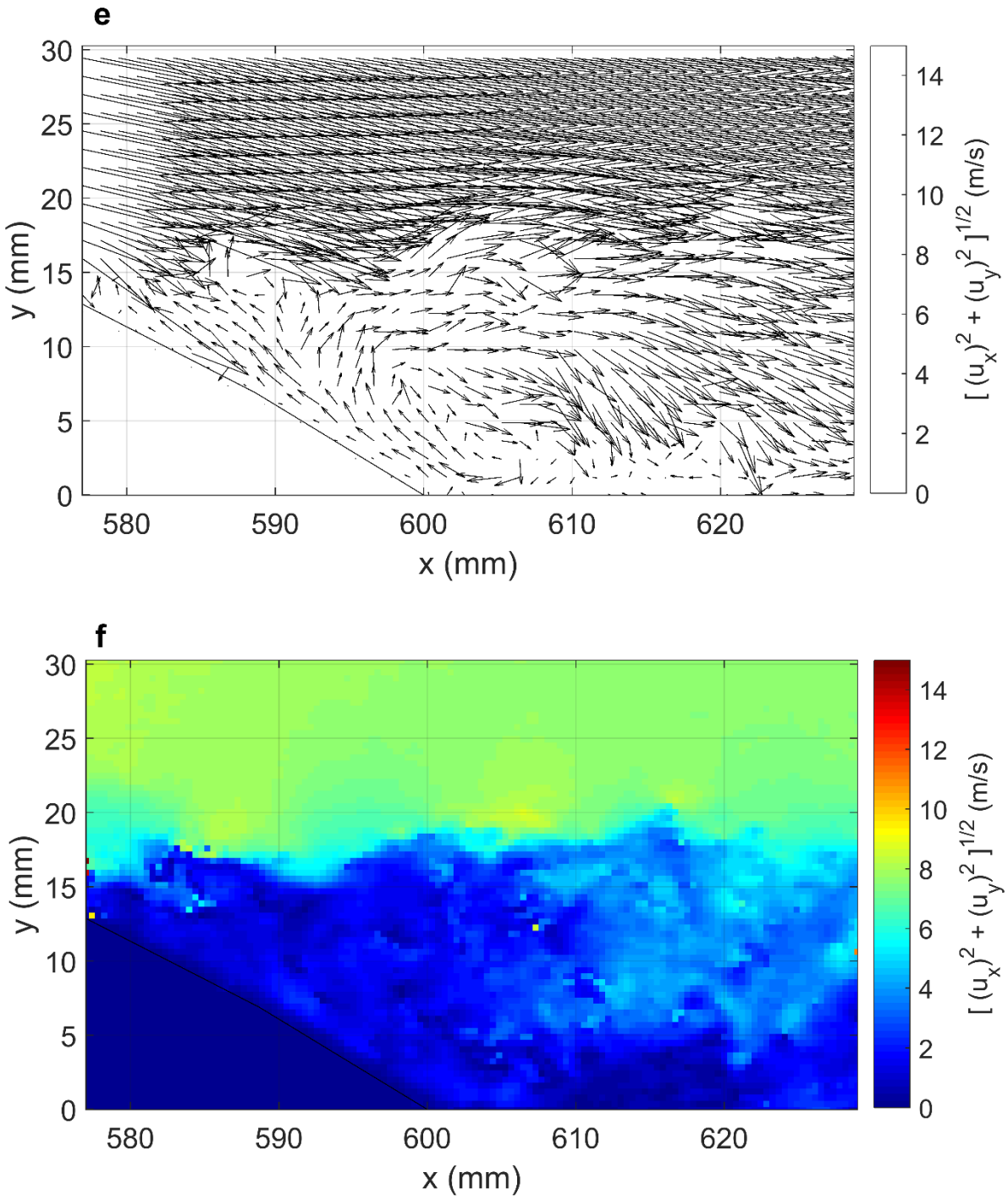

Fig.4.20. (e , f) Instantaneous velocity vector and magnitude fields in the wake region- unactuated case, $U_\infty = 7\ m/s$.

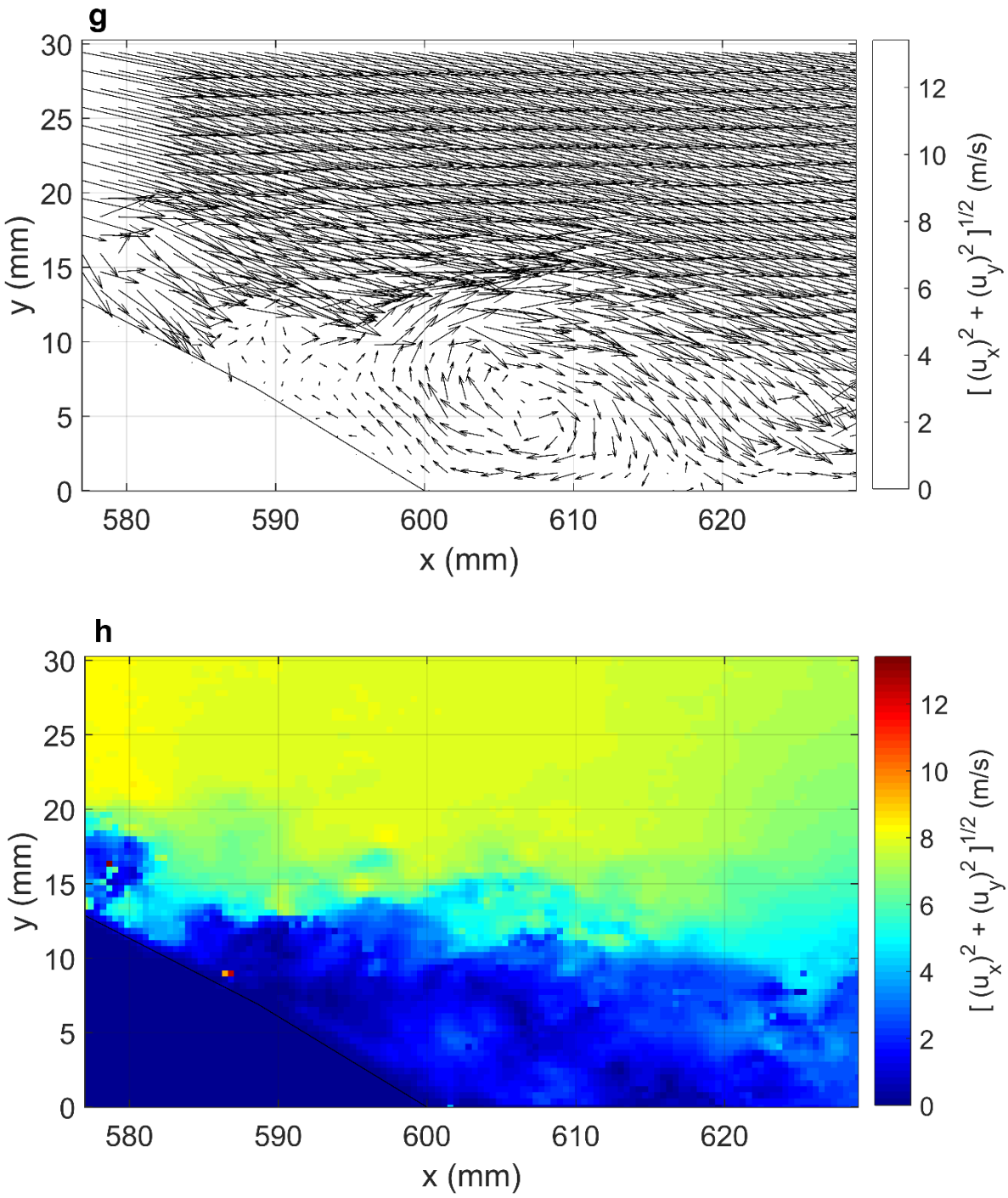

Fig.4.20. (g , h) Instantaneous velocity vector and magnitude fields in the wake region- unactuated case, $U_\infty = 7\ m/s$.

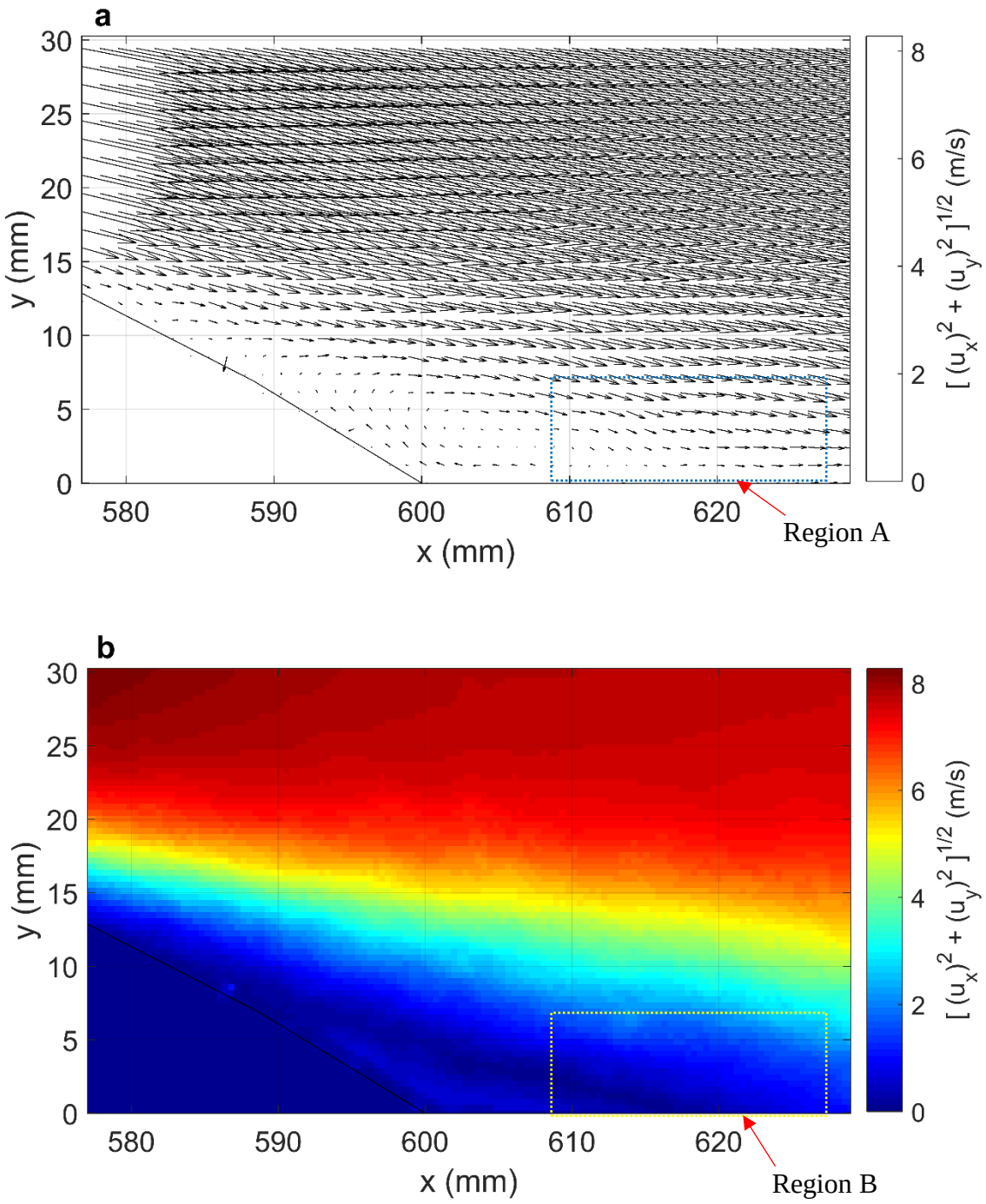

Fig.4.21. (a , b) Average velocity vector and magnitude fields, unactuated case, $U_\infty = 7\ m/s$.

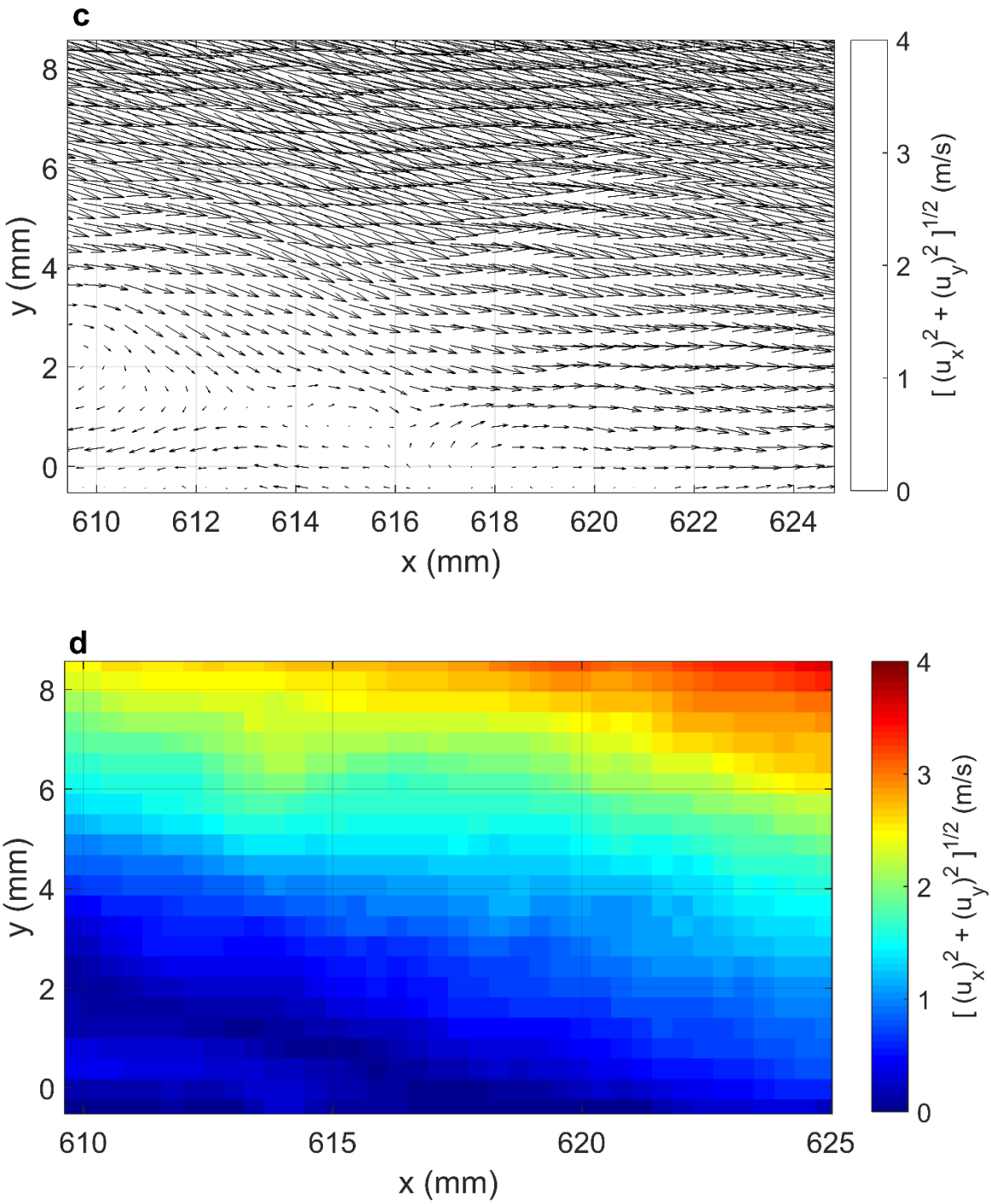

Fig.4.21. (c , d) Average velocity vector and magnitude fields, closer view near the reattachment point with smaller display grid factor, Regions A and B of Fig.4.21(a , b) - unactuated case, $U_\infty = 7\ m/s$.

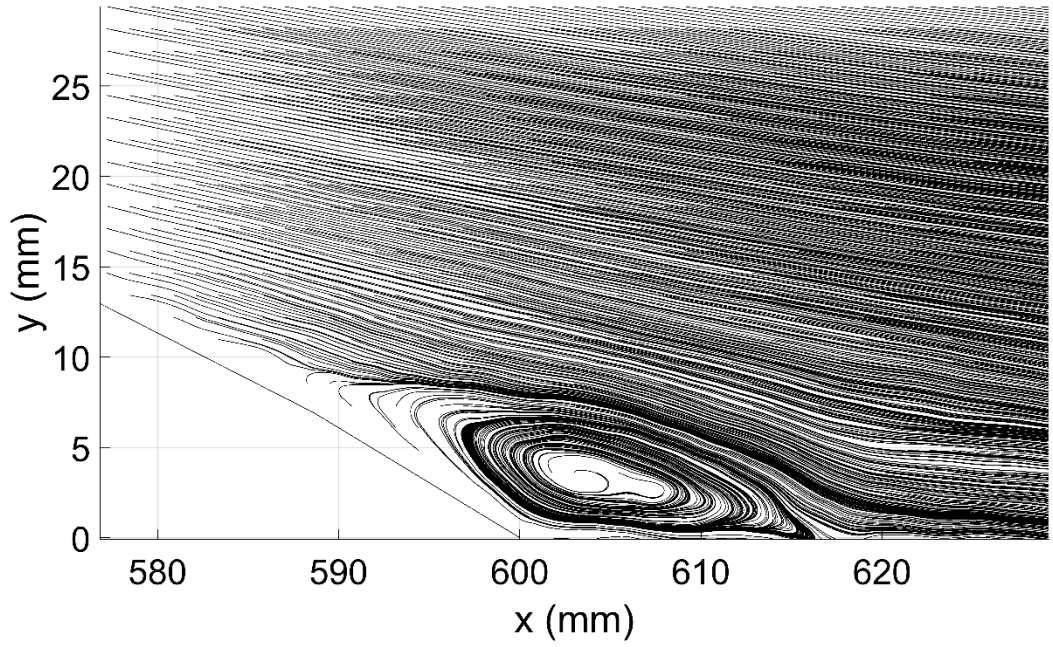

Fig 4.22. Streamlines profile - unactuated case, $U_\infty = 7\ m/s$.

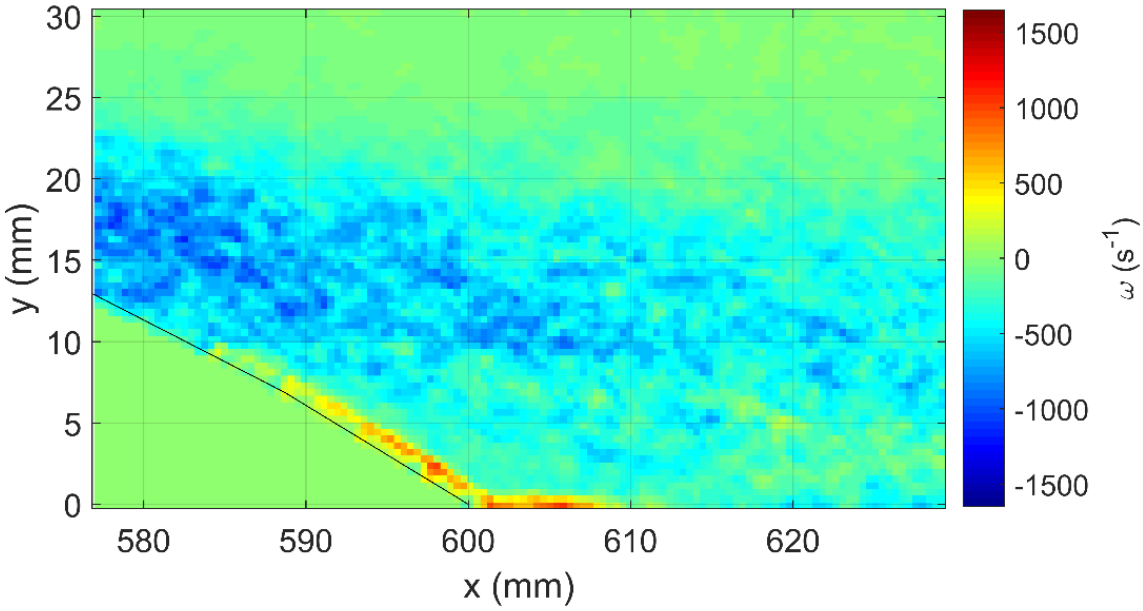

Fig.4.23. Vorticity Contour in the wake region- unactuated case, $U_\infty = 7\ m/s$.

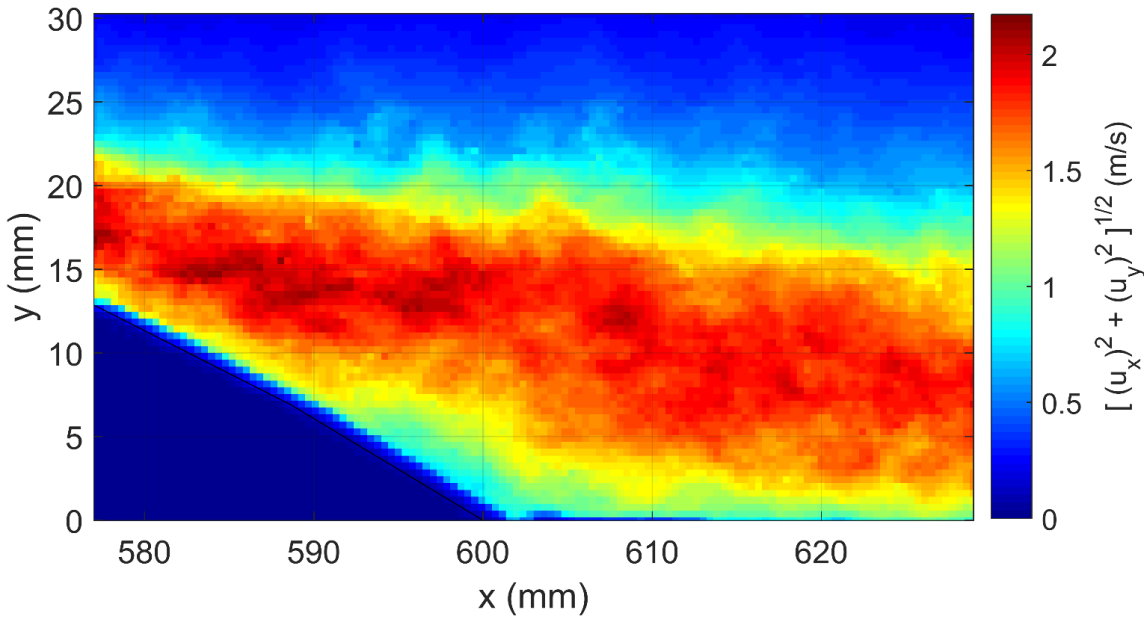

Fig.4.24. RMS velocity profile in the wake region- unactuated case, $U_\infty = 7\ m/s$.

4.4- Flow Separation and its control over the Hump Model- Actuated Case

In this section, the results of HWA measurements in the wake region, the PIV results as well as the pressure measurements on the hump surface for actuated cases are depicted.

4.4.1- Measurements of Flow Features by HWA Technique- Actuated Case

In the first phase of study of the effects of synthetic jet actuators on the characteristics of the wake region, the influence of angular position of actuators array for 8 angular positions of actuators is investigated. The actuator array is positioned at 8 different angular positions including $\phi = 0$, 5, 9.5, 12.5, 15, 17.5, 20 and 25 degrees. The Sine wave with actuation voltage of 23Vp-p and frequency of 960 Hz was used while the VR was set on value of 1.50. The profiles of velocity fluctuations is shown by Fig.4.25. The effects of different waveforms including Sine, Square, Pulse and Triangle waves on the velocity fluctuations in the wake region is shown by Fig.4.26.

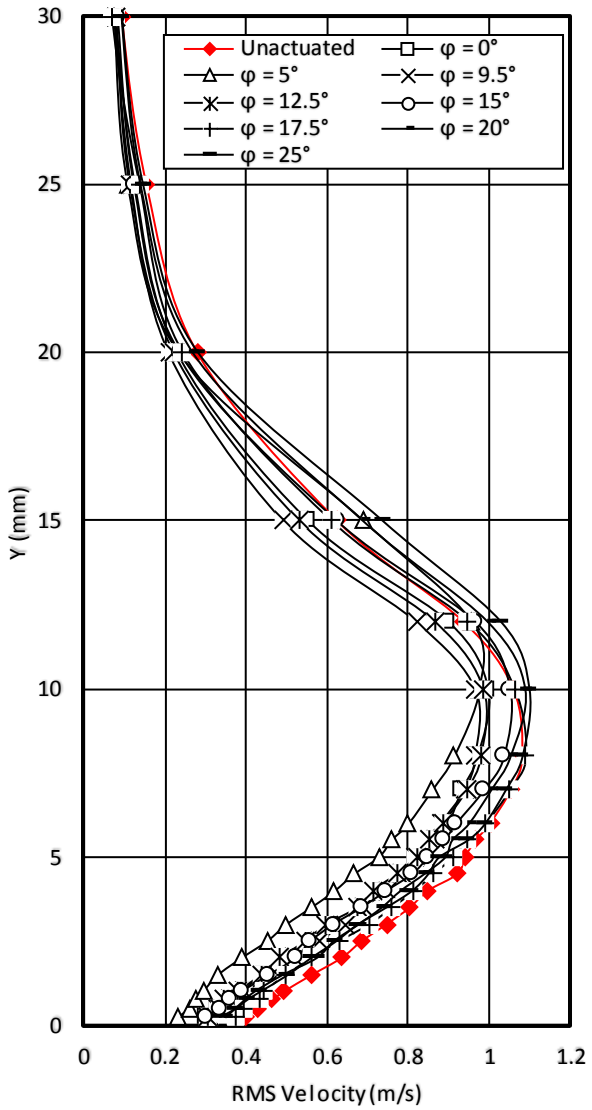

Fig.4.25. RMS Velocity profiles for angular positions of SJAs in plane Z= 0, Sine Wave, VR=1.50, Fr = 960 Hz, $U_\infty = 7\ m/s$.

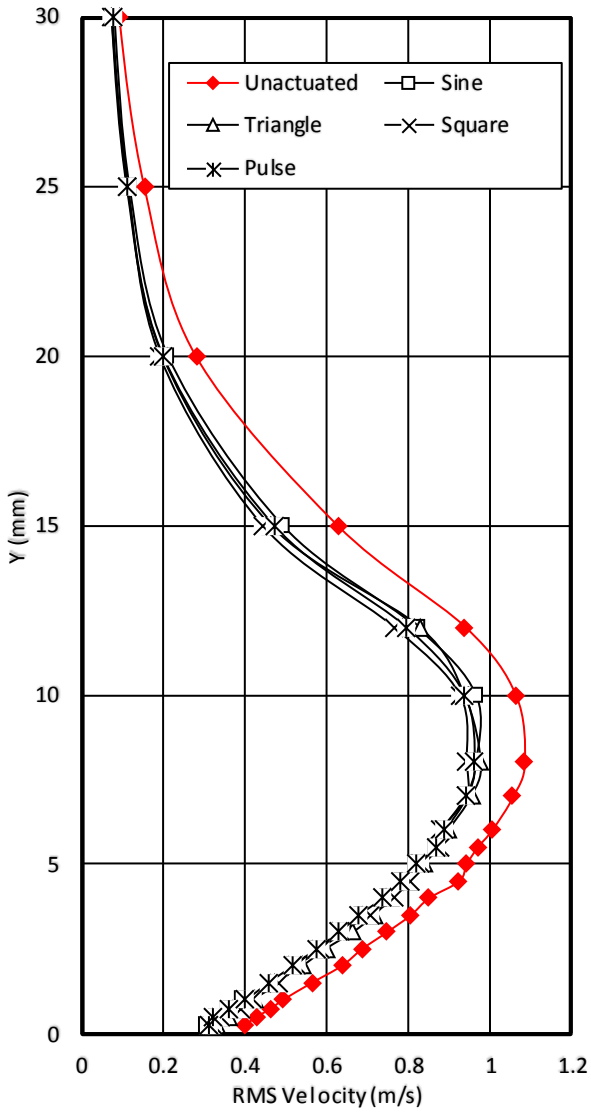

Fig.4.26. RMS Velocity profiles for different waveforms in plane Z= 0.Sine Wave, VR=1.50, Fr = 960 Hz, $\phi = 9.5°$, $U_\infty = 7\ m/s$.

4.4.2- Measurements of Flow Features by PIV Technique- Actuated Case

In the first phase of study of actuated case by PIV technique, while the ratio of peak exit jet velocity to free stream velocity of cross flow (VR) kept constant at value of 1.5, the angular position of actuators was changed by rotation of hump about its central axis. The actuated cases have been studied for 8 angles of $\phi = 0$, 5, 9.5, 12.5, 15, 17.5, 20 and 25 degrees. The hump apex is located at angle of 0 degree while the hump trailing edge is

located at angle of about 33 degree. The instantaneous velocity vector fields for angular position of $\phi = 0$ degree in the wake region is shown by Fig 4.27.

Figs 4.27 (a, c, e) show the velocity vectors and corresponding velocity magnitudes are shown in Figs 4.27 (b, d, f). It should be noted that for all actuated cases three selected samples of instantaneous velocity field is shown. Figs4.28-4.31, show the average of velocity vector and magnitude fields, the streamlines, the vorticity contour as well as RMS velocity profiles, respectively.

This Space Intentionally Left Blank.

Sine Wave, Velocity Ratio of 1.50, Angular Position: $\phi = 0°$

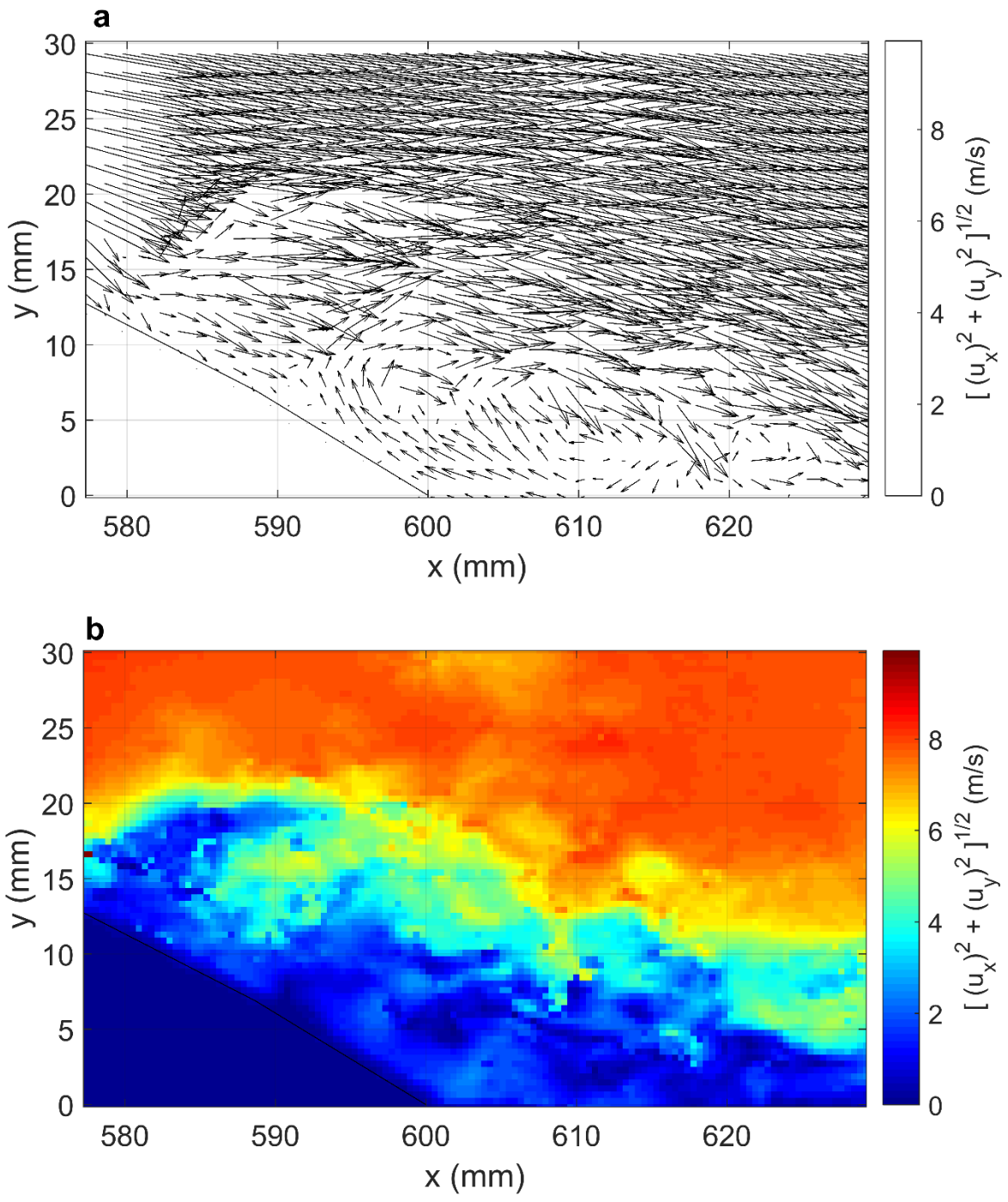

Fig.4.27. (a , b) Instantaneous velocity vector and magnitude fields in the wake region-actuated case, Sine wave, VR=1.5, Angular position: $\phi = 0°, U_\infty = 7\ m/s$.

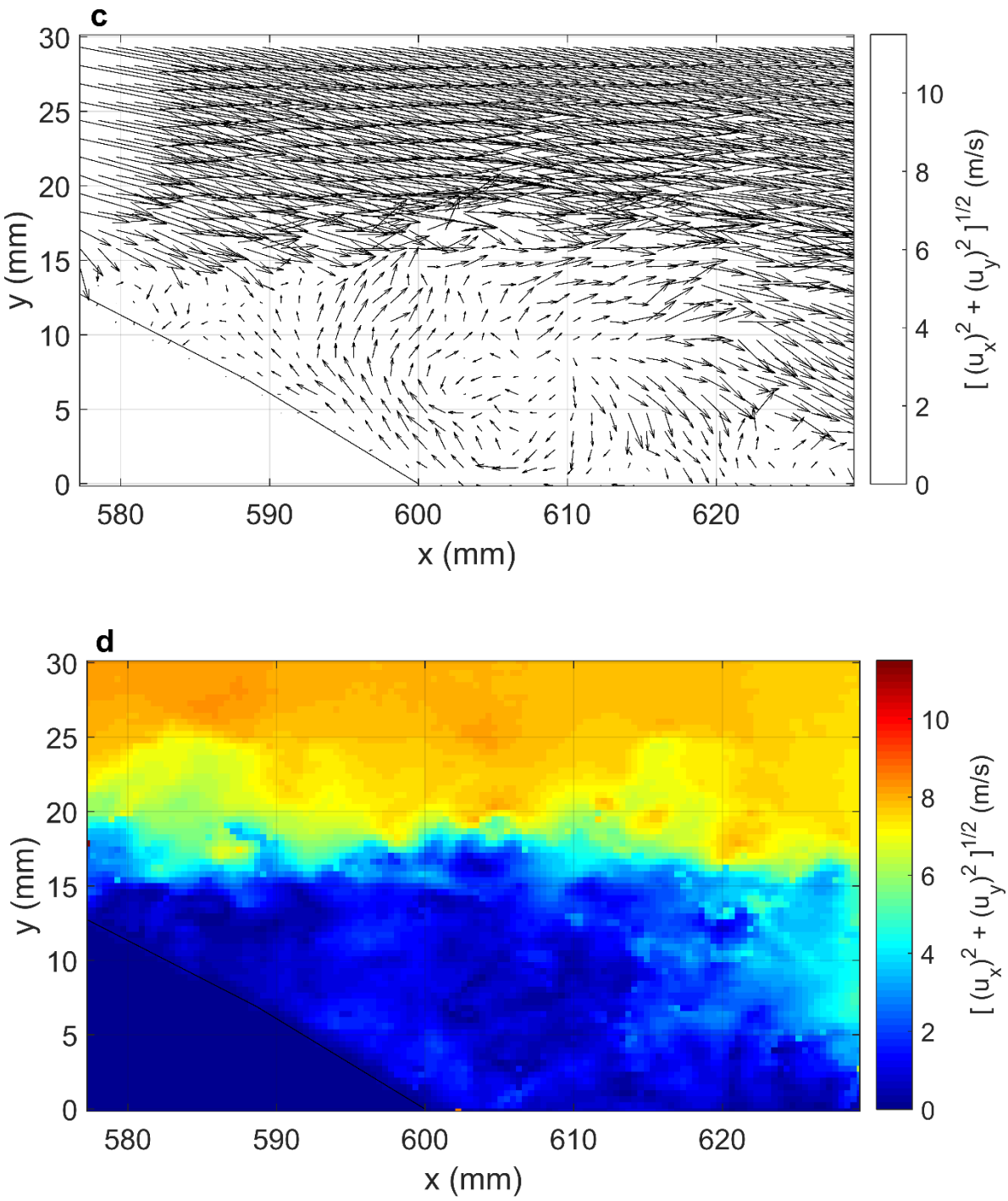

Fig.4.27. (c , d) Instantaneous velocity vector and magnitude fields in the wake region-actuated case, Sine wave, VR=1.5, Angular position: $\phi = 0°, U_\infty = 7\ m/s$.

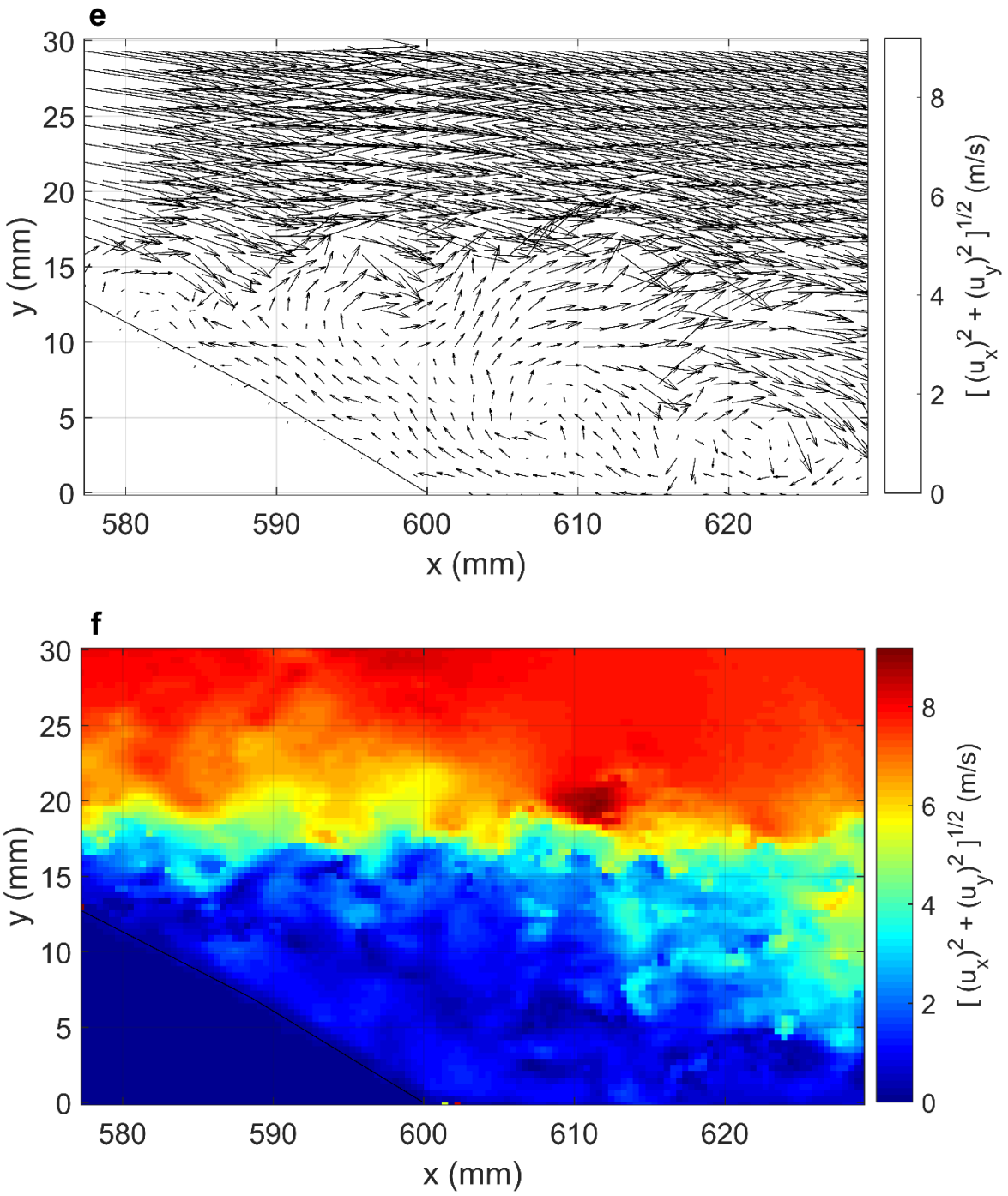

Fig.4.27. (e, f) Instantaneous velocity vector and magnitude fields in the wake region-actuated case, Sine wave, VR=1.5, Angular position: $\phi = 0°, U_\infty = 7\ m/s$.

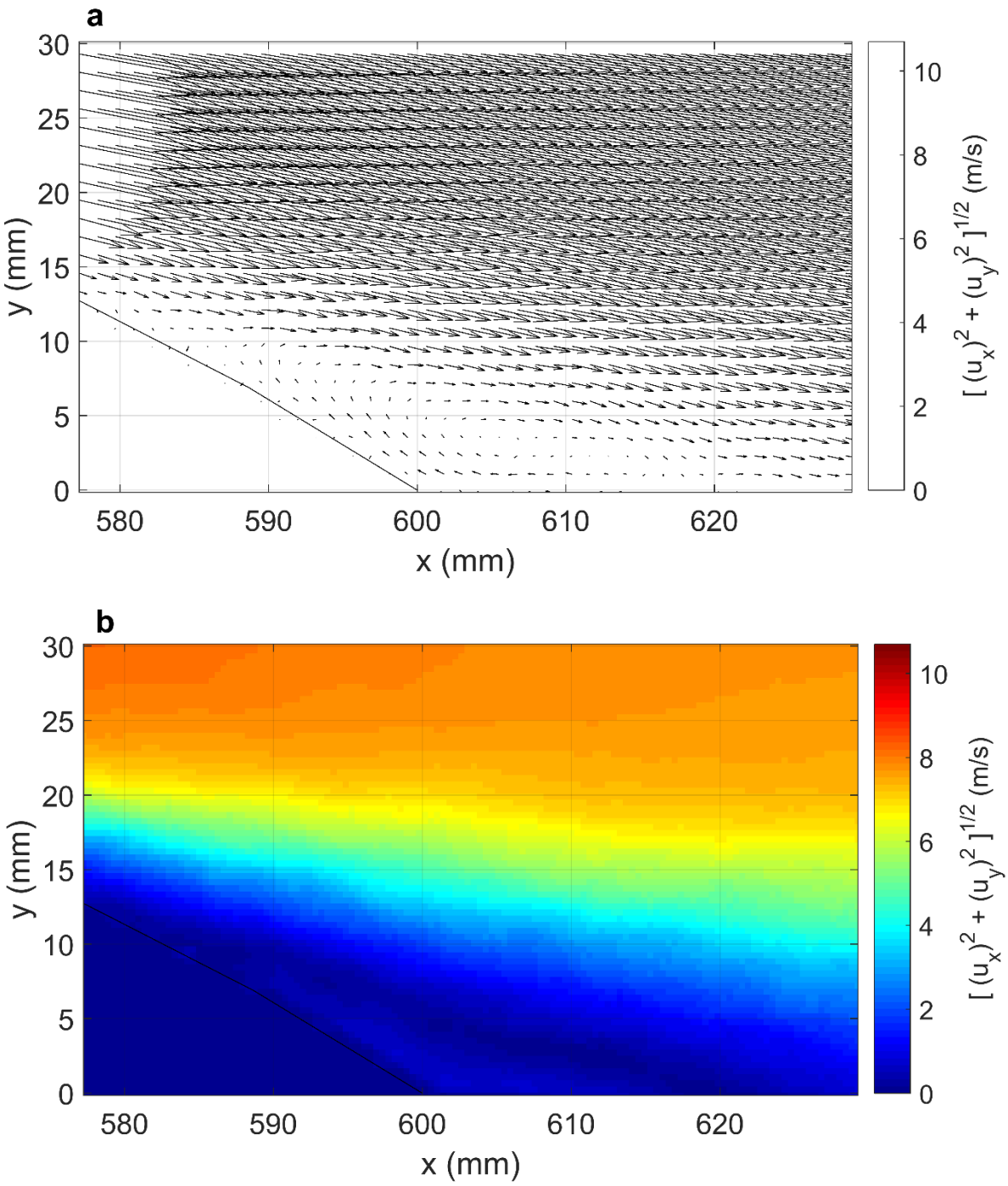

Fig.4.28. (a , b) Average velocity vector and magnitude fields in the wake region-actuated case, Sine wave, VR=1.5, Angular position: $\phi = 0°, U_\infty = 7\ m/s$.

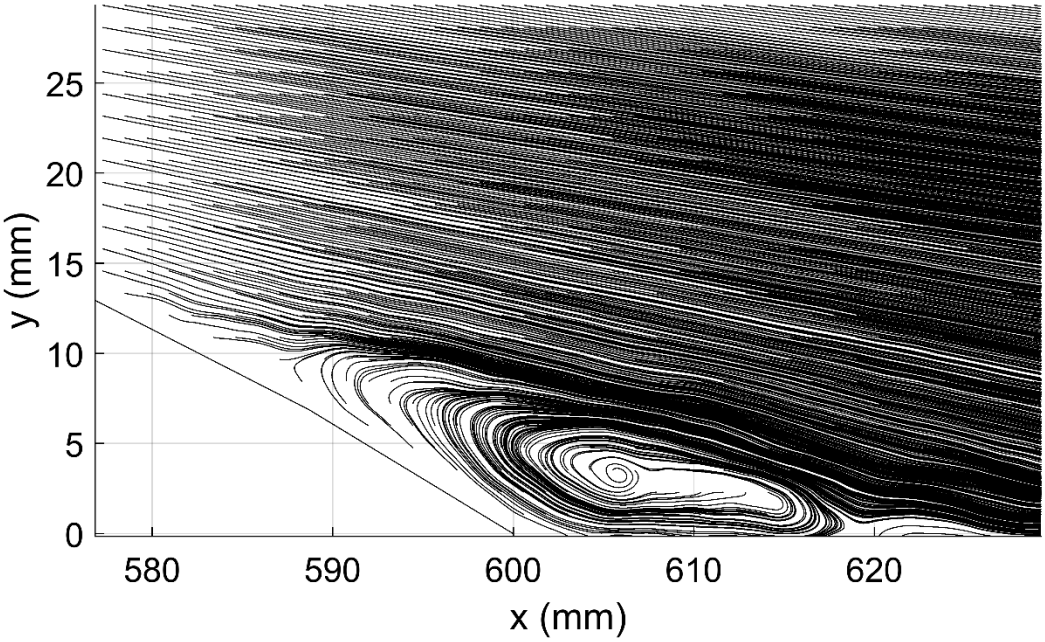

Fig.4.29. Streamlines profile, actuated case, Sine wave, VR=1.5, Angular position: $\phi = 0°, U_\infty = 7\ m/s$.

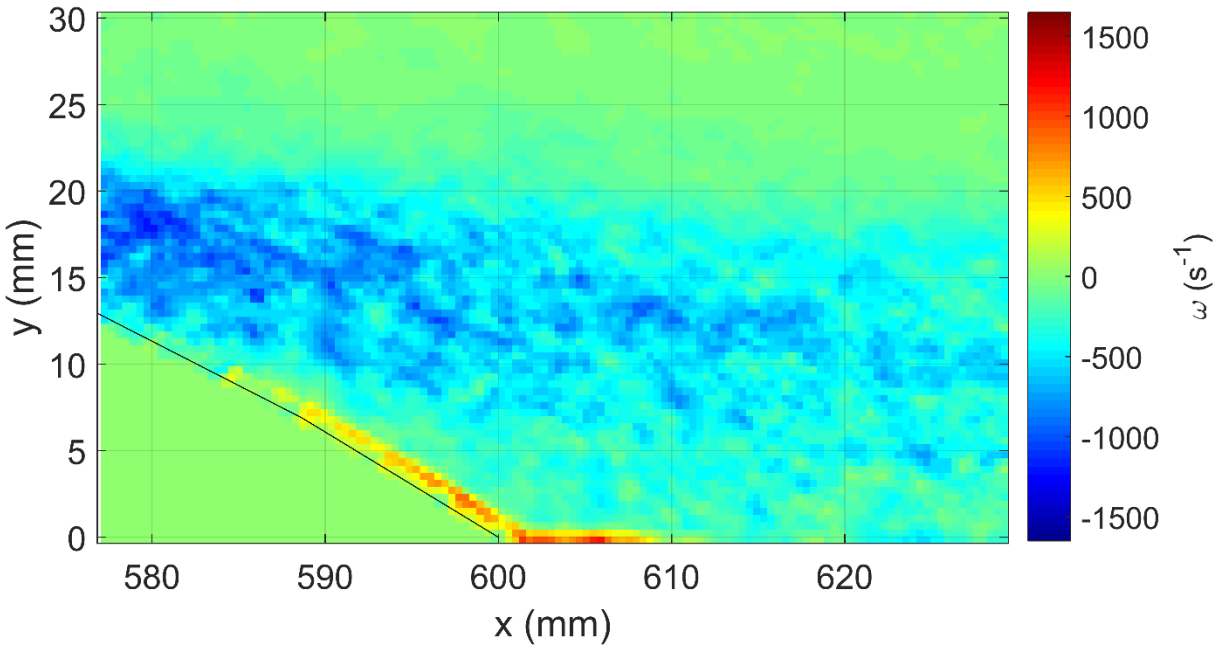

Fig.4.30. Vorticity contour, actuated case, Sine wave, VR=1.5, Angular position: $\phi = 0°, U_\infty = 7\ m/s$.

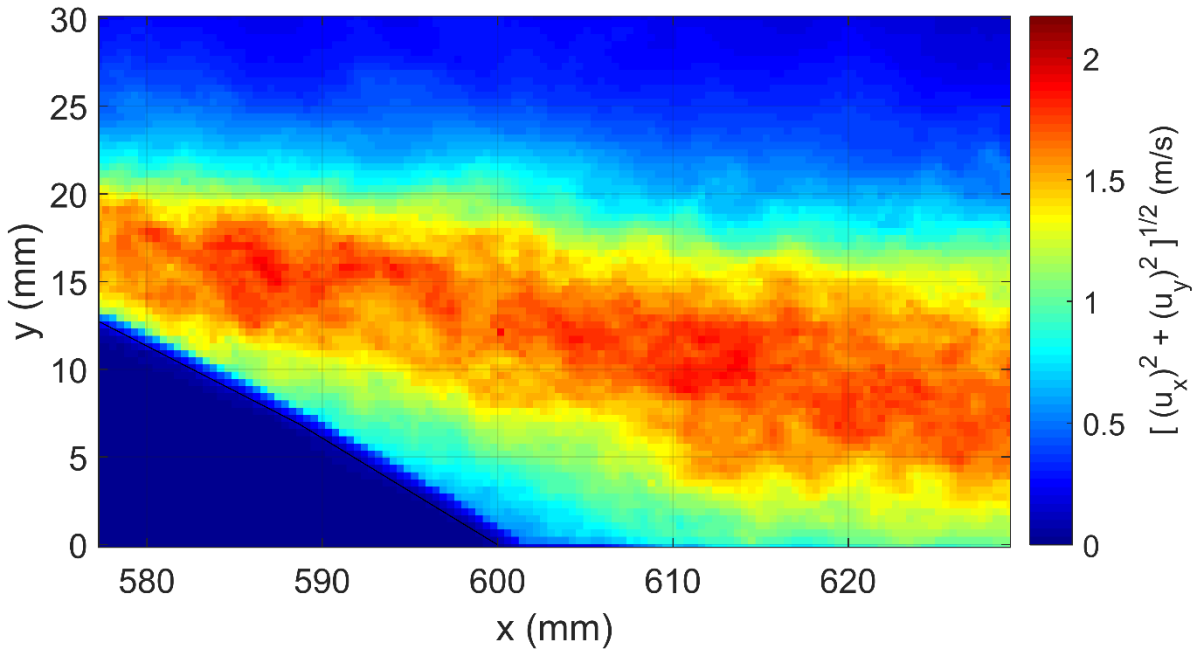

Fig.4.31. RMS Velocity contour, actuated case, Sine wave, VR=1.5, Angular position: $\phi = 0°, U_\infty = 7\ m/s.$

The profiles of 3 selected samples of instantaneous velocity vectors and magnitudes fields as well as the profile of average velocity vector and magnitude filed, streamlines profiles, vorticity contours profile and RMS velocity profile for velocity ratio of 1.5 at angular position of $\phi = 9.50^{\circ}$ with Sine wave as driving waveform are shown in Figs.4.32-4.36.

The profiles of instantaneous velocity vectors and magnitudes, average velocity fields of 100 pairs of images as well as the streamlines and vorticity and RMS velocity magnitude profiles for angular positions of 5^o, 12.5^o, 17.5^o, 20^o and 25^o are provided in Appendix D.

Sine Wave, Velocity Ratio of 1.50, Angular Position: $\phi = 9.5°$

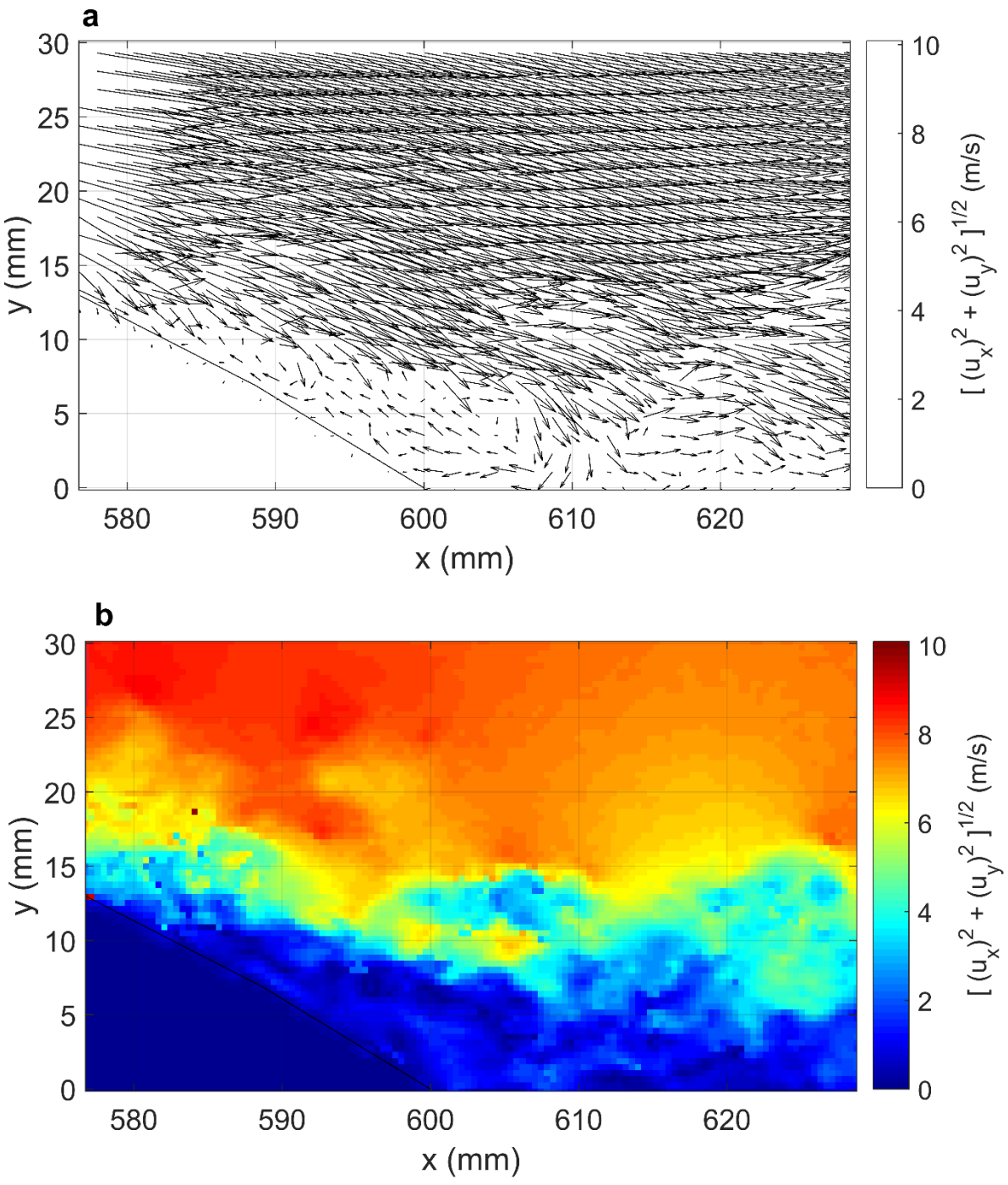

Fig .4.32. (a , b) Instantaneous velocity vectors and magnitude fields in the wake region-actuated case, Sine wave, VR=1.5, Angular position: $\phi = 9.5°$, $U_\infty = 7\ m/s$.

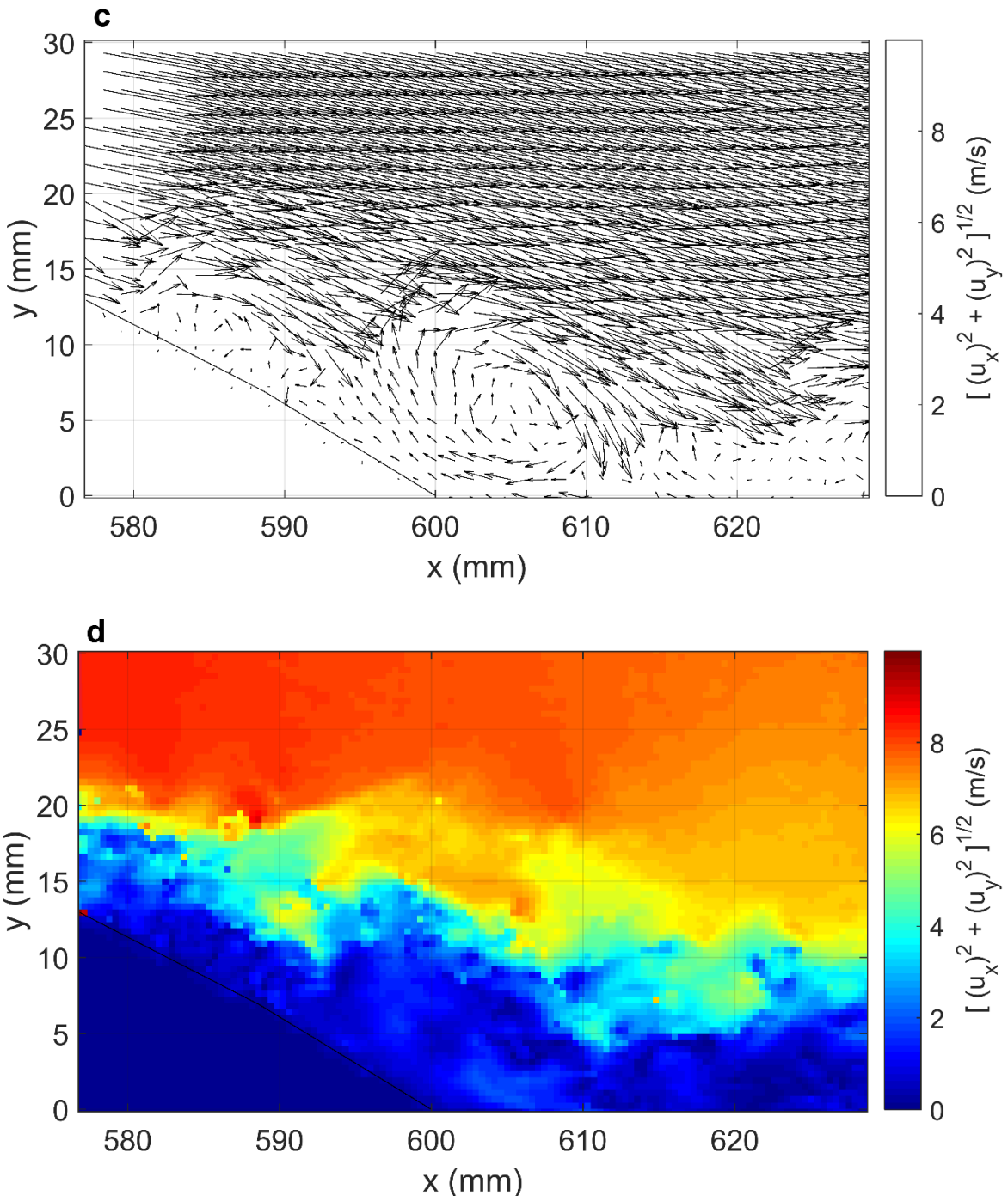

Fig. 4.32. (c , d) Instantaneous velocity vectors and magnitude fields in the wake region-actuated case, Sine wave, VR=1.5, Angular position: $\phi = 9.5°, U_\infty = 7\ m/s$.

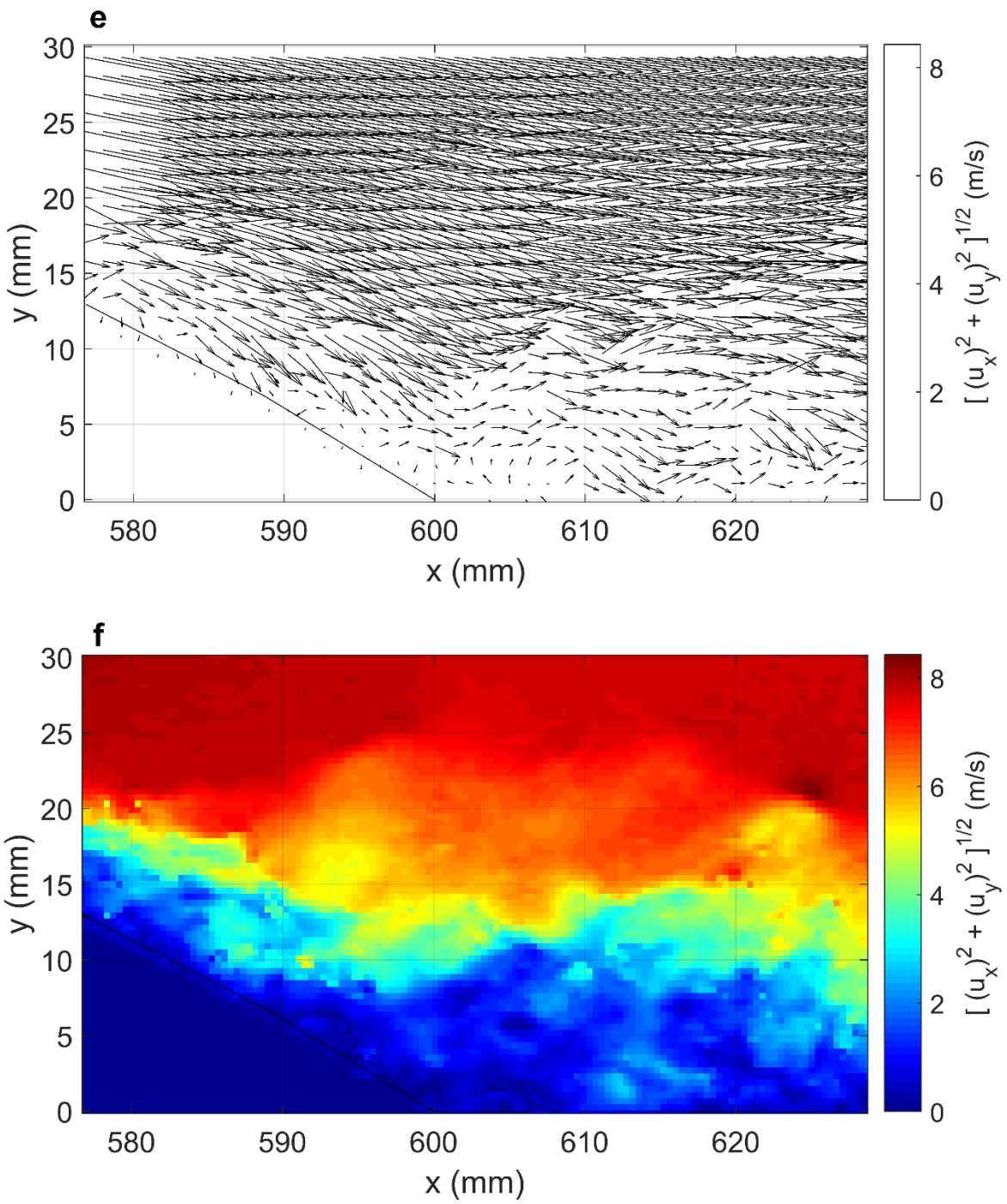

Fig.4.32. (e , f) Instantaneous velocity vectors and magnitude fields in the wake region-actuated case, Sine wave, VR=1.5, Angular position: $\phi = 9.5°, U_\infty = 7\ m/s$.

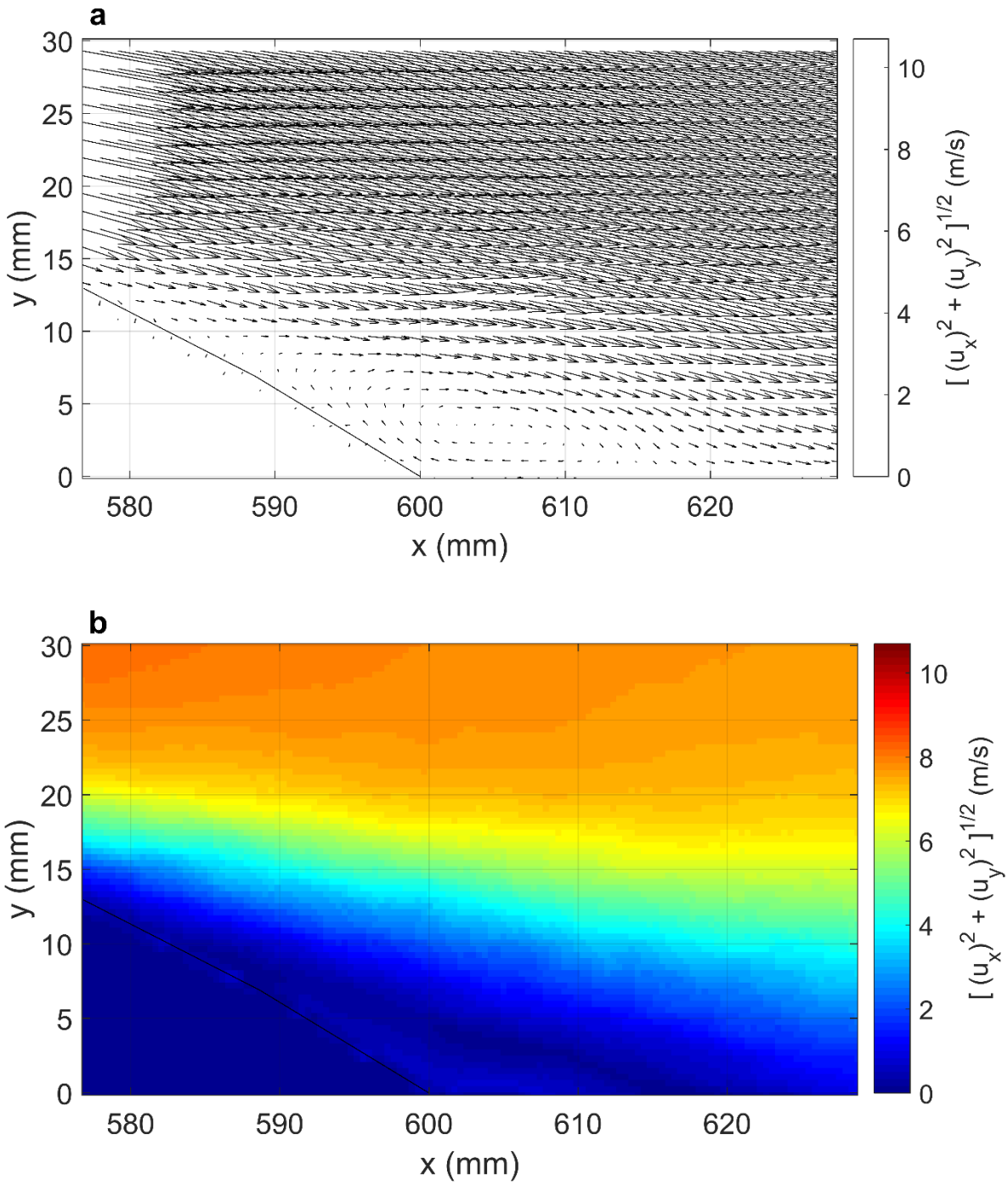

Fig.4.33 (a , b) Average velocity vector and magnitude fields in the wake region- actuated case, Sine wave, VR=1.5, Angular position: $\phi = 9.5°$, $U_\infty = 7\ m/s$.

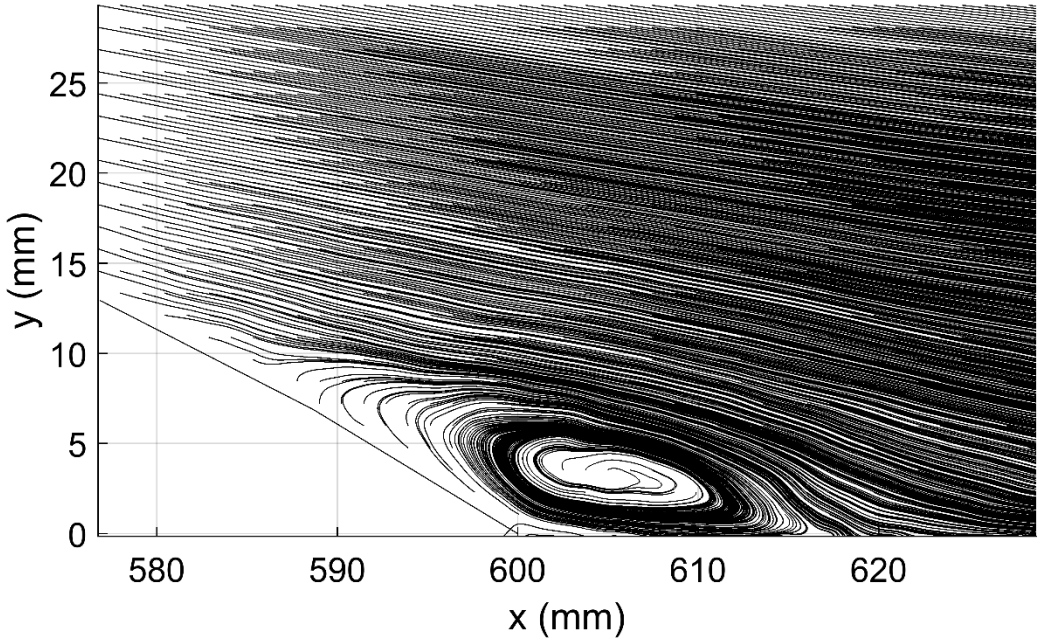

Fig.4.34. Streamlines profile, actuated case, Sine wave, VR=1.5, Angular position: $\phi = 9.5°$, $U_\infty = 7\ m/s$.

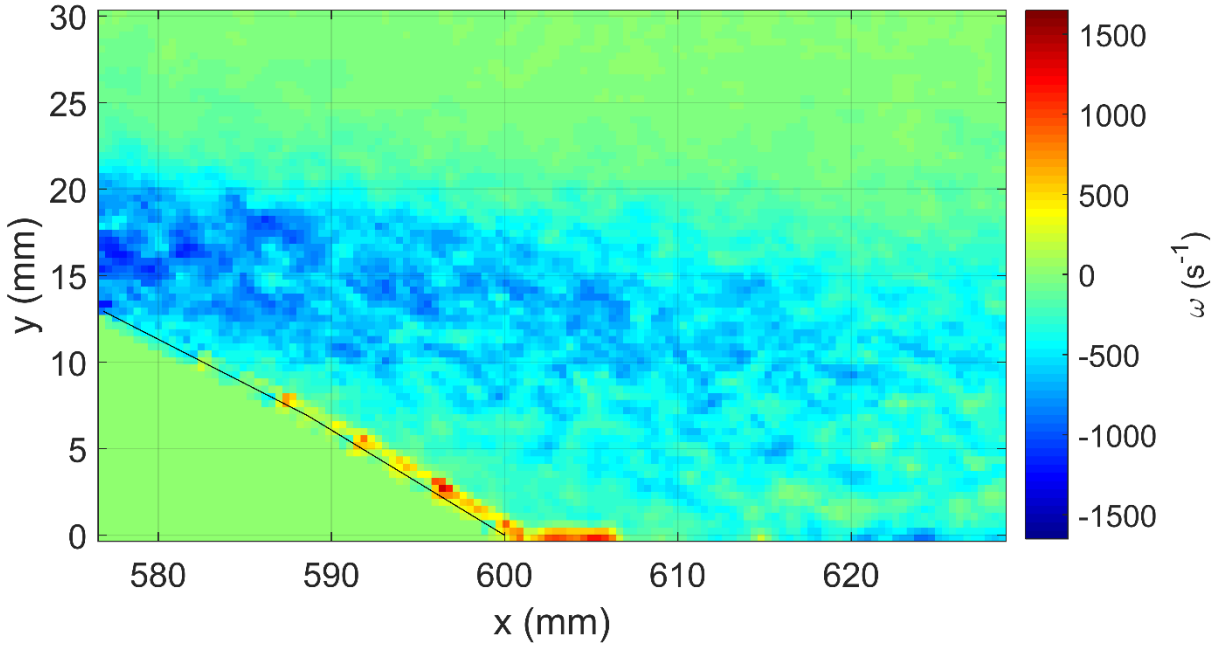

Fig.4.35. Vorticity contour, actuated case, Sine wave, VR=1.5, Angular position: $\phi = 9.5°$, $U_\infty = 7\ m/s$.

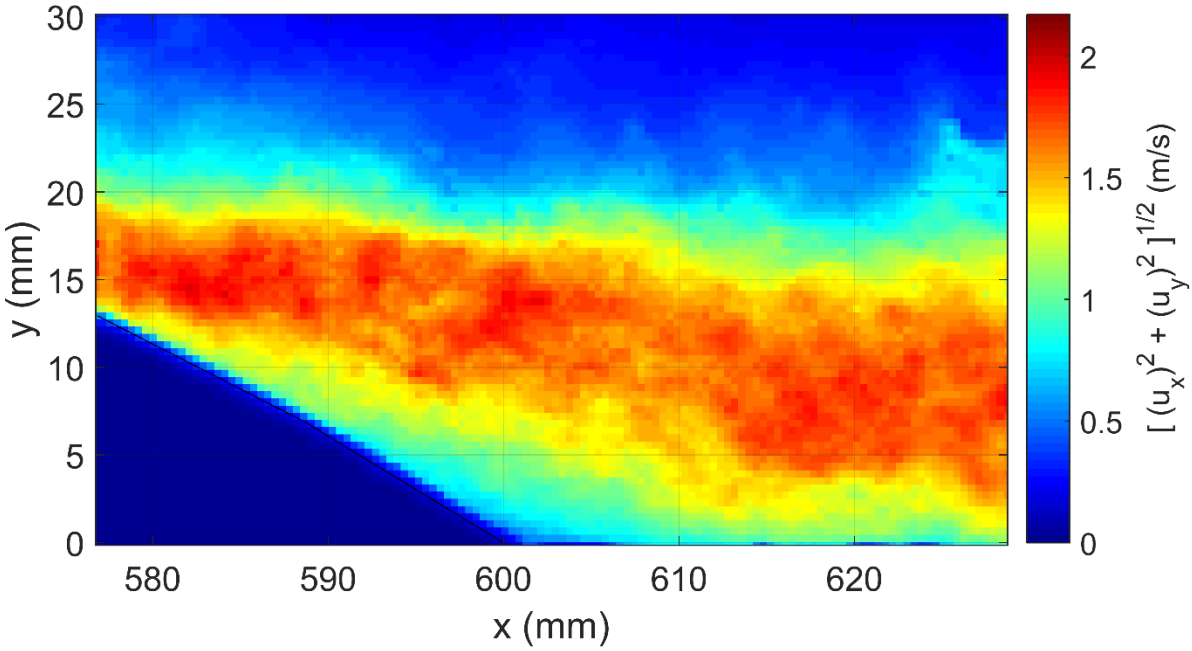

Fig.4.36. RMS velocity contour, actuated case, Sine wave, VR=1.5, Angular position: $\phi = 9.5°, U_\infty = 7\ m/s.$

The investigation of influence of actuators angular position on the location of separation and reattachment points for VR of 1.5 shows that the best performance of the synthetic jet actuators at velocity ratio of 1.50 is achieved at angular position of $\phi = 15^{\circ}$. The maximum reduction of recirculation region occurs at this angular position. . The criteria for identification of separation and reattachment point have been explained in Chapter 5-Section .5.3.2.

The profiles of instantaneous velocity vectors and magnitudes, average velocity fields, streamlines, vorticity contour profile as well as RMS velocity profile for angular position of $\phi = 15^{\circ}$ and VR= 1.50 are shown in Figs.4.37-4.41.

Sine Wave, Velocity Ratio of 1.50, Angular Position: $\phi = 15°$

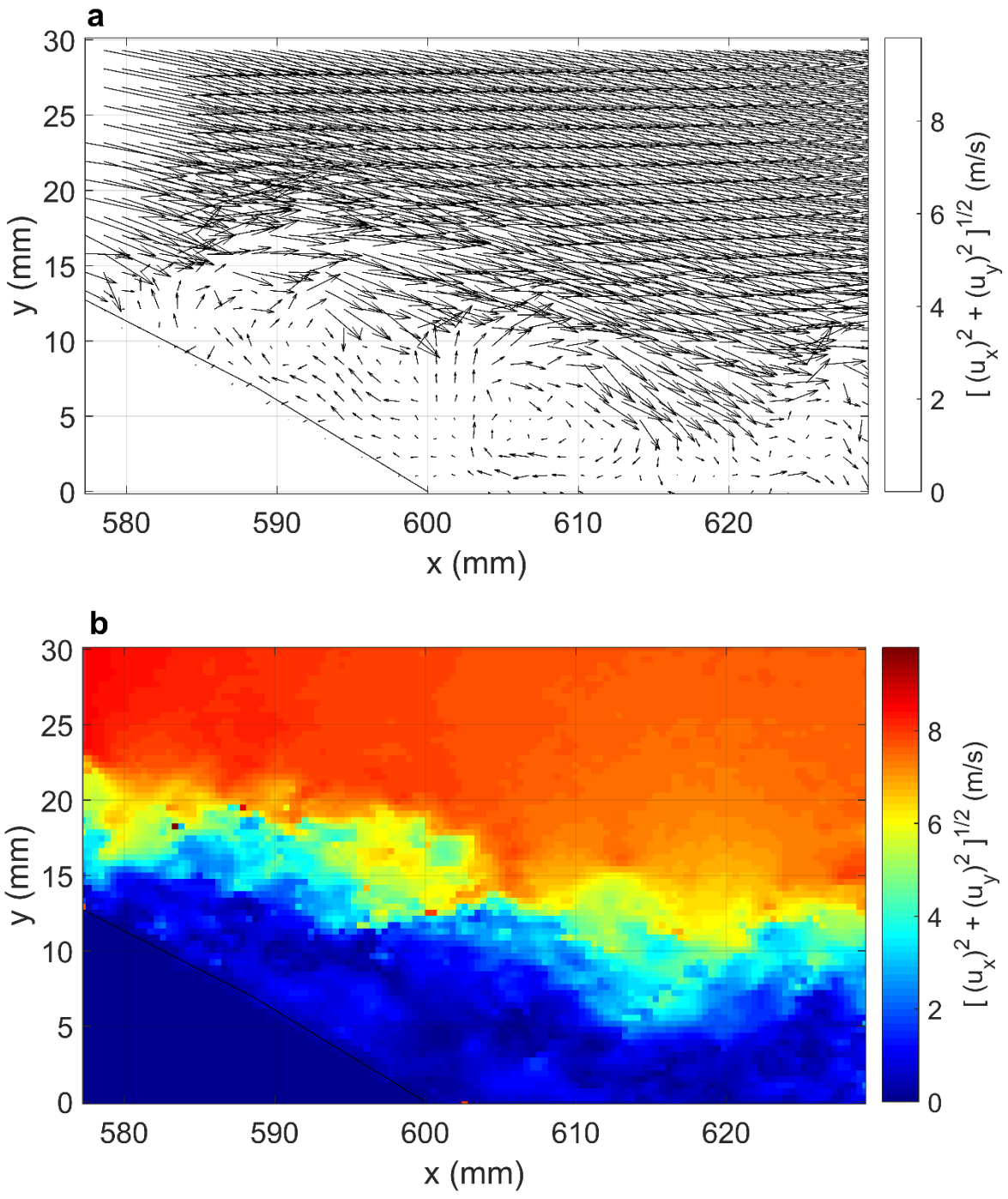

Fig.4.37. (a , b) Instantaneous velocity vector and magnitude fields in the wake region-actuated case, Sine wave, VR=1.5, Angular position: $\phi = 15°, U_\infty = 7\ m/s$.

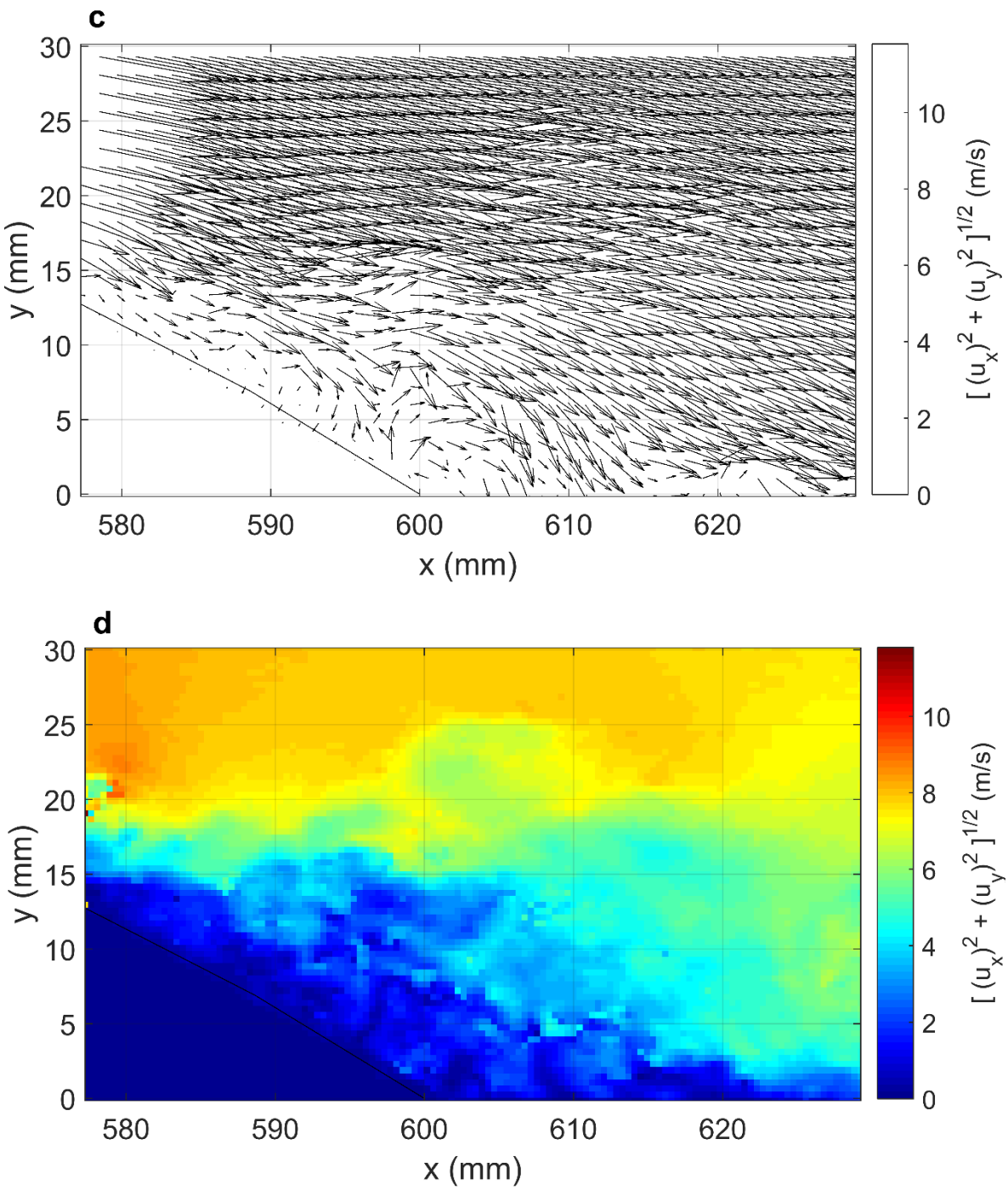

Fig.4.37. (c , d) Instantaneous velocity vector and magnitude fields in the wake region-actuated case, Sine wave, VR=1.5, Angular position: $\phi = 15°, U_\infty = 7\ m/s$.

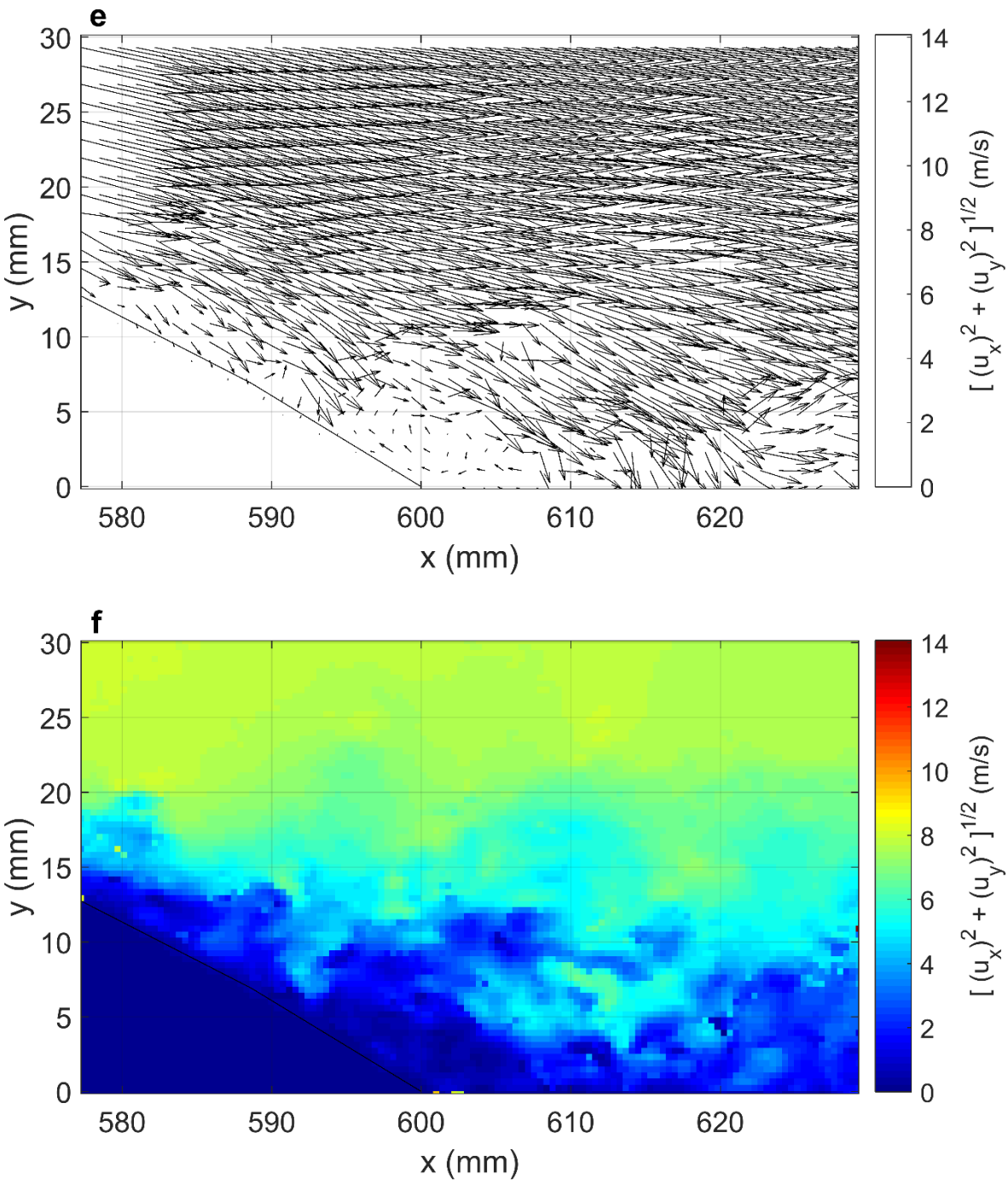

Fig.4.37. (e , f) Instantaneous velocity vector and magnitude fields in the wake region-actuated case, Sine wave, VR=1.5, Angular position: $\phi = 15°, U_\infty = 7\ m/s$.

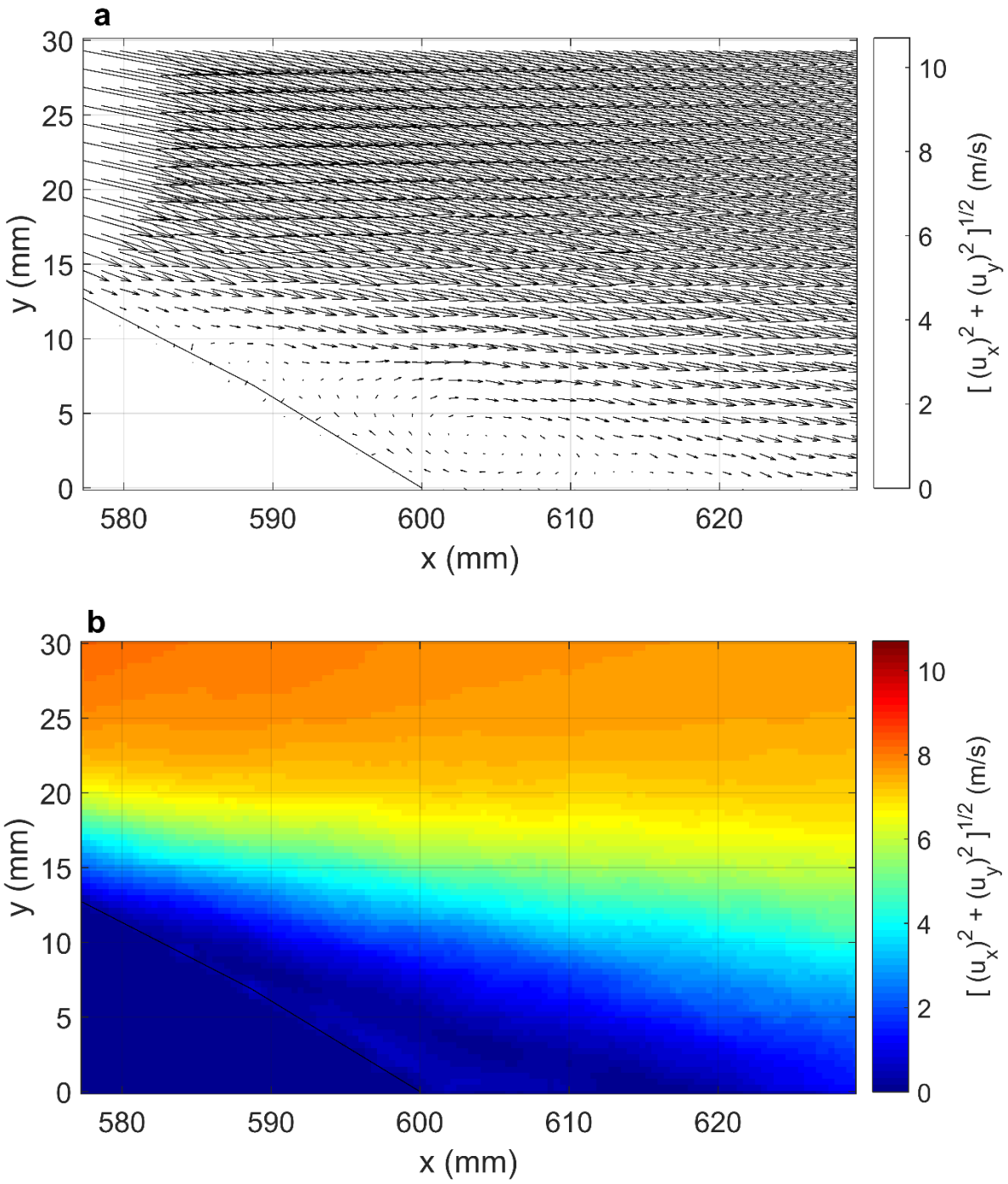

Fig.4.38 (a , b) Average velocity vector and magnitude fields (a, b) in the wake region- actuated case, Sine wave, VR=1.5, Angular position: $\phi = 15°, U_\infty = 7\ m/s$.

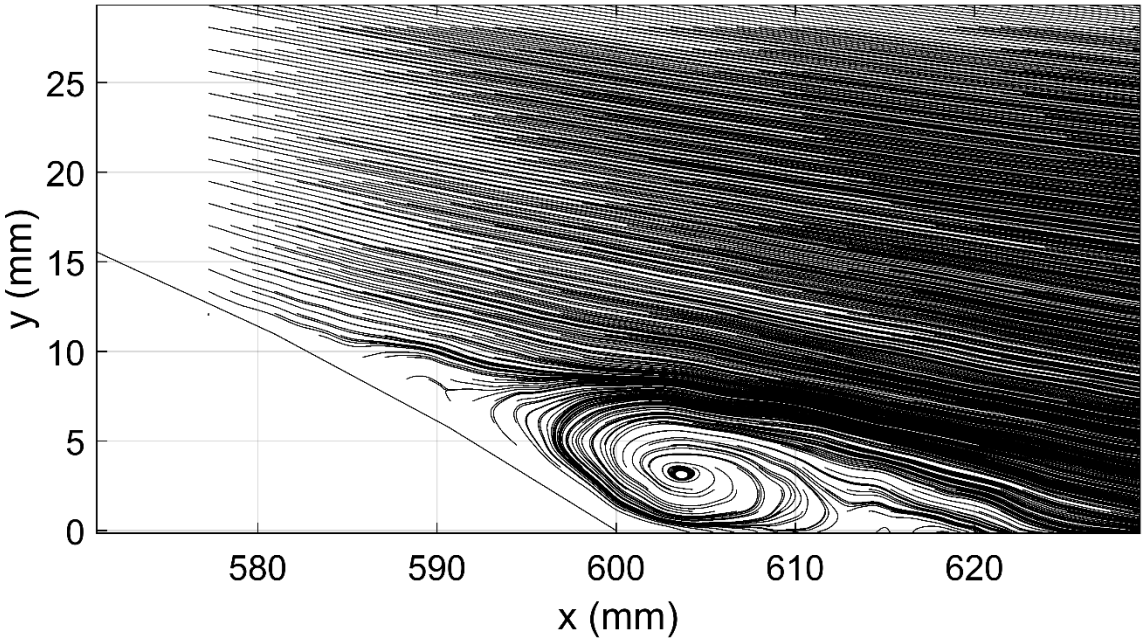

Fig .4.39. Streamlines profile, actuated case, Sine wave, VR=1.5, Angular position: $\phi = 15°, U_\infty = 7\ m/s$.

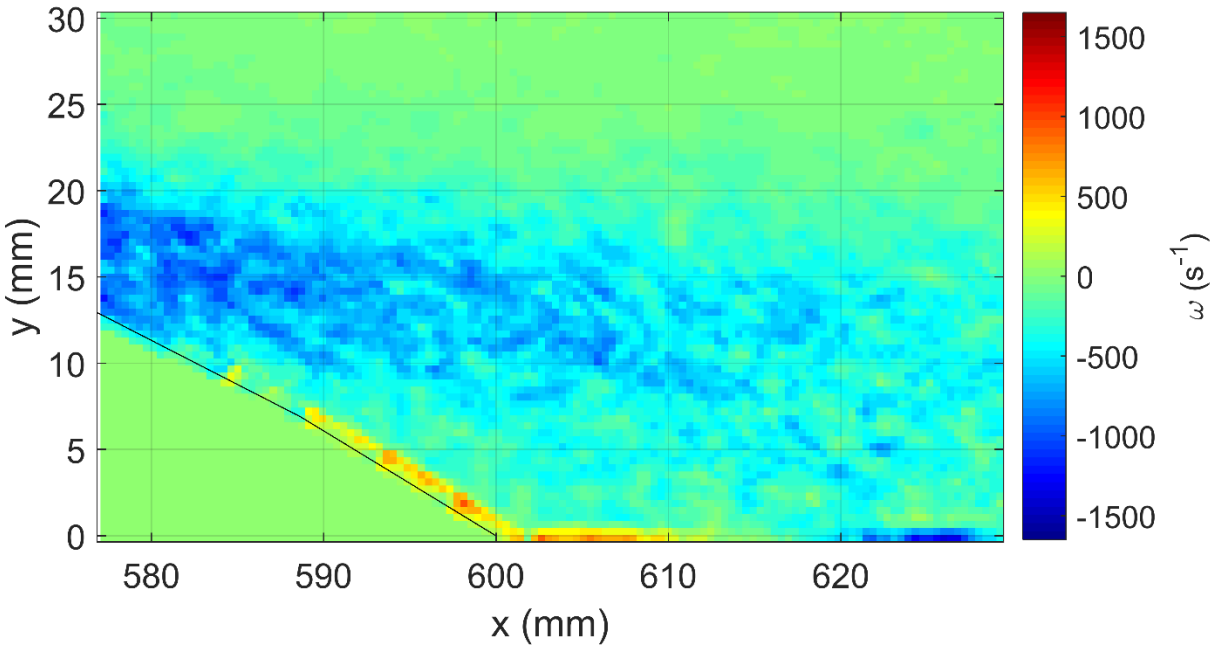

Fig.4.40. Vorticity contour, actuated case, Sine wave, VR=1.5, Angular position: $\phi = 15°, U_\infty = 7\ m/s$.

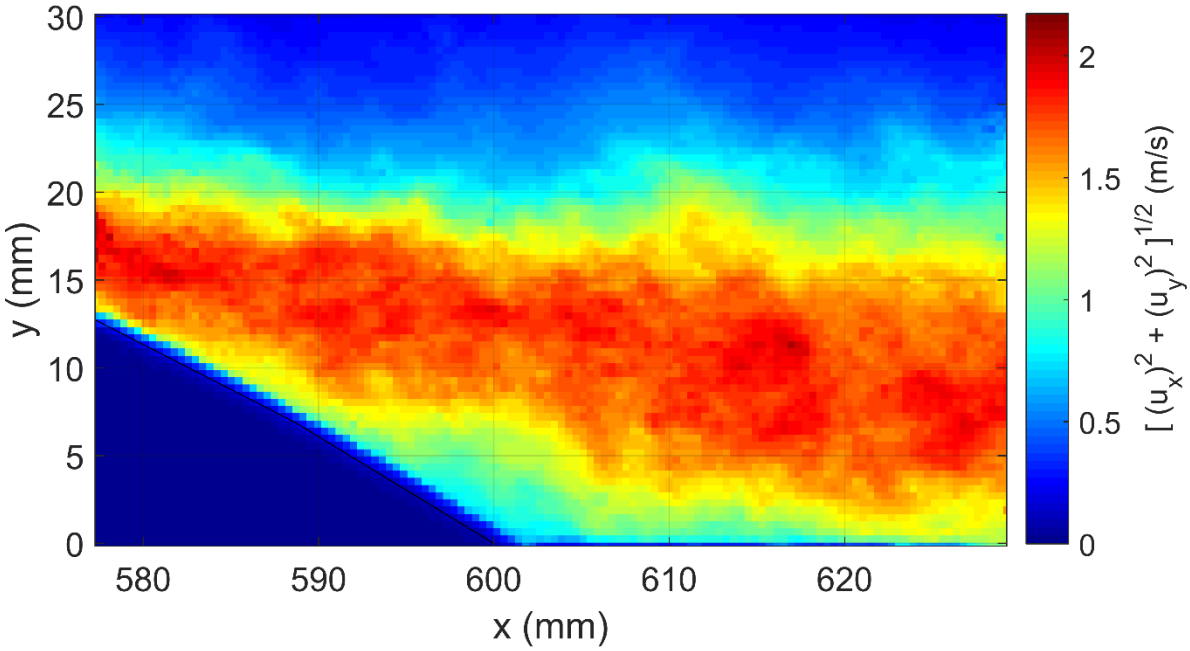

Fig.4.41. RMS Vorticity contour, actuated case, Sine wave, VR=1.5, Angular position: $\phi = 15°, U_\infty = 7\ m/s$.

In the next stage of study, while the position of actuators is kept constant at angular position of $\phi = 15^{\circ}$, the velocity ratio VR is changed for selected values of 1.15, 1.50, 1.85 and 2.2. The profiles of instantaneous and average velocity vectors and magnitudes fields as well as streamlines profiles, vorticity contour profile and RMS velocity profile for velocity ratio of 1.15 at angular position of $\phi = 15^{\circ}$ are shown in Figs.4.42-4.46.

Sine Wave, Velocity Ratio of 1.15, Angular position: $\phi = 15°$

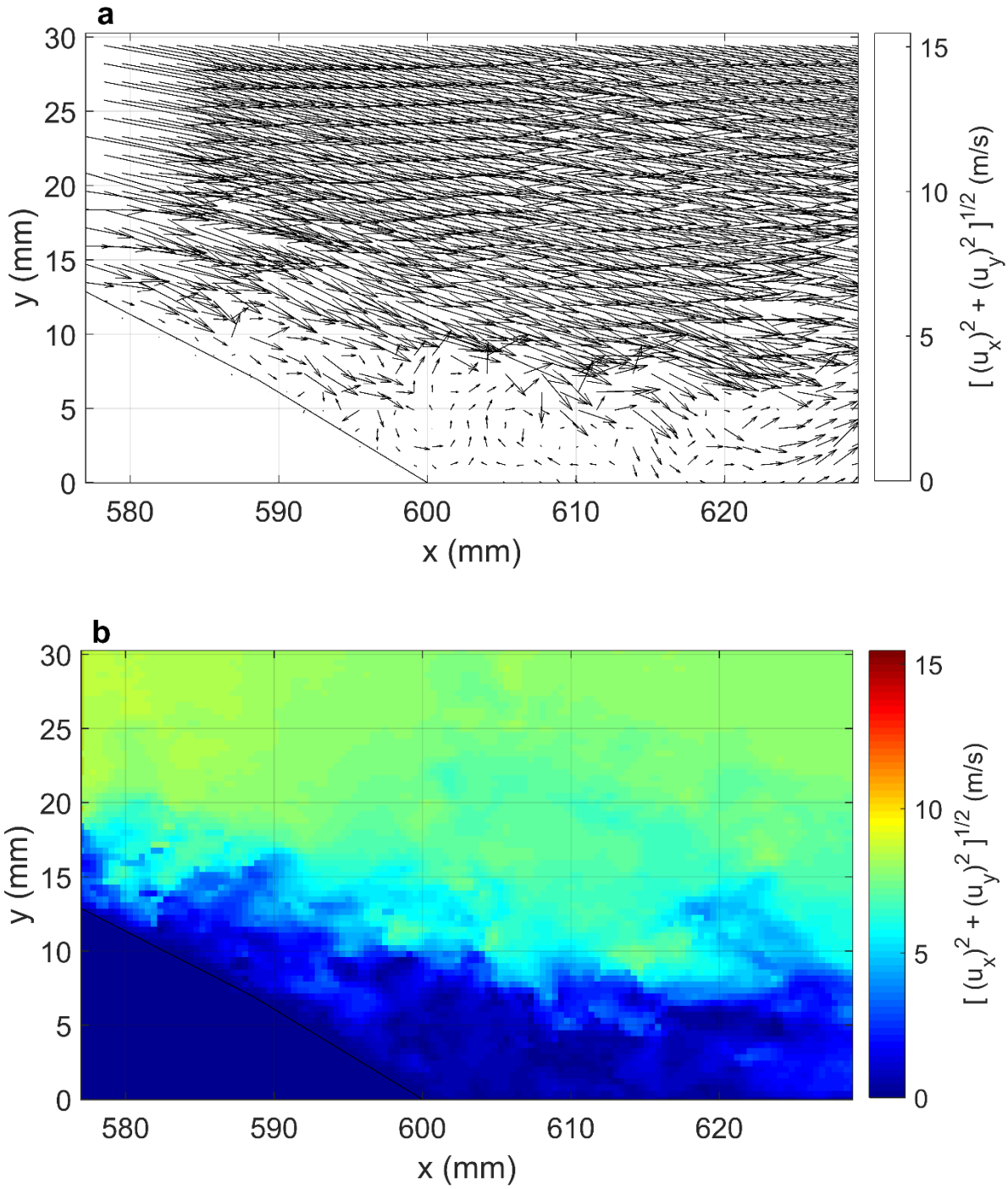

Fig.4.42. (a , b) Instantaneous velocity vector and magnitude fields in the wake region-actuated case, Sine wave, VR=1.15, Angular position: $\phi = 15°, U_\infty = 7\ m/s$.

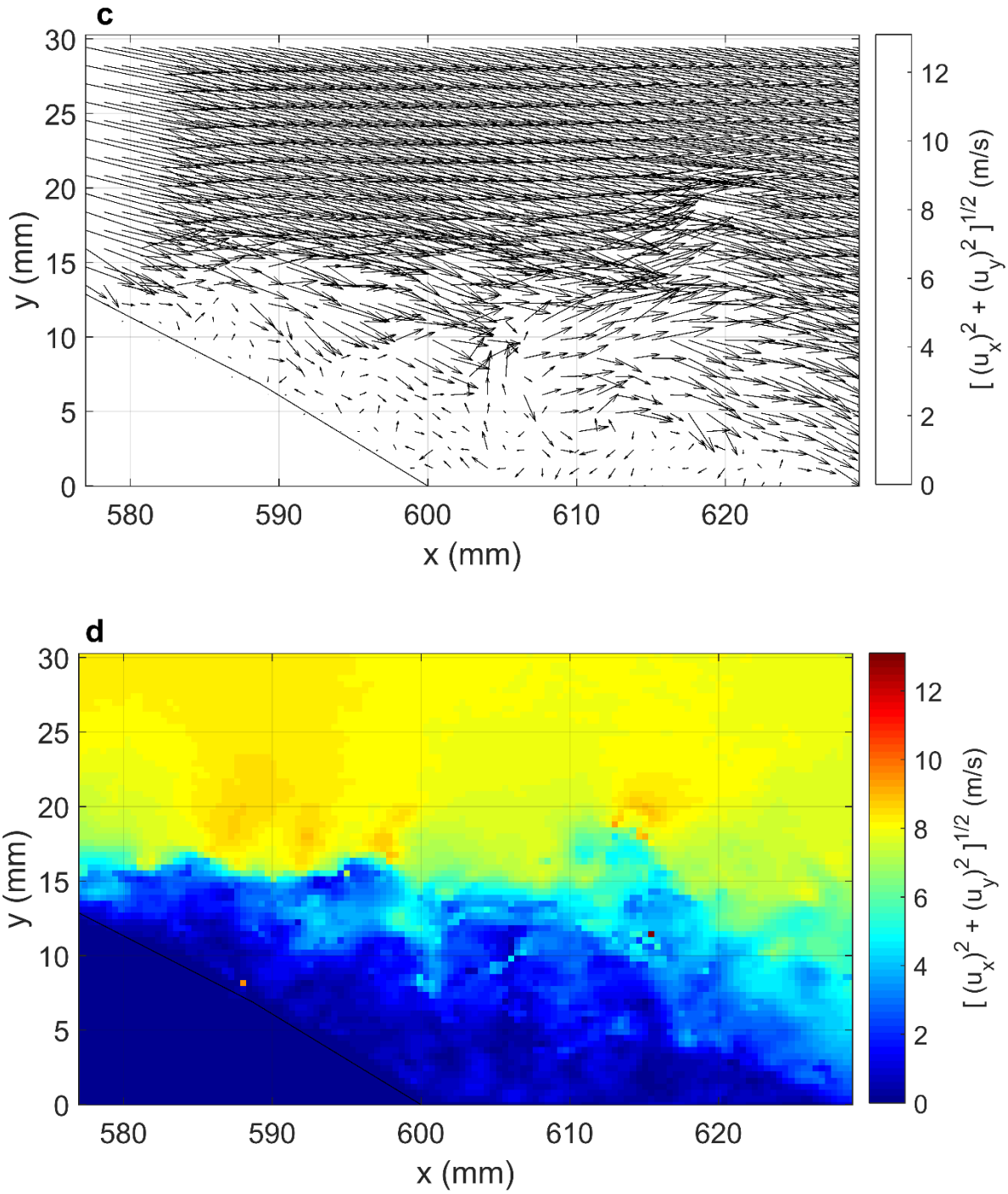

Fig.4.42. (c , d) Instantaneous velocity vector and magnitude fields in the wake region-actuated case, Sine wave, VR=1.15, Angular position: $\phi = 15°, U_\infty = 7\ m/s$.

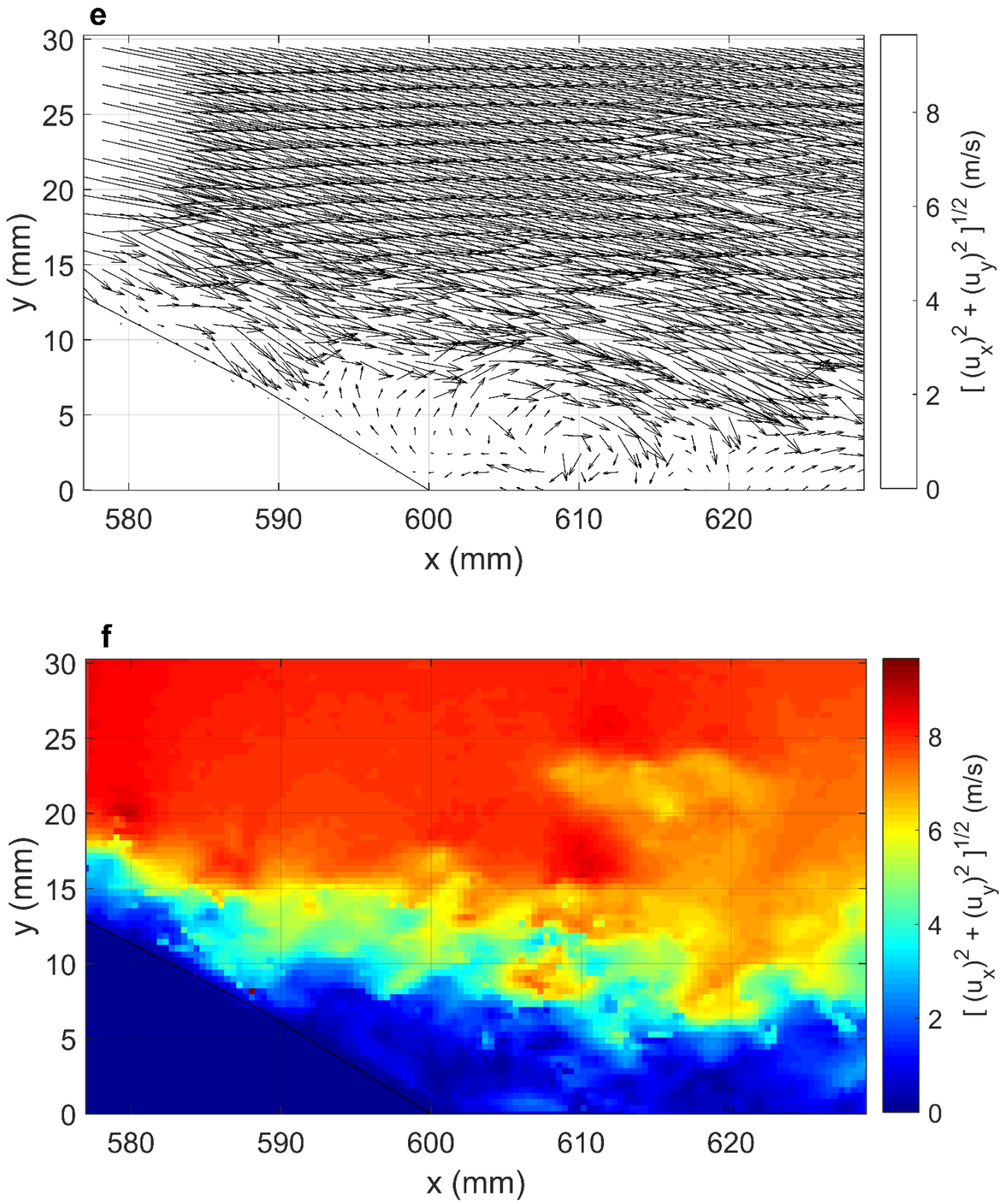

Fig.4.42. (e , f) Instantaneous velocity vector and magnitude fields in the wake region-actuated case, Sine wave, VR=1.15, Angular position: $\phi = 15°, U_\infty = 7\ m/s$.

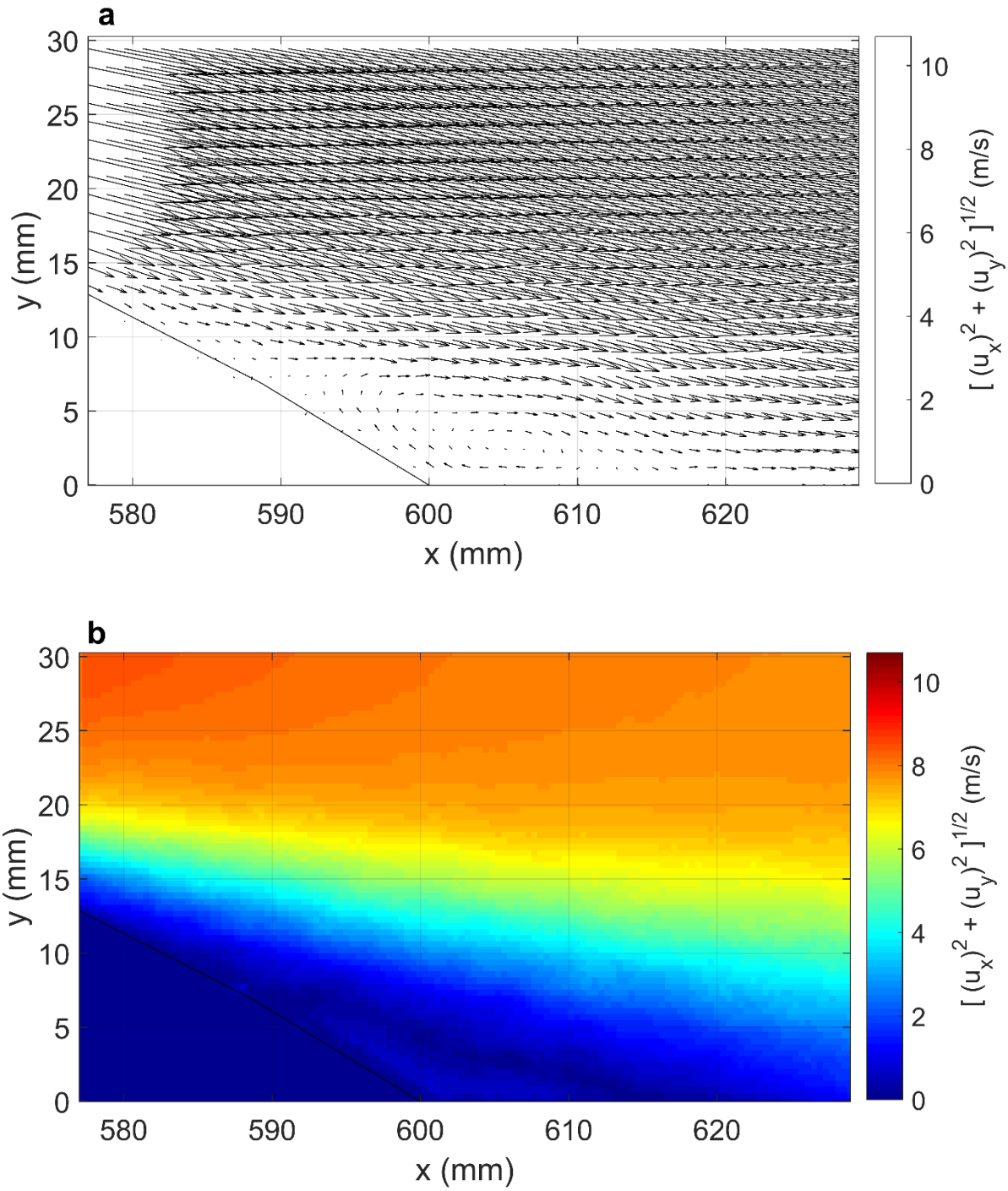

Fig.4.43. (a , b) Average velocity vector and magnitude fields (a, b) in the wake region-actuated case, Sine wave, VR=1.15, Angular position: $\phi = 15°, U_\infty = 7\ m/s$.

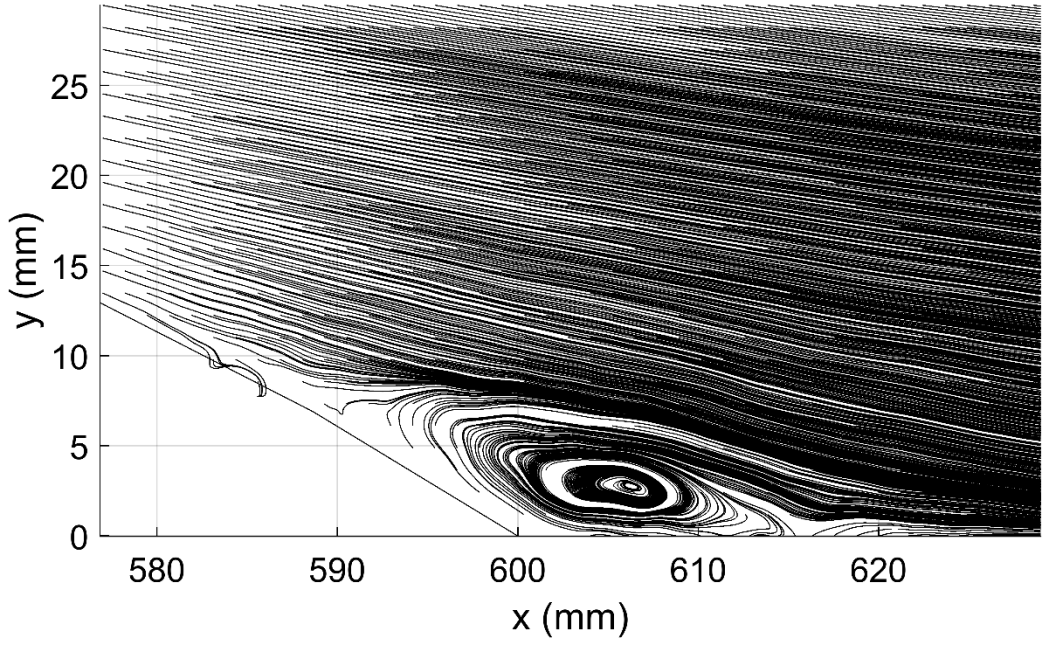

Fig.4.44. Streamlines profile, actuated case, Sine wave, VR=1.15, Angular position: $\phi = 15°, U_\infty = 7\ m/s$.

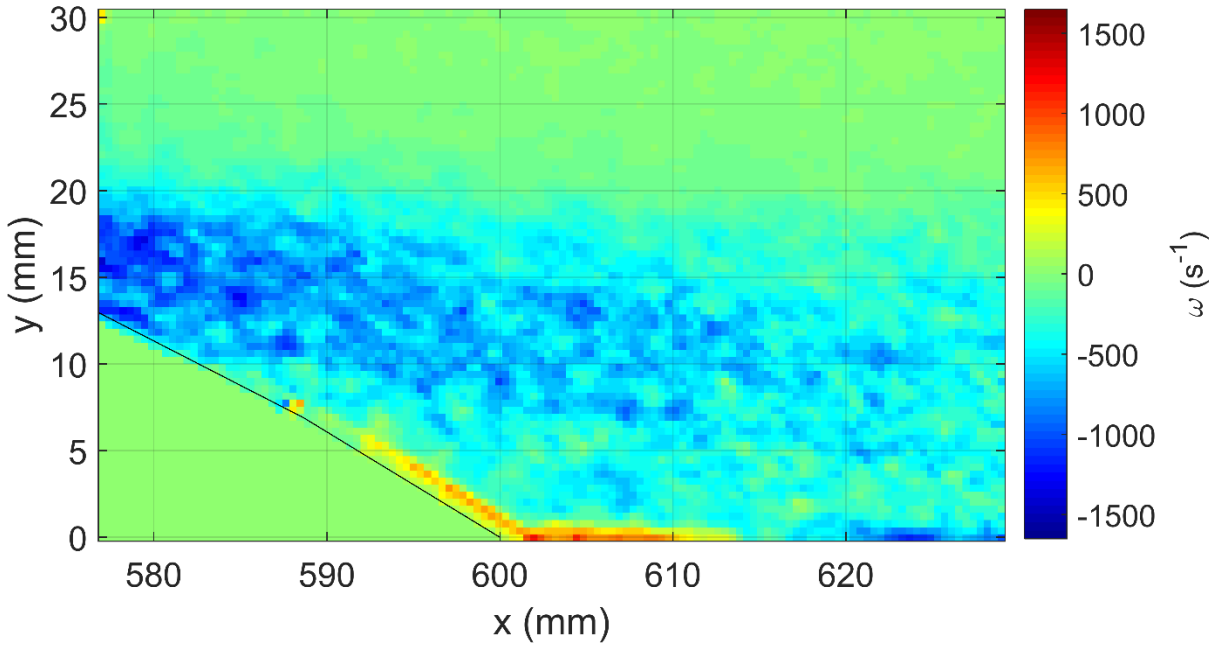

Fig.4.45. Vorticity contour, actuated case, Sine wave, VR=1.15, Angular position: $\phi = 15°, U_\infty = 7\ m/s$.

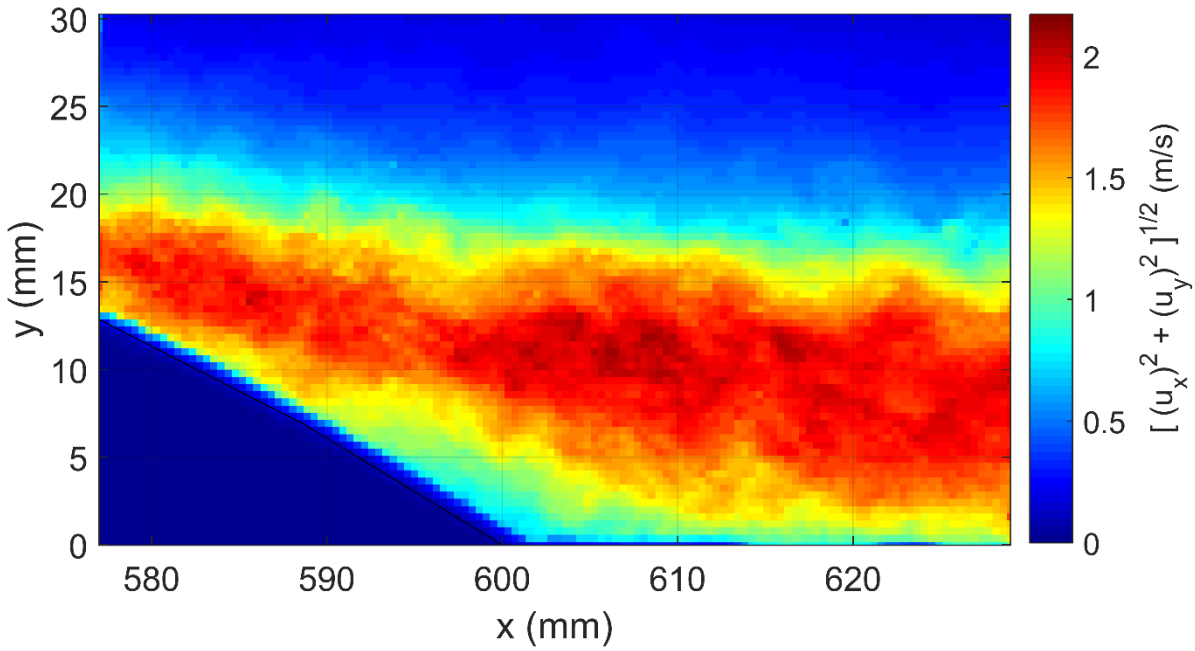

Fig.4.46. RMS velocity contour, actuated case, Sine wave, VR=1.15, Angular position: $\phi = 15°, U_\infty = 7\ m/s$.

The profiles of instantaneous and average velocity vectors and magnitudes fields as well as streamlines profiles, vorticity contour profile and RMS velocity profile for velocity ratio of 1.85 at angular position of $\phi = 15^{\circ}$ are depicted in Figs.4.47-4.51. Additionally, the profiles of Velocity RMS, instantaneous and average velocity vectors and magnitudes fields as well as streamlines profile and vorticity contour profile for velocity ratio of 2.2 at angular position of $\phi = 15^{\circ}$ are shown in Figs.4.52-4.56.

Sine Wave, Velocity Ratio of 1.85, Angular Position: $\phi = 15°$,

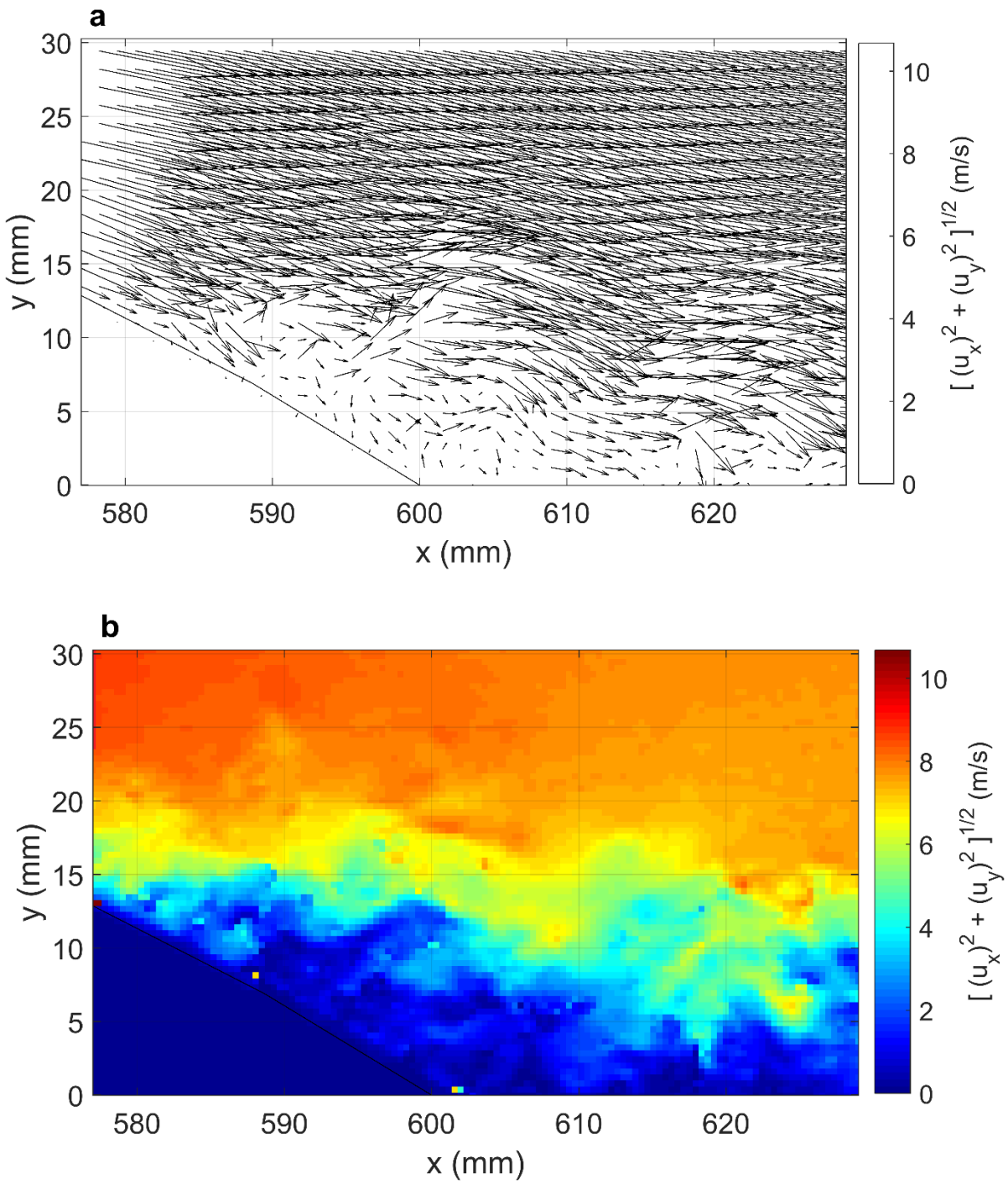

Fig.4.47 (a, b) Instantaneous velocity vector and magnitude fields in the wake region-actuated case, Sine wave, VR=1.85, Angular position: $\phi = 15°, U_\infty = 7\ m/s$.

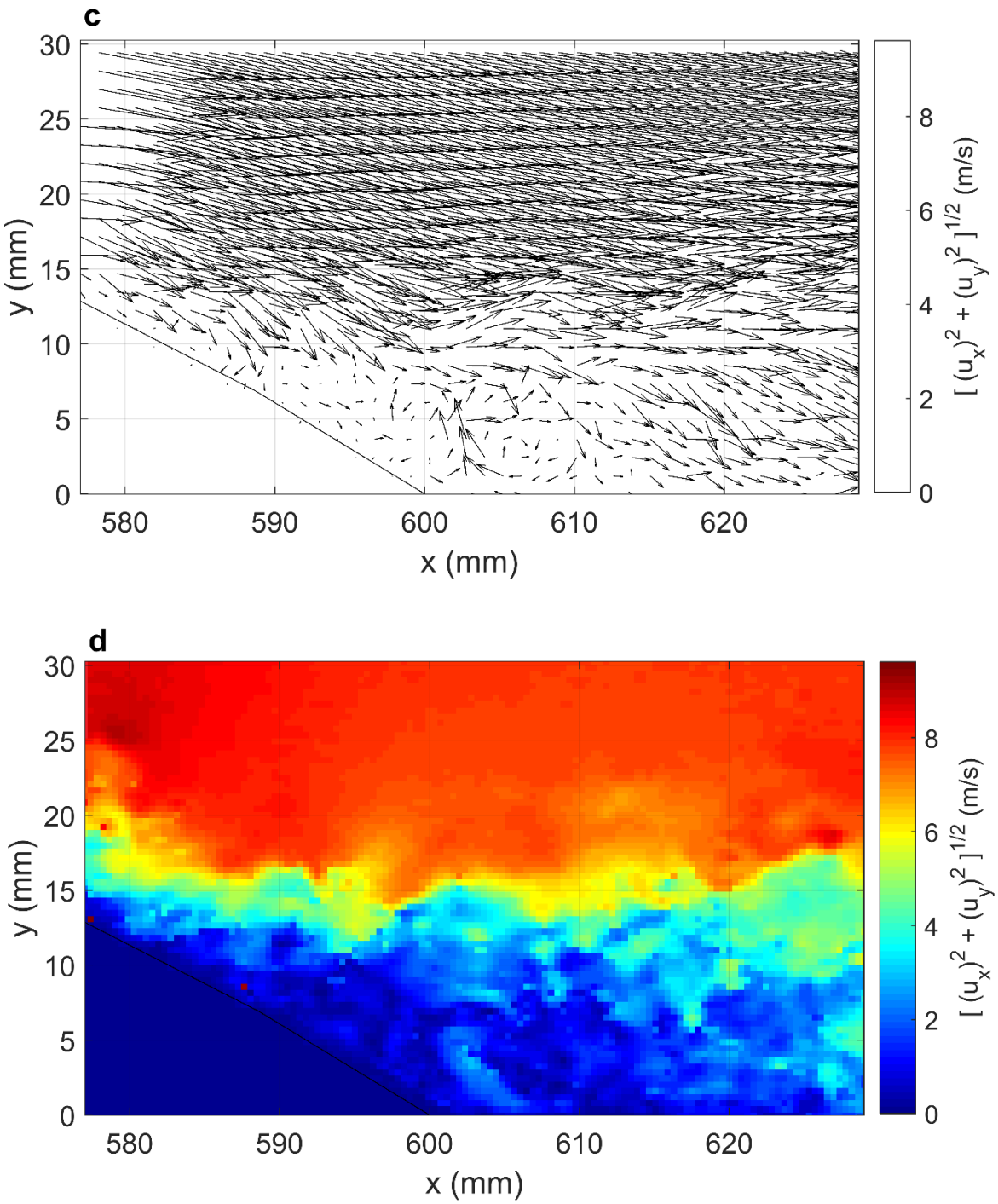

Fig.4.47. (c, d) Instantaneous velocity vectors and magnitude fields in the wake region-actuated case, Sine wave, VR=1.85, Angular position: $\phi = 15°, U_\infty = 7\ m/s$.

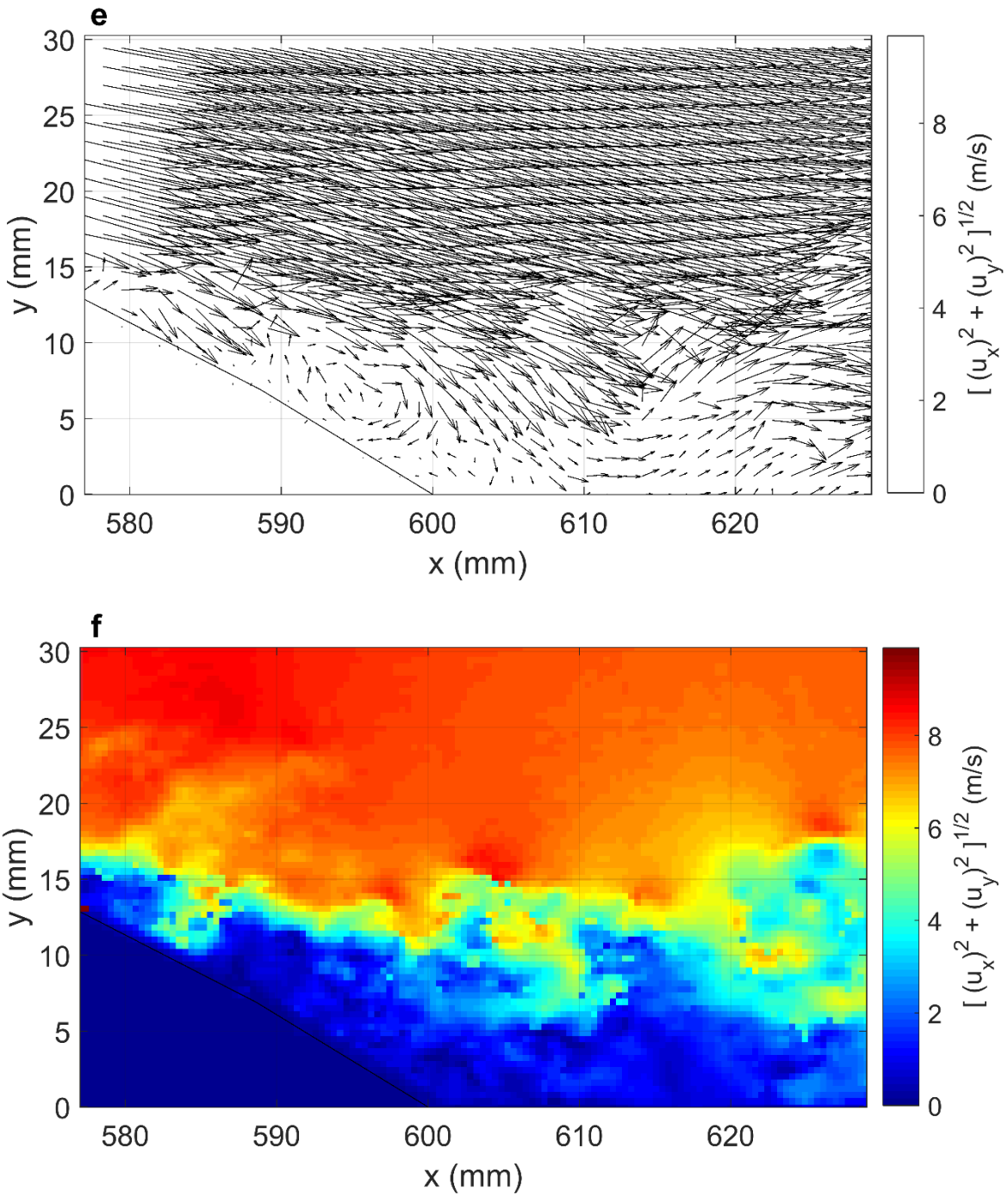

Fig.4.47. (e, f) Instantaneous velocity vectors and magnitude fields in the wake region-actuated case, Sine wave, VR=1.85, Angular position: $\phi = 15°, U_\infty = 7\ m/s$.

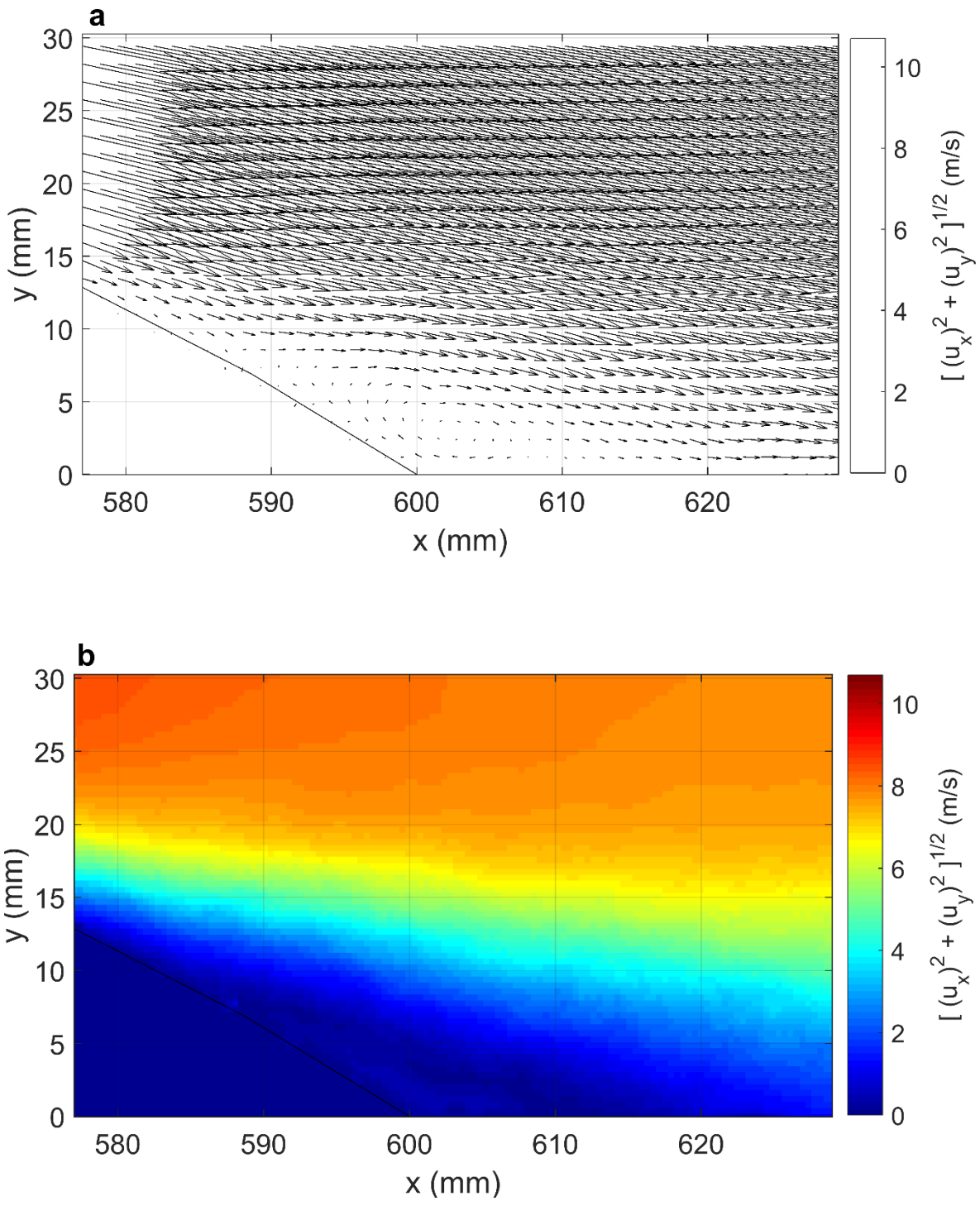

Fig.4.48. (a , b) Average velocity vectors and magnitude fields in the wake region-actuated case, Sine wave, VR=1.85, Angular position: $\phi = 15°, U_\infty = 7\ m/s$.

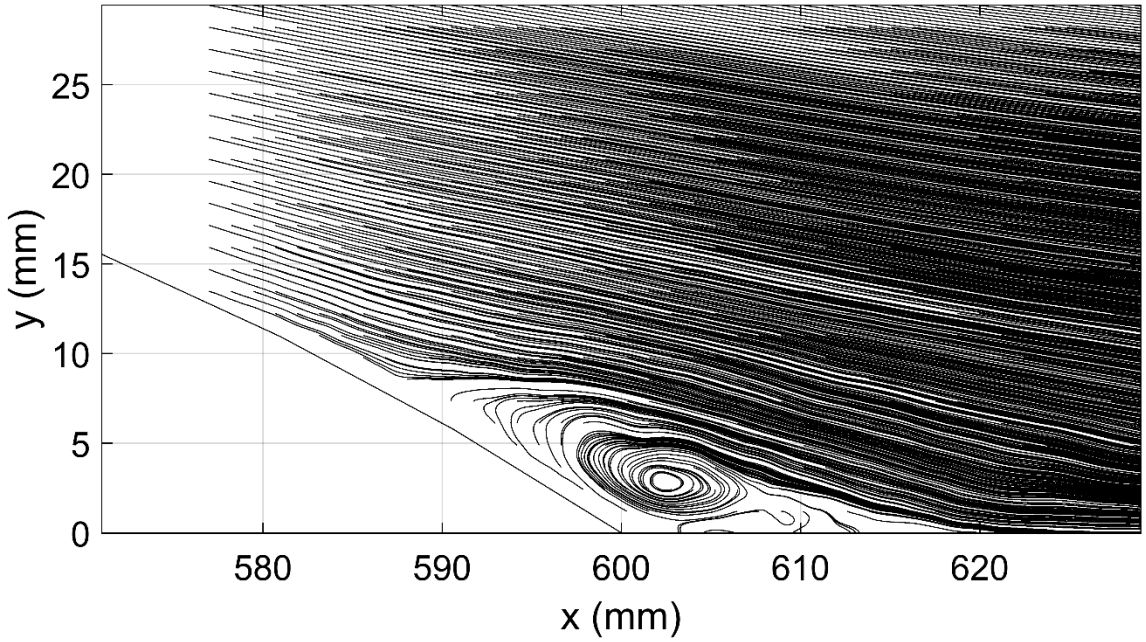

Fig.4.49. Streamlines profile, actuated case, Sine wave, VR=1.85, Angular position: $\phi = 15°, U_\infty = 7\ m/s$.

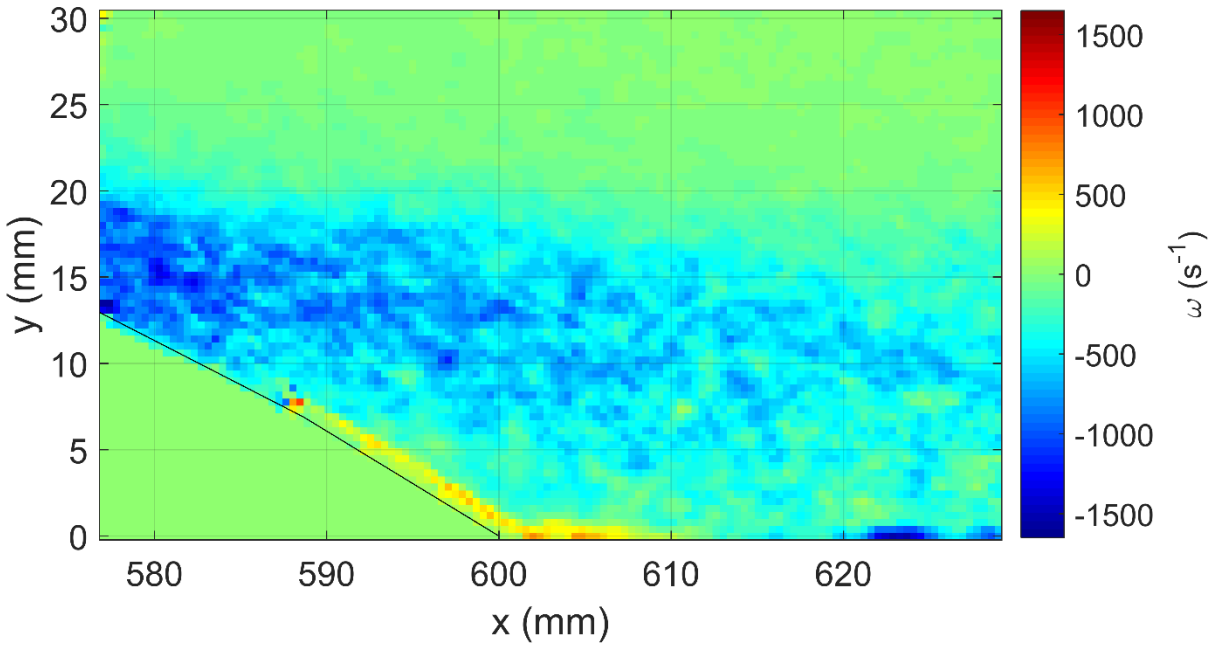

Fig.4.50. Vorticity contour, actuated case, Sine wave, VR=1.85, Angular position: $\phi = 15°, U_\infty = 7\ m/s$.

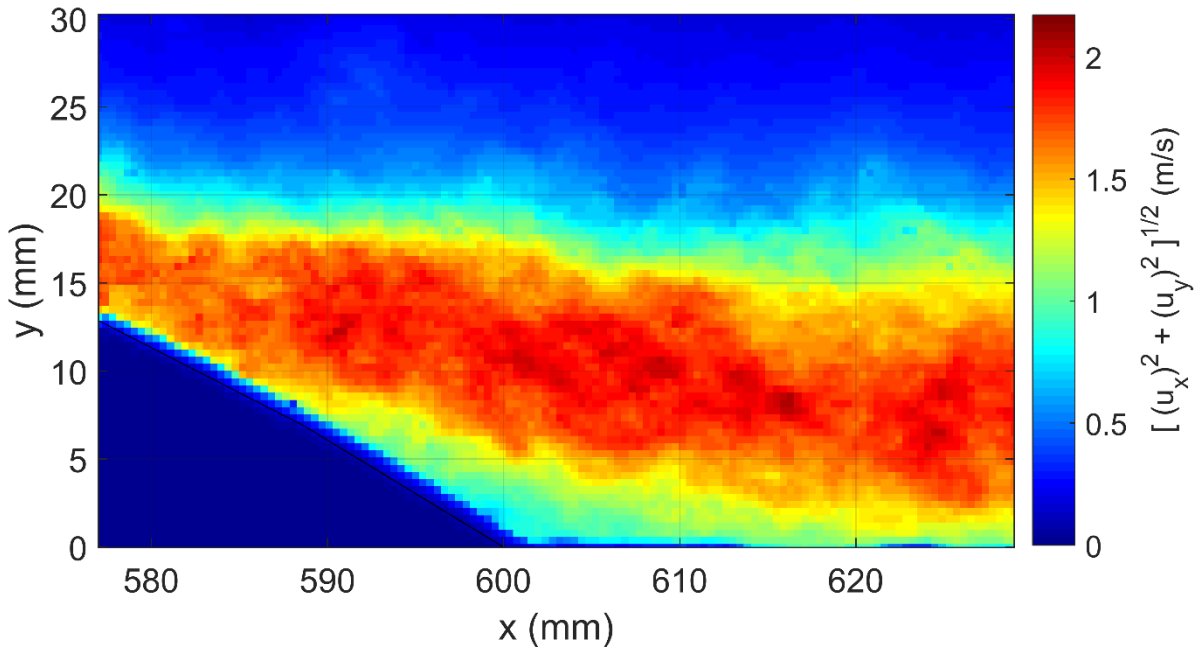

Fig.4.51. RMS velocity contour, actuated case, Sine wave, VR=1.85, Angular position: $\phi = 15°, U_\infty = 7\ m/s$.

Sine Wave, Velocity Ratio of 2.2, Angular Position: $\phi = 15°$,

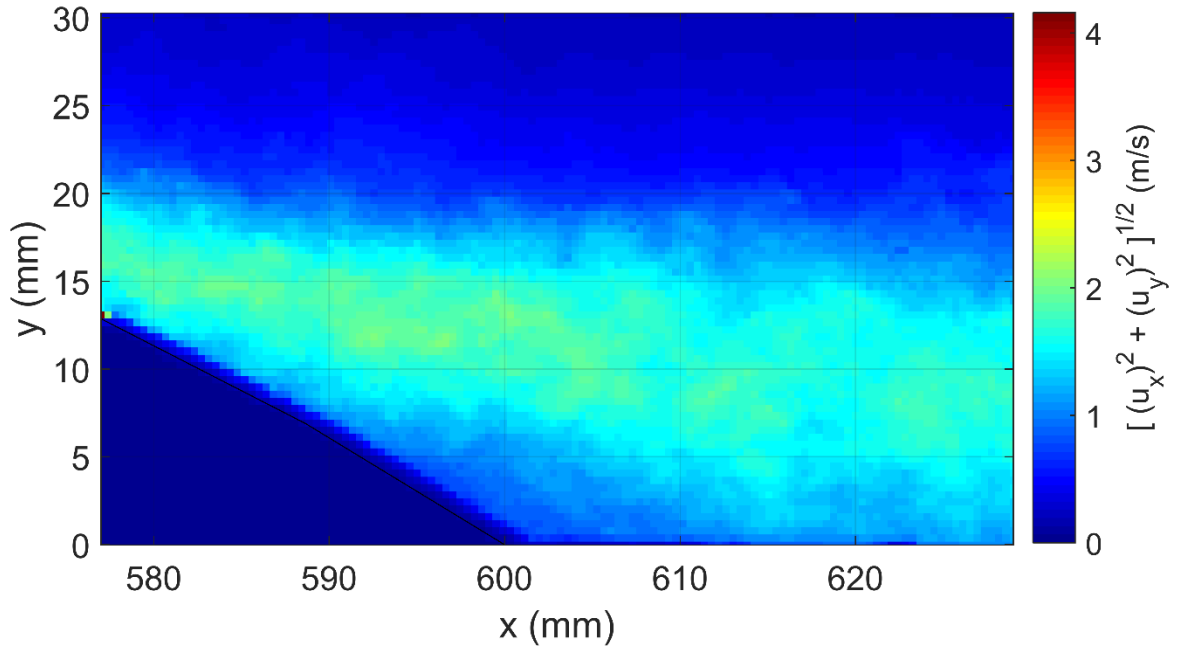

Fig.4.52. RMS velocity contour, actuated case, Sine wave, VR=2.2, Angular position: $\phi = 15°, U_\infty = 7\ m/s$.

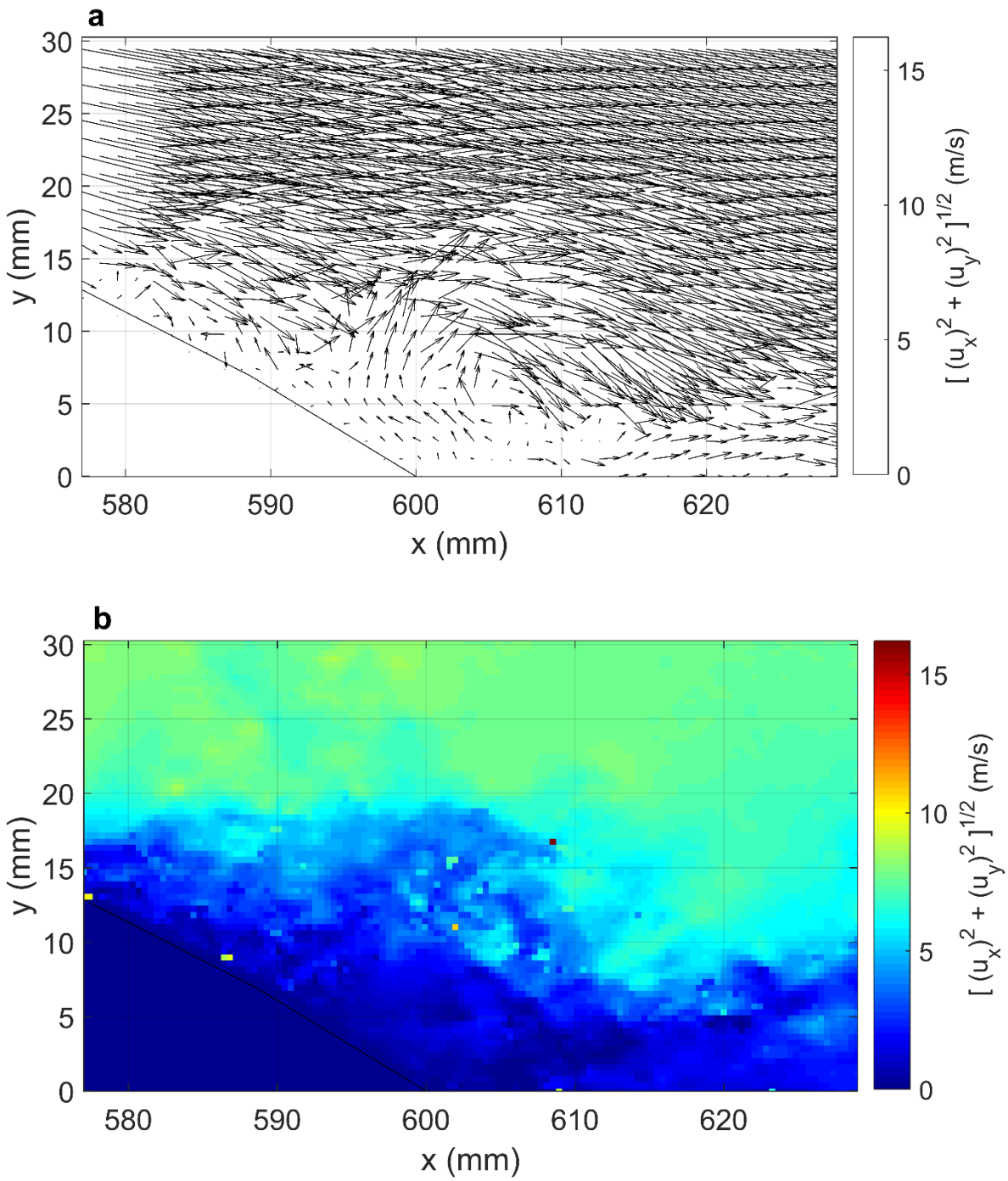

Fig.4.53 (a , b) Instantaneous velocity vector and magnitude fields in the wake region-actuated case, Sine wave, VR=2.2, Angular position: $\phi = 15°, U_\infty = 7\ m/s$.

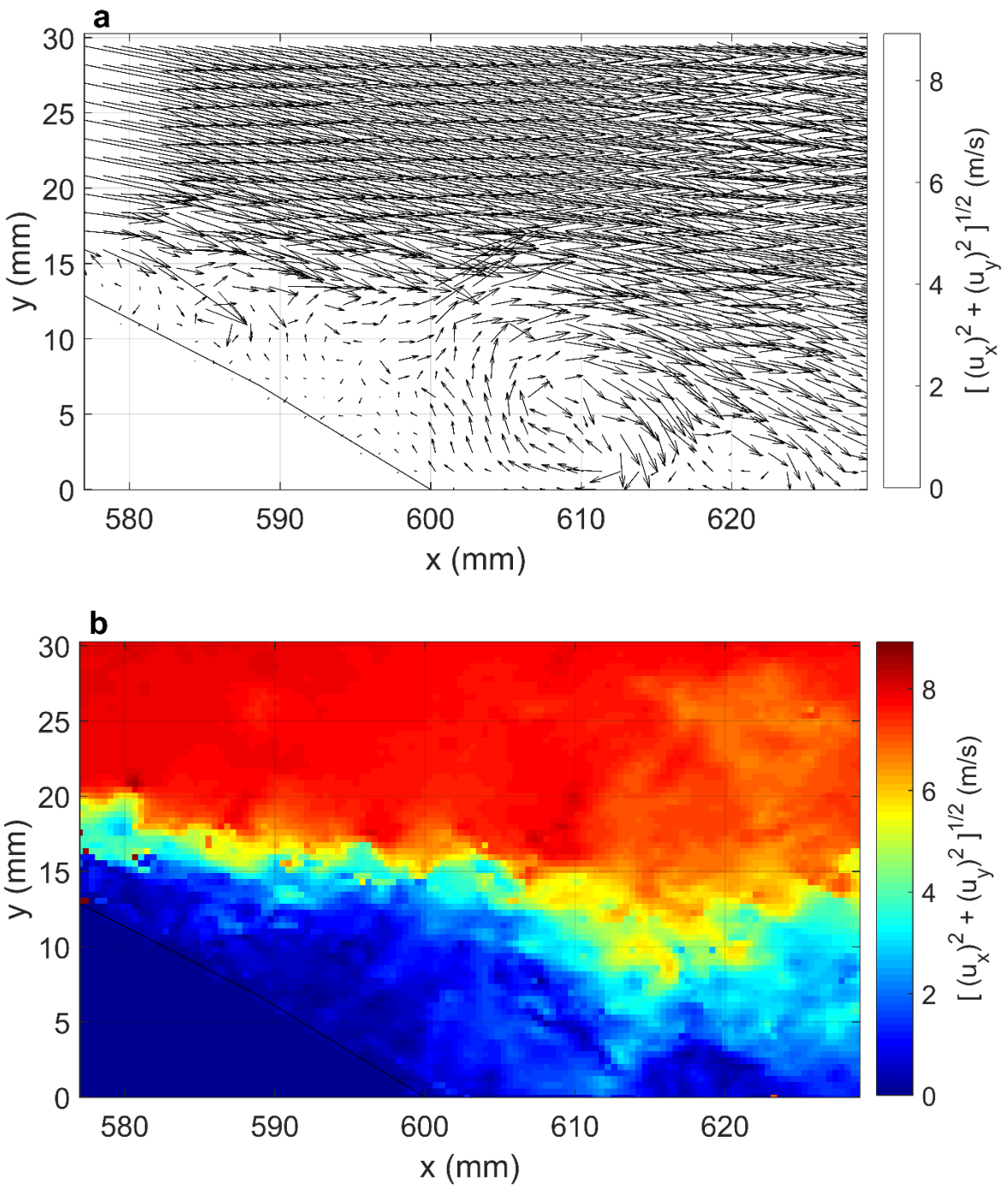

Fig.4.53. (c , d) Instantaneous velocity vector and magnitude fields in the wake region-actuated case, Sine wave, VR=2.2, Angular position: $\phi = 15°, U_\infty = 7\ m/s$.

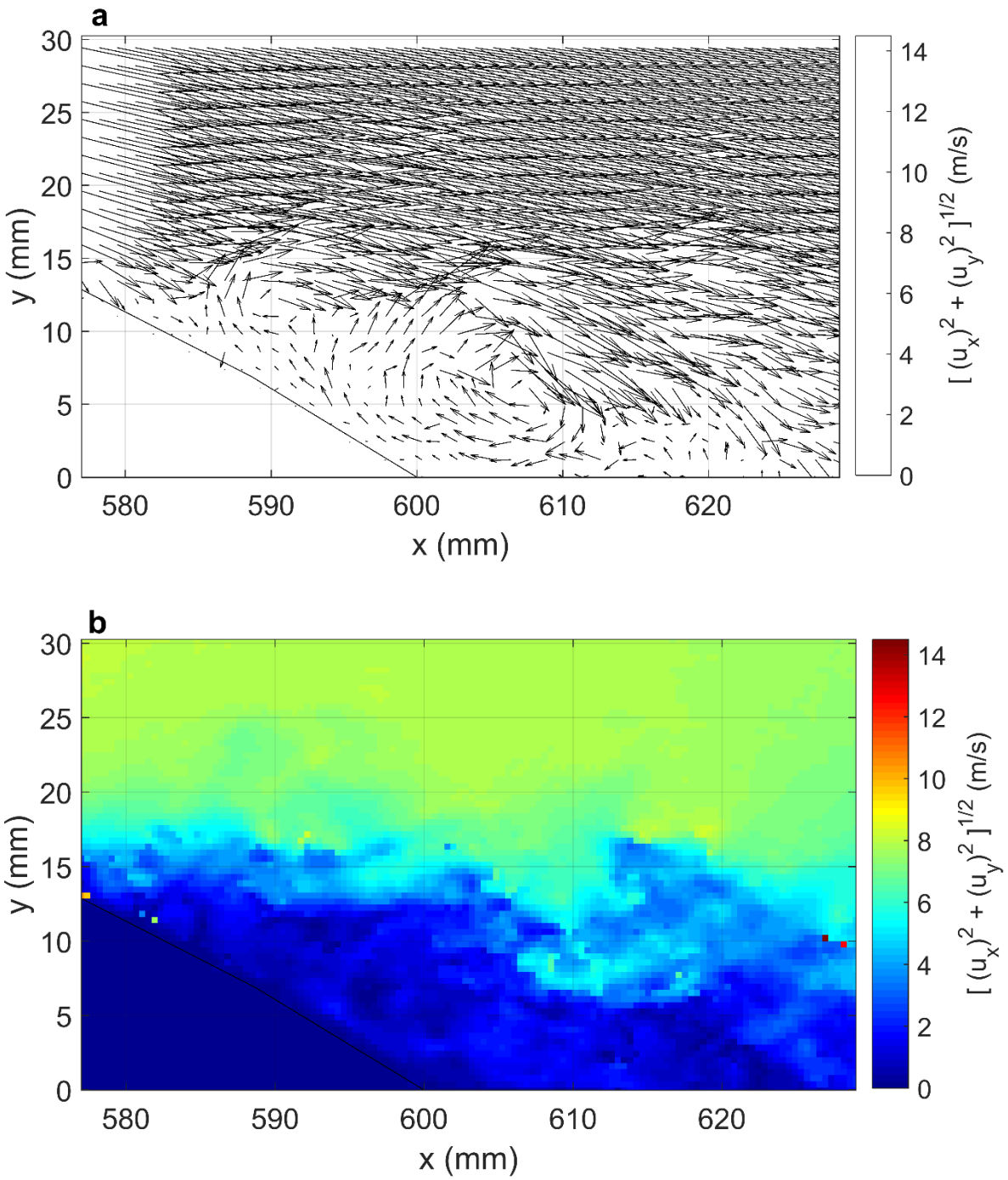

Fig.4.53 (e , f) Instantaneous velocity vectors and magnitude fields in the wake region-actuated case, Sine wave, VR=2.2, Angular position: $\phi = 15°, U_\infty = 7\ m/s$.

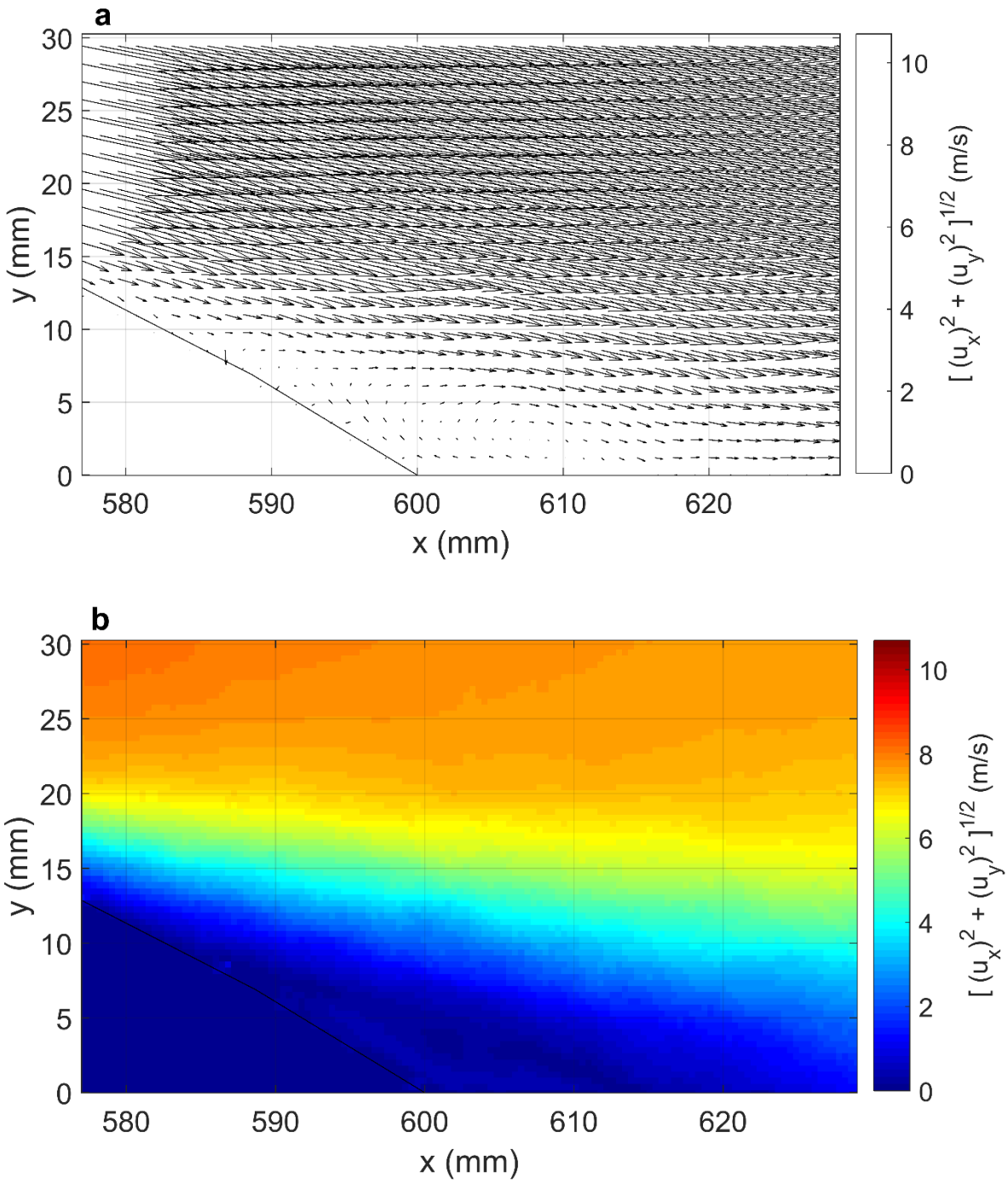

Fig.4.54 (a , b) Average velocity vectors and magnitude fields in the wake region-actuated case, Sine wave, VR=2.2, Angular position: $\phi = 15°, U_\infty = 7\ m/s$.

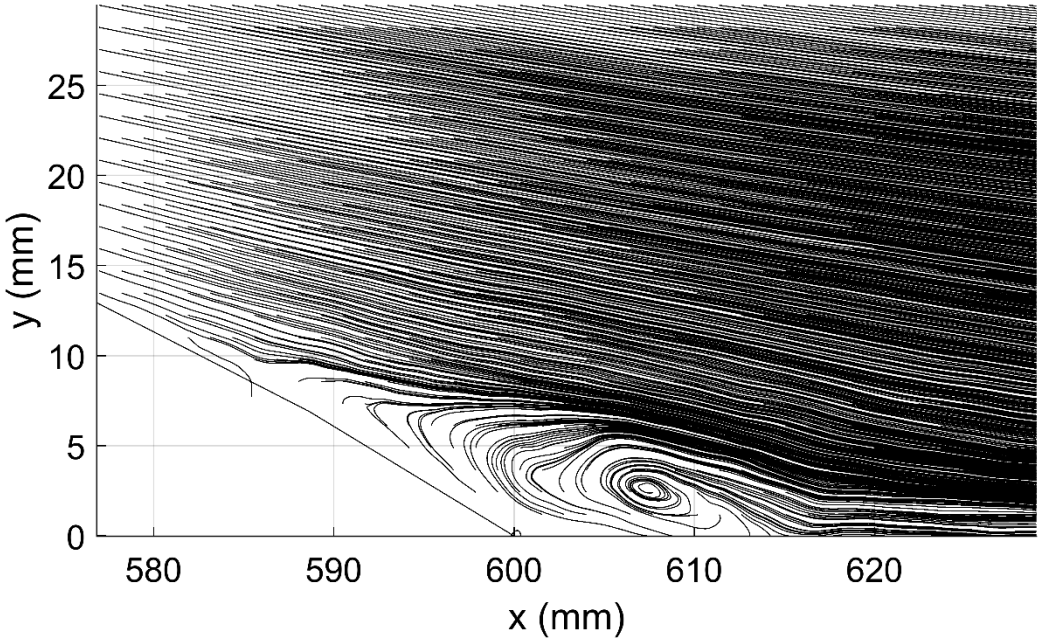

Fig.4.55. Streamlines profile, actuated case, Sine wave, VR=2.2, Angular position: $\phi = 15°, U_\infty = 7\ m/s$.

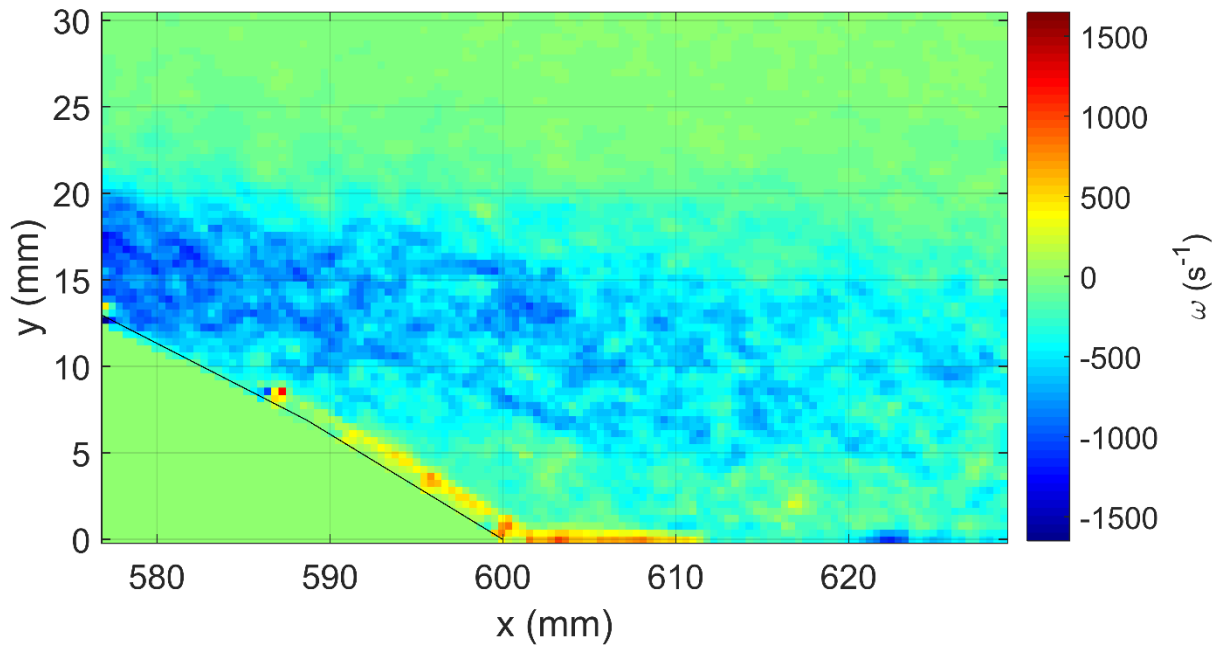

Fig .4.56. Vorticity contour, actuated case, Sine wave, VR=2.2, Angular position: $\phi = 15°, U_\infty = 7\ m/s$.

The investigation of the impact of velocity ratio VR on the location of separation and reattachment points at constant angular position of $\phi = 15^{\circ}$ shows that the best performance of the synthetic jet actuators is achieved at velocity ratio of 1.85. The details will be discussed in the next chapter.

In the last phase of study, the effects of Square wave on the separation control is investigated for selected values of VR including 1.5, 1.85 and 2.2 while the angular position of actuators was kept constant at $\phi = 15^{\circ}$.

The successful performance of Square wave to suppress the velocity fluctuations in the wake region as shown in earlier section (Fig.4.26) was the main motivation to also investigate the effect of Square wave on the flow characteristics in the wake region. The impact of velocity ratio on the performance of synthetic jet actuators while the piezo electric diaphragms are derived by Square wave is explained in the next chapter.

The profiles of 3 selected samples of instantaneous velocity vectors and magnitudes fields as well as the profile of average velocity vector and magnitude filed, streamlines profiles, vorticity contours profile and RMS velocity profile for velocity ratio of 1.5 at angular position of $\phi = 15^{\circ}$ with Square wave as driving waveform are shown in Appendix D in Figs.D.26-D.30, respectively.

The profiles of 3 selected samples of instantaneous velocity vectors and magnitudes fields as well as the profile of average velocity vector and magnitude filed, streamlines profiles, vorticity contours profile and RMS velocity profile for velocity ratio of 1.85 at angular position of $\phi = 15^{\circ}$ with Square wave as driving waveform are shown in Figs.4.57-4.61, respectively.

Square Wave, Velocity Ratio of 1.85, Angular Position: $\phi = 15°$,

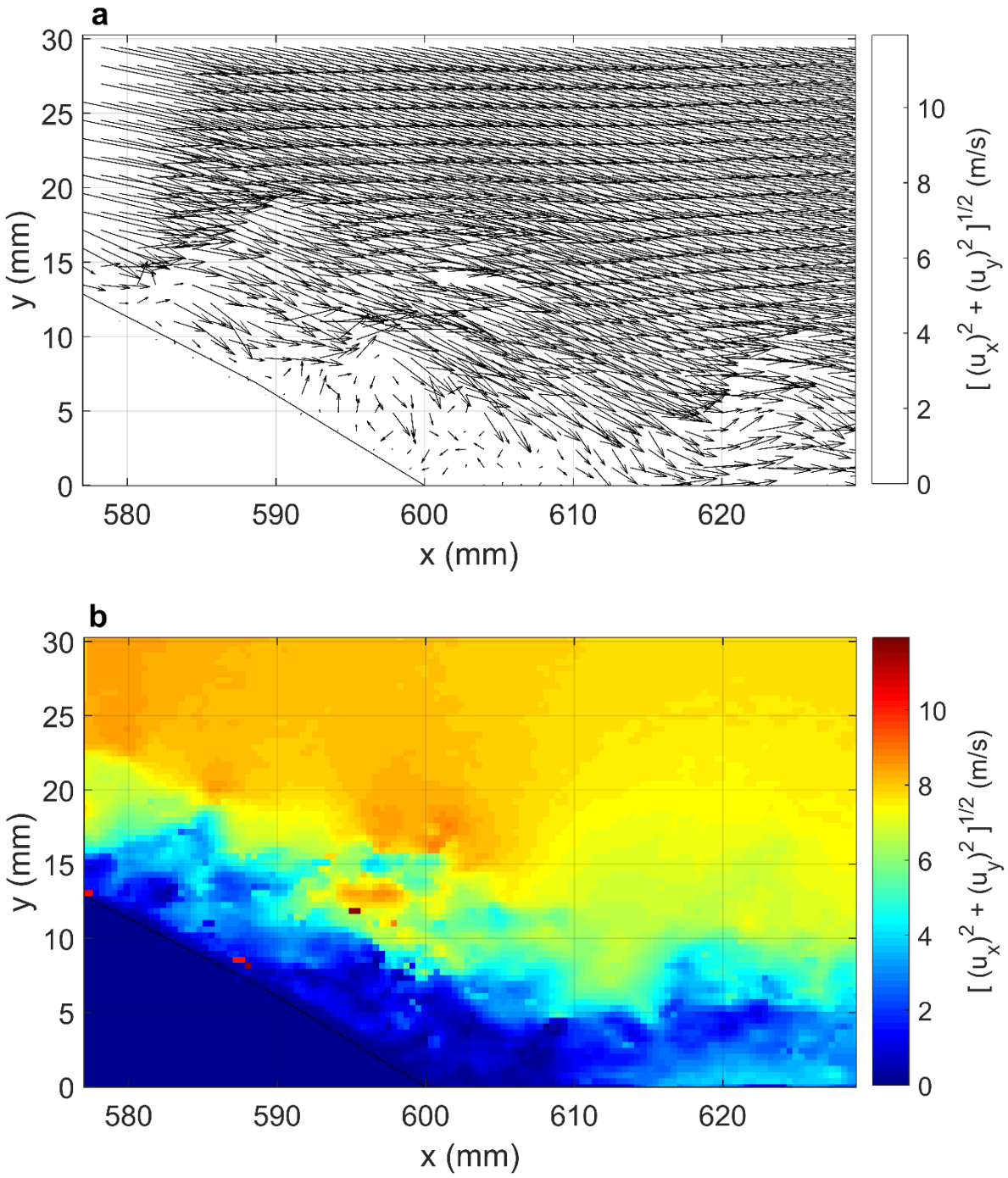

Fig.4.57 (a , b) Instantaneous velocity vector and magnitude fields in the wake region-actuated case, Square wave, VR=1.85, Angular position: $\phi = 15°, U_\infty = 7\ m/s$.

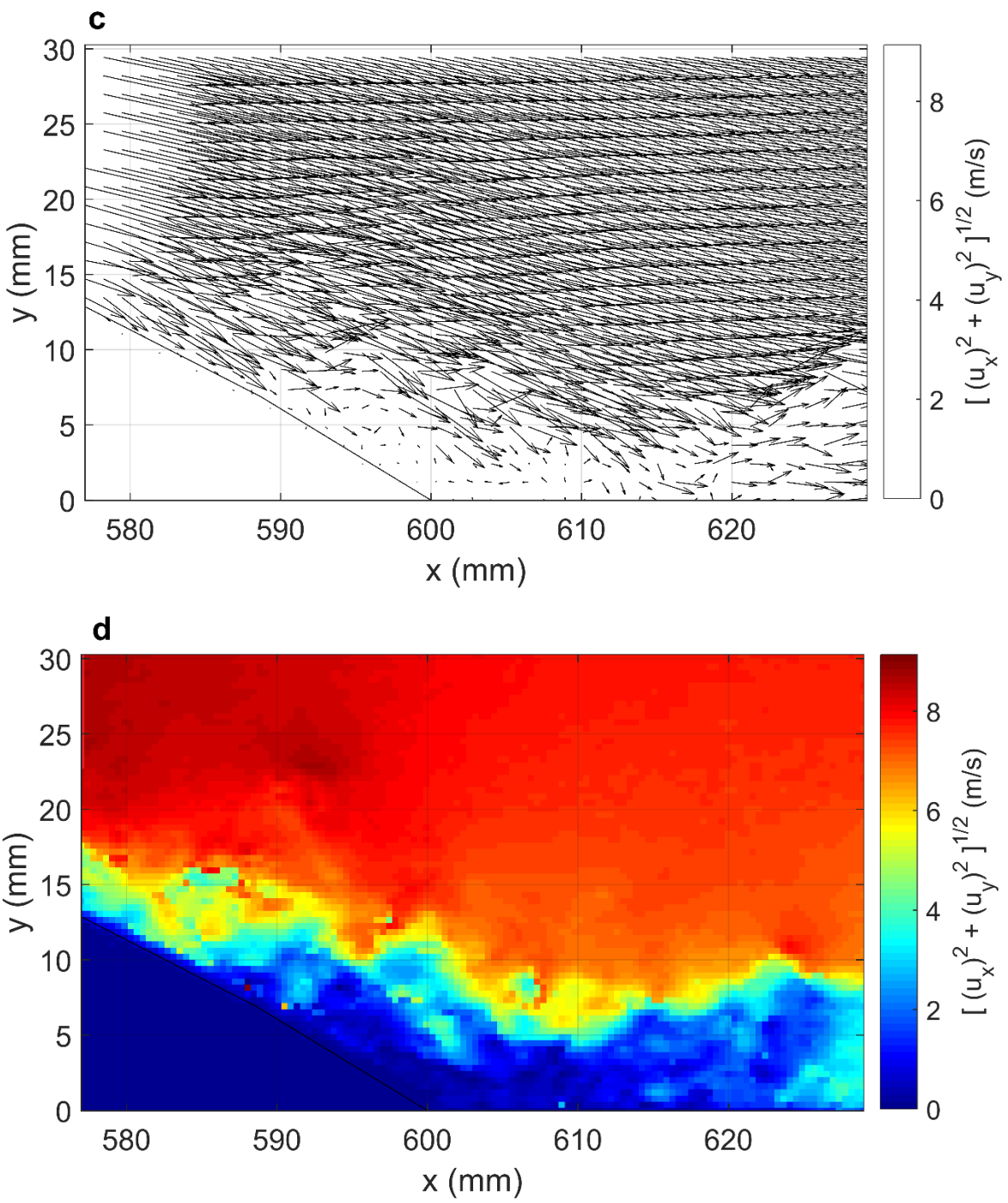

Fig.4.57. (c , d) Instantaneous velocity vector and magnitude fields in the wake region-actuated case, Square wave, VR=1.85, Angular position: $\phi = 15°, U_\infty = 7\ m/s$.

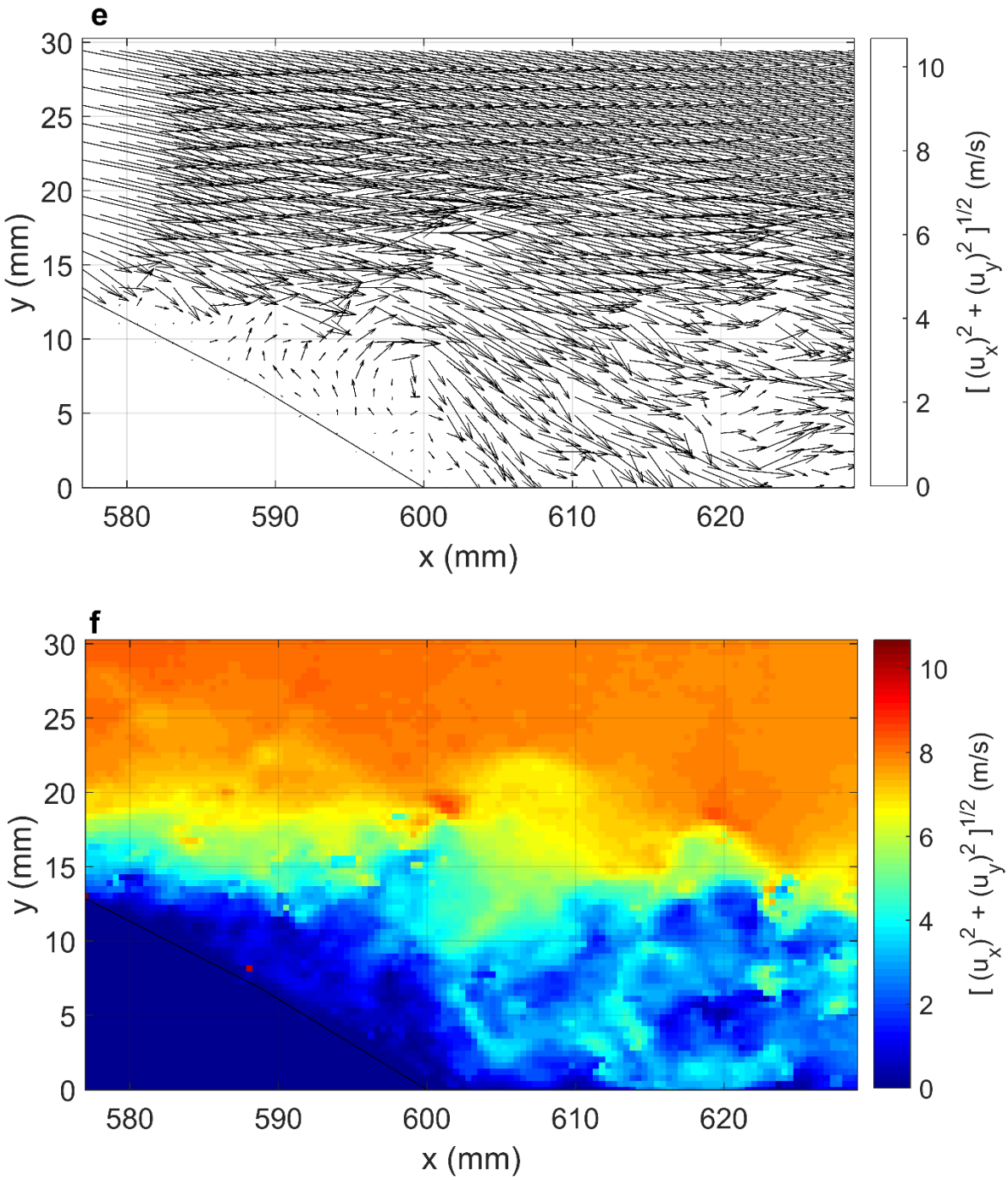

Fig.4.57. (e , f) Instantaneous velocity vector and magnitude fields in the wake region-actuated case, Square wave, VR=1.85, Angular position: $\phi = 15°, U_\infty = 7\ m/s$.

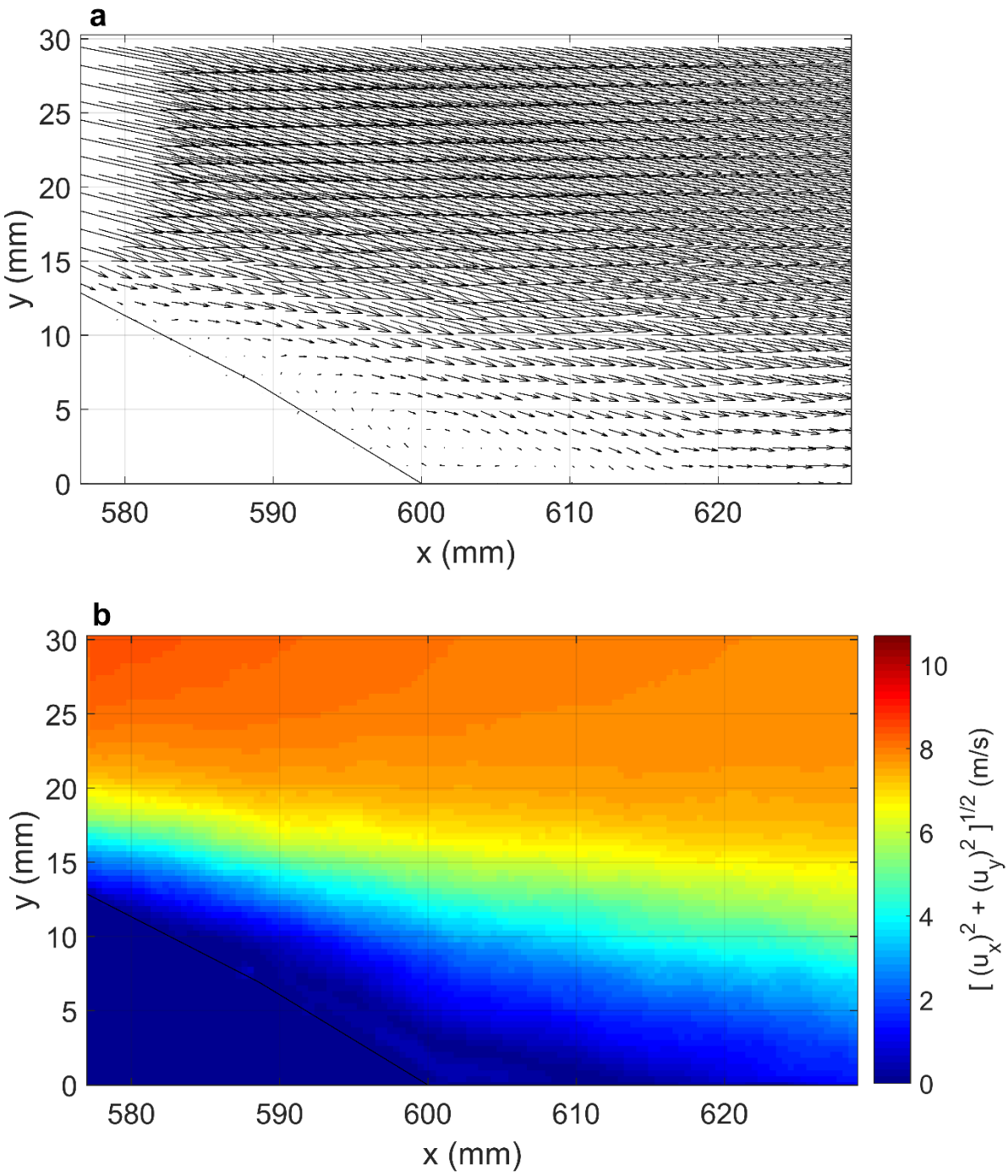

Fig.4.58. (a , b) Average velocity vectors and magnitude fields in the wake region-actuated case, Square wave, VR=1.85, Angular position: $\phi = 15°, U_\infty = 7\ m/s$.

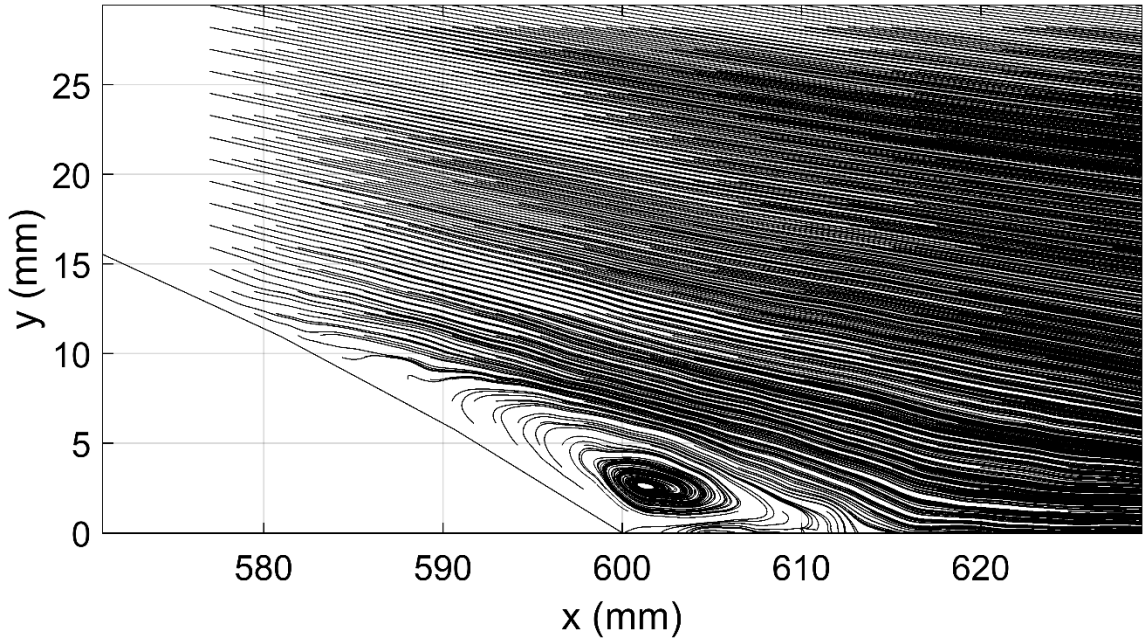

Fig.4.59. Streamlines profile- actuated case, Square wave, VR=1.85, Angular position: $\phi = 15°, U_\infty = 7\ m/s$.

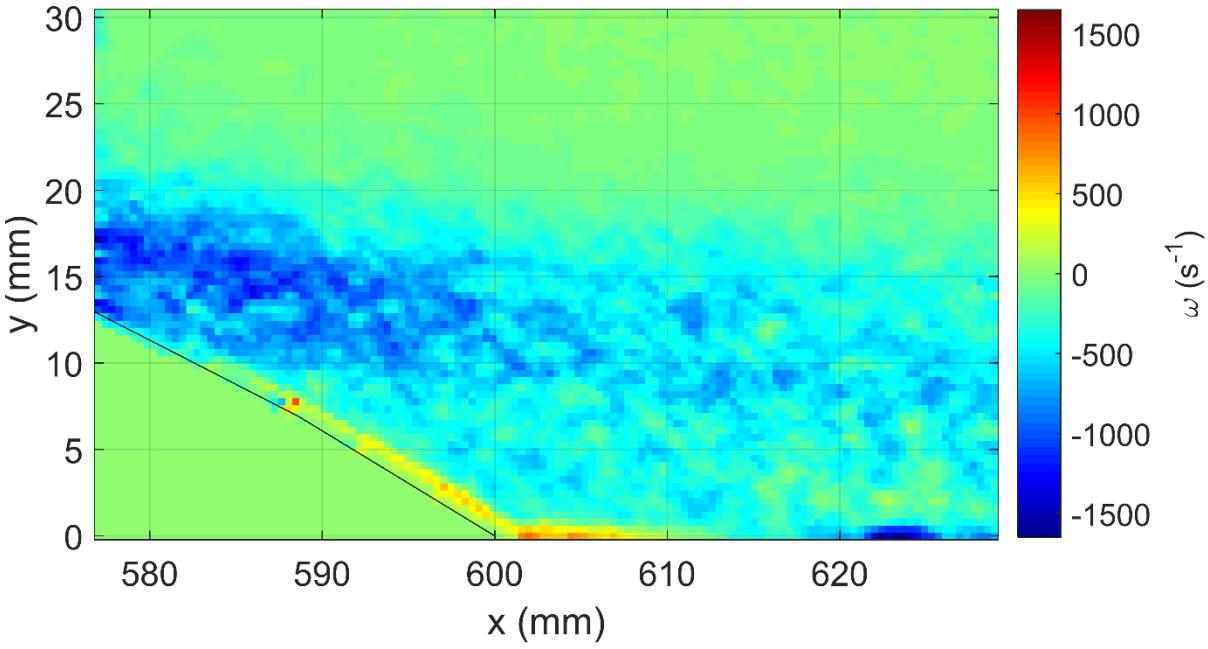

Fig.4.60. Vorticity contour- actuated case, Square wave, VR=1.85, Angular position: $\phi = 15°, U_\infty = 7\ m/s$.

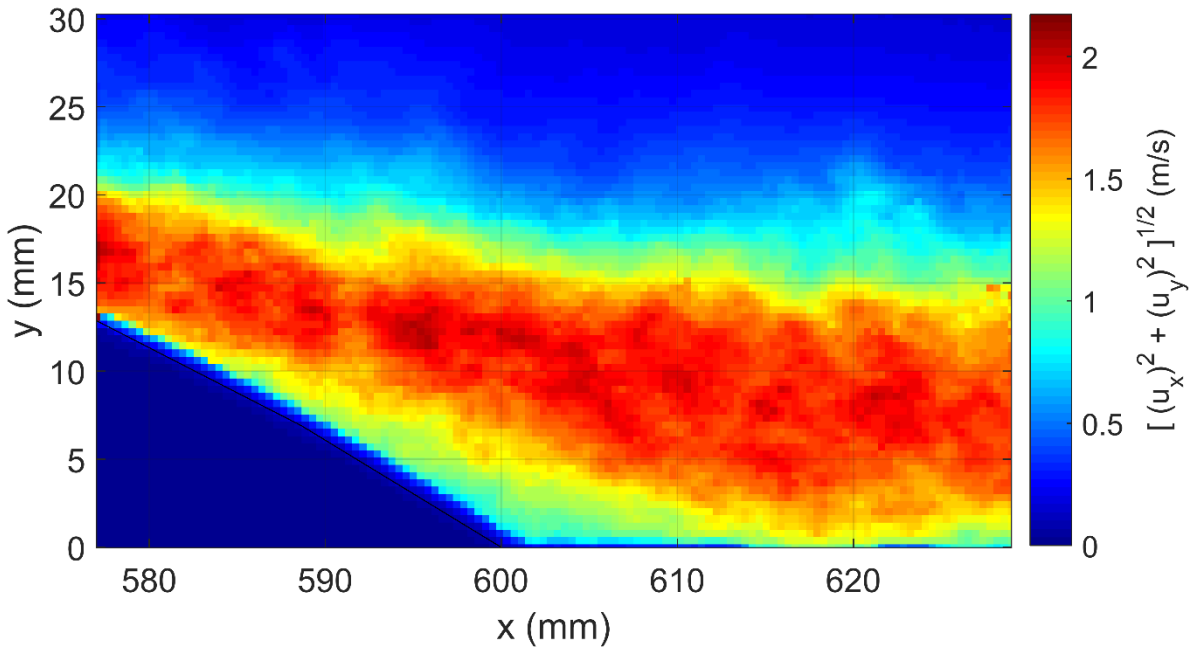

Fig.4.61. RMS velocity contour, actuated case, Square wave, VR=1.85, Angular position: $\phi = 15°, U_\infty = 7\ m/s$.

The profiles of 3 selected samples of instantaneous velocity vectors and magnitudes fields as well as the profile of average velocity vector and magnitude filed, streamlines profiles, vorticity contours profile and RMS velocity profile for velocity ratio of 2.2 at angular position of $\phi = 15^{\circ}$ with Square wave as driving waveform are shown by Figs.4.62-4.66, respectively.

Square Wave, $\phi = 15°$, Velocity Ratio of 2.2

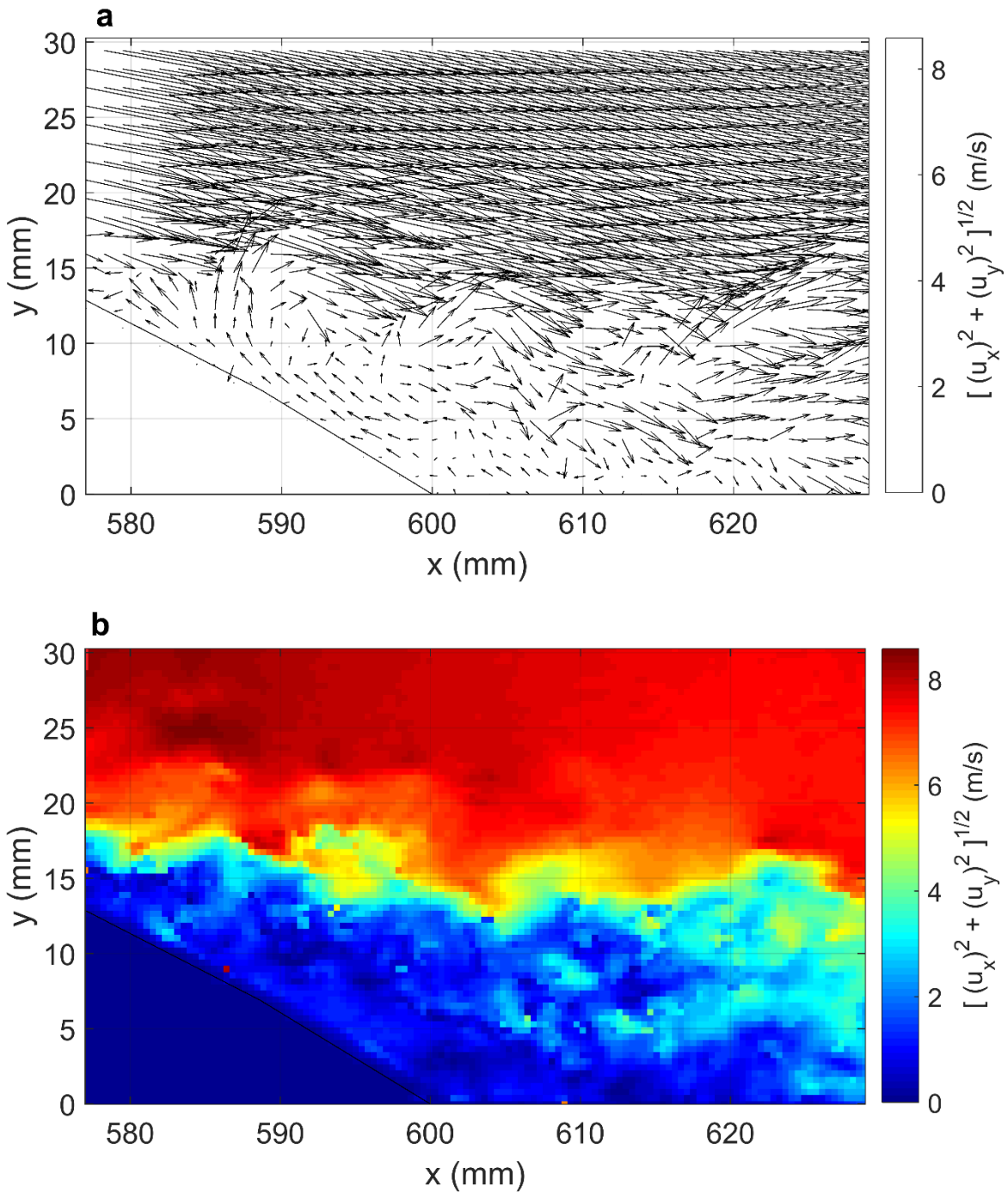

Fig.4.62. (a , b) Instantaneous velocity vector and magnitude fields in the wake region-actuated case, Square wave, VR=2.2, Angular position: $\phi = 15°, U_\infty = 7\ m/s$.

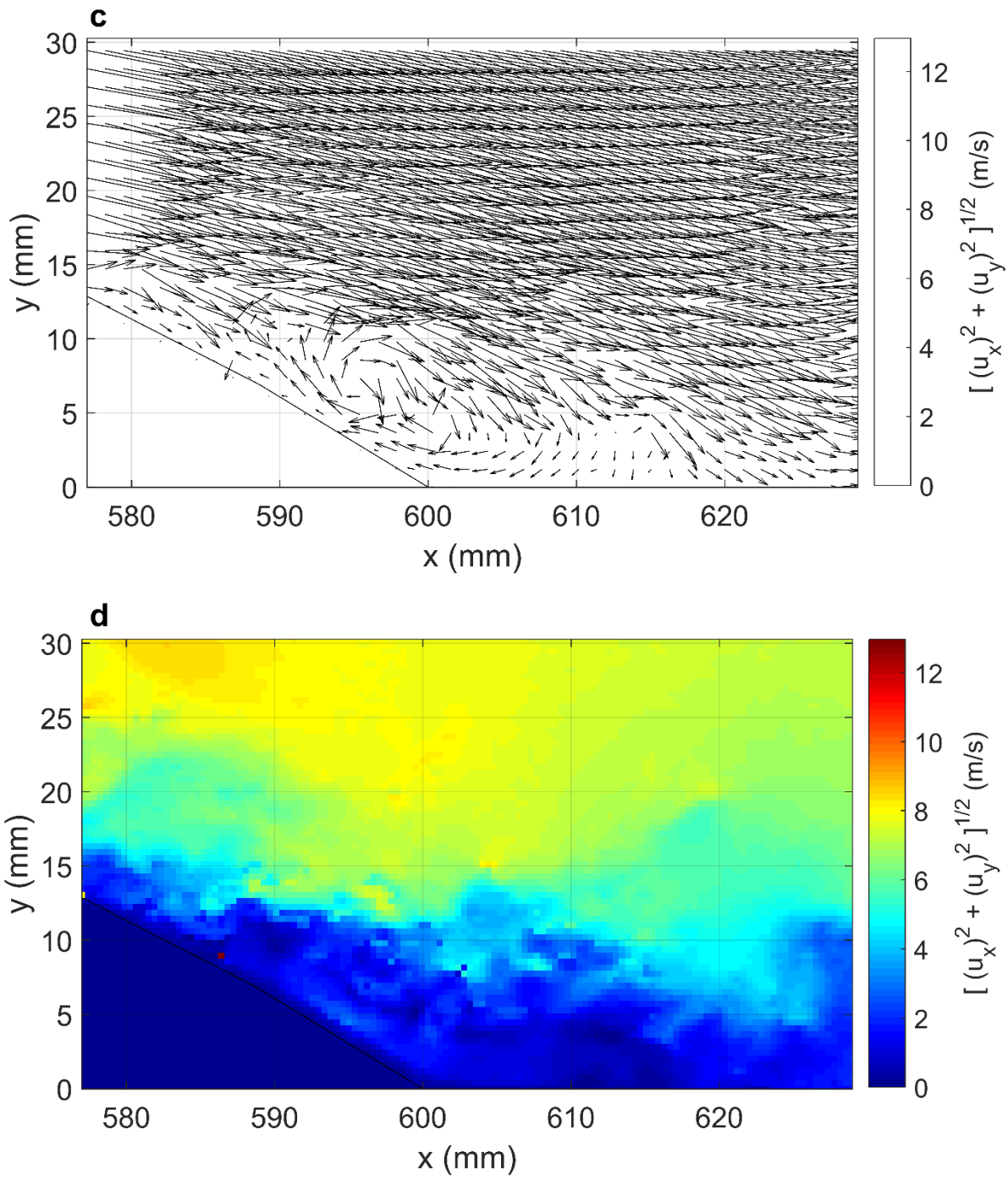

Fig.4.62. (c , d) Pairs of instantaneous velocity vector and magnitude fields in the wake region- actuated case, Square wave, VR=2.2, Angular position: $\phi = 15°, U_\infty = 7\ m/s$.

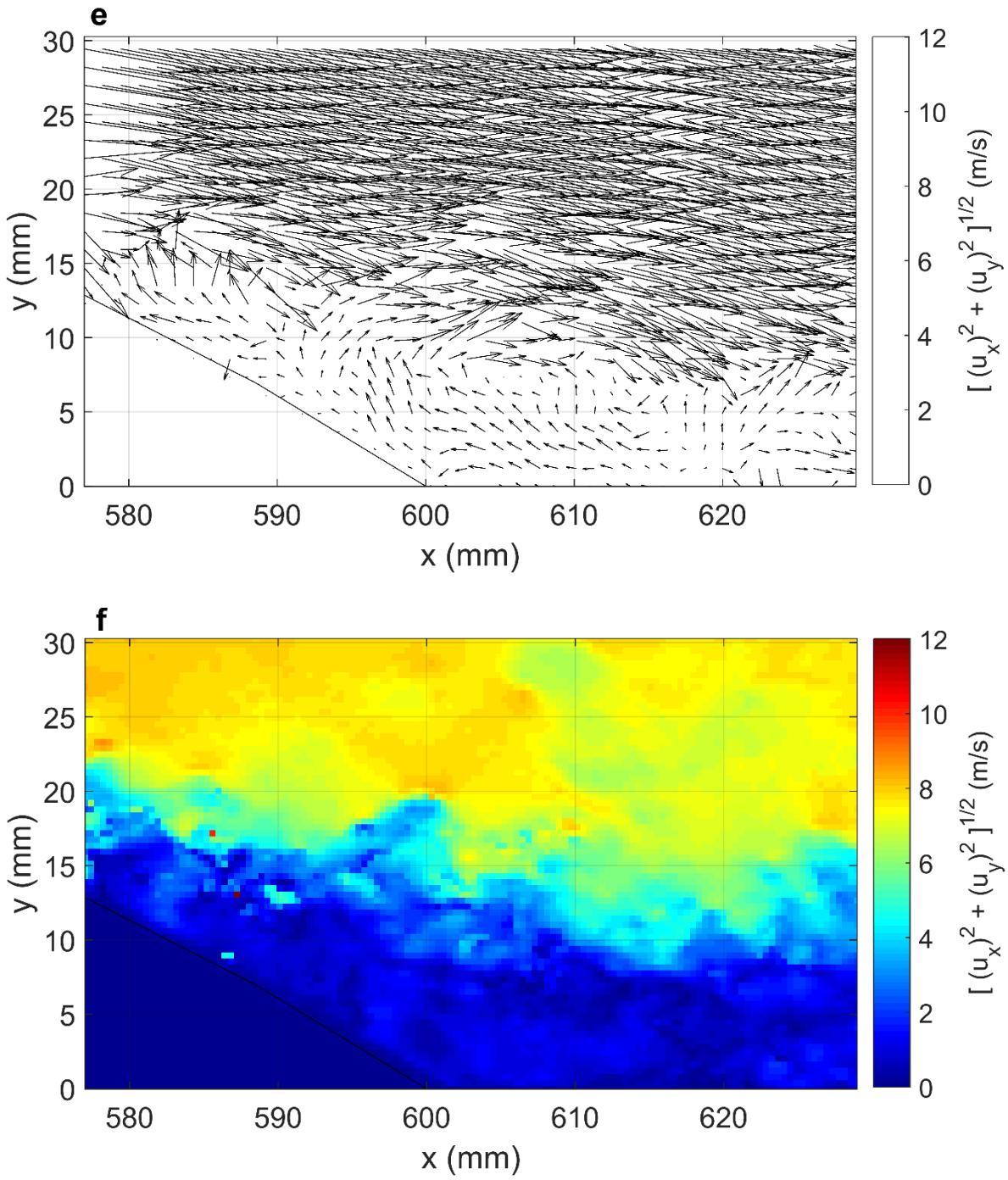

Fig.4.62. (e , f) Instantaneous velocity vector and magnitude fields in the wake region-actuated case, Square wave, VR=2.2, Angular position: $\phi = 15°, U_\infty = 7\ m/s$.

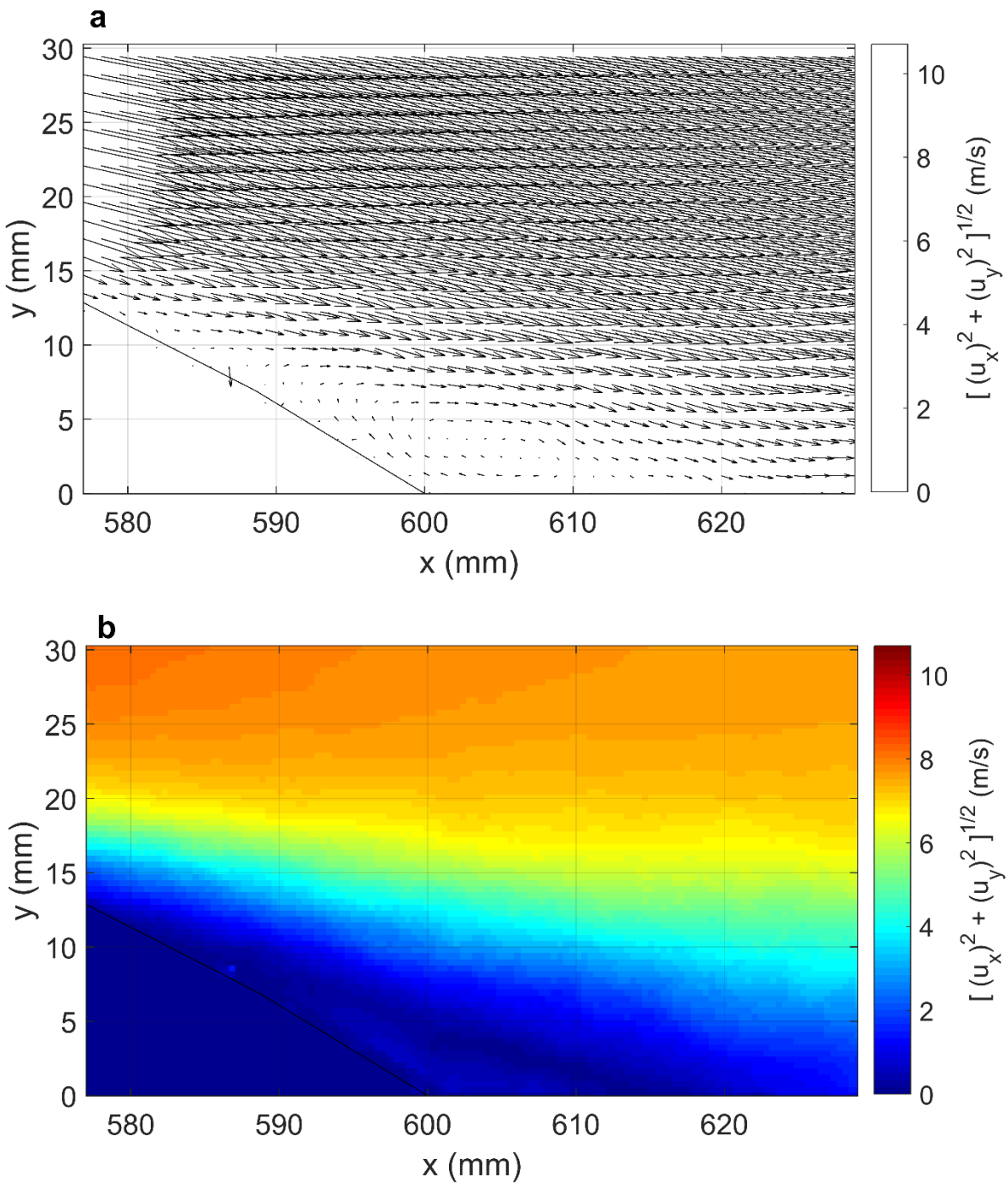

Fig.4.63. (a , b) Average velocity vectors and magnitude fields in the wake region-actuated case, Square wave, VR=2.2, Angular position: $\phi = 15°, U_\infty = 7\ m/s$.

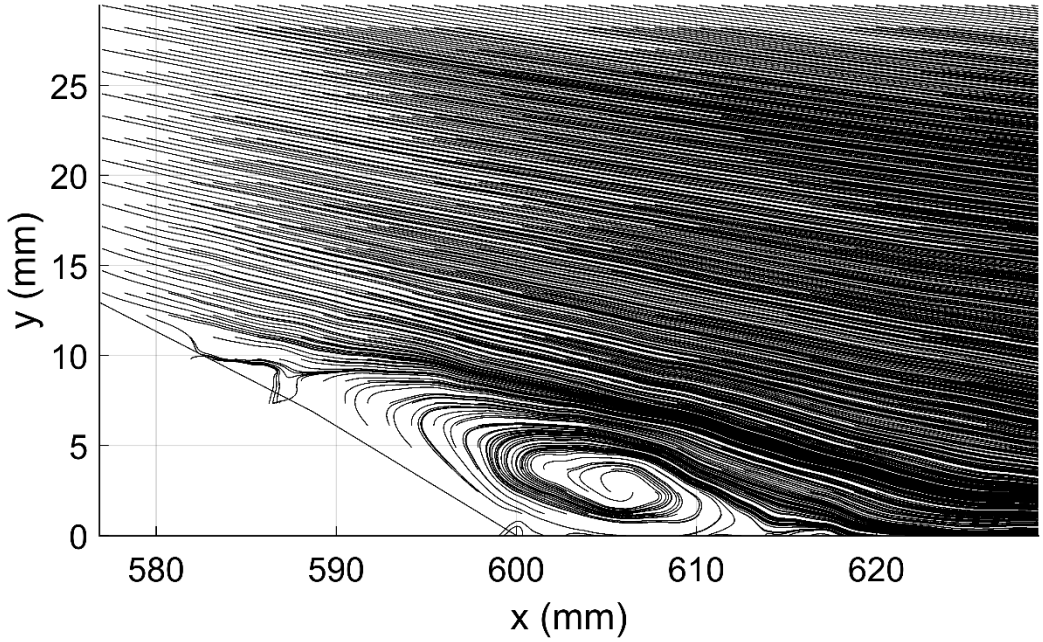

Fig.4.64. Streamlines profile- actuated case, Square wave, VR=2.2, Angular position: $\phi = 15°, U_\infty = 7\ m/s$.

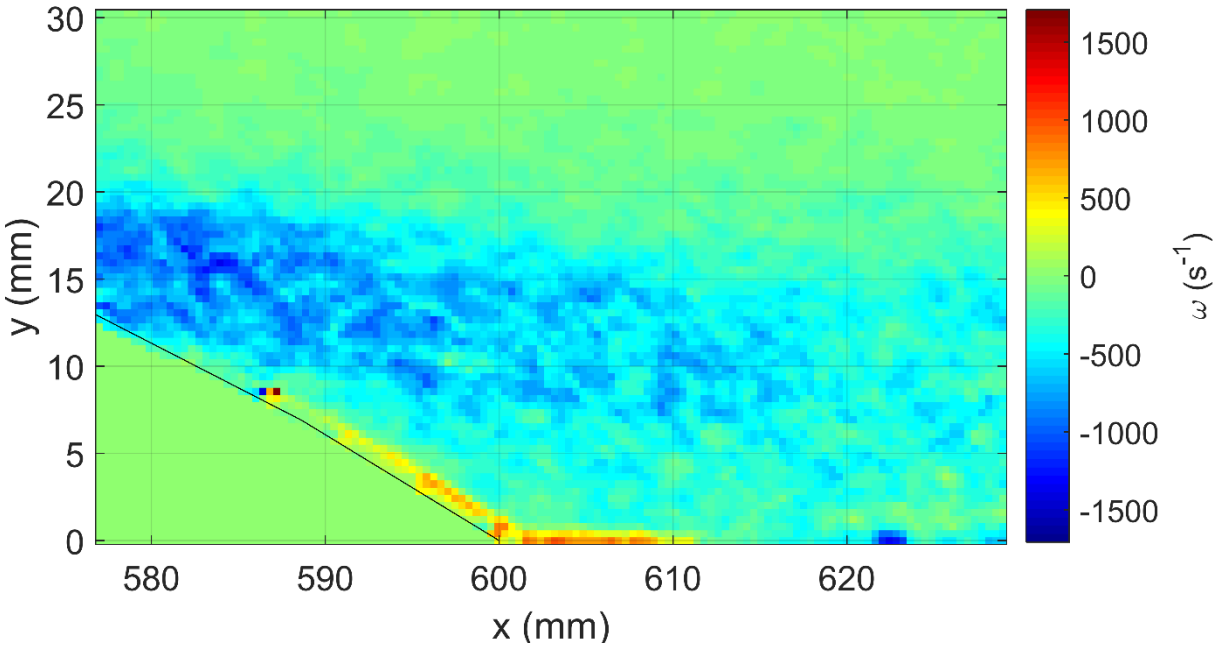

Fig.4.65. Vorticity contour- actuated case, Square wave, VR=2.2, Angular position: $\phi = 15°, U_\infty = 7\ m/s$.

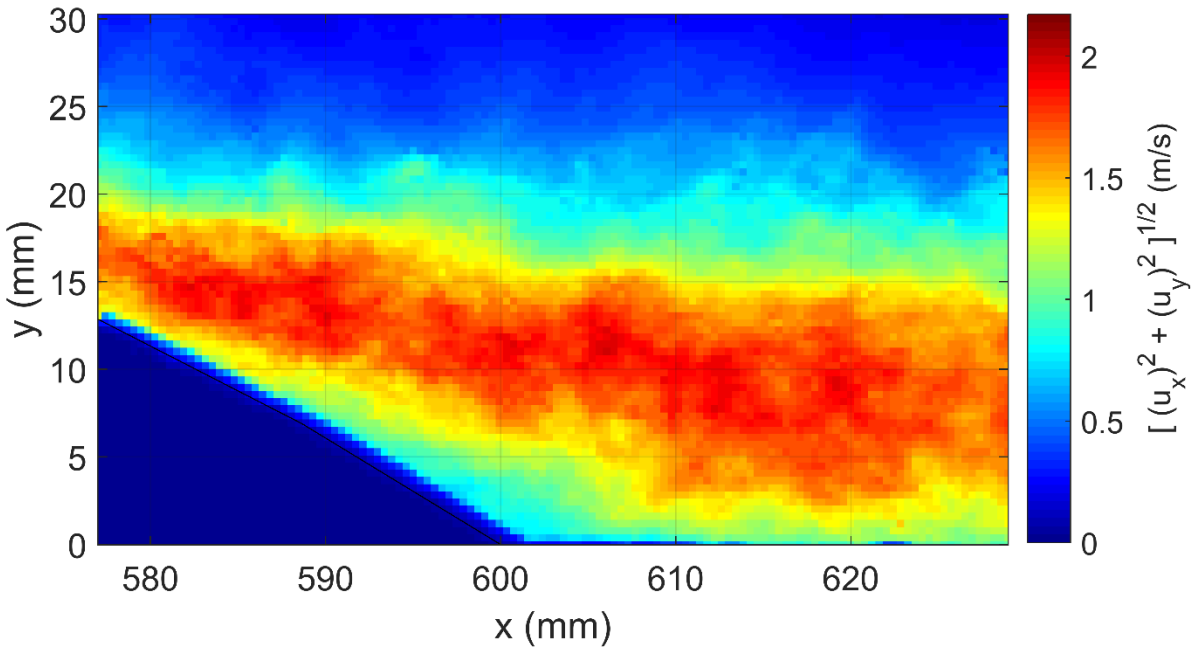

Fig.4.66. RMS velocity contour- actuated case, Square wave, VR=2.2, Angular position: $\phi = 15°, U_\infty = 7\ m/s$.

4.5- Numerical Results

In this section, the results of simulations of single actuator in quiescent conditions (no cross–flow) and flow separation over the hump model for both unactuated and actuate cases are presented.

4.5.1 Unsteady State – Unactuated Case

It was observed that the code running for less than two residence times (0.28 second) is enough for the solution to be stable from statistical point of view but the time-averaged results is shown here over time interval of 0-0.28 seconds. The velocity boundary layer profile as well as the turbulent kinetic energy profile at X= 0.3 m (before the flow reaches the hump) are depicted by Figs.4.67 and 4.68, respectively.

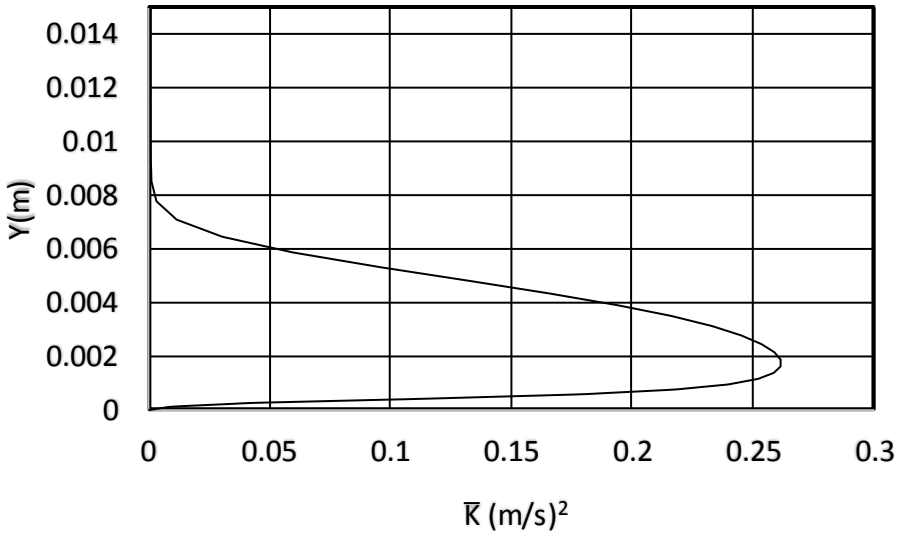

Fig.4.67. Average turbulent kinetic energy at X =0.3 m, $U_\infty = 7m/s$.

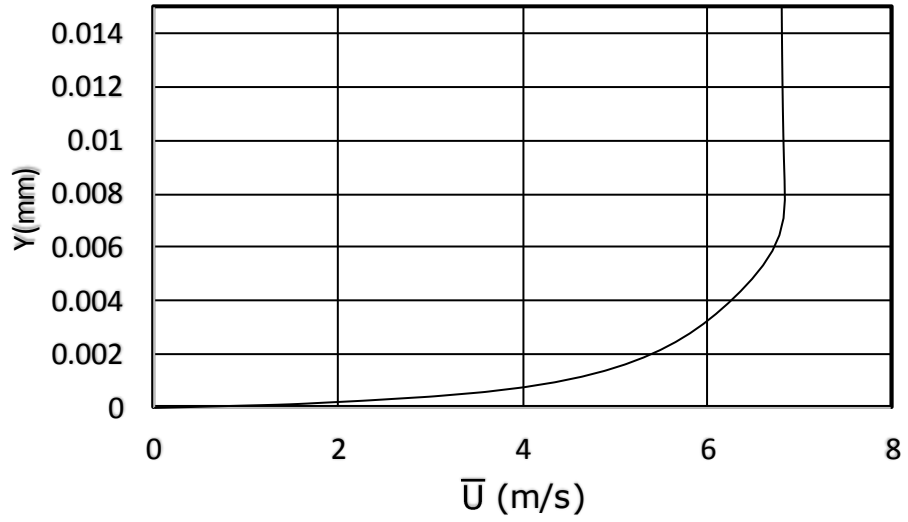

Fig.4.68. Velocity profile in the boundary layer at X =0.3 m, $U_\infty = 7m/s$.

The profiles of turbulent kinetic energy, velocity and pressure contours as well as velocity field and streamlines are presented by Figs.4.69 -4.73, respectively.

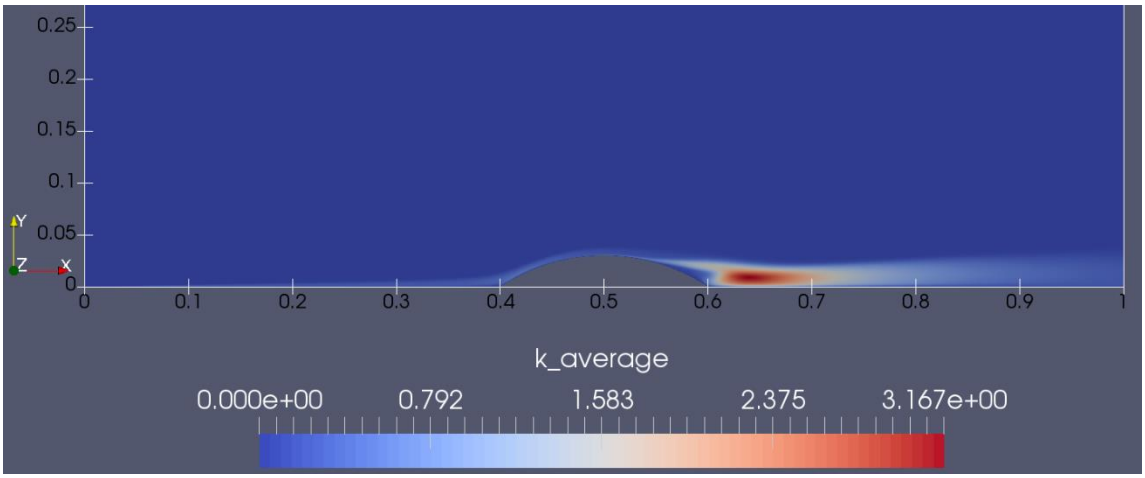

Fig.4.69. Turbulent kinetic energy contour, unactuated case, $U_\infty = 7m/s$.

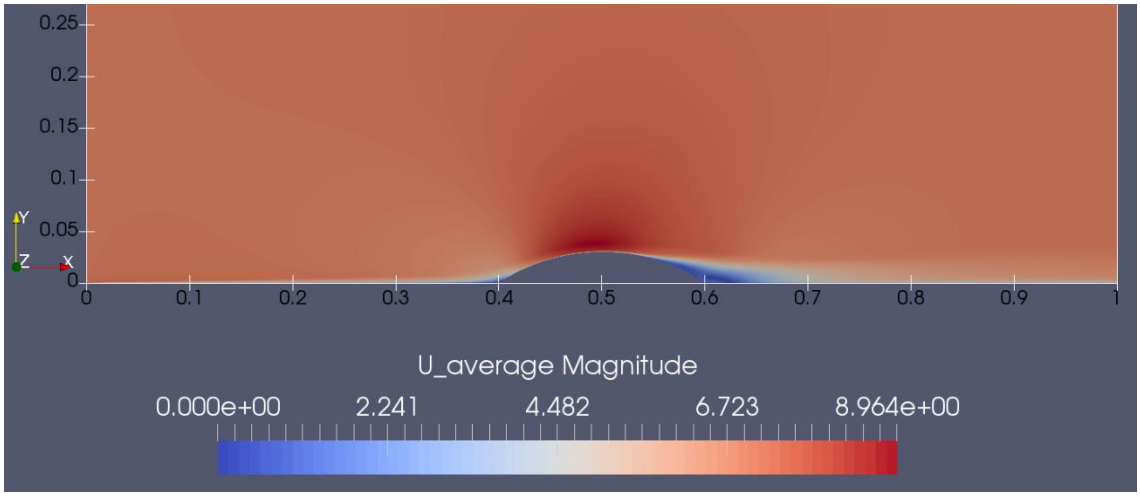

Fig.4.70. Velocity contour, unactuated case, $U_\infty = 7m/s$.

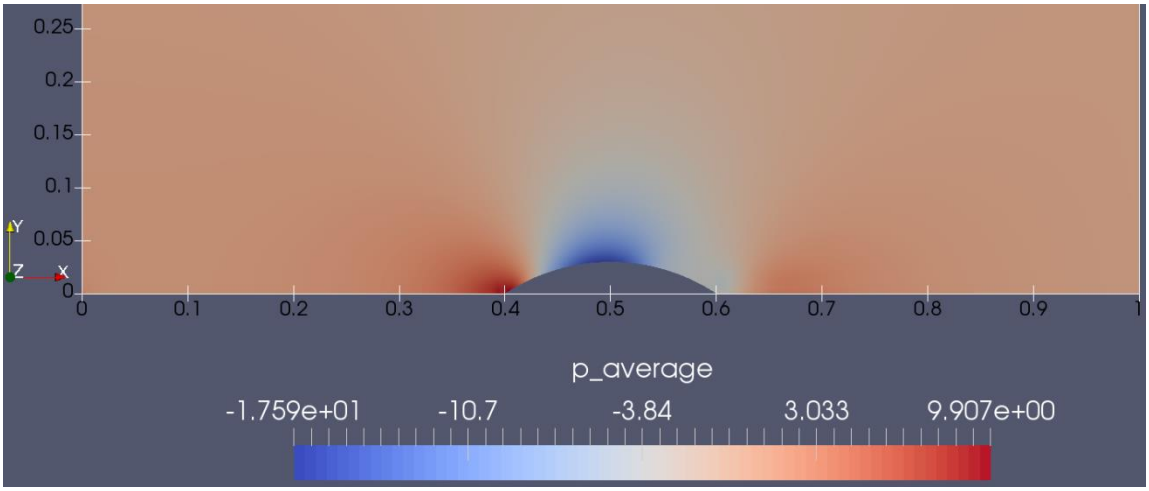

Fig.4.71. Pressure contour, unactuated case, $U_\infty = 7m/s$.

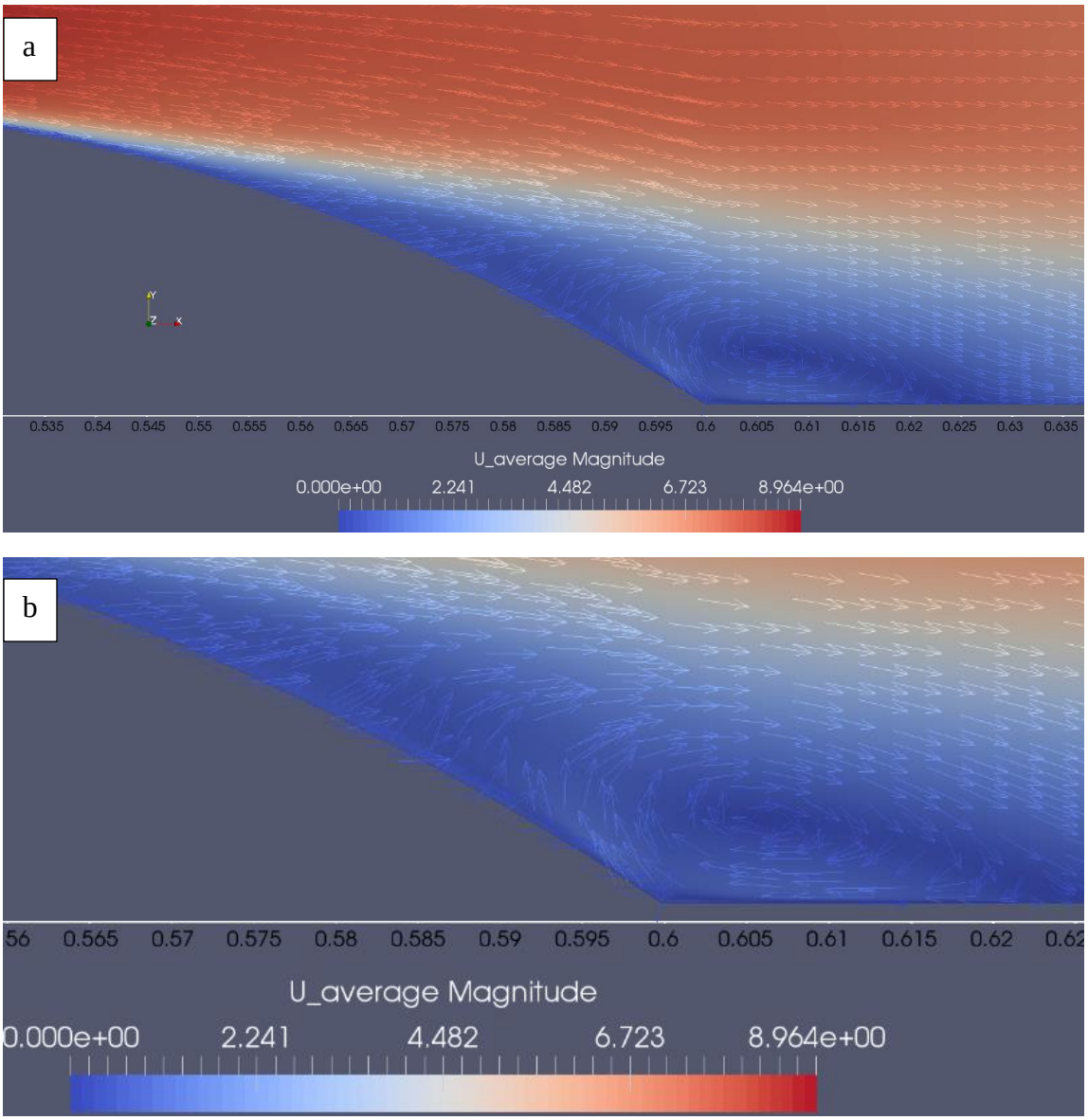

Fig.4.72. (a). Velocity field, unactuated case, $U_\infty = 7m/s$, and (b) Closer view of the wake region.

The profile of streamlines is attained by employing adaptive integrator (Runge-Kutta 4-5) and the seeds for the streamlines are generated by using a high resolution line source in Y-direction at Y= 0.607 which is passed through the wake region.

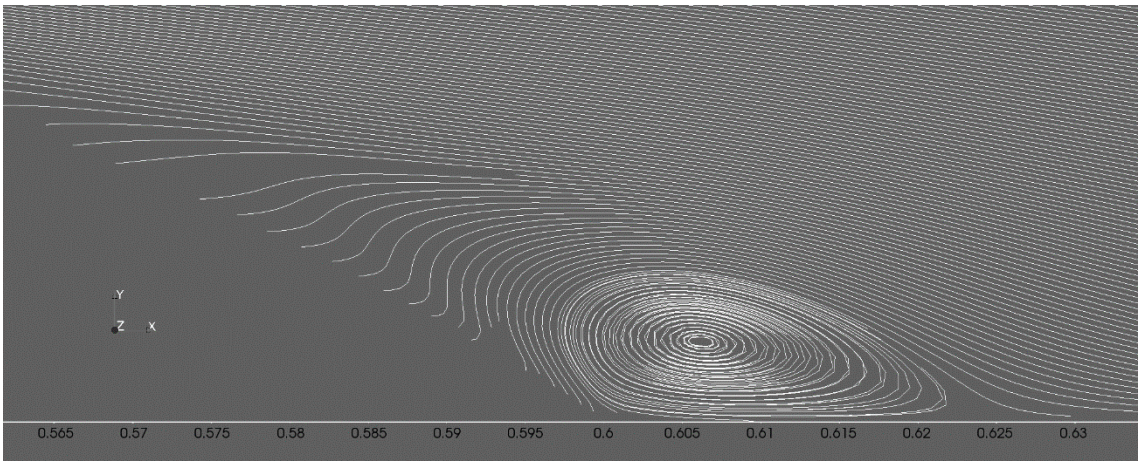

Fig.4.73. Streamlines profiles, unactuated case, $U_\infty = 7m/s$.

The profiles of surface pressure and standard deviation of surface pressure as well as minimum wall shear stress are shown by Figs.4.74-4.76, respectively.

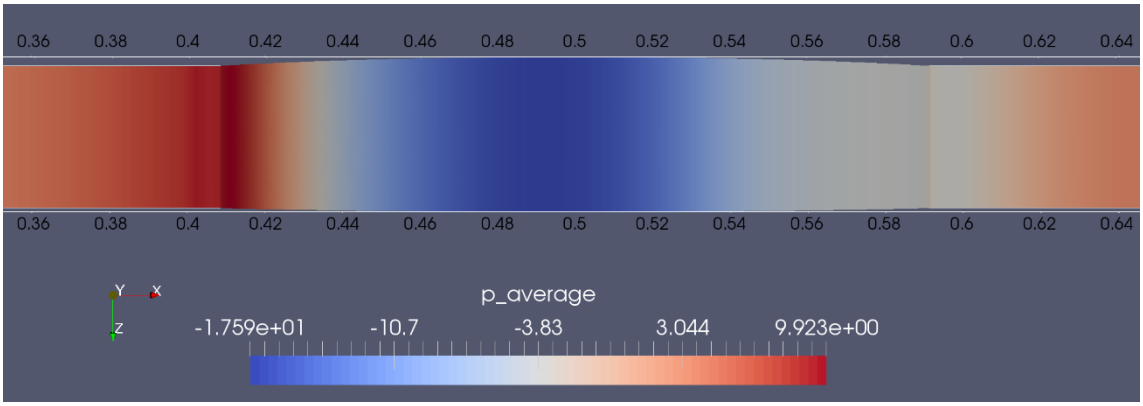

Fig.4.74. Surface pressure profile, unactuated case, $U_\infty = 7m/s$.

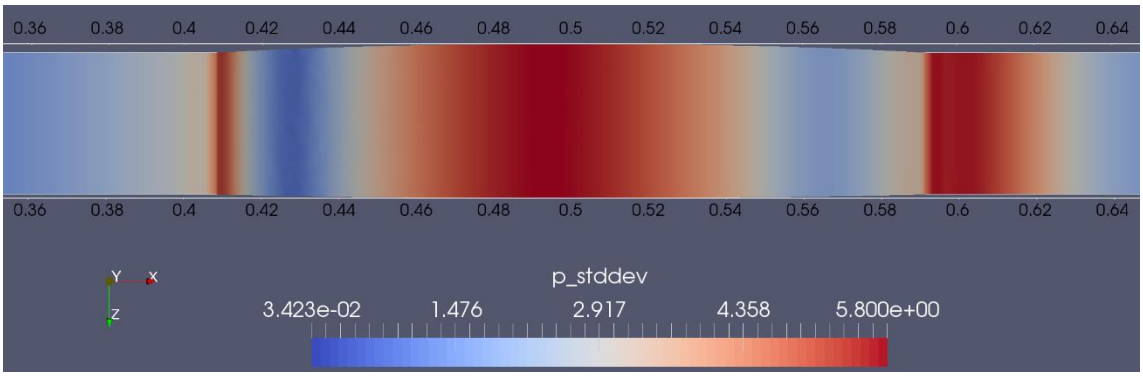

Fig.4.75. Standard deviation of surface pressure profile, unactuated case, $U_\infty = 7m/s$.

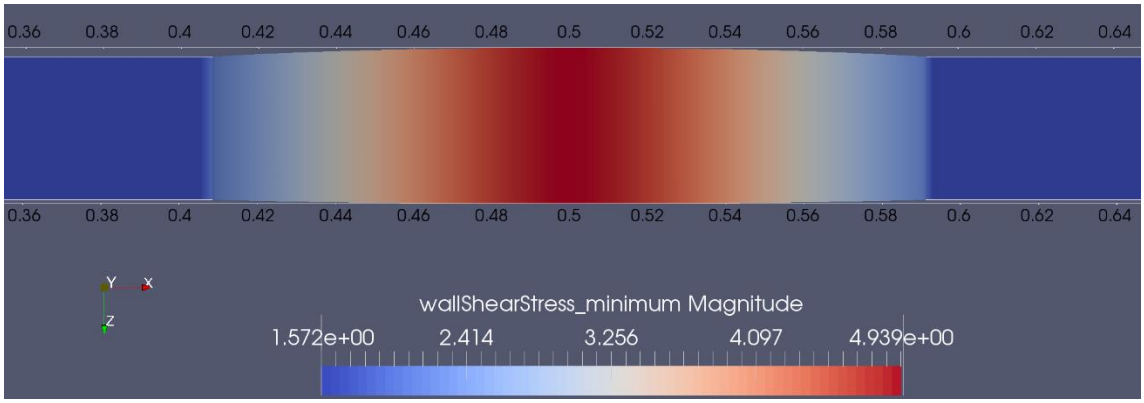

Fig.4.76. Minimum wall shear stress profile, unactuated case, $U_\infty = 7m/s$.

4.5.2 Unsteady State –Actuated Case

In this section, the results of simulations of single actuator in quiescent conditions (no cross-flow) and the interaction of synthetic jet actuators with cross flow are presented.

4.5.2.1- Single SJA in Quiescent Condition (No Cross-Flow)

The location of synthetic jet actuator implementation is important to have a successful operation to either delay separation or completely remove it. The best location to implement the synthetic jet actuators is somewhere close to the separation point, the estimated separation point for unactuated case from previous section is around 20-25 mm upstream of hump trailing edge, then the synthetic jet actuators should be implemented in vicinity of the estimated location. This can be attained by rotation of the hump model around central axis in span wise direction by angle rotation of 9.5 degree. The history of velocity component in y direction and in the center of the outlet of middle orifice of SJA is shown in Fig.4.77. It should be noted that the velocity component in y direction is the dominant component of velocity at the center of orifice outlet because the orifice axis is mainly in y direction.

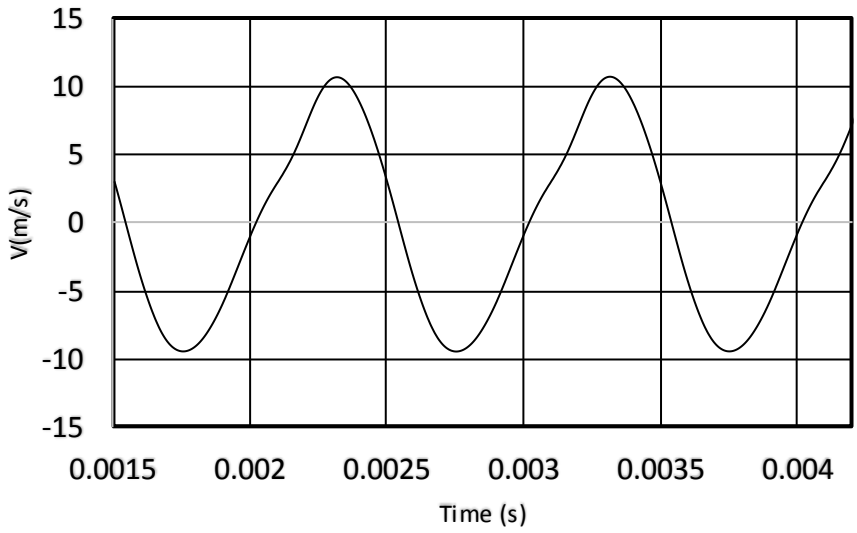

Fig.4.77. History of velocity component in y-direction in the center of orifice outlet, quiescent conditions .

The pressure and velocity contours in blowing phase are shown by Figs.4.78- 4.80, respectively.

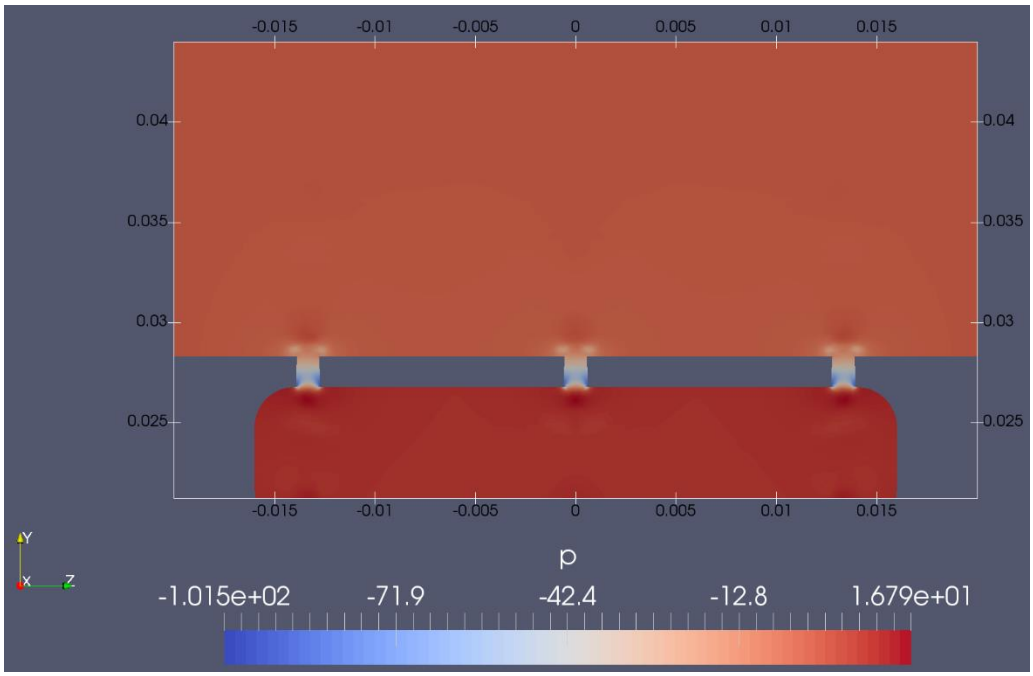

Fig.4.78. Pressure contour of single actuator, blowing phase, quiescent conditions, Z-Y plane.

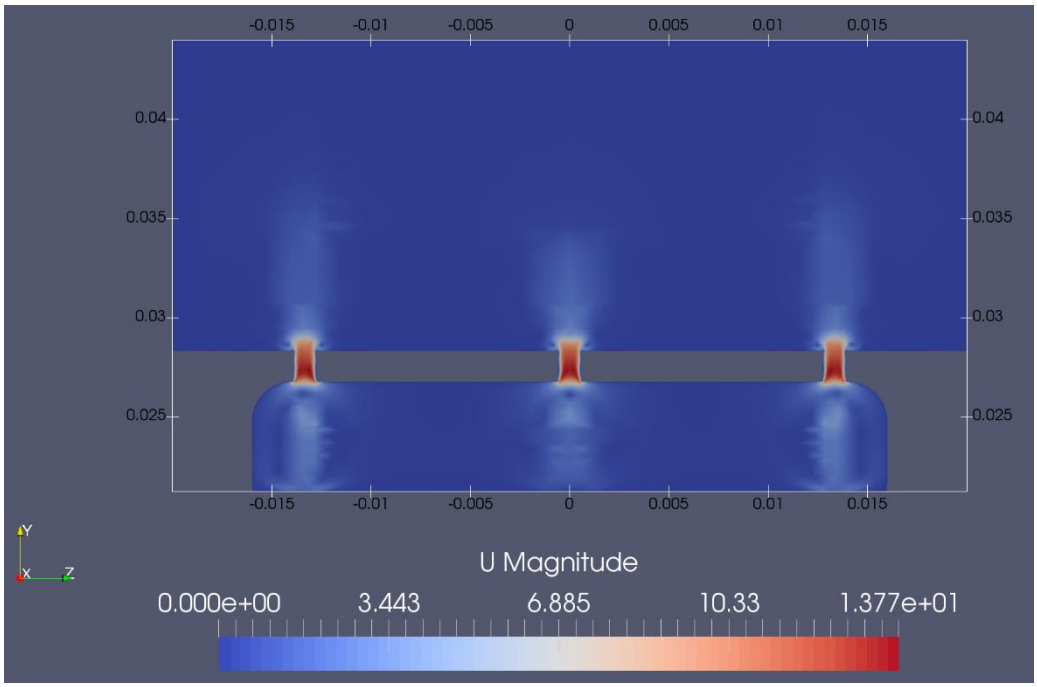

Fig.4.79. Velocity contour of single actuator, blowing phase, quiescent conditions, Z-Y plane.

This Space Intentionally Left Blank.

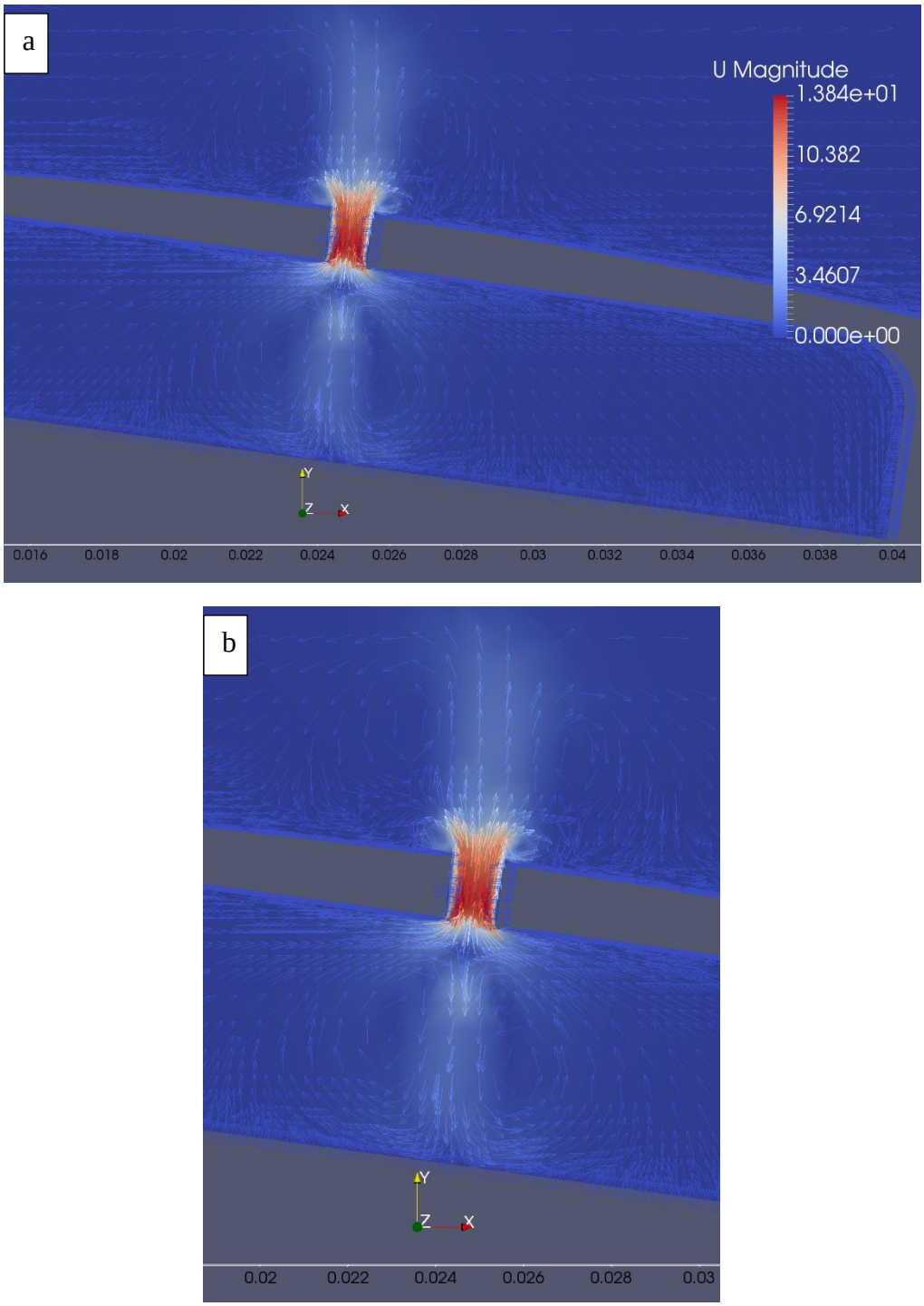

Fig.4.80. (a) Velocity profile, blowing phase, quiescent conditions, X-Y plane and (b) Closer view of generated vortex ring at the orifice outlet.

The profiles of velocity fields in X-Y and Z-Y planes as well as the vorticity contour in log-scale are depicted by Figs.4.81-4.82, respectively.

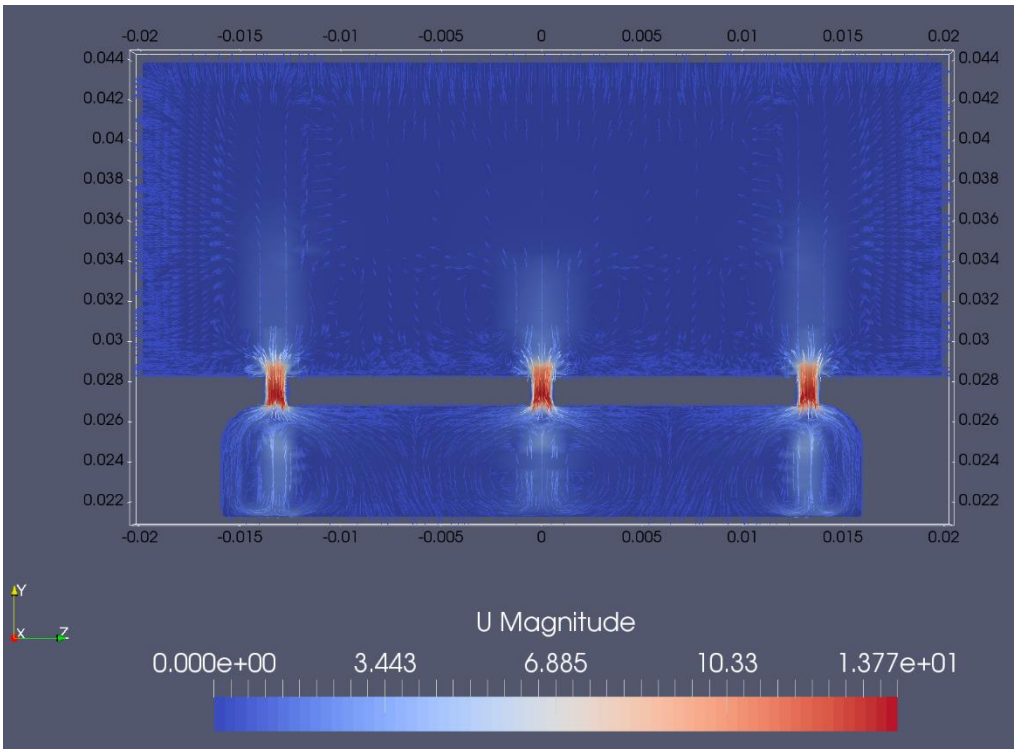

Fig.4.81. Velocity profile, blowing phase, quiescent conditions, Z-Y plane.

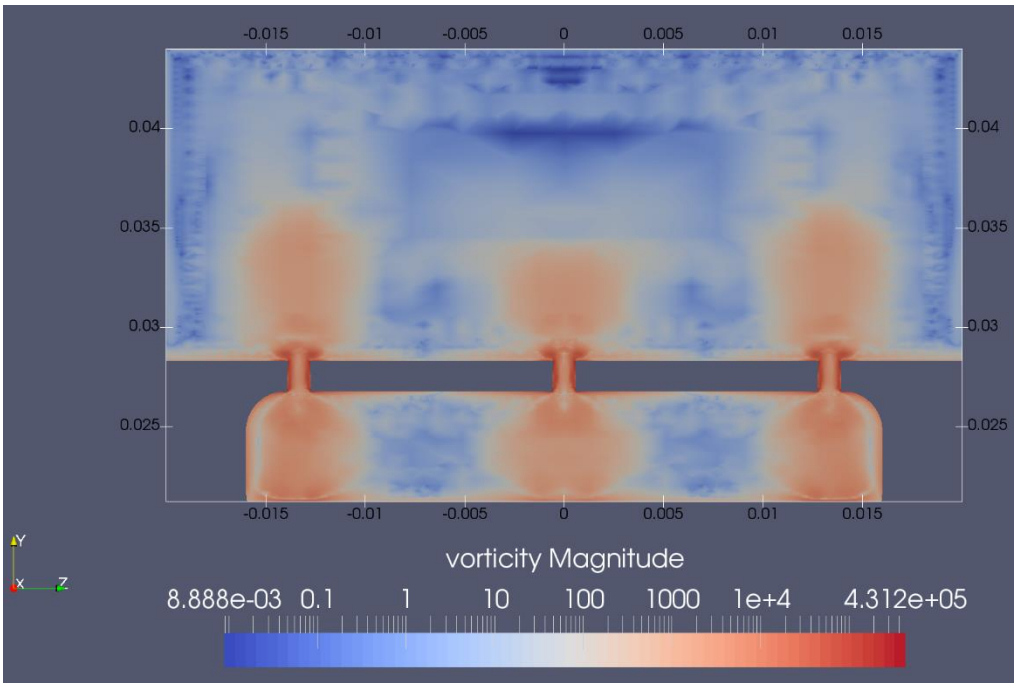

Fig.4.82. Vorticity contour of single actuator, blowing phase, log scale, quiescent conditions, Z-Y plane.

The vorticity profile in Z-Y plane and along line Z= 0.0006 m in blowing phase is shown by Fig.4.83.

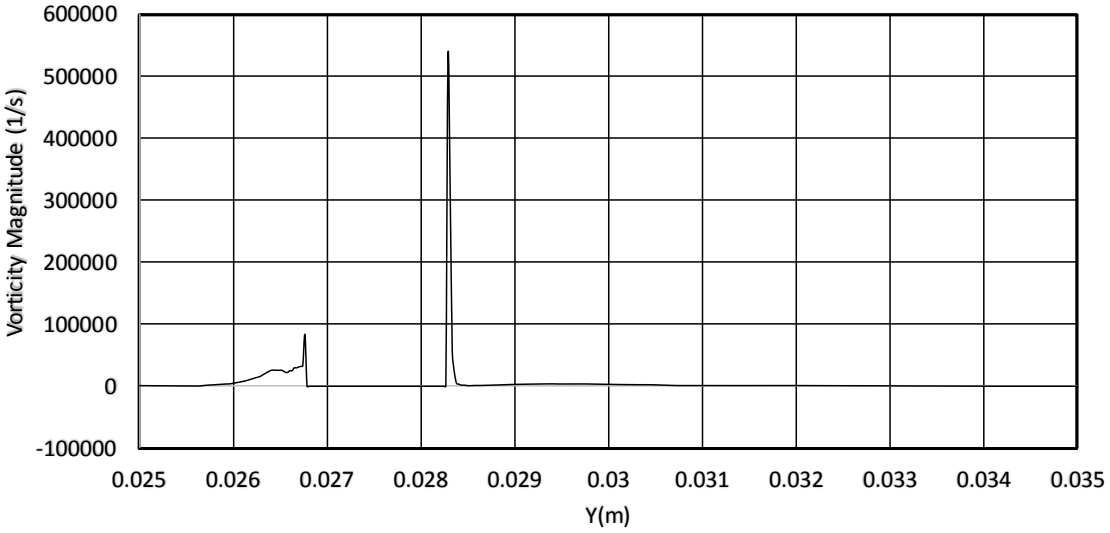

Fig.4.83. Vorticity magnitude profile in Z-Y plane along line Z =0.0006 m, blowing phase, quiescent conditions.

4.5.2.2- Interaction of Synthetic Jet Actuators with a Uniform Cross-Flow

In this section the results of the simulation of the interaction of actuators with uniform cross flow is presented. The instantaneous and time- averaged velocity fields for different times are shown by Figs.4.84-88.

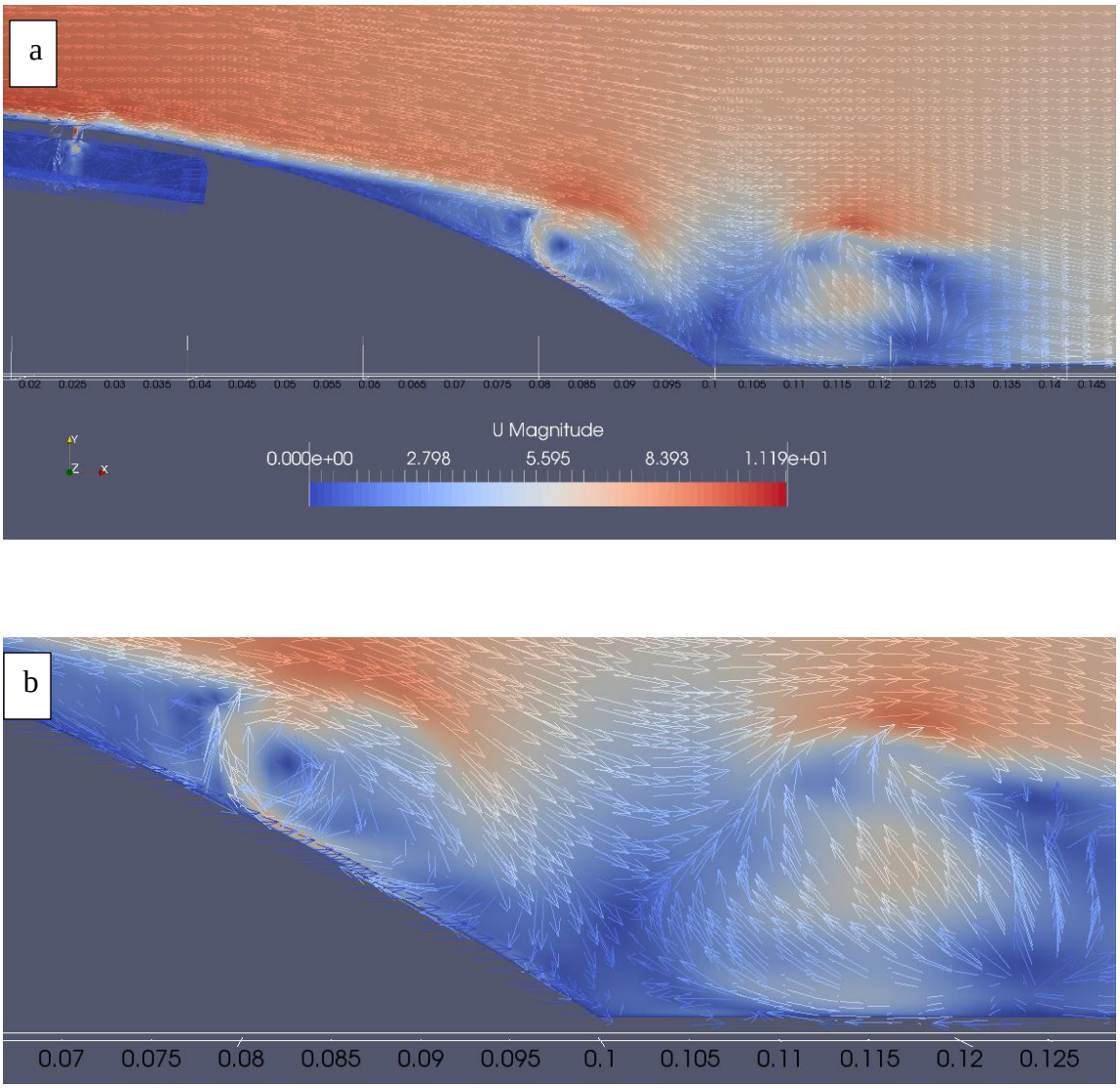

Fig.4.84. (a). Instantaneous velocity field, Time=0.05 s, actuated case, $\phi = 9.5°, U_\infty = 7\ m/s$, and (b) Closer view of the wake region.

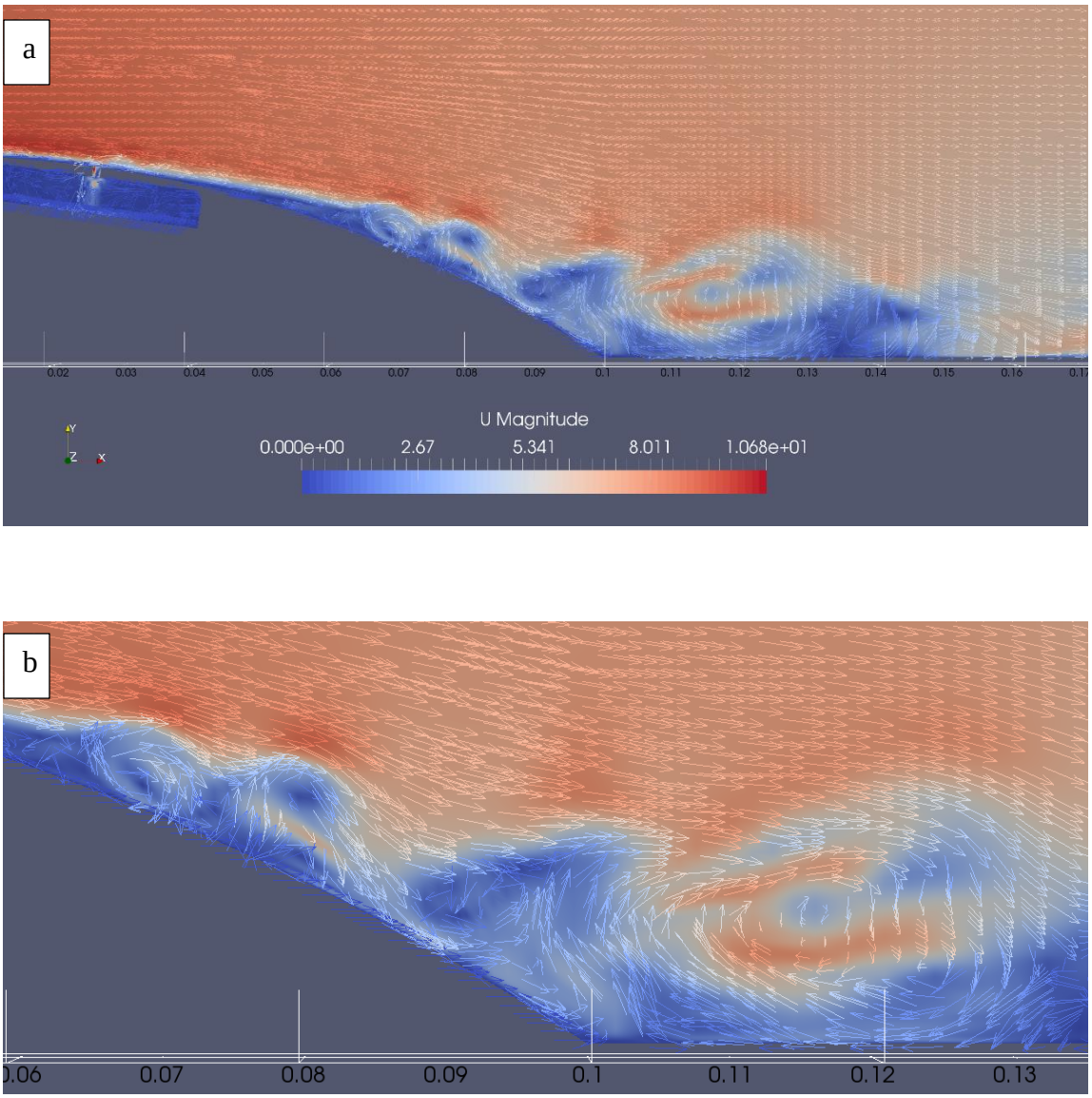

Fig.4.85. (a) Instantaneous velocity field, Time=0.075 s, actuated case, $\phi = 9.5°, U_\infty = 7\ m/s$, and (b) Closer view of the wake region.

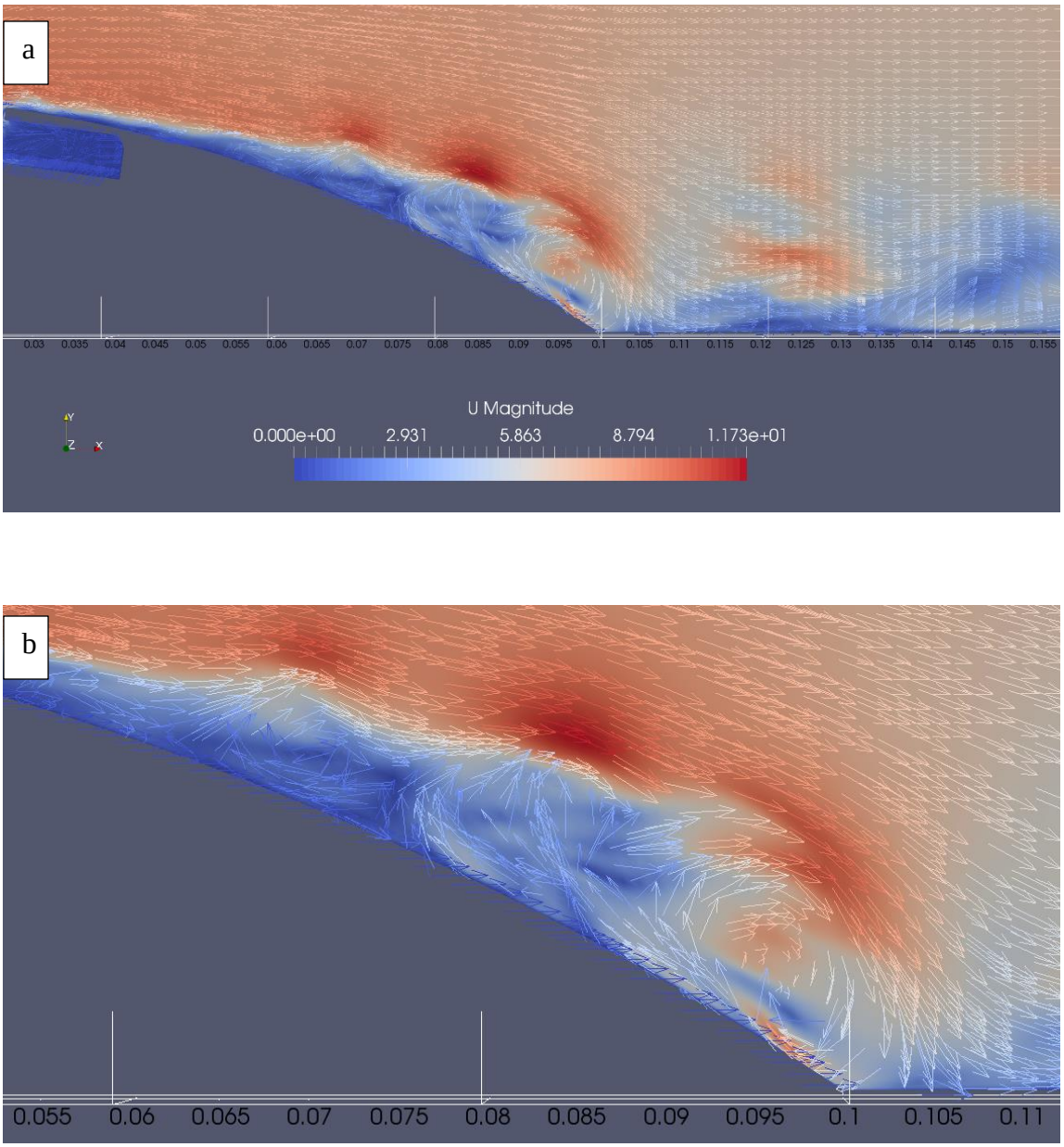

Fig.4.86. (a) Instantaneous velocity field, Time=0.15 s, actuated case, $\phi = 9.5°, U_\infty = 7\ m/s$, and (b) Closer view of the wake region.

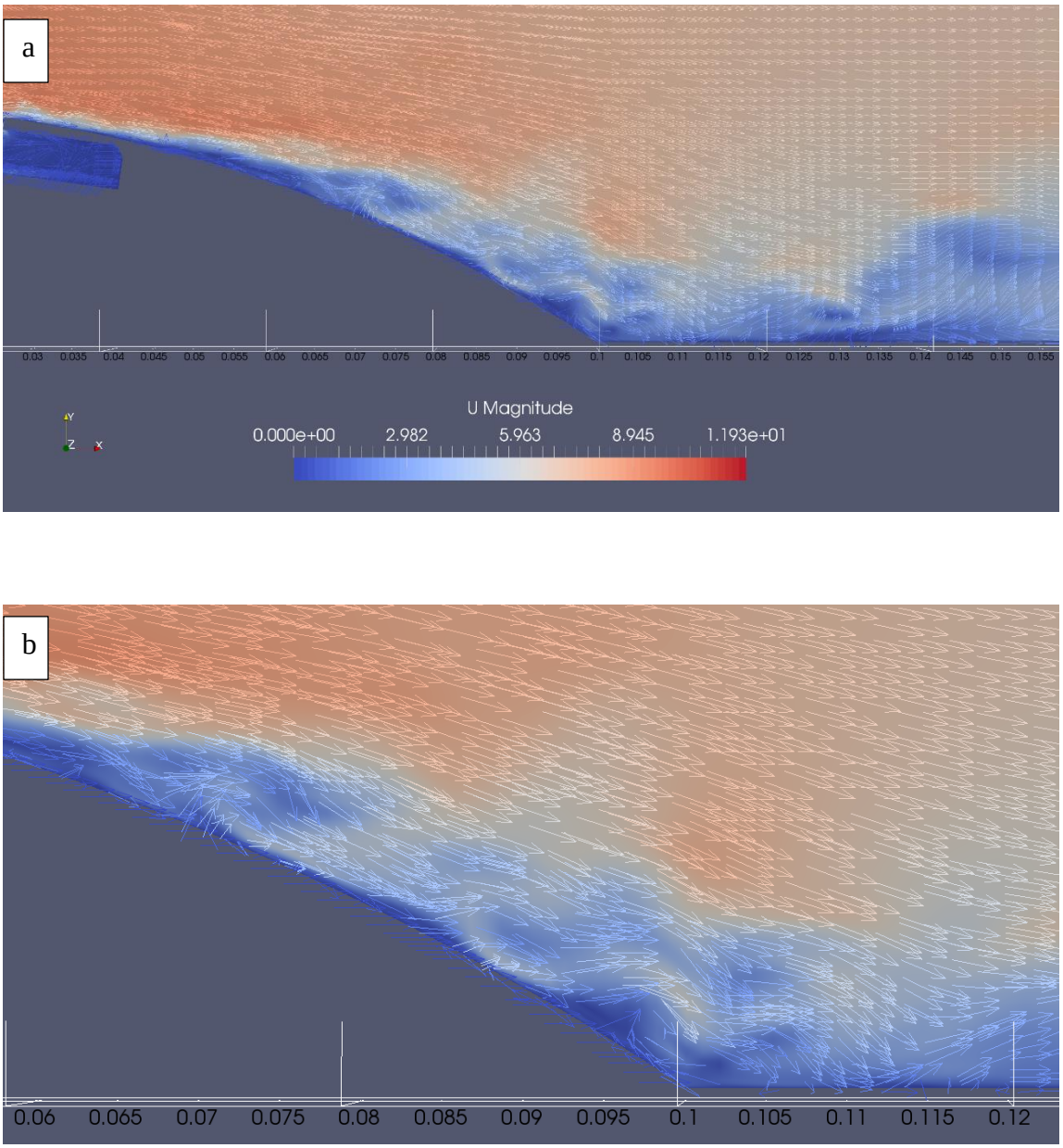

Fig.4.87. (a) Instantaneous velocity field, Time=0.20 s, actuated case, $\phi = 9.5°, U_\infty = 7\ m/s$, and (b) Closer view of the wake region.

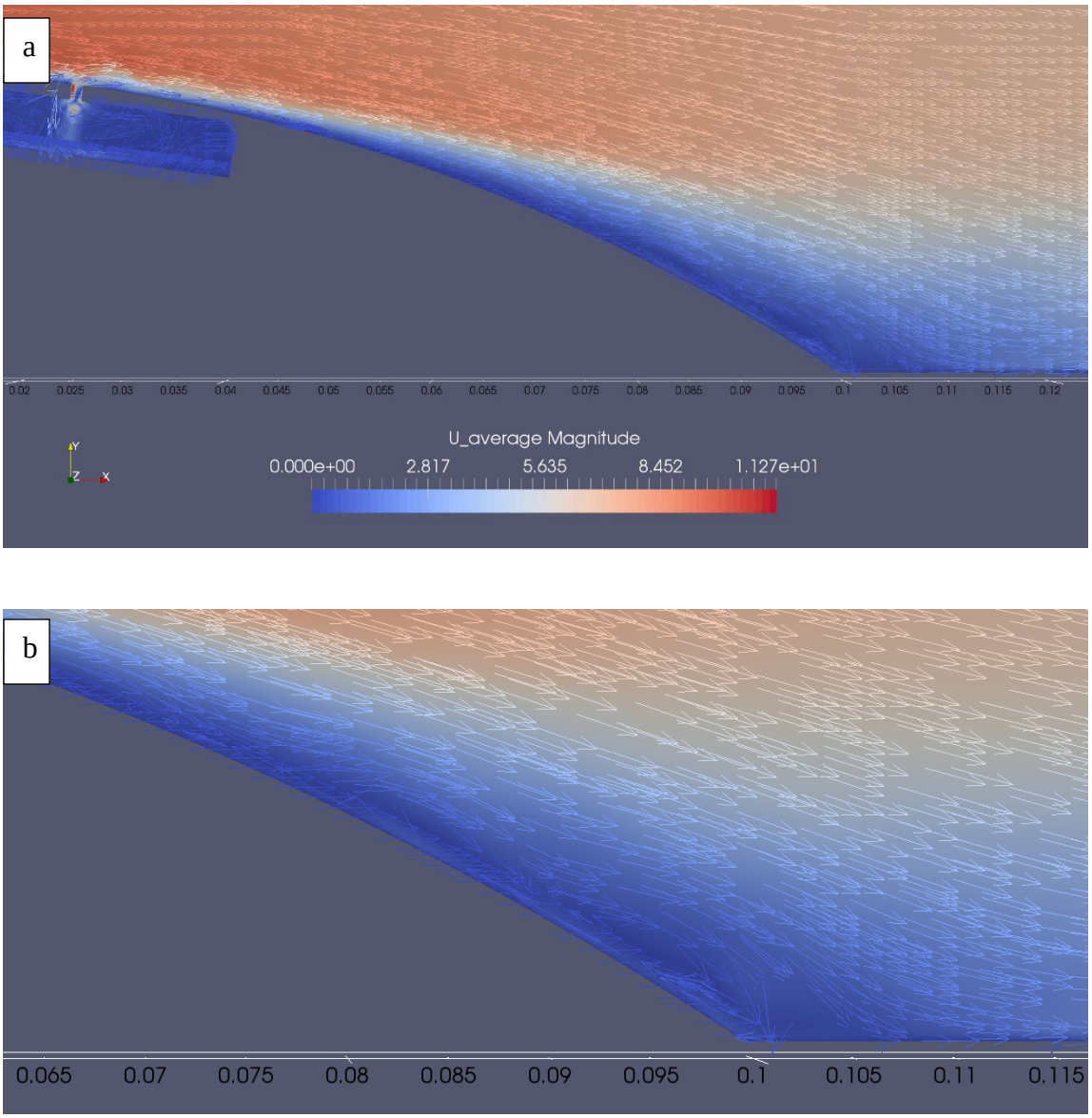

Fig.4.88. (a) Time averaged velocity field, actuated case, $\phi = 9.5°, U_\infty = 7\ m/s$, and (b) Closer view of the wake region.

The profiles of time averaged velocity contour, pressure contours and average wall shear stress on the hump surface are shown by Figs.4.89-4.92, respectively.

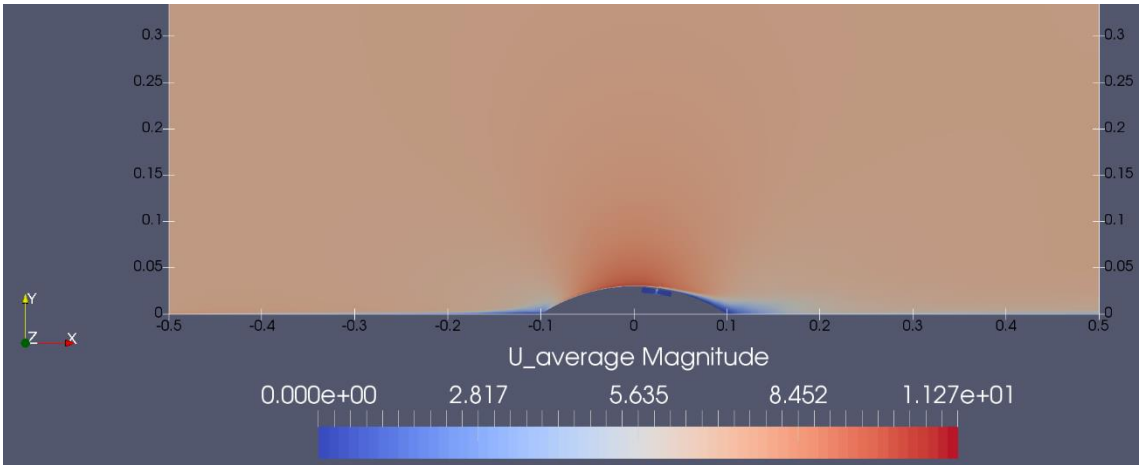

Fig.4.89. Time averaged velocity contour, actuated case, $\phi = 9.5°, U_\infty = 7\ m/s$.

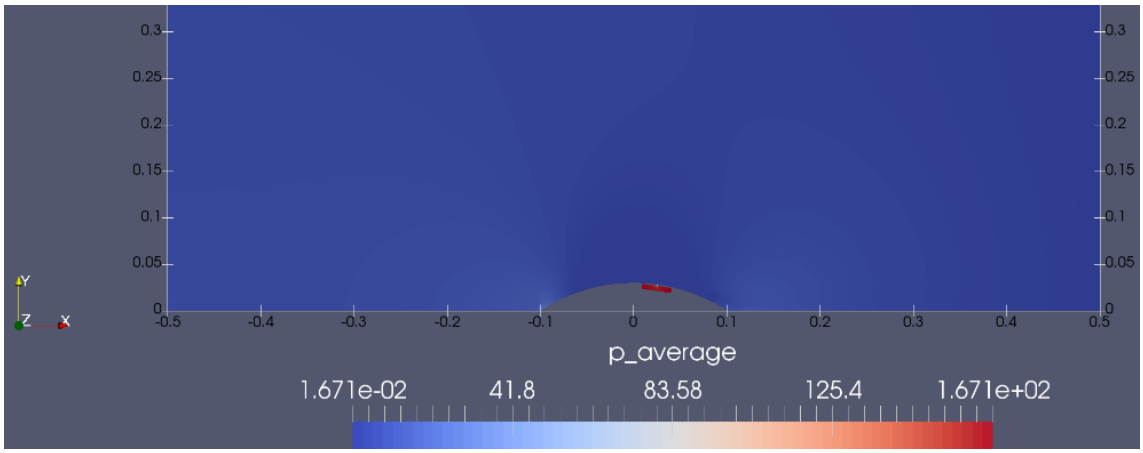

Fig.4.90. Time averaged pressure contour, actuated case, $\phi = 9.5°, U_\infty = 7\ m/s$.

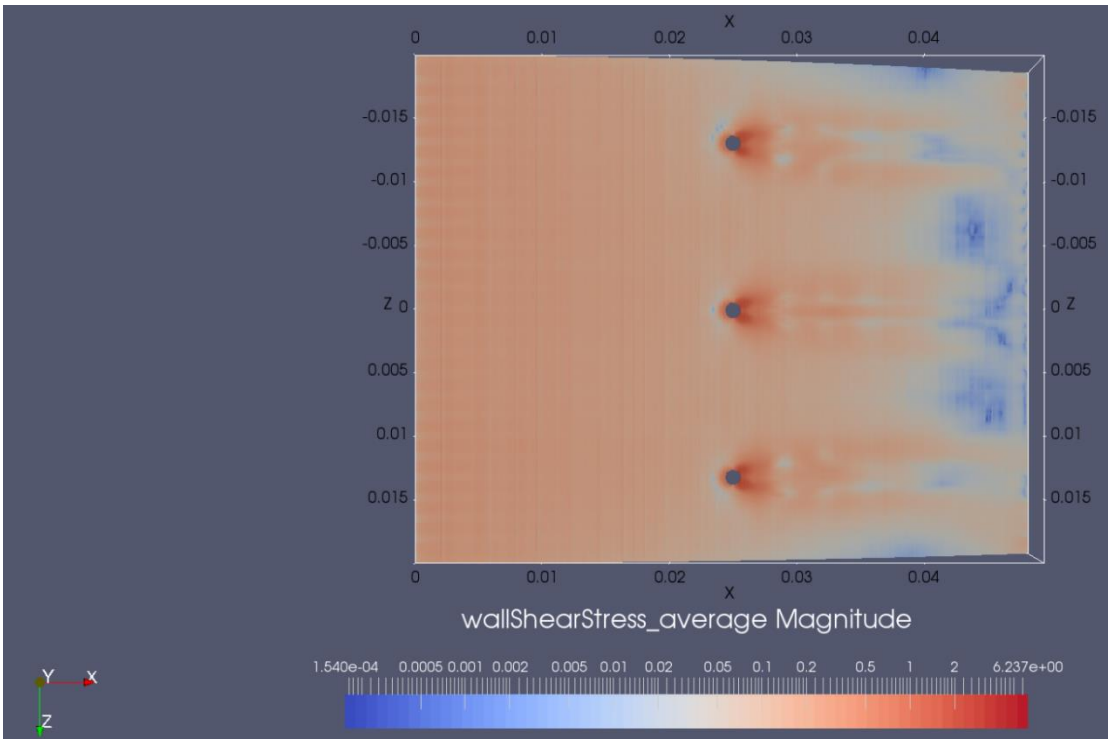

Fig.4.91. Time averaged wall shear stress profile on the hump surface contains actuators, $\phi = 9.5°, U_\infty = 7\ m/s$.

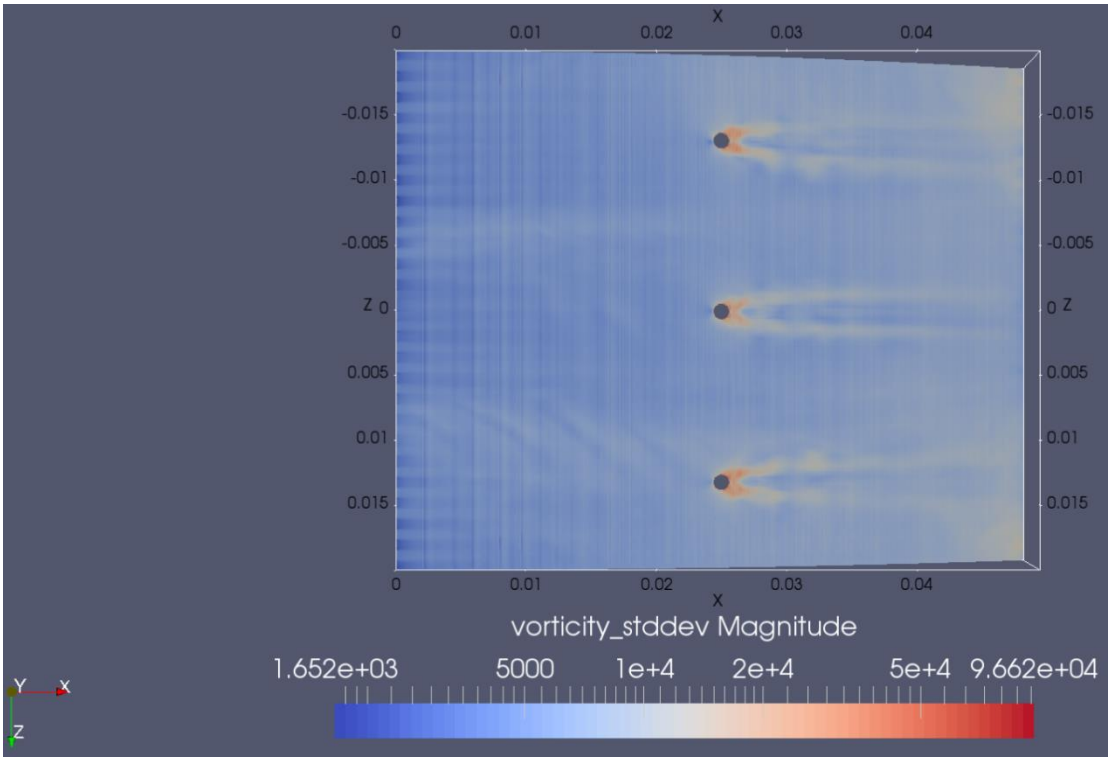

Fig.4.92. Time averaged vorticity profile in near wall region downstream of actuators, $\phi = 9.5°, U_\infty = 7\ m/s$.

Fig.4.93 shows the profile of average shear stress on the surface of the hump model and floor of the test section.

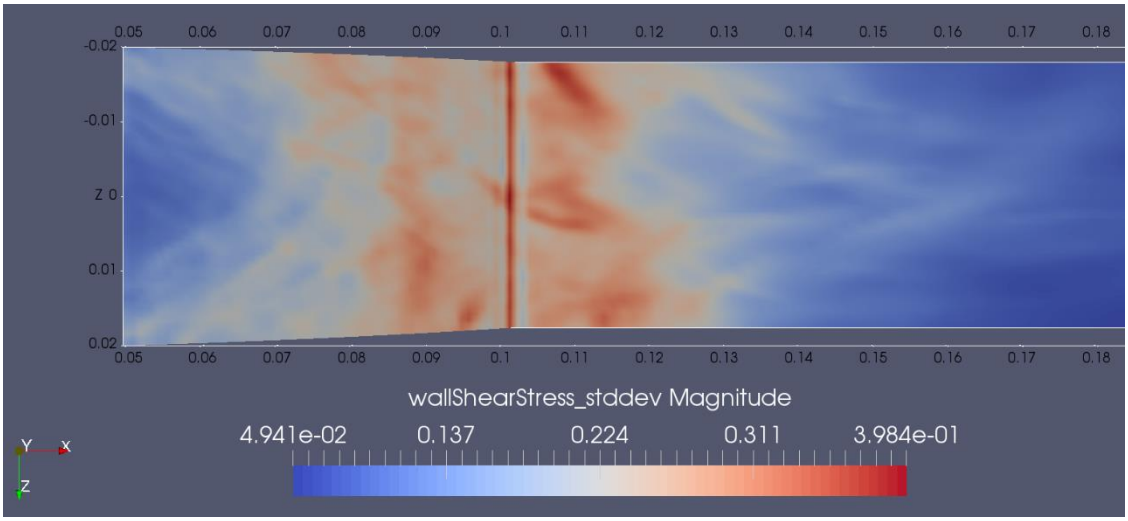

Fig.4.93. Time averaged wall shear stress -stddev profile on the hump surface and the floor of the test section (downstream of actuators), $\phi = 9.5°, U_\infty = 7\ m/s$.

4.6-Summary

In this chapter, the results of experimental measurements of flow quality of the wind tunnel and measurements of characteristics of single actuator in quiescent conditions by Hot Wire Anemometry (HWA) technique are presented. Also, the results of measurements of flow separation over the hump model for both baseline case and actuated case by using both Hot Wire Anemometry (HWA) technique and Particle Image Velocimetry (PIV) technique are presented. In addition, the results of numerical simulation for characteristics of single actuator in quiescent conditions as well as the numerical analysis for flow separation over hump model for both unactuated and actuated cases are shown.

In Chapter 5, the above-mentioned experimental and numerical results will be discussed in detail.

Chapter 5- Discussion

In this chapter, the results of experimental studies including wind tunnel flow quality measurements, measurements of characteristics of single actuator in quiescent flow conditions and flow separation over the hump model for both unactuated and actuated cases. In addition, the results of numerical simulations including the simulation of flow separation over the hump model for baseline case, simulation of single actuator in quiescent flow condition as well as the interaction of cross flow with synthetic jet actuators are discussed. Also, the numerical measurements are compared with corresponding measurements by both Hot Wire Anemometry (HWA) and Particle Image Velocimetry techniques.

5.1- Wind Tunnel Flow Quality

Velocity profiles for lines located in planes Z = 150, Z = 0 and Z = -150 are shown in Fig. 4.2 (a)-(c). However, the travel distance of the traverse unit which carries the hot wire probe in vertical direction is 10 cm, and therefore to cover the whole height of the test section, it was required to change the probe direction (upward or downward) for some cases and stop the wind tunnel to remove and reconnect the hot wire probe. Despite this, the velocity profiles show an almost uniform velocity magnitude outside of the boundary layers. Fig.4.2(c) shows a deficit of velocity magnitude around height of 400 mm. This is due to the presence of the traverse system with its edge (at Z=-170 mm) located near to the measurement plane of Z=-150 mm – hence the flow separation a wake region with lower velocity. It should be noted that this region is sufficiently far from the flow region of interest, i.e. near and downstream of the hump apex with the height of 30 mm above the floor level and far from the ceiling of the test section. It is also worth mentioning that measurements with the probe positioned at an angle, to keep it far away from traverse system, were also attempted. However, it was found that changing the prongs angle would affect the acquired voltage value and consequently the value of measured velocity.

Therefore, after hot wire probe calibration, not only the hot wire should be perpendicular to the flow direction, but in addition, the prongs of hot wire probe should also be positioned at the same angle as in the calibration process. The measured turbulence intensity in plane Z=0 mm at X= 550 mm is shown in Fig. 4.2 (d). The average turbulence

intensity outside the boundary layer is about 0.66%, however it is observed that probe positioning affects the measured turbulence intensity, e.g. while the probe position is changed from downward position (calibration position) to upward position, the measured turbulence intensity increased about 0.1 %. This probably can be relevant to change of rate of convective heat transfer from the hot wire sensor to the surrounding fluid by changing prongs positioning.

Fig. 4.3 shows the velocity profile in near wall region and the estimated boundary layer thickness is around 7 mm. However, it should be noted that although the resolution of traverse unit is 0.005 mm, the first measurement point was considered at height of 0.25 mm as there was the risk of hot wire probe breaking for heights less than 0.25 mm.

5.2- Characteristics of Single Actuator in Quiescent Flow Conditions

Fig.4.4 depicts the frequency response of a synthetic jet actuator. The actuator arrays with orifice diameter of 1.2 mm and same diaphragm type was used by Azzawi (2016), however it is found that it is not possible to attain maximum exit jet velocity of 10.5 m/s at the orifice outlet if the diaphragms are actuated below their maximum allowable voltage range (30 Vp-p). On the other hand, if they are actuated with high voltage above their maximum allowable voltage range, after a while their performance is decreased and output velocity experiences a continuous drop. To find the appropriate orifice size, 5 different configurations of cavities were considered including 3 cavities contain 2, 3 and 5 orifices with orifice diameter of 1mm, and 2 other cavities contain 2 and 3 orifices with orifice diameter of 1.5 mm. It was found that the cavity contains 3 orifices with orifice diameter of 1 mm would supply the velocity requirement at the orifice outlet within allowable voltage range and at Helmholtz frequency of 960 Hz. The calculated Helmholtz frequency is 925.88 Hz which is smaller about 3.6 % than the theoretical value calculated by Eq.(2.3).

It should be noted the measured Helmholtz frequency for 12 SJAs is not same and it varies approximately in range of 820 Hz to 1200 Hz and sometimes it is not easy to discern the Helmholtz frequency as it shifts toward the resonance frequency of the diaphragm, e.g. for cavity case contain 3 orifices with diameter of 1.5 mm, the peak jet velocity is

increased 36% in comparison with cavity case contain 3 orifices with diameter of 1.2 mm, however the Helmholtz frequency is shifted from 1000 Hz to 1350 Hz.

The peak exit jet velocity response of a synthetic jet actuator shows a linear relationship between the actuation voltage and the peak exit jet velocity as shown by Fig.4.5.

The profile of time history of exit jet velocity at height of 0.5 mm shows two distinct peaks as depicted by Fig.4.6. The actuator is excited by the Helmholtz frequency of 960 Hz with actuation voltage of 22 V p-p. It should be noticed that the measured signal by Hot Wire Anemometry system contains no information about the flow direction as the single hot wire probe is insensitive to the flow direction and therefore it cannot recognize the positive and negative velocities and it would be leading to confusion in discerning the velocity direction specially in oscillatory flow cases. However, the problem can be resolved for synthetic jet actuator cases as long as the single hot wire probe is positioned in the plane above orifices such as the current case. During blowing phase, the fluid leaves the actuator through the orifice with a very small cross section area ($7.85 \times 10^{-7} m^2$) , while it is drawn into the orifice from a big area of the entire region out of the orifice. This big difference between the exit and entry areas makes a significant difference between the velocity magnitude during blowing and suction phases and consequently the velocity magnitude during blowing phase is much bigger than the velocity magnitude during suction phase. This influence is more intensified and the peak velocity of exit jet during suction phase is promptly vanished while the hot wire probe is drawn away more from the orifice outlet. This effect can be seen from the time history of exit jet velocity for height of Y = 1.5 mm above the orifice as shown by Fig4.7. This feature of synthetic jet actuators is very helpful to ascertain velocity direction in case it is not easy to measure the displacement of piezo-electric diaphragm or synchronize it with velocity data acquisition.

The magnitude of peak velocity of exit jet experiences a continuous drop in stream-wise direction for measurements heights between $0.5\ mm \leq y \leq 15.5\ mm$ above the orifice outlet as depicted by Fig.4.8. As it is seen, the rapid decrease of jet momentum is seen as the hot wire probe is drawn away from the orifice outlet. Therefore, the features of exit jet to make it capable to interact with the cross flow to affect the boundary layer should be investigated carefully.

The power spectrum density profile of time history of exit jet velocity shown by Fig.4.6 by employment of Welch's method shows a dominant frequency of 960.1 Hz and its harmonics as illustrated by Fig.4.9. The dominant frequency of 960.1 Hz (which is the same frequency of actuation of piezo diaphragm) in the power spectrum and its harmonics which are integer multiple of the fundamental frequency confirms the generation of vortex rings with coherent structures above the orifice outlet. Two other dominant frequencies of 400.4 Hz and 560.3 Hz alongside their harmonics is observed in Fig.4.9 which can possibly relevant to the suction phase, however it is hard to tell which frequency is exactly relevant to suction phase. Fig.4.10 show the power spectrum profile at height of Y =15.5 mm above the orifice. As it is clear, the power of dominant frequency relevant to generation of vortex rings and its harmonics are considerably decreased and probably the vortex rings have lost their coherency at a distance far from the orifice outlet and the strength of exit jet has been decreased due to the considerable energy dissipation. This point can be confirmed by Fig.4.10 as the dominant frequencies relevant to suction phase are not present. It should be noted this profiles are relevant to the middle orifice of the actuators and the investigation of power spectra of right and left orifices showed that the flow features above the right and left orifices are not exactly same and therefore the flows above these orifices is not symmetric with respect to the middle orifice.

5.3- Flow Separation over the Hump Model- Unactuated Case

In this section, the results of flow measurements by HWA technique and PIV techniques in and out of the wake region is discussed.

5.3.1- Measurements of Flow Features by HWA Technique –Unactuated Case

As mentioned in previous chapter, the flow features for the baseline case has been measured for 3 free stream velocities including 7, 9 and 12 m/s, however the measurements for actuated cases were carried out only for free stream velocity of 7m/s. The measurements are carried out along four lines in the wake region which are located at X= 570-600 mm as shown in Fig. 4.11. It is observed that the location of maximum velocity fluctuations in the wake region moves toward the hump wall from the height of 10 mm to heights of 8 and 7 mm by increasing the free stream velocity from 7 to 9 and 12

m/s, respectively. The results show that increasing the free stream velocity can be used as a way to suppress the velocity fluctuations and consequently delay the flow separation.

The hot wire probe for other measurement lines was traversed vertically from height of 1 mm above the hump surface to out of the wake region as it was not easy to close the hot wire probe to lower heights by using the reflection effect of the hump surface since it was matt black. The same trend also is observed on these measurement lines and the location of maximum velocity fluctuations in the wake region moves toward the hump wall by increasing the free stream velocity. As it can be seen by Fig.4.12, the inflection points of velocity profiles is around the maximum RMS velocity.

As Fig.4.13 shows, the vertical domain behind hump which experiences the velocity fluctuations is increased from X= 570 mm to X = 600 mm and therefore the width of recirculation region is increased as the measurement location is approached to the hump trailing edge.

As it is seen from the profiles, the height of the location of maximum RMS velocity is decreased in the stream-wise direction as the hump height is decreased. The velocity profiles for measurement line at X = 590 mm is shown by Fig.4.14. The same trend for velocity profiles is seen on this measurement line as it is observed for the measurement line at trailing edge, however the height of inflection point of velocity profiles is slightly increased as hump height is increased upstream of the hump trailing edge. Fig4.15 shows the trajectory of maximum RMS velocity in the wake region, as it is seen the maximum velocity fluctuation occurs in measurement line of X = 590 mm and as the hump height is decreased in the stream wise direction, the location of maximum RMS velocity also is decreased, indeed it shows the shear layer follow the hump profile.

Figs. 4.16-19 show the profiles of the power spectral density estimate for 5 heights on the measurement line at X= 570-600 mm, respectively. As it is expected, the signal analysis shows that the maximum energy dissipation occurs at the height with the maximum RMS velocity as shown by figures.

Local maximum frequencies is seen in the spectra, but a distinct peak relevant to the vortex shedding frequency is not observed. Indeed, the identified local broadband peak for 3 free

stream velocities (see Appendix C for free stream velocities of 9 m/s and 12 m/s) are not following a linear relationship with respect to their corresponding free stream velocities. It should be noted that the spikes with frequency value of about 88 Hz in the power spectrum profiles is relevant to the shedding production by the supportive cylindrical bar of the hot wire mounting system which transmits as vibrations onto the hot wire. The comparison of Fig.4.13 to the corresponding figures for free stream velocity and for measurement on line X = 570 mm show that increasing the free stream velocity helps the flow to delay the separation phenomenon. As the reverse flow is seen on line X = 570 mm for free stream velocity of 7m/s, while it is vanished by increasing the free stream velocity to 9m/s and 12m/s as it is shown by Figs. C1 and C7.

5.3.2- Criteria of Identification of Reattachment and Separation Points Location in PIV Studies

Prior to discussion of PIV results, in this section the criteria for identification of reattachment point location and separation point location are explained. The reattachment point is located between reverse flow and forward flow with zero velocity magnitude. In case, there is no vector with exactly zero value velocity, an interpolation is done by considering the velocity magnitude of reverse and forward flows and their locations to find the location of reattachment point with zero velocity magnitude. This criteria have been used for all cases in this research, e.g. the velocity vector field near a reattachment point for one of cases (actuated case with VR =1.5 and actuators angular position of 9.5^{o}) is shown in Fig.5.1. As it can be seen, the identified location is between reverse and forward flows, the identified location for reattachment point in this case is at X = 616.25 mm. The magnitude of velocity components at any point of velocity field was shown by DaVis software by moving the mouse on screen. Therefore, by identification of reverse and forward flows, the reattachment point can be easily found manually.

The separation point is located between forward and reverse flows and the shear stress at this point is zero. Of course, PIV measurements in this research were carried out in two dimensions and there is no information about the flow field in span-wise direction to define the shear stress along the separation line in span wise direction. Therefore, it was

tried to find the point between the forward and reverse flows, in addition the direction of vectors was considered in identification of separation point.

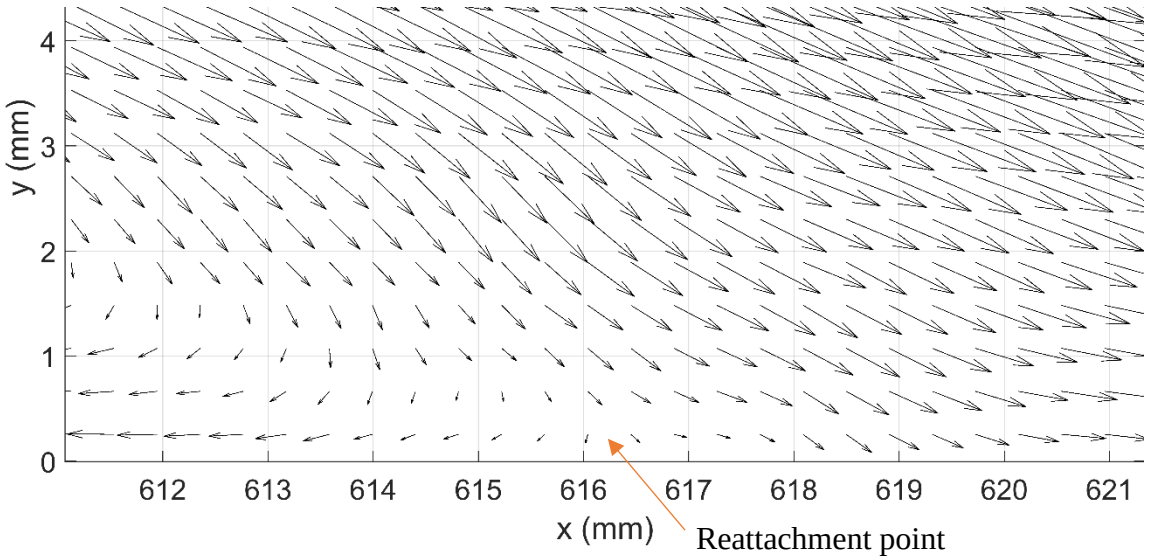

Fig.5.1. Identification of reattachment point by velocity vector field.

The vector directions in near wall regions are downward and make a negative angle with the axis along stream wise direction (x –axis) when the separation has not been occurred yet, while the vector directions are slightly upward and make a positive angle with axis along stream-wise direction in the vicinity of separation point as it can be seen in Fig.5.2.

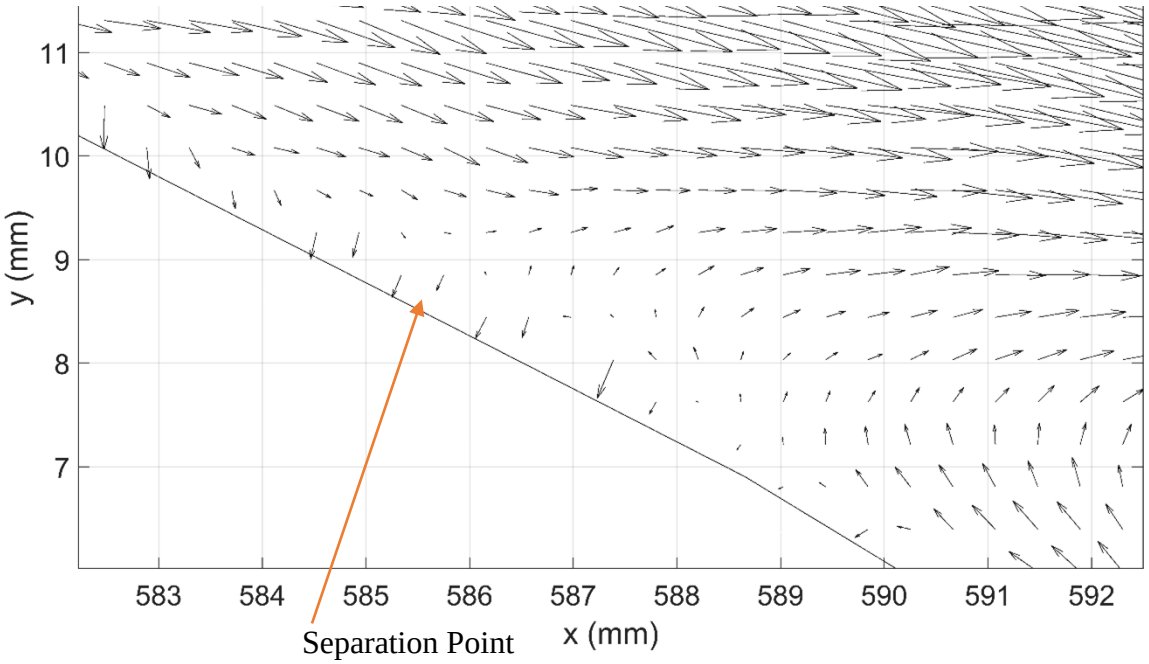

Fig.5.2. Identification of separation point by velocity vector field.

5.3.3- Measurements of Flow Features by PIV Technique-Unactuated Case

In this section the results of experiments by Particle Image Velocimetry (PIV) technique for baseline case is discussed. For PIV measurements, 100 images in double frame mode were acquired for each case. Investigation of velocity vector fields (see Fig.4.20) shows the complexity of flow behavior in the wake region. It is not easy to describe flow feature quantitatively and location of critical points such as separation and reattachment points are changing instantaneously. For example, comparison of Figs.4. 20(a) and 4.20(b) show the movement of the core of separation bubble from X= 610 to upstream at around X= 605 mm. Additionally, the width of recirculation region is changed. This mixing in the wake region relevant to the separation and recirculation causes more entropy generation and consequently more losses. Indeed, turbulent eddies which are produced due to the separation get their additional kinetic energy from the potential energy of the flow (energy conservation principle) and consequently the pressure drag is increased due to the separation.

A good filtering of instantaneous velocity field has been obtained by application of complex cleaning methods such as background subtraction, mask application, etc. at the different stages of post-processing of PIV results to increase the signal to noise ratio and to avoid misinterpretation of flow separation phenomenon, but these techniques are not capable of removing the outliers in the results due to the dependency of the removal criteria to the choice of a threshold value (Westerweel and Scarano, (2005), Cavazzini et al. (2012)). The most common technique to overcome this problem to be able to interpret physics of flow separation quantitatively in the wake region, is to average the instantaneous PIV flow fields, so the average of 100 images is calculated to enhance the quality of the resulting flow field.

The average of velocity vector and magnitude fields, the streamlines, the vorticity contour as well as RMS velocity profiles are shown in Figs.4.21-24, respectively. The average velocity vector field (shown in Fig.4.21(a)) depicts that the reattachment point with zero value of velocity which is between forward and reverse flow downstream of the separation point is located at X = 621.05 mm. The separation point with zero value of shear stress which is between forward and reverse flows is identified at X= 582 mm. Therefore, the

estimated recirculation region length is about 39.05 mm. The closer view of the average velocity field with higher display grid factor in Regions A and B from Figs.4.21 (a, b) are shown in Figs.4.21 (c, d). The figures show the physics of flow near the reattachment point with reverse and forward flow with very low velocity values upstream and downstream of the reattachment point, respectively. The vorticity contour profile show large vortical structure downstream of the hump trailing edge due to the flow separation behind the hump as shown by Fig.4.23. As it can be seen, the maximum value of rotation happens in very near hump wall in the wake region and near to hump trailing edge.

The streamline profile (Fig.4.22) shows the border between the region of recirculating flow and free flow, as it can be seen, the maximum predicted width of wake region above the hump trailing edge is around Y= 10-12 mm, this is the same location of Maximum RMS velocity predicted by Hot wire results. Therefore, it can be concluded that the maximum velocity fluctuations occurs around the border of recirculating flow region and free flow.

Velocity fluctuations measurement by PIV predicts a maximum RMS value at Y=12 mm above the hump trailing edge shown by Fig.4.24 which is in a good agreement with hot wire anemometry technique results. As it is clear from both vorticity and RMS velocity profiles, the fluctuations are considerable until height of 25 mm above the trailing edge and it is decreased for heights higher than this value.

As in the current research, the flow experiences severe fluctuations in the wake region and the flow gradient in direction perpendicular on the hump wall is high, therefore, the elliptical weighting factors (2:1) also is applied for final interrogation window size of 32 pixel × 32 pixel with 50 percent overlap which improves the accuracy of the vector field computation.

5.4- Flow Separation and its control over the Hump Model- Actuated Case

In this section, the results of HWA measurements, the PIV results on the hump surface for actuated cases area discussed.

5.4.1- Measurements of Flow Features by HWA Technique-Actuated Case

The successful implementation of synthetic jet actuators depends on several geometrical and operational parameters such as the location of actuators, actuation frequency, peak exit jet velocity to free stream velocity ratio (VR) as well as the actuation waveform. However, generally it is recommended that the actuators should be positioned close to the separation points but in this research the actuators array is positioned at different angles to see how the velocity fluctuations as well as the reattachment point and separation point are affected.

The profiles of velocity fluctuations shown by Fig.4.25 reveals that the actuators have positive effect to suppress the velocity fluctuation in near wall regions (Y<10 mm) for all angles. However, for angles 17.5, 20 and 25 degrees, not only the velocity fluctuations is not suppressed anymore in upper layers , even it is slightly increased in comparison with the unactuated case, the effects of actuators is faded away at layers upper than Y= 45 mm. The reason for increasing the velocity fluctuations in intermediate layers for the above-mentioned angular positions and specifically for angular position of 20 and 25 degree can be relevant to the closeness of these positions to the predicted location of separation point which is around angular position of 26.1 degree. Probably the generated vortex rings by actuators do not interact properly in the lower layers with cross flow and diffuses to the upper layers by making more fluctuations and without perfect effect on the vortex trajectory in upstream of the separation point.

Fig.4.26 depicts the influence of different waveforms including Sine, Square, Pulse and Triangle waves on the velocity fluctuations in the wake. As it is clear all periodic waveforms have a positive influence to suppress the flow oscillations, however their performance is not same in different shear layers. For example, the Sine wave has a better performance in very near wall region (Y<1.5 mm) to reduce fluctuations. Pulse function is slightly more effective than other waveforms in layers with 1.5 mm < Y <5.5 mm.

The square function has a better performance for upper layers with Y >8 mm which is probably due to the more momentum injection and mixing in the boundary layer and faster transition between blowing and suction phases. The Triangle function is the less effective waveform to reduce the fluctuations in the wake region. The hot wire measurements at the

actuator outlet show that peak exit jet velocity for both Square and Pulse Waves are higher than Sine and Triangle functions at the same actuation voltage and frequency. The measurements show that the implementation of Square and Pulse increase the peak exit jet velocity ratio from 1.5 to 1.85 which is more effective to suppress the velocity fluctuations as well as to reduce the recirculation width as it is confirmed by PIV results.

The magnitude of generated peak jet velocity by Square and Pulse wave is about 23% bigger than the generated ones by Sine and Triangle waves. To achieve the VR of 1.85, the Sine and Triangle waves should be implemented at voltage of 29 Vp-p. Therefore, energy costs can be reduced by implementation of Square and Pulse wave instead using Sine wave and Triangle wave.

5.4.2- Measurements of Flow Features by PIV Technique- Actuated Case

In the first phase of study of actuated case by PIV technique, while the ratio of peak exit jet velocity to free stream velocity of cross flow (VR) was kept constant at value of 1.5, the angular position of actuators array was changed to study the influence of angular positions of actuators on the characteristics of recirculating flow. Same selected angular positions in HWA study were used in this study.

The investigation of the velocity vector fields and streamline profiles for angular position of 0-degree (shown by Figs.4.27-4.29) shows that the actuators are not effective at this position to change the wake region features considerably. Comparison of instantaneous velocity vector fields (Figs.4.27 (a , c, d)) with corresponding instantaneous vector fields of unactuated case shows the core of separation bubble is around location of X = 610 mm and the width of recirculation region has not been influenced by synthetic jet actuators. As it is seen from velocity vector fields (Fig.4.28) and the streamlines profile (Fig.4.29), the location of reattachment point is almost constant in comparison with unactuated case, however the location of separation point slightly is pushed down-stream. It should be noted that the reattachment point for position of 0-degree is identified at location of X= 621.6 mm which is slightly (0.55 mm) more than the unactuated case. This difference should be relevant to the errors, or slightly different free stream velocity in comparison with the unactuated case as it was not possible to set the wind tunnel free stream velocity

at exactly same value for all cases due to the limited resolution of the frequency of fan invertor (which is 0.1 Hz) and atmospheric conditions.

The comparison of vorticity contour for angular position of 0-degree (Fig 4.30) with the corresponding profile for unactuated case, shows the injection of vortical structure in wake region has no considerable effect on the vorticity magnitude in lower layers in wake region. However, the vorticity magnitude increases in upper layer while the vortex trajectory is not affected. Apparently, generated vortical structures are not highly coherent when they reach to the place where separation occurs and therefore an effective interaction with separation boundary layer is not happened.

Fig.4.31 shows the suppressing of velocity fluctuations in the intermediate layers of wake region and close to the location of synthetic jet actuators (around X = 580 mm) in comparison with corresponding profile from unactuated case (Fig.4.24). However, SJAs are not effective enough to greatly affect the size of separation bubble as they are relatively far from the separation point (around 26.35 mm).

Figs.4.32-4.36 depict the instantaneous and average velocity fields, streamlines, vorticity contour as well as RMS velocity profile for angular position of $\phi = 9.50^{\circ}$. Figs.4.32 (a) and (c) depict the contraction of recirculation region and simultaneously the near wall regions have been reenergized as the vectors size are increased due to the transfer of momentum from higher layers to lower layers. The core of separation bubble is pushed back to upstream of X = 610 mm as it seen from Figs. 4.32 (a, c and e) as well as Fig.4.33. This positive influence of actuators is also confirmed by profiles of streamlines as shown by Fig.4.34. The comparison of RMS velocity profile (shown in Fig.4.36) with unactuated case and also with actuated case with angular position of $\phi = 0^{\circ}$ show that the level of fluctuations in near wall region and in the domain of (X = 590 mm-610 mm) has been decreased. This can be relevant to the transfer of higher-energy fluid from upstream and upper layers to downstream and lower layers by generated vortical structures by synthetic jet actuators. This can be confirmed by carefully investigation of vorticity contour (Fig.4.35) by vorticity contours of unactuated case as well as actuated case with angular position of $\phi = 0^{\circ}$. Comparison of results shows the diffusion of vortical structure to the lower layers by increasing actuators angular position to $\phi = 9.50^{\circ}$, e.g. in domain of X =

600-610 mm, the diffusion of vortical structures occurs (and as a result higher momentum) to layers below Y = 5 mm. Altogether, the reattachment point is pushed upstream around 4.8 mm and separation point is pushed down stream around 3.6 mm, therefore the length of recirculation region is decreased 21.56%. This case also have been investigated numerically (in addition of unactuated case) and the results will be compared with numerical simulations.

The profiles of instantaneous velocity vector fields, average velocity fields of 100 pairs of images as well as the streamlines and vorticity and RMS velocity magnitude profiles for angular positions of 5^o, 12.5^o, 17.5^o, 20^o and 25^o are provided in Appendix D. The investigation show by gradual increase of angular position of actuators, the generated vortical structures are more influential to affect the separated boundary layer as the actuator array is getting closer to the predicted location of separation point in unactuated case which is at X = 0.582 m.

As the velocity vectors and streamlines profiles depict, the best performance of synthetic jet actuators with velocity ratio of 1.5 is observed at angles of 15 and 17.5 degree by pushing back the reattachment point about 8.05 and 6.17 mm, respectively as shown by corresponding figures.

Figs.4.37-4.41 depicts the velocity vectors fields, streamlines, vorticity contour as well as RMS velocity profile for angular position of $\phi = 15^{\circ}$. Investigation of instantaneous velocity vector fields (Figs.4.37 (c) and 4.37(e)) show the positive effect of actuators on the movement of core of recirculating flow to upstream near the hump trailing edge, the instantaneous velocity vectors show the shrinkage of wake region and their comparison with the corresponding vector fields of the unactuated case shows the flow struggling to reattach upstream.

The profiles of average velocity vectors and streamlines (Figs.4.38-39) also show the movement of the location of core of separation bubble toward the hump trailing edge. As it is clear from figures, the flow field is changed after switching on synthetic jet array. The comparison of vorticity contours from angular position of 0-degree to angular position of 15-degree show the gradual increase of vorticity magnitude and simultaneously the vortex

trajectory approaches to the hump wall (see Fig.4.40), whatever the actuators array gets closer to the location of separation point. The depth of diffusion of vortical structure is increased and even the near wall region around X = 620 mm are affected. By applying the synthetic jet actuators, the congested, continuous large vortex structures in the wake region are broken down and the near-wall flow is re-energized to overcome flow separation. The periodic vortex structures form at the orifice outlet, and convect downstream, and the vortices lead to the stabilization of the boundary layer flow and reduce the local adverse pressure gradient. Consequently, the separation of the flow is delayed.

RMS velocity profile (Fig.4.41) show almost the same trend as described for angular position of $\phi = 9.5^{\circ}$, however, the fluctuations slightly is increased out of wake region which can possibly relevant to the escape of some vortical structure to upper layers out of wake region and increasing mixing and as a results more velocity fluctuations.

Figs.5.3 and 5.4 summarize the influence of actuators position on the location of separation and reattachment points for VR of 1.5. The results show that the best performance of actuators to reduce the length of recirculation region is achieved at angles between 15º -17.5º for VR of 1.5.

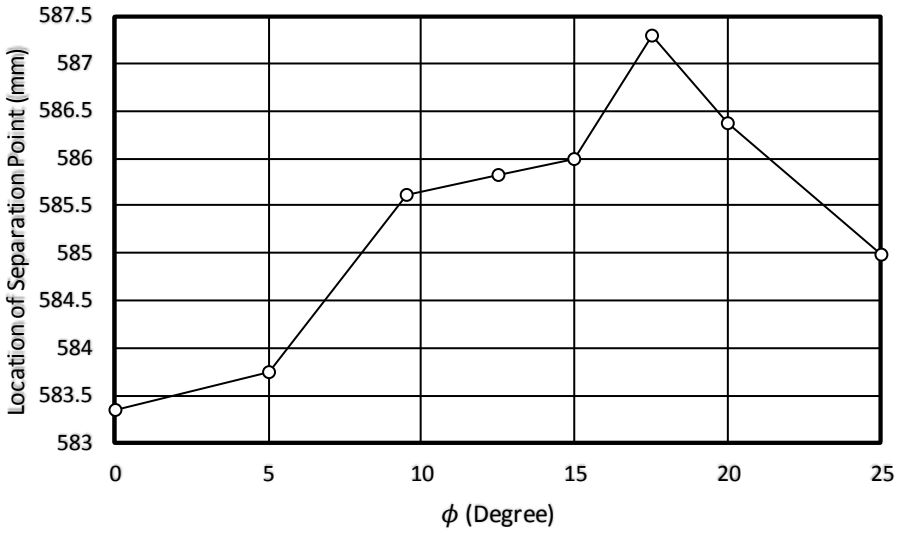

Fig 5.3. SJAs angular position influence on the separation point location, VR=1.5, Sine Wave, $U_{\infty} = 7\ m/s$.

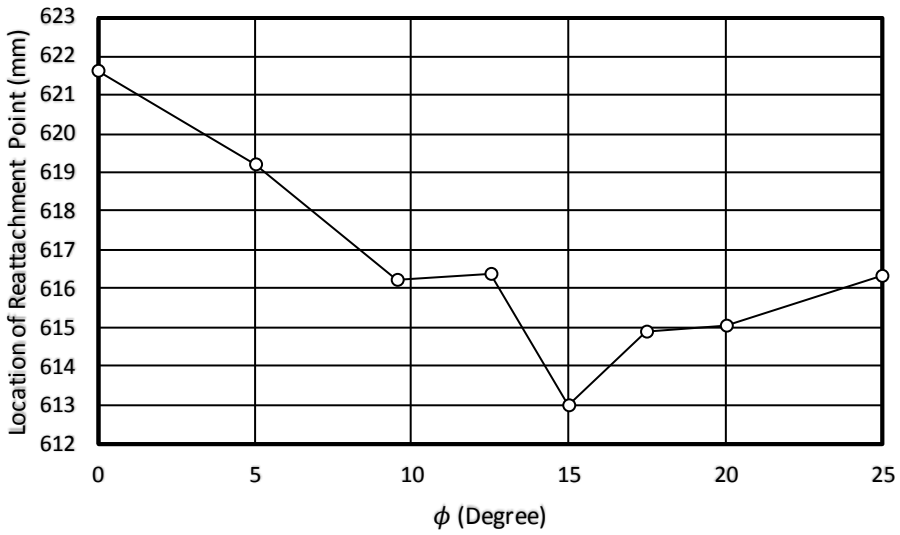

Fig 5.4. SJAs angular position influence on the reattachment point location, VR=1.5, Sine Wave, $U_\infty = 7\ m/s$.

The profile of the percentage of the reduction of recirculation region length is shown in Fig.5.5. As it is clear from figure, the best performance of actuators happens at $\phi = 15^\circ$ with 30.86% reduction of recirculation region length and angular position of $\phi = 0^\circ$ is the less effective angular position to influence the characteristics of the wake region.

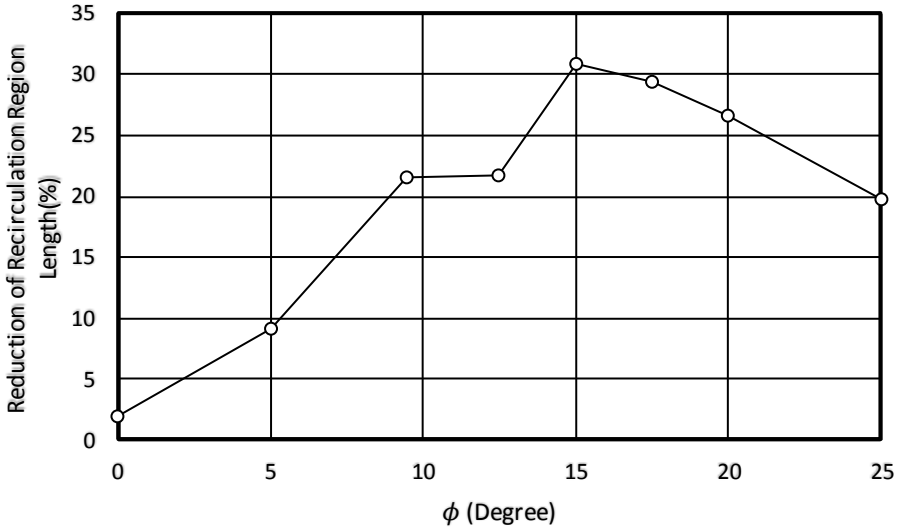

Fig 5.5. SJAs angular position influence on the reduction of recirculation region length, VR=1.5, Sine Wave, $U_\infty = 7\ m/s$.

The comparison of the results for different angular positions of actuators array with the angular position of separation point (which is located at angular position of 26.1°), reveals the best location for actuators array is somewhere upstream and close to the separation point location. For example, the distance of orifices on the hump surface for angular positions of $\phi = 15^{\circ}$ and $\phi = 17.5^{\circ}$ from the separation point location is 11.2 and 8.7 mm, respectively.

In the second phase of study, while the position of actuators was kept constant at angular position of $\phi = 15^{\circ}$, the velocity ratio VR was changed for selected values of 1.15, 1.50, 1.85 and 2.2. Figs.4.42-4.46 depict the instantaneous and average velocity fields, streamlines, vorticity contour as well as RMS velocity profile for velocity ratio of 1.15 at angular position of $\phi = 15^{\circ}$. As it is shown in Figs.4.42 (a, c, e), 4.43 and 4.44, the core of recirculation region has been moved downstream by decreasing the velocity ratio. The investigation of results for velocity ratio of 1.15 shows that decreasing the velocity ratio to value below the velocity ratio of 1.50 would not improve the performance of actuators and even it is deteriorated. The reason should be relevant to the lower momentum of exit jet for velocity ratio of 1.15 and consequently the generated counter rotating vortices can not reach to the upper layers with higher momentum and as a results the weakened boundary layer cannot be re-energized.

Comparison of vorticity contour (Fig.4.45) with vorticity contour of case with velocity ratio of 1.50 at angular position of $\phi = 15^{\circ}$, shows the existence of bigger congested and unbroken vortical structure in the wake region due to abovementioned reason.

Fig.4.46 shows the velocity fluctuations has been increased by decreasing the velocity ratio to 1.15 in comparison with case of velocity ratio of 1.50.

Figs.4.47-4.51 show the results for the profiles of instantaneous and average velocity vectors and magnitudes fields, streamlines profiles, vorticity contours as well as RMS velocity for velocity ratio of 1.85 at angular position of $\phi = 15^{\circ}$, respectively. The investigation of instantaneous vector fields for velocity ratio of 1.85 show the effectiveness of synthetic jet actuators to reduce both the width and length of recirculation region. As it can be seen from the Figs.4.47 (c) and 4.47 (e), the core of separation bubble

has been pushed back around the hump trailing edge and even upstream of the hump trailing edge. Interestingly the near wall regions have been reinforced and transfer of momentum from upper layers to the near wall regions is obvious as the vectors magnitude have been increased in near wall regions. Comparison of Figs.4.20 (a, c , e) from unactuated case with Figs.4.47 (a ,c, e) in near wall region in domain of X = 580 mm – X =590 mm confirms the transfer of momentum and reinforcing the retarded boundary layer. The average velocity vector fields as well as streamlines profile (Figs.4.48 and 4.49) show the considerable effect of synthetic jet actuators on the characteristics of wake region in comparison with unactuated case.

Comparison of contour of vorticity shown in Fig.4.48 with corresponding figure from un actuated case show the considerable effect of synthetic jet actuators on the vortex trajectory. The vortex trajectory it is pushed down form the height of around 25 mm to below the height of 20 mm and clockwise vorticity (negative values) increases in the vicinity of the hump wall.

Figs.4.52-4.56 show the results for the profiles of RMS velocity, instantaneous and average velocity vectors and magnitudes fields, streamlines profiles and vorticity contour for velocity ratio of 2.2 at angular position of $\phi = 15^{\circ}$, respectively.

Investigation of all figures reveals the overall performance of synthetic jet actuators is very close to the case of velocity ratio of 1.50. However, the profile of RMS velocity (Fig.4.52) shows higher velocity fluctuations in comparison to other cases, which probably is relevant to more momentum injection into flow field due to more powerful exit jet at orifice outlet with velocity of 15.4 m/s.

Investigation of all cases shows the best performance of synthetic jet actuators occurs at velocity ratio of 1.85. The influence of VR on the location of the reattachment point, separation point and the length of recirculation region is summarized by Table 5.1.

Table 5.1 Influence of Velocity Ratio VR on the Wake Region Features- Sine Wave.

VR	*1.15*	*1.50*	*1.85*	*2.2*
Location of Separation point (mm)	*586.39*	*586*	*588.6*	*586.44*
Location of Reattachment point (mm)	*615.35*	*613*	*611*	*614*
Reduction of Recirculation Region Length (%)	*25.84*	*30.86*	*42.63*	*29.42*

As it is shown by Table 5.1, the increase of VR to value of 1.85 reduces the length of recirculation region around 12 % more than the case with VR of 1.5, the results show that the depth of diffusion of generated train of vortex rings is not enough with velocity ratios of 1.15 and 1.50 to interact with the upper layers to bring high momentum fluid into the retarded boundary layer. On the other hand, increasing the velocity ratio to values beyond velocity ratio of 1.85, not only does not improve the performance of synthetic jet actuators, but even the performance of actuators is deteriorated in comparison with case of velocity ratio of 1.85. However, using the velocity ratio still has positive effects on the characteristics of the wake region and its effectiveness is very similar to the velocity ratio of 1.50. Deterioration of performance of actuators by increasing the velocity ratio beyond value of 1.85, can be probably relevant to escape of generated vortex rings or generated counter rotating vortices to very higher layers out of the boundary layer without traveling to downstream to transfer higher momentum fluid to retarded boundary layer and increasing the mixing.

Therefore, the selection of optimum velocity ratio is a key parameter to have a proper interaction of vortex rings in appropriate layers to transfer higher momentum fluid from upper layers to the low momentum layers in the weakened boundary layer.

Generally, the synthetic jet actuators influence the flow field in three stages: first, impinging of cross flow with the generated train of vortex rings leads to production of pairs of counter rotating vortices, then interaction and mixing of the generated pairs of counter rotating vortices with higher momentum flow in upper layers occur and large-scale flow structures relevant to the separated shear layer are broken down into small-scale structures, and finally higher momentum fluid is transferred to near wall region and

convect downstream and the retarded boundary layer is reenergized and as a results flow separation is delayed.

Comparison of vorticity contours for all cases shows that the vorticity generation on the wall and the vicinity of hump trailing edge is reduced in actuated mode, the same trend was reported by Suzuki (2006) via a DNS method. Comparison of RMS velocity profiles of unactuated and actuated cases shows the suppression of velocity fluctuations in upper layers by switching of actuators and moving the region with high fluctuations toward the hump wall as shown by Figs.4.24 and 4.49.

In the last phase of experimental study, the effects of Square wave on the separation control is investigated for selected values of velocity ratio including 1.5, 1.85 and 2.2.

Figs.4.57-4.61, show the instantaneous and average velocity fields, streamlines, vorticity contour as well as RMS velocity profile for Square wave and velocity ratio of 1.85 at angular position of $\phi = 15^{\circ}$, respectively.

As it is obvious, the core of separation bubble has been pushed back significantly toward the hump trailing edge in comparison with the unactuated case as well as the width of recirculation region is reduced. This positive influence can be seen in Figs. 4.57 (a, c and e). Such as Sine Wave case with the VR of 1.85, more and bigger vortical structures are generated by actuators upstream of the separation and then bigger vortical structures around reattachment point and near wall region for unactuated case are broken down to smaller ones after switching on actuators. Investigation of average vector field (Fig.4.58) and streamlines profile (Fig.4.59) show the movement of reattachment point around 10.8 mm upstream and separation point around 7 mm downstream, respectively. Therefore, the length of recirculation region is reduced about 44.17 %, which is slightly more than the reduction achieved by implementation of Sine wave at the same velocity ratio.

From diffusion equation, the vorticity flux on the wall is proportional to the pressure gradient (Koumoutsakos et al. (1994)), therefore the clockwise vorticity (negative value) is produced more upstream of the separation point in a favorable pressure gradient, while the counter clock wise vorticity is produced more in an adverse pressure gradient, by switching on the SJAs, the adverse pressure gradient is decreased and consequently the

production of counter clock wise vorticity on the wall is decreased as it can be seen from vorticity profiles (see Figs.4.60 and 4.23). Trajectory of vortex is changed toward the hump surface and generally to near wall region in actuated case, the effect of SJAs to change the vortex trajectory toward the wall also was observed by Tang et al. (2014) and Salunkhe et al (2016) through tomographic PIV measurement for flow control over a straight wing model.

Figs.4.62-4.66, show the velocity vector fields, streamlines, vorticity contour as well as RMS velocity profile for Square wave and velocity ratio of 2.2 at angular position of $\phi = 15^{\circ}$, respectively. The trends and overall performance of synthetic jet actuators is very close to the corresponding case of Sine wave.

The influence of velocity ratio on the location of the reattachment point, separation point and the length of recirculation region is shown by Table 5.2.

Table 5.2 Influence of Velocity Ratio VR on the Wake Region Features -Square Wave.

VR	*1.50*	*1.85*	*2.2*
Location of Separation point (mm)	*585.60*	*589*	*586*
Location of Reattachment point (mm)	*615.96*	*610.80*	*613.64*
Reduction of Recirculation Region Length (%)	*22.25*	*44.17*	*29.23*

The results show that the performance of Sine Wave is slightly better than Square wave to suppress fluctuations in the wake region for VR value of 1.85, however the effect of both waves on the reduction of recirculation length is almost same.

5.5- Flow Separation and its control over the Hump Model by Numerical Simulations

In this section, the results of simulations of single synthetic jet actuator in quiescent conditions (no cross-flow) as well as simulations of flow separation over the hump model for both baseline and actuated cases are discussed and the results are compared with experimental results by HWA and PIV techniques.

5.5.1 Unsteady State – Unactuated Case

For this case, the solution was stabilized after 12000 iterations while the time step was considered 0.000015s, which gives the maximum Courant number of 0.80. Keeping the Courant number below 1 helps to maintain both accuracy and stability of the solution. Figs.4.67 and 4.68 depict the turbulent kinetic energy profile and the velocity boundary layer profile as well as at X= 0.3 m, respectively. As it was expected, the maximum of velocity fluctuations occur in near wall region (Y = 2 mm) and it is disappeared out of boundary layer. The time-averaged results predict the thickness of boundary layer around 7 mm at a distance of 0.3 m from the test section inlet (X=0.3 m). The predicted value is in high agreement with the predicted hot wire results as shown in Fig.5.6. Both methods predict 7mm thickness for the boundary layer. It should be noted that due to the lack of previous numeri results for this geometry and flow conditions, it was not possible to do a numerical verification. Also, the higher resolution was not simulated because of excessive computational cost as well as high agreement of both numerical and experimental methods in prediction of boundary layer thickness, which shows the y^+ value has been chosen correctly to resolve the boundary layer,

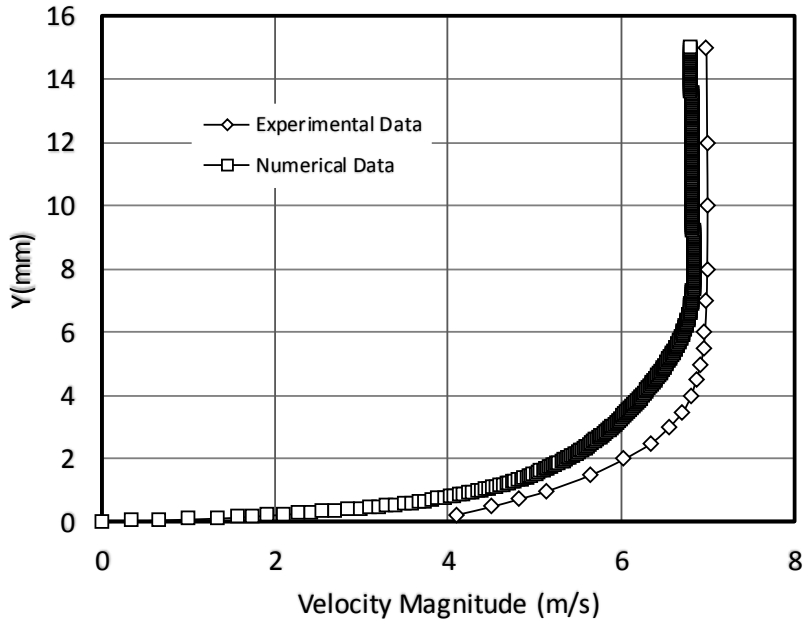

Fig 5.6. Prediction of boundary layer thickness- numerical data vs. experimental data, $U_\infty = 7\ m/s$.

The profiles of turbulent kinetic energy, velocity and pressure contours as well as velocity vector field and streamlines are depicted in Figs 4.69-4.73, respectively. As it is expected, the most energy dissipation occurs in the wake region downstream of the hump apex due to high velocity fluctuations in this region (Fig.4.69). Indeed, the conversion of potential energy of the flow to kinetic energy of the eddies occurs in the wake region. Velocity contour (Fig.4.70) as well as velocity profile at X = 0.3 show that the flow has been fully developed upstream of the hump leading edge. The maximum velocity and minimum pressure occur around the hump apex as it is clear form velocity and pressure contour in Fig.4.71. The flow experience the maximum pressure at hump leading edge due to sudden impingement to the hump body at hump leading edge. The predicted reattachment point with zero value of velocity which is between forward and reverse flow downstream of the separation is at location of X = 0.624 m, the prediction is in good agreement predicted location by PIV experiment which is at location X = 0.621m. Investigation of velocity vectors (Fig.4.72) shows the flow is separated approximately at X =0.575-0.580.

The profile of streamlines shown in Fig.4.73 has been attained by employing adaptive integrator (Runge-Kutta 4-5). The seeds for the streamlines are generated by using a high resolution line source in Y-direction at Y= 0.607 which is passed through the wake region. The predicted reattachment point by streamlines profile is in good agreement with PIV results. The identification of the location of separation point with zero value of shear stress which is also between forward and reverse flows is not easy as reattachment point as it is hard to predict the separation point merely with velocity vectors and streamlines profiles. Therefore, it is tried to also use the surface shear stress as well as surface pressure profiles on the hump wall to get a better approximation from the location of separation point in addition of information of pressure and shear stress values on the hump surface.

The profiles of average surface pressure and standard deviation of surface pressure as well as minimum wall shear stress are shown in Figs. 4.74-4.76, respectively. The profile of shear stress shows the minimum of wall shear stress occurs downstream of the hump trailing edge in the wake region and the maximum value occurs at the hump apex which the maximum velocity is attained due to the Venturi effect. It should be noted that a tiny recirculation region also has been predicted above the hump leading edge due the sudden

changes in pressure because of hump geometry. The sudden changes of the values of pressure and wall shear stress around region between locations X = 0.575 – X = 0.580 should be relevant to the separation phenomenon, which is in agreement with the velocity vector filed. The predicted location for separation point by PIV results is at X = 0.582 which is close to the predicted value by numerical analysis.

It should be noted the turbulence length scale is considered equal to the honeycomb pitch, this physical quantity which describes the size of the large energy-containing eddies in a turbulent flow can be related to the physical size of the problem . Because the turbulence eddies are restricted by the geometry of the problem, e.g. side walls of the test section, then this length scale logically should not be larger than the dimensions of the model and test section, otherwise it means that the turbulent eddies are larger than the problem size which is not meaningful from physical point of view.

5.5.2 Unsteady State –Actuated Case

In this section, the results of simulations of single synthetic jet actuator in quiescent conditions (no cross-flow) and the interaction of synthetic jet actuators with cross flow are discussed and the results are compared with experimental results by PIV technique.

5.5.2.1- Single SJA in Quiescent Conditions (No Cross-Flow)

As explained earlier, the actuator is simulated in quiescent conditions to maintain the velocity ratio of 1.5 at the outlet of orifices. To simulate the movement of cavity diaphragm for generation of vortex rings at the orifices outlet with zero net mass flux, a time varying boundary condition as stated by Eq. (3-37) is assumed at the diaphragm patch which is corresponding to the cavity inlet. This amplitude value is found by using slaveMesh for quiescent flow conditions. After, a few trial and errors, the value of 0.0365 m/s for velocity amplitude is found to satisfy the desired boundary condition at the orifices outlet. It should be noted that the continuity equation does not work for the actuator and we cannot simply relate the velocity values at the diaphragm patch to the orifice outlet by continuity equation due to the net zero mass flux feature of actuator. The value of maximum velocity at the outlet of orifice is stablished after 15 cycles. However, the smaller time step ($1 \times 10^{-6} s$) is considered for actuated case in comparison to unactuated

case to capture better the interaction of small Vortical structures with the cross flow, but it was found that the solution is time dependent for time steps equal or smaller than $1.5 \times 10^{-5} s$.

The history of velocity component in y direction which is the dominant component is shown in Fig 4.77. It should be noted that the velocity component magnitude in x and z directions are not considerable in comparison to velocity component magnitude in y direction because the angular position of actuator is 9.5 degree with respect to y-axis and consequently the exit jets of orifices are mainly in y-direction. The pressure and velocity contours in blowing phase are shown by Figs. 4.78 and 4.79, respectively. As it is seen the fluid reaches to the maximum velocity (or minimum pressure) before the orifice exit and some kinetic energy loss occurs due to the area expansion at the orifice outlet and consequently the exit jet experiences a velocity magnitude drop out of orifices.

The profiles of velocity fields in X-Y and Z-Y planes as well as the vorticity contour in log-scale are depicted by Figs. 4.80-82, respectively. The evolution of vortex rings out of orifices can be seen by velocity vectors (Fig.4.80 (b)) and vorticity contour shown in Fig.4.82. Fluid is drawn into the cavity from environment around the orifice outlet during the piezo electric diaphragm's down-stroke. During the diaphragm up-stroke, fluid is ejected through the orifice, producing a vortex ring as shown by Fig.4.80. Vortex rings are generated in both suction and blowing phases, and by repeating cycles, a sequence of vortices is produced that propagate away from the orifice under their own self-induced velocity.

The maximum of vorticity strength occurs at orifice outlet and its strength is faded away at a distance of around 9 mm above the orifice, this means that the vortex ring is sufficiently strong to cover the whole boundary layer thickness to interact with the cross flow to generate the pairs of counter rotating vortices to influence the boundary layer. The vorticity profile in Z-Y plane and along line Z= 0.0006 m in blowing phase is shown by Fig.4.83. As it is seen, the maximum of vorticity occurs immediately before orifice inlet and orifice outlet and its experiences a severe drop after orifice outlet. It should be noted that the distance of $0.026792 \leq Y \leq 0.028271$ with zero vorticity is corresponding to the orifice wall.

5.5.2.2- Interaction of Synthetic Jet Actuators with Uniform Cross-Flow

In this section the results of the simulation of the interaction of actuators with uniform cross flow is discussed. The instantaneous and time- averaged velocity fields for different times are shown by Figs.4.84-4.88.

The instantaneous velocity fields show the unsteadiness of flow in the wake region, in addition of recirculated flow, the wave-like patterns is seen downstream of the hump trailing edge (Figs.4.85 and 4.87). This wave-like patterns is not seen in unactuated case probably due to three reasons: firstly, the flow is mainly 2 dimensional in absence of synthetic jet actuators, secondly, the periodic feature of synthetic jet actuator is added to the flow feature in actuated case and finally the flow field above orifices is not symmetric with respect to the midplane (Z=0). The investigation of flow field shows that there is no recirculated region 15 mm downstream of hump trailing edge however the wave like pattern is seen in earlier times of solution downstream of this point. Therefore, the results show the effectiveness of synthetic jet actuators to push back the reattachment point to upstream and the flow separation is delayed. It should be noted that the predication of wave-like patterns with RANS simulation is in agreement with prediction of flow filed by PIV results as show in relevant chapter.

The time averaged results show the reattachment point is pushed back to around 8 mm downstream of the hump trailing edge (Fig.4.88). The predicted reattachment point by time averaged PIV results for angular position of 9.5 degree is around 16 mm downstream of the hump trailing edge as it was discussed in previous chapter and shown in Fig.5.1. Two small recirculation regions in neighborhood of X = 0.09 m upstream of the hump trailing edge is predicted by RANS simulation which is different to some extent by flow pattern predicted by PIV result. The reasons for difference can be relevant to limited size of the used interrogation windows to calculate velocity vectors based on cross-correlating the intensity distributions and in addition the PIV method is not able to measure velocity component along the z-axis (towards / or away from the camera). Therefore, this component might not only be missed, it probably can introduce an interference in the data for the x/y-components. Of course, these problems do not exist in Stereoscopic PIV, as

two cameras are used to measure all three velocity components. The drawbacks of URANS technique itself should not be forgotten.

The profiles of time averaged velocity contour, pressure contours and average wall shear stress on the hump surface as well as vorticity profile in near wall regions are shown by Figs.4.89-4.92, respectively. The comparison of velocity and pressure contours (Figs.4.89 and 4.90) with the unactuated case show the effectiveness of synthetic jet actuators on the reduction of the size of separation bubble and width of recirculation region. The profile of average shear stress shown in Fig.4.91 on the part of hump surface contains synthetic jet actuators shows the trace of generated pair of counter rotating vortices on the hump surface (due to the interaction of vortex rings with the cross flow), the pair of counter rotating vortices have responded to surface shear stress and has formed a pattern as it is seen by Figs. 4.91. Fig.4.92 show the difference between the magnitude of the vorticity relevant to pairs of the counter rotating vortices with adjacent flow field in near wall regions. It seems if the distance between the orifices was slightly smaller, the actuators were probably more capable to cover the regions with lower shear stress to avoid the starting of instabilities of the flow and the onset of separation.

Fig.4.93 shows the profile of average shear stress on the surface of the hump model and floor of the test section, as it can be seen the flow separation is delayed by moving the separation point toward the hump trailing edge. The contour of reattachment point shows the location is not constant in stream wise direction, and it is changing between 10 mm to 20 mm downstream of the hump trailing edge which means a reduction of 5 to 15 mm of recirculation length by pushing back of the reattachment point in actuated case. The delay of boundary layer flow separation is caused by introduction of vortex rings and consequently generation of pairs of counter rotating vortices into the boundary layer by implementation of synthetic jet actuators. The generated vortical structures interact with the cross flow and transfer the high momentum flow from outer flow into the near wall regions and the weakened boundary layer is re-energized. Based on PIV results, the reattachment point is pushed back to around 16 mm downstream of the hump trailing edge. Despite the drawbacks of 2D PIV measurement, which was mentioned earlier as well as

the drawbacks of URANS technique itself, the predictions of numerical simulations are in reasonable agreement with PIV results.

5.6- Summary

The flow separation control over the hump model investigated by using synthetic jet actuators. The effects of angular position of actuators, velocity ratio VR as well as waveform was investigated by using both Hot Wire Anemometry (HWA) and Particle Image Velocimetry (PIV) techniques. The hot wire anemometry results showed the effectiveness of synthetic jet actuators for all angular positions while the angular position was changed from the hump apex to near the hump trailing edge, however velocity fluctuations in upper layers was increased for angular positions close to hump trailing edge. The effects of 4 waveforms was investigated at same voltage and frequency of actuation and result showed the Square wave has better performance to suppress the velocity fluctuation with generation of higher velocity ratio VR. The PIV results revealed the best performance of actuators for VR of 1.5 occurs at angle of $\phi = 15^{\circ}$. The influence of velocity ratio on the synthetic jet actuators performance was studied and the results show that better flow separation control can be achieved with velocity ratio of 1.85 with 42.63 and 44.17% reduction of the length of recirculation region by implementation of Sine and Square waves, respectively.

Wall resolved RANS simulations of fluid flow over the hump model were performed by employing K-Omega SST model by OpenFOAM software. Merging and stitching techniques were utilized to get the best features of BlockMesh and snappyHexMesh grid generation tools of OpenFOAM software which was very helpful to save computational cost. Results show the effectiveness of synthetic jet actuators by delaying the flow separation and pushing back the reattachment point toward the hump trailing edge due to flow structure changing by interaction of generated vortical structures with separated shear layers. However, the predictions of separation flows in fluid dynamics field always is challenging but the comparison of numerical results with experimental data shows that the K-Omega SST model can be used as a good strategy for prediction of flow separation and its control.

Chapter 6- Conclusions

Referring back to section 1.2 of Aim and Objectives of the research, the following conclusions can be drawn from the current study:

1. Following objective 1, a low speed closed circuit wind tunnel with velocity range of 0-25 m/s is designed and manufactured to enable current project. The Hot Wire Anemometry (HWA) measurements showed an almost uniform velocity magnitude outside of the boundary layer with reasonable low turbulence intensity of the wind tunnel.
2. A hump model has been designed and manufactured at the workshop of University of Huddersfield to enable current research. This hump model can be used for further studies about flow separation and its active flow control. Pressure measurement taps have been predicted for future studies to study the flow features in near regions of the hump wall. This corresponds to objective 2.
3. Objective 3 has been achieved by geometrical optimization of synthetic jet actuators array through a series of Hot Wire Anemometry (HWA) experiments in quiescent conditions (without cross flow) by considering five different cavity configurations. Higher exit jet velocity up to 15.5 m/s can be achieved in allowable voltage range of piezo electric diaphragms.
4. Investigation of the characteristics of separated flow over hump model was carried out by identification of the onset of flow separation location, size of separation bubble, reattachment point location and shear layer vorticity over the existing model for baseline case by utilization of Hot Wire Anemometry (HWA) and Particle Image Velocimetry (PIV) techniques. This achievement is corresponding to objective 4.
5. Objective 5 has been achieved through a series of comprehensive Hot Wire Anemometry (HWA) measurements in the wake region. Local broadband peaks were observed in the power spectra of the measured signals in the wake region by measurements for baseline case for three different free stream velocities including 7, 9 and 12 m/s , however a distinct peak relevant to the vortex shedding frequency was not observed. Indeed, the identified local broadband peaks don’t follow a

linear relationship with respect to their corresponding free stream velocities. The signal analysis showed that the maximum energy dissipation in the wake region occurs at the height with the maximum RMS velocity

6. Following objective 6, Hot Wire Anemometry (HWA) measurements in actuated case show the effectiveness of all driving waveforms including Sine, Triangle, Square and Pulse waves to suppress the velocity fluctuations in the wake region. The experimental results revealed the superiority of Square wave over the Sine wave to achieve the same aerodynamic performance at lower actuation voltage.

   The magnitude of generated peak jet velocity by Square and Pulse wave is 23% bigger than the generated ones by Sine and Triangle waves. Therefore, energy costs can be reduced by implementation of Square and Pulse wave instead using Sine wave and Triangle wave. Investigation of the influence of both geometrical and operational parameters including the angular position of actuators, actuation voltage (peak exit jet velocity of actuators to the free stream velocity of cross flow (Velocity Ratio VR)) and waveform on the performance of synthetic jet actuators revealed that all parameters are important to have a successful flow separation control. The Particle Image Velocimetry (PIV) results revealed that the best location of synthetic jet actuators to achieve the best performance is somewhere upstream and close to the separation point, e.g. 8-11 mm upstream of the separation point.

   The results showed that the best performance of synthetic jet actuators can be achieved at angular position of 15 degree and velocity ratio of 1.85 with 42.6 and 44.2% reduction of the length of recirculation region by implementation of Sine and Square waves, respectively.

   The synthetic jet actuators influence the flow field in three stages: first, the cross flow impinges on the train of vortex rings produced by synthetic jet actuators which leads to generation of pairs of counter rotating vortices in flow field, then the pairs of counter rotating vortices interact with the higher momentum flow in upper layers, mixing occurs and large-scale vortical structures relevant to the separated shear layer are broken down into small-scale structures. In the third stage, higher momentum flow is transferred to near wall region and convect

downstream and also the vortex trajectory is changed toward the hump wall, and as a result, the retarded boundary layer is reenergized and flow separation is delayed.

7. Wall resolved RANS simulations of fluid flow over the hump model were performed by employing K-Omega SST model using OpenFOAM software. Numerical simulations for characteristics of single actuator in quiescent conditions as well as the numerical analysis for flow separation over hump model for both unactuated and actuated cases in unsteady state were carried out. The Merging and Stitching techniques were utilized to generate computational grids for simulations of actuated case which was very helpful to considerably reduce the computational costs. The synthetic jet actuator was fully simulated in this study by considering both cavity and oscillations of piezoelectric diaphragm. The Interaction of generated vortical structures by synthetic jet actuators with cross flow was simulated in three dimensions to investigate the performance of active flow control on the characteristics of flow in the wake region. The unsteady results show the effectiveness of synthetic jet actuators by delaying the flow separation and pushing back the reattachment point toward the hump trailing edge. Also, numerical simulations revealed more information about flow behavior in span wise direction which can be used in optimization of synthetic jet actuators performance, e.g. the CFD results suggest to decrease the distance between orifices to delay the onset of instabilities more and as a result more delay of flow separation phenomenon.

   The numerical simulations were in reasonable agreement with experimental data and confirms that the URANS approach can be used as a good strategy for predication of flow separation and its control. This achievement is corresponding to objective 7.

Recommendations for Future Research:

1. Tomographic PIV measurements is suggested to improve the accuracy of the results. In the current research, the PIV measurements were carried out in two dimensions. Therefore, in addition of missing velocity in span-wise direction, probably it can introduce an interference in the data for velocity components in

stream-wise and wall-normal directions. These problems can be eliminated by Tomographic PIV measurements as several cameras are utilized to measure all three-velocity components, hence the accuracy of results will be improved and more information about flow behavior in span-wise direction would be revealed.

2. Numerical simulation of interaction of cross flow by synthetic jet actuators using other numerical techniques such as Large Eddy Simulation (LES), as the RANS model is probably less capable to capture transient turbulent structures in comparison to LES model. Using LES approach will improve the accuracy of the solution and will eliminate the resolution shortages of URANS method in recirculation region. As another interesting exercise, the effect of geometrical parameters including orifice depth, cavity size as well as the distance between orifices on the performance of active flow control can be investigated numerically either by RANS approach or LES technique.
3. Pressure measurements on the hump surface to investigate the flow characteristics in near wall region, these measurement can be used to calculate pressure coefficient, lift and drag forces as well as the velocity of eddies in near wall region.
4. The effects of the generated acoustic noise of individual synthetic jet actuator on the performance of adjacent synthetic jet actuators as well as the overall performance of the array of SJAs is not considered in the current study. The study of the effects of noise generation by SJAs on the performance of active flow control can be an interesting exercise. Additionally, out of phase operation of adjacent SJAs as well as using lobed orifices can be considered as two solutions to reduce or eliminate the probable generated noise by SJAs. Investigation of the influence of both suggested solutions on the performance of active flow control is recommended.

Publications in Preparation

1. Mohammad Ja'fari, Artur J. Jaworski and Aldo Rona, Experimental Study of Boundary Layer Flow Separation Control over the Hump Model using Synthetic Jet Actuators
2. Mohammad Ja'fari, Artur J. Jaworski and Aldo Rona, Wall Resolved RANS Simulation of Boundary Layer Flow Control over Hump Model by Synthetic Jet Actuators

References

Adrian, R.J. Statistical properties of particle image velocimetry measurements in turbulent flow. Laser Anemometry in Fluid Mechanics-III. LADOAN-Inst. Sup. Tec., Lisbon. (1988), pp: 115-129.

Adrian, R.J. Westerweel, J. Particle Image Velocimetry, Cambridge University Press, 2011.

Amitay, M., Glezer, A. Role of actuation frequency in controlled flow reattachment over a stalled airfoil, AIAA J. 40 (2002) 209–216.

Amitay, M., Honohan, A.M., Trautman, M., Glezer, A. Modification of the aerodynamic characteristics of bluff bodies using fluidic actuators, (1997) AIAA Paper No. 97–2004.

Amitay, M., Horvath, M., Michaux, M., Glezer, A. Virtual aerodynamic shape modification at low angles of attack using synthetic jet actuators, (2001) AIAA Paper No. 2001–2975.

Amitay, M., Smith, D.R., Kibens, V., Parekh, D.E., Glezer, A. Aerodynamic flow control over an unconventional airfoil using synthetic jet actuators, AIAA J. 39 (2001) 361–370.

Atabak Fadai-Ghotbi, Christophe Friess, Remi Manceau, Jacques Borée. A seamless hybrid RANS LES model based on transport equations for the subgrid stresses and elliptic blending. Physics of Fluids, American Institute of Physics, 2010, 22 (5), pp.055104. 10.1063/1.3415254. hal-02132038

Aram, S., Shan, H.: Synchronization effect of an Array of sweeping jets on a separated flow over a wall-mounted hump. In: AIAA AVIATION Forum, 17–21 June 2019, Dallas, Texas, AIAA Paper 2019–3396. pp. 1–16 (2019)

Aubrun S, Alvi F and Kourta A. Separation flow control on a generic ground vehicle using steady microjet arrays. Proc.5th Flow Control Conference, Chicago, Illinois, USA, AIAA Paper 2010-4701, 2010.

Azzawi, I.D.J. Application of Synthetic Jet Actuators for Modification of Separated Boundary Layers. PhD thesis, University of Leeds, 2016.

Barlow, J.B., Rae W.H., Pope, A., "Low Speed Wind Tunnel Testing", John Wiley & Sons, 1996

Bazdidi-Tehrani, A. Abouata, M. Hatami and N. Bohlooli. Investigation of effects of compressibility, geometric and flow parameters on the simulation of a synthetic jet behavior, The Aeronautical Journal March 2016 Volume 120 No 1225, pp 521–546.

Bazdidi-Tehrani, F., Jahromi, M., Karami, M. and Javadi, A. Numerical analysis of a zero net mass flux jet in a quiescent medium, Proceedings of 16th Annual Conference of CFD Society Canada, University of Saskatchewan, Saskatoon, Canada, 2008.

Bell, J. H., and R. D. Mehta. Contraction Design for Small Low-Speed Wind Tunnels. [NASA contractor report], NASA CR-177488. Washington, DC: National Aeronautics and Space Administration, 1988.

Bohl, W., Elmendorf, W. Technische Stromungslehre, 14th ed. Vogel-Fachbuch: W urzburg, Germany, 2008; pp.260–302.

Bruun, H.H. Hot-Wire Anemometry, Principles and Signal Analysis. Oxford Science Publications, 1995.

Calvert and Farrar, An engineering data book, 3rd edition, MacMillan, 2008.

Capizzano, F., Catalano, P., Marongiu, C. & Vitagliano, P. L. U-RANS modelling of turbulent flows controlled by synthetic jets. AIAA-2005-5015.

Cappelli, D. and Mansour, N. N., \Performance of Reynolds Averaged Navier-Stokes Models in Predicting Separated Flows: Study of the Performance of Reynolds Averaged Navier-Stokes Models in Predicting Separated Flows: Study of the Hump Flow Model Problem," 31st AIAA Applied Aerodynamics Conference, No. AIAA 2013-3154, 2013.

Carmichael, B.H. Low Reynolds number airfoil survey. NASA Contractor Report-165803. 1 (1981).

Cattafesta III L.N and Sheplak M. Actuators for active flow control. Annual Review of Fluid Mechanics, Vol. 43, pp 247-272, 2011.

Chang, P.K. Separation of flow. J. Franklin Inst. 1961, 272, 433–448.

Chatlynne, E., Rumigny, N., Amitay, M., Glezer, A. Virtual aero-shaping of a Clark-Y airfoil using synthetic jet actuators, (2000) AIAA Paper No. 2001–732.

Ciuryla, M., Liu, Y., Farnsworth, J., Kwan, C., Amitay, M. Flight control using synthetic jets on a Cessna 182 model, J. Aircraft 44 (2007) 642–653.

Colebrook C.F.[1938]. "Turbulent Flow in Pipes," J. Inst. Civ. Eng. Land., vol. 11, pp. 133-156.

Crook A., Wood N. Measurements and Visualizations of Synthetic Jets. AIAA Paper 2001-0145.

Dantec LTD, http://www.dantecdynamics.com/solutions-applications/solutions/fluid mechanics/particle-image-velocimetry-piv/measurement-principles-of-piv/.[accessed 03/07/2020].

Desalvo, M., Whalen, E., Glezer, A. High-lift enhancement using fluidic actuation, (2010) AIAA Paper No. 2010–863.

Duvigneau, R., Hay, A and Visonneau, M. Study on the optimal location of a synthetic jet for stall control. Proc. 3rd AIAA Flow Control Conference, San Francisco, California, USA, AIAA Paper 2006-3679, 2006.

Eckert, W.T., Mort, K.W., Jope, J., "Aerodynamic Design Guidelines and Computer Program for Estimation of Subsonic Wind Tunnel Performance", NASA TN D-8243, 1976

Einstein, A. Berichtigung zu meiner Arbeit: 'Eine neue Bestimmung der Moleküldimensionen'. 1911, Ann.Phys. (Lpz) 339, 591-59.

Einstein, A. Eine neue Bestimmung der Moleküldimensionen. Annalen der Physik, 1906, 19, 289-306.

Eri, Q., Hong, L., Li, T., & Wang, Q. (2018). Effect of ambient temperature on piston-type synthetic jet actuator. Proceedings of the Institution of Mechanical Engineers, Part G: Journal of Aerospace Engineering, 232(6), 1077–1086.

Evans, S., Hodson, H., Hynes, T., Wakelam, C and Hiller S.J. Controlling separation on a simulated compressor blade using vortex generator jets. Proc. 4th Flow Control Conference, Seattle, Washington, USA, AIAA Paper 2008-4317, 2008.

Feero, A.M, Lavoie, P and Sullivan, E.P. Influence of cavity shape on synthetic jet performance, Sensors and Actuators A: Physical, doi:10.1016/j. sna2014.12.004.

Fisher, R., Nishino, T., and Savill, M., "Numerical Analysis of a Bidirectional Synthetic Jet for Active Flow Control," AIAA Journal, Vol. 55, No. 3, 2017, pp. 1064–1069. doi:10.2514/1.J055081

Flatt, J. The history of boundary layer control research in the United States of America, [In:] Boundary Layer and Flow Control: its Principles and Application, G.V. Lachmann (Edit.), New York, Pergamon Press, 1961.

Franck, J., Colonius, T. Effects of actuation frequency on flow control applied to a wall-mounted hump. AIAA J. 50, 1631–1634, 2012.

F.R.Menter, 'Improved two-equation k-ω turbulence model for aerodynamic flows', NASA TM-103975, (1992).

Gad-el-Hak M. Flow Control: Passive, Active, and Reactive Flow Management. Cambridge University Press, 2000.

Gallas, Q., Holman, R., Raju, R and Mittal, R. Low dimensional modeling of zero-net mass-flux actuators. Proc. 2nd AIAA Flow Control Conference, Portland, Oregon, USA, AIAA Paper 2004-2413, 2004.

Gaster, M. On the stability of parallel flows and the behavior of separation bubbles. Dissertation, Queen Mary College, University of London (1963).

Genc, M.S., Karasu, I., Acikel, H.H., Akpolat, M.T. Low Reynolds Number Flows and Transition. In Low Reynolds Number Aerodynamics and Transition, Genc, M.S. Ed.; InTech: Rijeka, Croatia, 2012; pp. 1–28.

Gilarranz, J.L., Rediniotis, O.K. Compact, high-power synthetic jet actuators for flow separation control. AIAA 2001-0737, 39th aerospace sciences meeting and exhibit, Reno, USA, 8–11 January 2001.

Giovanna Cavazzini, Antoine Dazin, Giorgio Pavesi, Patrick Dupont, Gérard Bois. Post-processing methods of PIV instantaneous flow fields for unsteady flows in turbomachines. The Particle Image Velocimetry - Characteristics, Limits and Possible Applications, Intech, pp.97-120, 2012, ff10.5772/37273ff. ffhal-00794858f

Glezer, A., Amitay, M., and Honohan, A.M. Aspects of low and high frequency actuation for aerodynamic flow control. AIAA Journal, Vol. 43, pp 1501-1511, 2005.

Gomes L.D, Crowther W.D and Wood N.J. Towards a practical piezoceramic diaphragm based synthetic jet actuator for high subsonic applications effect of chamber and orifice depth on actuator peak velocity, Proc. 3rd AIAA Flow Control Conference, San Francisco, California, USA, AIAA Paper 2006-2859, 2006.

Greco, C., Ianiro, A., Tasarita, T and Cardone, G. On the near field of single and twin circular synthetic air jets, Int J Heat Fluid Flow, 2013, 44, pp 41-52.

Greenblatt, D., Paschal, K. B., Yao, C.-S. & Harris, J. A separation control CFD validation test case part 2. zero efflux oscillatory blowing. AIAA-2005-0485.

Greenblatt, D., Paschal, K. B., Yao, C.-S., Harris, J., Schaeffler, N. W. & Washburn, A. E. A separation control CFD validation test case part 1. baseline & steady suction. AIAA-2004-2220.

Gressick, W., Maldonado, V., Farnsworth, J. and Amitay, M. Active enhancement of wind turbine blades performance. Proc. 46th AIAA Aerospace Sciences Meeting and Exhibit, Reno, Nevada, USA, AIAA Paper 2008-1311, 2008.

Gritskevich, M.S., Garbaruk, A.V., Schütze, J., and Menter, F. R., Development of DDES and IDDES for the $k-\omega$ shear stress transport model," Flow, Turbulence and Combustion, Vol. 88, No. 3, 2012, pp. 431-449.

Helin, H.E and Watry, C.W. Effects of Trailing Edge Entrainment on Delta Wing Vortices. AIAA Journal, vol32, no4, pp802-804, (1994)

Holman, R., Uttarkar, Y., Mittal, R., Smith, B.L. and Cattafesta, L. Formation criterion for synthetic jets, AIAA J, 2005, 43, (10), pp 2110-2116.

Hong, G. Effectiveness of micro synthetic jet actuator enhanced by flow instability on controlling laminar separation caused by adverse pressure gradient, Sens. Actuators, A 132 (2006) 607–615.

Honohan, A.M., Amitay, M., Glezer, A. Aerodynamic control using synthetic jets, (2000) AIAA Paper No. 2000–2401.

Horton, H.P. Laminar separation bubbles in two and three dimensional incompressible flow. Dissertation, Queen Mary College, University of London (1968).

Idel'chik, I. E., Handbook of Hydraulic Resistance. AEC-TR-6630, The Israel Program for Scientific Translations Ltd., 1966.

Ishtiaq, A., Chaudhry, I.A., Sultan, T., Siddiqui, F.A., Farhan, M., Asim, M. The flow separation delay in the boundary layer by induced vortices, J Vis (2016). doi:10.1007/s12650-016-0396-0.

Iuso, G., Di Cicca, G. and Donelli, R. Flow field development of an axisymmetric synthetic jet, AIMETA, Firenze University Press, Florence, Italy, 2005.

Jabbal, M., Zhong, S. The near wall effect of synthetic jets in a boundary layer. International Journal of Heat and Fluid Flow. 2008 Feb 29; 29(1):119-30.

Jakirlic, S., Manceau, R., Saric, S., Fadai-Ghotbi, A., Kniesner, B., Carpy, S., Kadavelil, G., Friess, C., Tropea, C.and Boree, J., \LES, Zonal and Seamless Hybrid LES/RANS: Rationale and Application to Free and Wall-Bounded Flows involving Separation and Swirl," Numerical Simulation of Turbulent Flows and Noise Generation, edited by C. Brun, D. Juve, M. Manhart, and C.-D. Munz, Vol. 104 of Notes on Numerical Fluid Mechanics and Multidisciplinary Design, Springer Berlin eidelberg, 2009, pp. 253-282.

Jaworski, A. J. A Study of Pressure Fluctuations Caused by Vortex Breakdown. PhD Thesis, Imperial College of Science, Technology and Medicine, (1996)

Jenkins, L., Gorton, S.A., and Anders, S. Flow Control Device Evaluation for an Internal Flow with an Adverse Pressure Gradient, AIAA Paper 2002-0266, Jan. 2002.

Jin-Jun Wang, Yu-Long Ba & Li-Hao Feng (2014) Experimental investigation on laminar separation control for flow over a two-dimensional bump, Journal of Turbulence, 15:4, 221-240, DOI: 10.1080/14685248.2014.893059

Jin, Z., Wang, Y and Yang, Z. An experimental investigation into the effect of synthetic jet on the icing process of a water droplet on a cold surface, Int J Heat Mass Transfer, 2014, 72, pp 553-558.

Johari, H., Olinger, D. J. and Fitzpatrick, K. C. Delta Wing Control via Recessed Angled Spanwise Blowing. Journal of Aircraft, vol32, no4, pp804-810, (1995).

John, E.J. Gas Dynamics, 2ed Edition, Allyn and Bacon, pp 180, 1984.

Jones, B. Stalling. J. R. Aeronaut. Soc. 38, 753–770 (1934).

Jorgenson, Finn E. How to measure turbulence with hot-wire anemometers- a practical guide, DANTEC DYNAMICS, No: 9040U6151.2002-02-01.

Kara K, Kim D, Morris P J (2018) Flow separation control using sweeping jet actuator. AIAA Journal, vol. 56, pp 4604-4613. doi: 10.2514/1.J056715.

Keane, R.D and Adrian, R.J. Optimization of particle image velocimeters. Part I: Double pulsed-system, Meas. Sci. Technol., 1, 1990, 1202-1215.

Keane, R.D and Adrian, R.J. Optimization of particle image velocimeters. Part II: Double pulsed-system, Meas. Sci. Technol., 2, 1991, 963-974.

Keane, R.D and Adrian, R.J. Theory of cross-correlation PIV images, Appl. Sci. Res. 49, 1993, 191-215.

Kewei Xu, Yan Ren and Gecheng Zha, Numerical Investigation of NASA Hump Using Co-flow Jet for Separation Control, AIAA 2020-1058, doi.org/10.2514/6.2020-1058

Kim, M., Lee, B., Kim, C and Jung, K.J. Numerical study on flow characteristics of synthetic jets with rectangular and circular exits. Proc. 6th AIAA Flow Control Conference, New Orleans, Louisiana, USA, AIAA Paper 2012-3049, 2012.

Kim, Y.H and Garry K.P. Optimization of a rectangular orifice synthetic jet generator. Proc. 3rd AIAA Flow Control Conference, San Francisco, California, USA, AIAA Paper 2006-2862, 2006.

King, L.V. On the convection of heat from small cylinders in a stream of fluid: Determination of the convection constants of small platinum wires with applications to hot-wire anemometry. Phil. Trans. Roy. Soc. A214 (1914), 373-432.

Koklu M. Application of sweeping jet actuators on the NASA hump model and comparison with CFDVAL2004 Experiments. In: 47th AIAA flow control conference, Colorado, USA, 5–9 June 2017, paper no. AIAA-2017-3313.

Koklu, M. Steady and unsteady excitation of separated flow over the NASA hump model, 2018 Flow Control Conference, AIAA, AVIATION Forum, (AAIA 2018-4016)

Koklu, M. The Effects of Sweeping Jet Actuator Parameters on Flow Separation Control, 45th AIAA Fluid Dynamics Conference, AIAA AVIATION Forum, (AIAA 2015-2485).

Koopmans, E and Hoeijmakers, H.W.M. Experimental Research on Flow Separation control using synthetic jet actuators, 29th Congress of the International Council of the Aeronautical Sciences St. Petersburg Russia, September, 7-12, 2014

Koumoutsakos, P., Leonard, A. & Pepin, F. 1994. Boundary conditions for viscous vortex methods. J. Comput. Phys. 113, 52–61.

Krishnan, V., Squires, K.D. & Forsythe, J.R. Prediction of separated flow characteristics over a hump using RANS and DES. AIAA-2004-2224.

Kumar, A., Saha, A.K., Panigrahi, P.K., Karn, A. On the flow physics and vortex behavior of rectangular orifice synthetic jets, Exp. Therm. Fluid Sci., 103 (2019), pp. 163-181

Lambourne, N.C and Bryer, D.W. The Bursting of Leafing Edge Vortices: Some Observation and Discussion of the Phenomenon. Aeronautical Research Council, R&M 3282 (1961).

Lecordier, B., Mouqallid, M. CCD recording method for crosscorrelation PIV development in unstationary high speed flow. Exp. Fluids 17, 205, 1994.

Lee, S., Kim, K.J., Park, H.C. Modelling of an IPMC actuator-driven zero-net-mass-flux pump for flow control. Journal of intelligent material systems and structures. 2006 Jun 1;17(6):533-41.

Liang, Y., Kuga, Y., Taya, M. Design of membrane actuator based on ferromagnetic shape memory alloy composite for synthetic jet applications in: Sensors and Actuators A, Vol. 125, 2006, pp. 512–518.

Lin, J., Howard, F., and Selby, G. Small-Submerged Vortex Generators for a Turbulent Flow Separation Control, Journal of Spacecraft and Rockets, Vol. 27, No. 5, 1990, pp. 503-507.

Lin, J.C. Review of Research on Low-Profile Vortex Generators to Control Boundary-Layer Separation, Progress in Aerospace Sciences, Vol. 38, No. 4, 2002, pp. 389-420.

Lissaman, P.B.S. Low-Reynolds-number-airfoils. Annu. Rev. Fluid Mech. 15, 233–239 (1983).

Liu, Y., Wang, B. and Liu, S. Numerical simulation of high-power synthetic jet actuator flow field and its influence on mixing control, J Therm Sci, 2008, 17, (3), pp 207-211.

Mallinson S, Hong G, Reizes J. Some characteristics of synthetic jets. AIAA 3651:1999.

Maltby, R.L and Keating, R.F.A. The surface oil flow technique for use in low speed wind tunnels. In [2.1] , pp. 29-38, 1962.

Mane P. Experimental Design and Analysis of Piezoelectric Synthetic Jets in Quiescent Air. Master Dissertation. School of engineering Virginia Commonwealth University, 2005.

Mayle, R.E. The Role of Laminar-Turbulent Transition in Gas Turbine Engines. Journal of Turbomachinery, Vol. 113, 509-537, (1991).

McCormick D. C. Boundary Layer Separation Control with Directed Synthetic Jets. AIAA 2000-0519, United Technologies Research Center East Hartford, CT 06108.

McCormick, D. Shock-Boundary Layer Interaction Control with Low-Profile Vortex Generators and Passive Cavity, AIAA Paper 1992-0064, Jan. 1992.

Mcgregor, I. Regions of localised boundary layer separation and their role in nose stalling of aerofoils. Dissertation, Queen Mary College, University of London (1954).

Mehti Koklu, ‘’Steady and Unsteady Excitation of Separated Flow over the NASA Hump Model’’,AIAA 2018-4016, Session: Flow Separation Control, Jun 2018, doi:10.2514/6.2018-4016

Merzkirch.W, Techniques of flow visualizations, AGARD-AG-302, ISBN 92-835-04380 December 1987.

Mittal, R., Kotapati, R.B., Cattafesta, L.N. Numerical study of resonant interactions and flow control in a canonical separated flow, (2005) AIAA Paper No. 2005–1261.

Morel-Fatio, S., Pines, D.J., Kiddy, J. UAV performance enhancements with piezoelectric synthetic jet actuators, (2003) AIAA Paper No. 2003–394.

Morgan, P. E., Rizzetta, D. P. & Visbal, M. R. Large-eddy simulation of separation control for flow over a wall-mounted hump. AIAA-2005-5017.

Morgan, P.E., Rizzetta, D.P. & Visbal, M.R. Numerical investigation of separation control for flow over a wall-mounted hump. AIAA-2004-2510.

Mossi, K and Bryant, R. Characterization of piezoelectric actuators for flow control over a wing. Proc. 9th International Conference on New Actuators, Bremen, Germany, June 2004, pp 181-185

Mossi, K., P. Mane, R. Bryant. Velocity Profiles of Synthetic Jets using Piezoelectric Circular Actuators. AIAA Paper 2005-2341, Proceedings of 46th AIAA/ASME/ASCE/AHS/ASC Structures, Structural Dynamics & Materials Conference, Austin, TX, 18-21 April, 2005.

Mu, H.; Yan, Q.; Wei, W.; Sullivan, P.E. Unsteady simulation of a synthetic jet actuator with cylindrical cavity using a 3-D lattice Boltzmann method. J. Aerosp. Eng. 2018, 2018, 9358132.

Nani, D. J. and Smith, B.L. Effect of orifice inner lip radius on synthetic jet efficiency, Phys Fluids, 2012, 24, (11), pp 115110.

Nishri, B. & Wygnanski, I. Eff ects of periodic excitation on turbulent flow separation from a flap. AIAA J. 36, 547–556, 1998.

Ohanian, O. J. Ducted fan aerodynamics and modeling, with applications of steady and synthetic jet flow control. PhD Thesis. Virginia Polytechnic Institute and State University, 2011.

OpenFOAM, The OpenFOAM Fundation, User Guide, Version 5.0, 24th July 2017, http://openfoam.org.

Oyarzun, M.A and Cattafesta, L. Design and optimization of piezoceramic zero-net mass-flux actuators. Proc. 5th Flow Control Conference, Chicago, Illinois, USA, AIAA Paper 2010-4414, 2010.

Pavlova, A.A., Otani, K., Amitay, M. Active control of sprays using a single synthetic jet actuator, Int. J. Heat Fluid Flow 29 (2008) 131–148.

P.D. Welch. The use of fast fourier transform for the estimation of power spectra: A method based on time averaging over short, modified periodograms. In IEEE Trans. Audio Electroacoustics, volume AU-15, pages 70–73, June 1967.

Pick, P., Andrle, M., Skala, V., Matejka, M. The influence of Modulated Slotted Synthetic Jet Bypass of Hump. Engineering MECHANICS, Vol. 20, 2013, No. 3/4, p. 271–280.

PiezoDrive Ltd, http://www.piezodrive.com/product-pdm200.html, [accessed 22 Jun, 2017]

Polsenberg, A., Milano, M., Grazier, M., Fischer, K. and Burdick, J. Synthetic jet propulsion for small underwater vehicles, International Conference on Robotics and Automation, Barcelona, Spain, 2005.

Postl, D., Wernz, S. & Fasel, H. Case 3: direct numerical simulation on the Cray X1. In NASA Langley Workshop on CFD Validation of Synthetic Jets and Turbulent Separation Control, 2004.

Potsdam, M., and Le Pape, A. CFD investigations on a NACA0036 airfoil with active flow control. Proc. 4th Flow Control Conference, Seattle, Washington, USA, AIAA Paper 2008-3869, 2008.

Pramod, Salunkhea., Hui, Tangb., Yingying, Zhengc., Yanhua, Wu. PIV measurement of mildly controlled flow over a straight-wing model. International Journal of Heat and Fluid Flow 62 (2016) 552–559.

Prandtl L. Über Flüssigkeitsbewegung bei sehr kleiner Reibung. III Internationalen Mathematiker-Kongresses, Heidelberg, Germany, 1904.

Prandtl, L., "Attaining A Steady Stream in Wind Tunnels", NACA TM 726, October 1933.

Qayoum, A., Gupta, V., Panigrahi P.K, Muralidhar, K. Influence of amplitude and frequency modulation on flow created by a synthetic jet actuator. Sensors and Actuators A: Physical. 2010 Jul 31; 162(1):36-50.

Rathnasingham, R., Breuer, K.S. Active control of turbulent boundary layers, J. Fluid Mech. 495 (2003) 209–233.

Rivir, R.B., Sondergaard, R., Bons, J.P and Yurchenko, N. Control of separation in turbine boundary layers. Proc. 2nd AIAA Flow Control Conference, Portland, Oregon, USA, AIAA Paper 2004-2201, 2004.

Roscoe. R. 1952. The viscosity of suspensions of rigid spheres. British Journal of Applied Phy sics, Vol. 3. No. 8. p. 267- 69.

Sang-Hyuk Kim and Kwang-Yong Kim, ‘’Effects of Installation Conditions of Fluidic Oscillators on Control of Flow Separation’’. August 2019, AIAA Journal, doi: 10.2514/1.J058527

Sari´c, S. et al. “Comparative Assessment of Hybrid LES/RANS Models in Turbulent Flows Separating ˇ from Smooth Surfaces”. Advances in Hybrid RANS-LES Modelling. Ed. by S.-H. Peng and W. Haase. Vol. 97. Notes on Numerical Fluid Mechanics and Multidisciplinary Design. Springer Berlin Heidelberg, 2008, pp. 142–151.

Saric, S., Jakirlic, S. & Tropea, C. Computational analysis of locally forced flow over a wall-mounted hump at high-Re number. In Fourth Int’l Symp. Turbulence Shear Flow Phenomena (ed. J. A. C. Humphrey, J. K. Eaton, R. Friedrich, N. Kasagi, M. A. Leschziner & T. B. Gatski), 1189–1194, 2005

Sarpkaya, T. On Stationary and Travelling Vortex Breakdowns. Journal of Fluid Mechanics, v45, pp545-559, (1971)

Schlichting, H., Gersten, K., Krause, E. Grenzschicht-Theorie, 10th ed.; Springer-Verlag: Berlin/Heidelberg, Germany, 2006; pp. 377–408.

Schubauer, G.B and Spangenberg, W.G. Forced Mixing in Boundary Layers, Journal of Fluid Mechanics, Vol. 8, No. 01, 1960, pp. 10-32.

Schubauer, G.B., and Spangenberg, W.G. Effects of screen in wide angle diffuser, NACA TR 949.

Seifert, A. & Pack, L. G. Active flow separation control on wall-mounted hump at high Reynolds numbers. AIAA J. 40, 1363–1372, 2002.

Seifert, A., Darabi, A. & Wygnanski, I. Delay of airfoil stall by periodic excitation. J. Aircraft 33, 691–698, 1996.

Seifert, A., Pack, L.G. Oscillatory control of separation at high Reynolds numbers, AIAA J. 37 (1999) 1062–1071.

Settles, G.S, Teng, H.Y. Flow visualization methods for separated three-dimensional shock wave/turbulent boundary layer interactions. AIAA J. 21 (1983), 390-397.

Shah, H., Mathew, S., Lim, C.M. Numerical simulation of flow over an airfoil for small wind turbines using the $\gamma - Re_{\theta}$ model, Int J Energy Environ Eng (2015) 6:419–429.

Shih, C. and Ding, Z. Trailing Edge Jet Control of Leading Edge Vortices of a Delta Wing. AIAA Journal, vol34, no7, pp1447-1457, (1996).

Shmilovich, A. and Yadlin, Y. Active flow control for practical high-lift systems. Journal of Aircraft, Vol. 46, No. 4, July-August 2009

Smith, B. L. and Glezer, A. The Formation and Evolution of Synthetic Jets. Physics of Fluids, v10, no9, pp2281-229, (1998).

Smith, B. L. and Swift, G. A comparison between synthetic jets and continuous jets, J Exp Fluids, 2003, 34, (4), pp 46-472.

Smith, B.L., Trautman, M.A., Glezer, A. Controlled interactions of adjacent synthetic jets. AIAA 0669, 37th aerospace sciences meeting and exhibit, Reno, USA, 11–14 January 1999.

Smith, D.R., Amitay, M., Valdis, K., Parekh, D., Glezer, A. Modification of lifting body aerodynamics using synthetic jet actuators, (1998) AIAA Paper No. 98–209.

Smits, A.J. Lim, T.T. Flow Visualization Technique and Examples, Imperial College Press, 2000.

Smyk, E, Comparison of Acoustic Synthetic Jet Actuators with One and Two Diaphragms, Svratka, Czech R, 24th International Conference, Engineering Mechanics 2018, Svratka, Czech Republic, May 14 –17, 2018

Sollof, S. M., Adrian, R. J., & Liu, Z.C. Distortion compensation for generalized stereoscopic particle image velocimetry. Measurement Science and Technology, 8(12), 1441-1454,1997.

Souckova, N., Popelka, L., Matejka, M., Simurda, D. Eff ect of vortex generators on flow conditions of airfoil with deflected flap, In 21st International Symposium on Transport Phenomena, Kaohsiung City: National Kaohsiung University of Applied Sciences, 2010, S. 16-24. ISBN 978-986-6184-25-3, 2010.

Sparrow, E.M., Comb, J.W. Effect of interwall spacing and fluid flow inlet conditions on a corrugated-wall heat exchanger. Int. J. Heat Mass Transfer 26, 993-1005, 1983.

Stanbrook, A. The surface oil flow technique for use in high speed wind tunnels.In [2.1] , pp. 39-49, 1962.

Stocker, H. Taschenbuch der Physik, 5th ed.; Verlag Harri Deutsch: Frankfurt am Main, Germany, 2007.

Sturm, H., Dumstorff, G., Busche, P., Westermann, D and Lang, W. Boundary Layer Separation and Reattachment Detection on Airfoils by Thermal Flow Sensors, Sensors 2012, 12, 14292-14306; doi:10.3390/s121114292.

Suzuki. T. Effects of a synthetic jet acting on a separated flow over a hump, J. Fluid Mech. (2006), vol. 547, pp. 331–359.

Swift, K.M. An Experimental Analysis of the Laminar Separation Bubble at Low Reynolds Numbers, Msc. Thesis, University of Tennesee Space Institute, (2009).

Takao, S. Effects of a synthetic jet acting on a separated flow over a hump, J. Fluid Mech. (2006), vol. 547, pp. 331–359.

Tan, A.C.N. & Auld, J.D. Study of Laminar Separation Bubbles at Low Reynold Number Under Various Conditions. 11th Australasian Fluids Mechanics Conference, University of Tasmania, Hobart, Australia, (1992).

Tang, G. and Agarwal, R.K., Numerical simulation of flow control over NASA hump with uniform blowing jet and synthetic jet, 2018 Flow Control Conference, AIAA, AVIATION Forum, (AAIA 2018-4017)

Tang, H., Salunkhe, P., Zheng, Y., Du, J., Wu, Y. On the use of synthetic jet actuator arrays for active flow separation control. Experimental Thermal and Fluid Science 57 (2014) 1–10.

Tani, I. Low speed flows involving bubble separations. Prog. Aerosp. Sci. 5, 70–103 (1964).

Tensi, J., Boue, I., Paille, E. Dury G (2002) Modification of the wake behind a circular cylinder by using synthetic jets. J Vis 5(1):37–44

Tesa, V. Enhancing impinging jet heat or mass transfer by fluidically generated flow pulsation, Chem Eng Res Des, 2009, 87, (2), pp 181-192.

Tesař, V., Kordík, J. and Daněk, M. Lift and separation control on wind turbine blades by vortices having streamwise oriented axes. Technical report, Institute of Thermo-mechanics ASCR v.v.i., Prague, October 2008.

Tian Y, Song Q and Cattafesta L. Control techniques for flows with large separated regions: A new look at scaling parameters. Proc. 3rd AIAA Flow Control Conference, San Francisco, California, USA, AIAA Paper 2006-2857, 2006.

Tian, Y., Song, Q., Cattafesta, L. Adaptive feedback control of flow separation, (2006) AIAA Paper No. 2006–3016.

TSI Incorporated, IFA 300 Constant Temperature Anemometer System, Instruction Manual, August 2000.

Ugrina S and Flatau A. Investigation of synthetic jet actuator design parameters. Proc. Smart Structures and Materials 2004: Smart Structures and Integrated Systems, San Diego, California, USA, Vol. 5390, pp 284-296, 2005.

Utturkar, Y., Mittal, R., Rampunggoon, P. and Cattafesta, L. Sensitivity of synthetic jets to the design of the cavity, 40th AIAA Aerospace Sciences Meeting and Exhibit, 14-17 January 2003, Reno, Nevada, US.

Vasile J and Amitay M. Interaction of a finite span synthetic-jet and a cross-flow over a swept back finite wing. Proc. 6th AIAA Flow Control Conference, New Orleans, Louisiana, USA, AIAA Paper 2012-2948, 2012.

Viken, S. A., Vatsa, V. N., Rumsey, C. L. & Carpenter, M. H., 2003 “Flow control analysis of the hump model with RANS tools.” AIAA Paper 2003-218

Vukasinovic, J. and Glezer, A. Spot-cooling by confined, impinging synthetic jet, ASME Summer Heat Transfer Conference, 20-23 July 2003, Las Vegas, Nevada, US.

Wallis, R.A., "Axial Flow Fans and Ducts", John Wiley and Sons, 1983

Wang, J., Ba, Y. and Feng, L. Experimental investigation on laminar separation control for flow over a two dimensional bump, J Turbul, 2014, 15, (4), pp 221-240.

Wang, J.J., Feng, L.H., Xu, C.J. Experimental investigations on separation control and flow structure around a circular cylinder with synthetic jet, Sci. China Ser. E–Tech. Sci. 50 (2007) 550–559.

Watson, M. The Use of Synthetic Jet Actuators for the Enhanced Control of Separated Flows. PhD Thesis, University of Manchester, 2004.

Watson, M., Jaworski, A. J. and Wood, N. J. A Study of Synthetic Jets from Rectangular and Dual-Circular Orifices. Aeronautical Journal, vol. 107, pp 427-434, 2003.

Wattendorf, F.L., Factors Influencing the Energy Ratio of Return Flow Wind Tunnels, 5th International Congress for Applied Mechanics, Cambridge, Sept.12-16, 1938, p. 52.

Wernet, M.P. Particle Displacement Tracking Applied to Air Flows, Fourth International Conference on Laser Anemometry, Cleveland, OH, pp 327-335, August 5-9, 1991.

Westerweel, J. & Scarano, F. (2005). Universal outlier detection for PIV data, Experiments in Fluids, vol. 39, pp. 1096-1100.

White, F.M. (2004). Fluid Mechanics, McGraw-Hill, Inc, 4th edition.

White, Frank. [1994]. Fluid Mechanics 3rd Edition, pp. 314, 328. New York, NY: McGraw-HiU Inc.

Wood J., Sahni O., Jansen K., Amitay M. Experimental and numerical investigation of active control of 3-D flows, AIAA Pap. 2009–4279, 2009.

Woodward, D.S. An investigation of the flow in separation bubbles. Dissertation, Queen Mary College, University of London (1970).

Xia, Z. and Luo, Z. Physical factor of primary jet vectoring control using synthetic jet actuators, Appl Math Mech (English edition), 2007, 28, (7), pp 907-920.

Yang, A.S. Design analysis of a piezo electrically driven synthetic jet actuator. Smart Materials and Structures, Vol. 18, No. 12, 2009.

You, D., Wang, M. AND Moin, P. Large-eddy simulation of flow over a wall-mounted hump with separation control, Center for Turbulence Research Annual Research Briefs, 223-234, 2005.

Young, A.D., Horton, H.P. Some results of investigations of separation bubbles. AGARD CP 4, 779–811 (1996).

Zhong, S., Garcillan, L., Wood N.J. Dye visualisation of inclined and skewed synthetic jets in a cross flow. Aeronautical Journal. 2005; 109(1093):147-55.

Zhong, S., Jabbal, M., Tang, H., Garcillan, L., Guo, F., Wood, N., Warsop, C., Toward the design of synthetic–jet actuators for full-scale flight conditions, Flow, Turbul. Combust. 78 (2007) 283–307.

Zhou, J. Numerical investigation of the behaviour of circular synthetic jets for effective flow separation control. Ph.D Dissertation. University of Manchester, 2010.

Zhou, J., Tang, H., Zhong, S. Vortex roll-up criterion for synthetic jets, AIAA J. 47 (2009) 1252–1262.

Appendix A- Software Testing using Cylindrical Bar

The hot wire system performance, data acquisition software as well as sample size and sampling rate of data are checked out by doing a test on a circular cylinder with diameter D of 25 mm and length of 50 mm which is placed horizontally in the test section as shown by Fig A.1 . The wind tunnel speed was set on 14.25 m/s, which yields the Reynolds number of 24032.245.

The probe is mounted at a distance of 2D behind the cylinder in its wake region and it is traversed vertically at a distance of D above the centerline of the cylinder to a distance of D below the centerline of the cylinder. The sample size of 131072 points with sampling rate of 10 kHz is used to acquire data. The maximum RMS V values is observed at distances of D/2 above and the below of the cylinder center as shown by Fig A.2. The vortex shedding frequency of 116.8 Hz behind the cylinder identified by dominant frequency from power spectral density estimate shown in Fig A.3 yields a Strrouhal number fD/U_∞ of 0.2049, which is close to the theoretical value of about 0.2. Therefore, the sample size of 131072 points with sampling rate of 10 kHz is used to acquire data for all HWA experiments in this research.

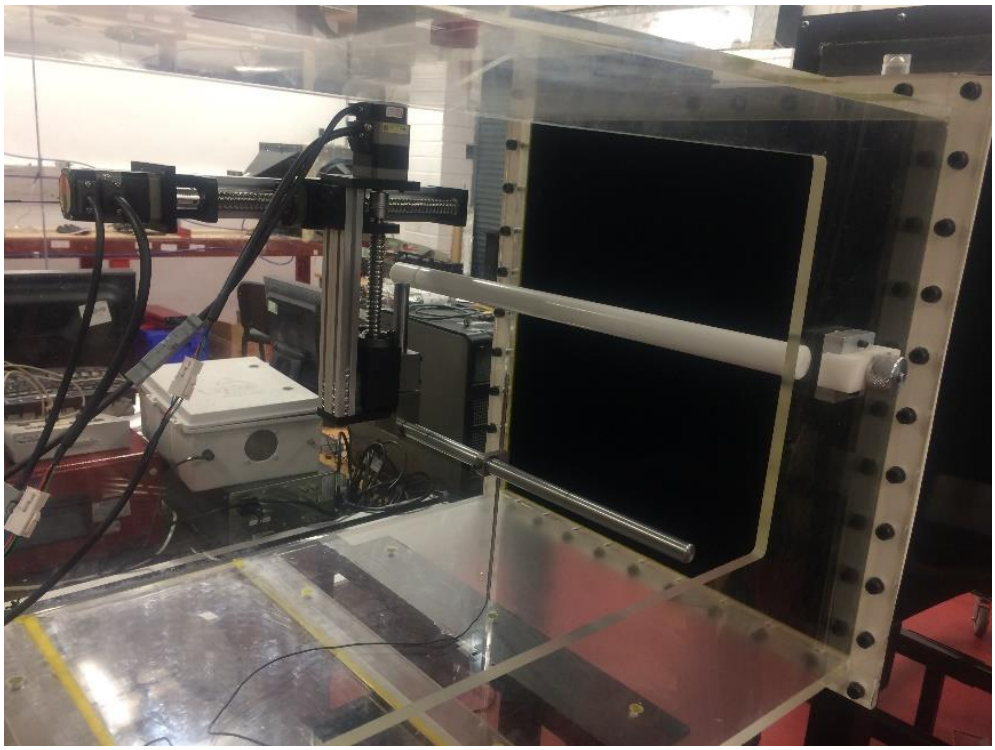

Fig A.1. The cylindrical bar in the test section.

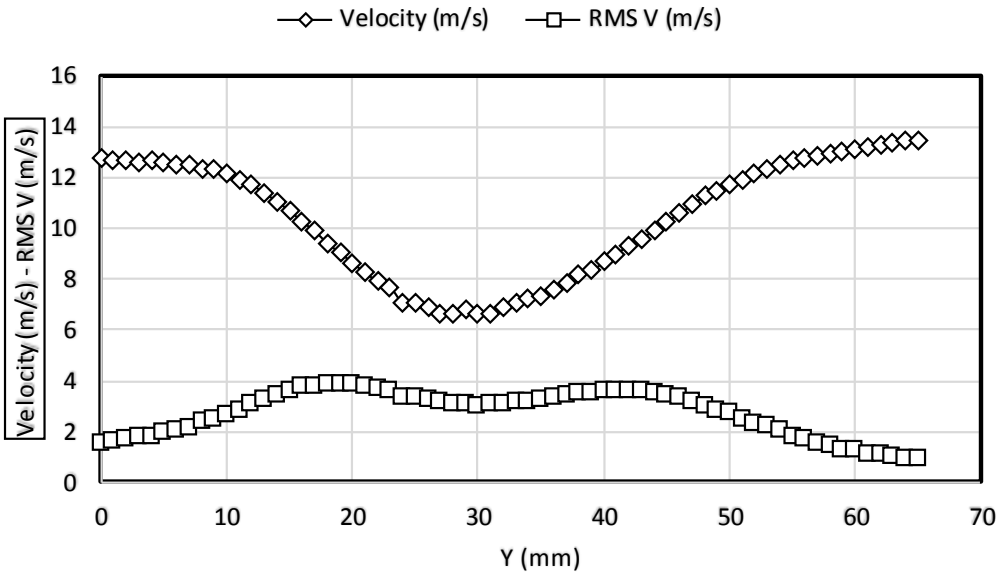

Fig A.2. Velocity and RMS V profile behind the cylindrical bar, $U_\infty = 14.25\ m/s$.

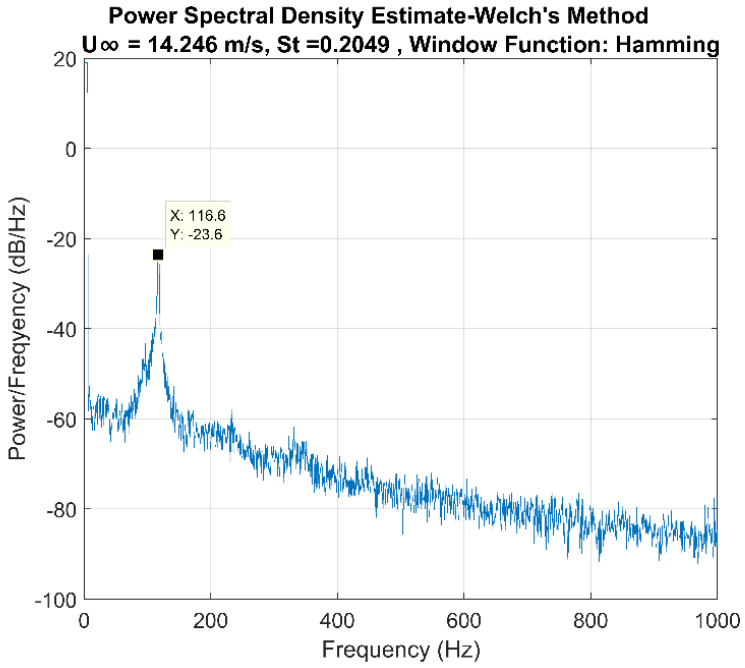

Fig A.3. Power spectral density profile, y = 40 mm, $U_\infty = 14.25\ m/s$.

Appendix B- MATLAB programs to help the HWA data processing

MATLAB script to generate 'frequency spectrum:

```
% MATLAB script to generate 'frequency spectrum'.
close all; clear all;
filename = '30.txt';              % Input(name of data file)
y = importdata(filename);
Fs = 10000;                       % Sampling frequency (Hertz)
T = 1/Fs;                         % Sample period
L = length(y);                    % Number of sample points
NFFT = 2^nextpow2(L);             % (Next power of 2) from length of y
t = (0:L-1)*T;                    % time vector
%w = rectwin(NFFT);               % Windowing functions
%w = triang(NFFT);
w = hamming(NFFT);
%w = hann(NFFT);
%w = kaiser(NFFT);
%w = blackman(NFFT);
%w = blackmanharris(NFFT);
%w = gausswin(NFFT);
%w = tukeywin(NFFT);
%w = taylorwin(NFFT);
Y = fft(y(:,2).*w,NFFT);                    % With Windowing Function
%Y = fft(y(:,2),NFFT);                      % Without Windowing Function
                                            %Plot single-sided power spectrum.
f = linspace(0,Fs/2,NFFT/2+1);
%Y = 2*abs(Y(1:NFFT/2+1)/L);                % Amplitude spectrum
%Ya = Y(1:NFFT/2+1).*conj(Y(1:NFFT/2+1))/L; % Power spectrum
Ya = 2*abs(Y(1:NFFT/2+1)).^2/Fs/L;          % Power spectrum
Yb = 10*log10(Ya);
%Yb = log10(Ya);
Yb(1:5) = -10;                        % Remove the large DC component
plot(f(1:10000),Yb(1:10000))          % X-Y Linear/Log scales
%set(gca,'XScale','lin');
%set(gca,'YScale','lin');
set(gca,'XScale','log');
set(gca,'YScale','log');
title('Power Spectral Density Estimate')
xlabel('Frequency (Hz)');
ylabel('Power/Freqyency (dB/Hz)');
grid on; fprintf('\r\r');
Xlim([0 5000]);
Ylim([-100 50]);
uresult(:,1) = f(1:10000);
uresult(:,2) = Yb(1:10000);
dlmwrite('output.dat', uresult);
```

MATLAB script to obtain the mean velocity and RMS values of the velocity fluctuations:

```
close all; clear all;
%
filename = 'FIRST EXP.W0003';
y = importdata(filename);
Fs = 4000; % Sampling frequency (Hertz)
T = 1/Fs;
L = length(y);
yMEAN = mean(y,1);
yRMS = sqrt(sum((y(:,2)-yMEAN(1,2)).^2/L));
fprintf('\r\nMean velocity is %5.3f m/s\r',yMEAN(1,2));
fprintf('RMS value is %5.3f m/s\r',yRMS);
NFFT = 2^nextpow2(L);
t = (0:L-1)*T;
f = Fs/2*linspace(0,1,NFFT/2+1);
Y = fft(y(:,2),NFFT)/L;
Y = 2*abs(Y(1:NFFT/2+1));
Y(1:5) = 0;
[Ym,YI] = max(Y);
%fprintf('Shedding Freq may be %8.3f (Hz)\r\r\r',f(YI));
%dlmwrite('test00.xls', uresult);
```

Appendix C- Additional Hot Wire Anemometry (HWA) Results

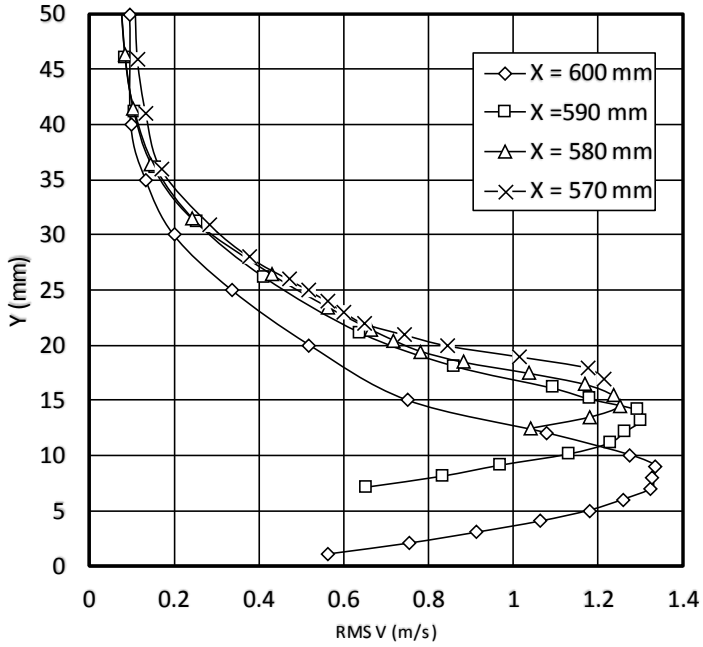

Fig C.1. RMS Velocity profiles in the wake region for free stream velocity of 9 m/s in plane Z = 0, $U_\infty = 9\ m/s$.

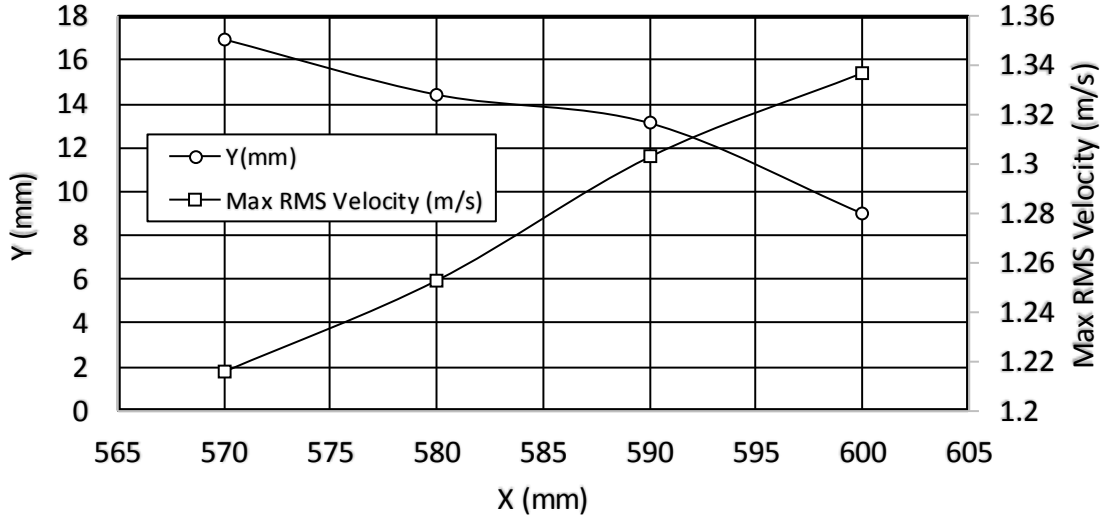

Fig C.2. Trajectory of Max RMS velocity in the wake region for free stream velocity of 9 m/s in plane Z = 0, $U_\infty = 9\ m/s$.

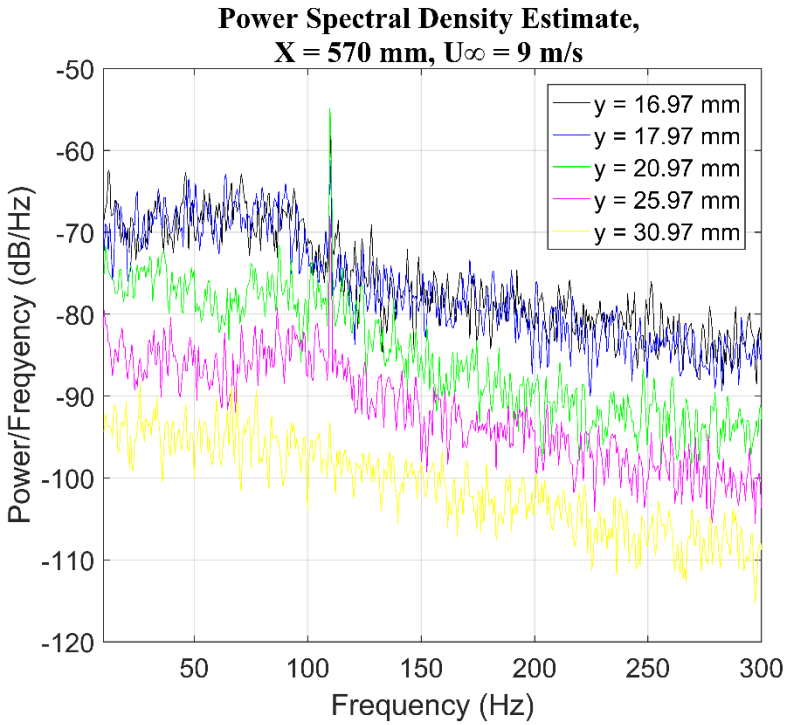

Fig C.3. Power spectral density profiles in and out of the wake region in plane Z =0 at X = 570 mm, $U_\infty = 9\ m/s$.

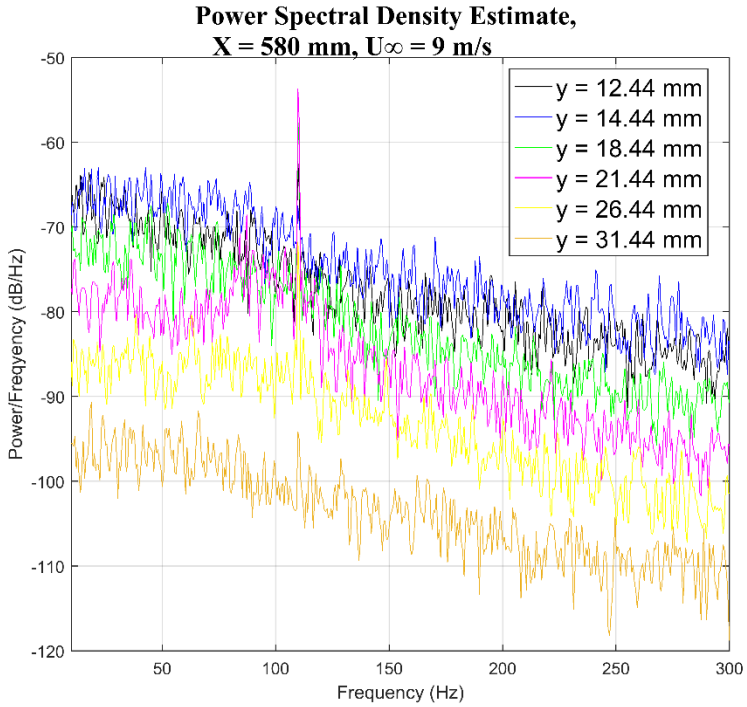

Fig C.4. Power spectral density profiles in and out of the wake region in plane Z = 0 at X = 580 mm, $U_\infty = 9\ m/s$.

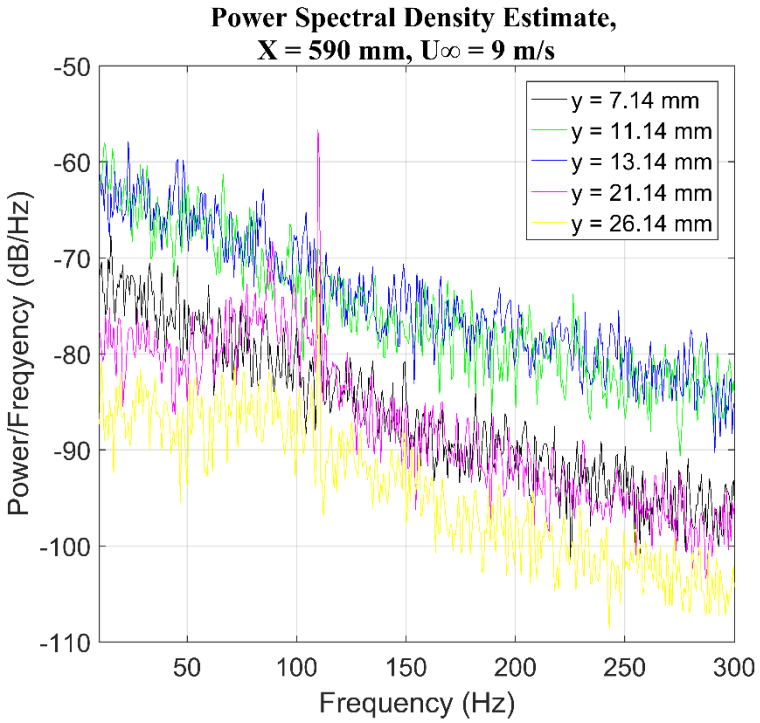

Fig C.5. Power spectral density profiles in and out of the wake region in plane Z = 0 at X = 590 mm, $U_\infty = 9\ m/s$.

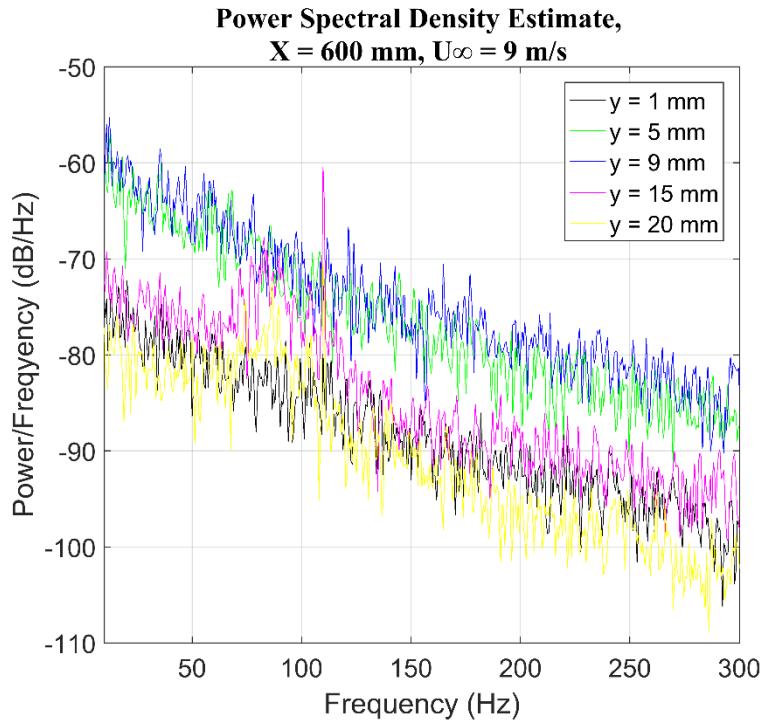

Fig C.6. Power spectral density profiles in and out of the wake region in plane Z = 0 at X = 600 mm, $U_\infty = 9\ m/s$.

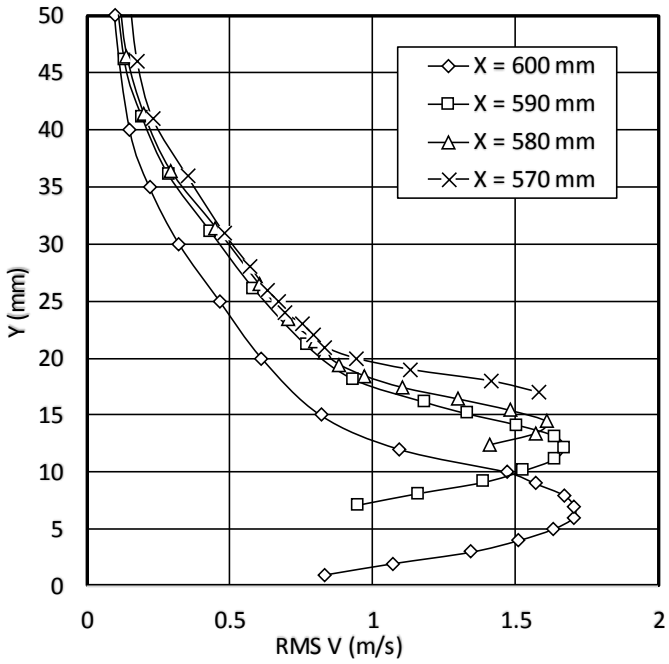

Fig. C.7. RMS Velocity profiles in the wake region for free stream velocity of 12 m/s in plane Z = 0, $U_\infty = 12\ m/s$.

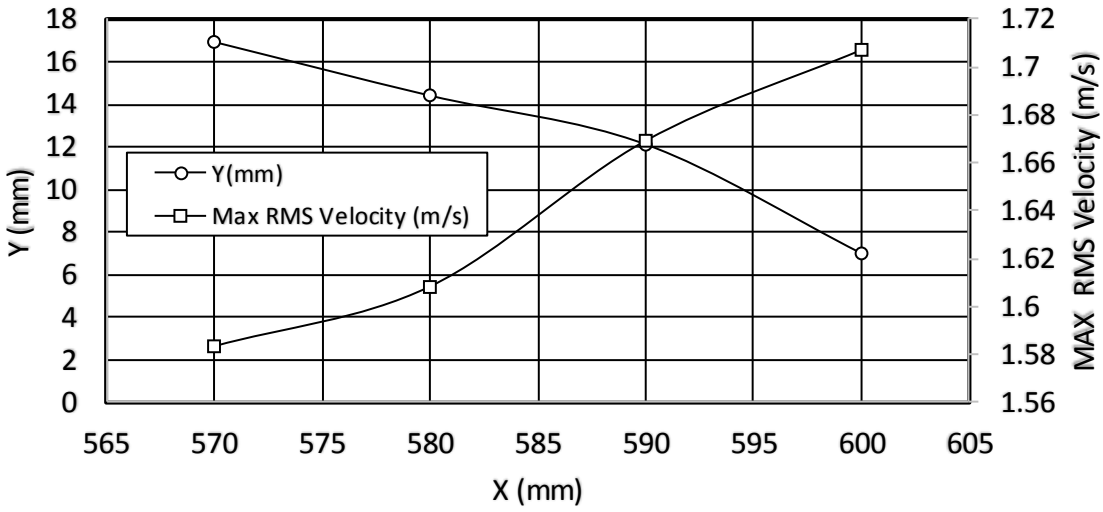

Fig C.8. Trajectory of Max RMS velocity in the wake region for free stream velocity of 12 m/s in plane Z = 0, $U_\infty = 12\ m/s$.

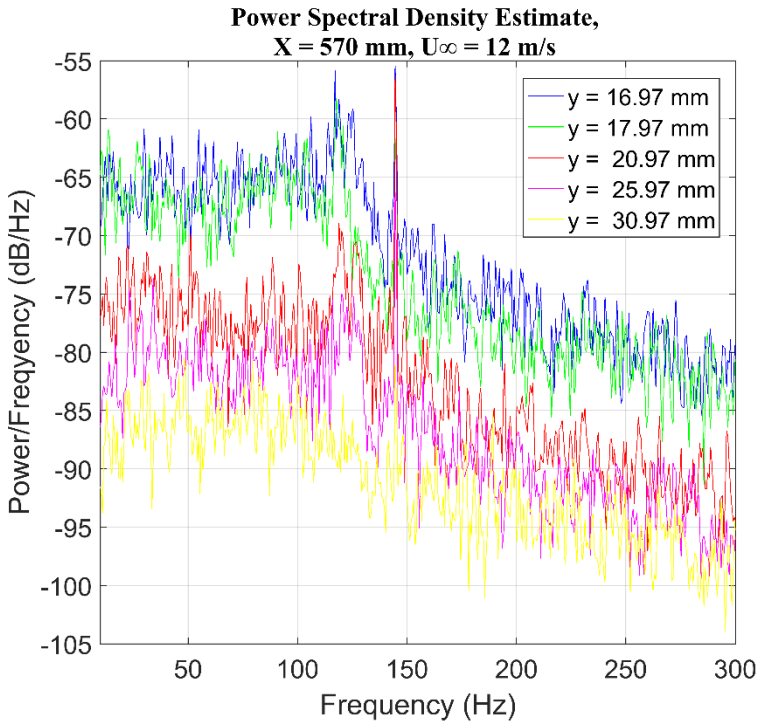

Fig C.9. Power spectral density profiles in and out of the wake region in plane Z = 0 at X = 570 mm, $U_\infty = 12\ m/s$.

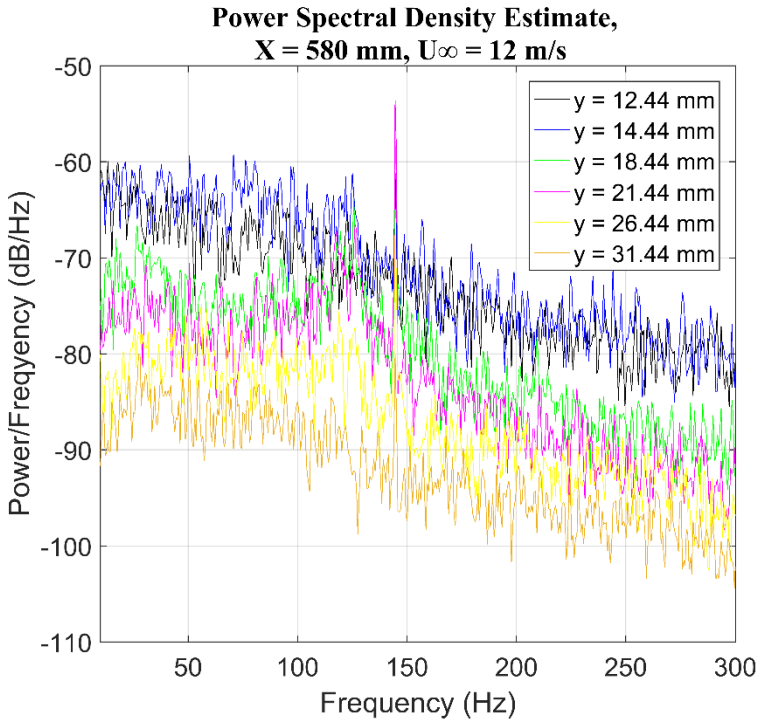

Fig C.10. Power spectral density profiles in and out of the wake region in plane Z = 0 at X = 580 mm, $U_\infty = 12\ m/s$.

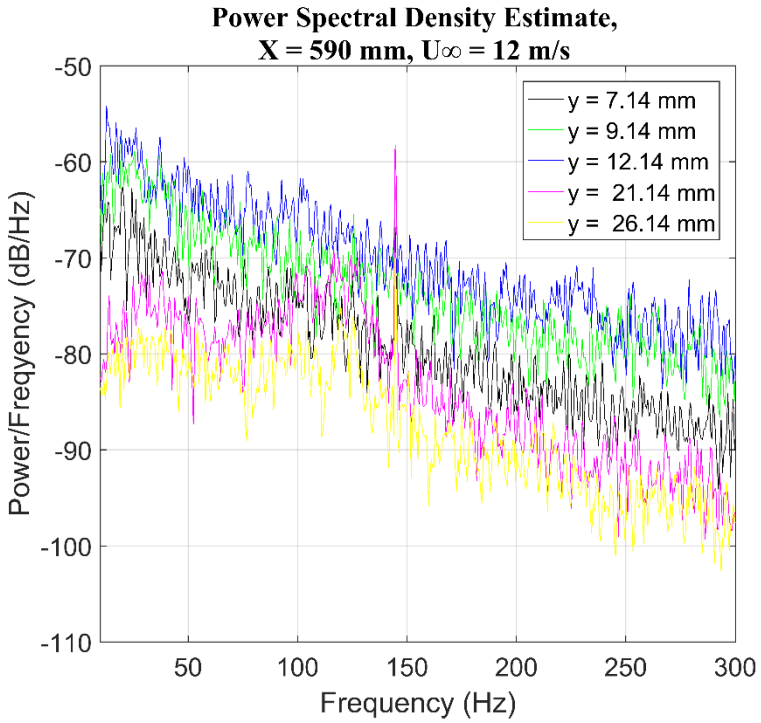

Fig C.11. Power spectral density profiles in and out of the wake region in plane Z = 0 at X = 590 mm, $U_\infty = 12\ m/s$.

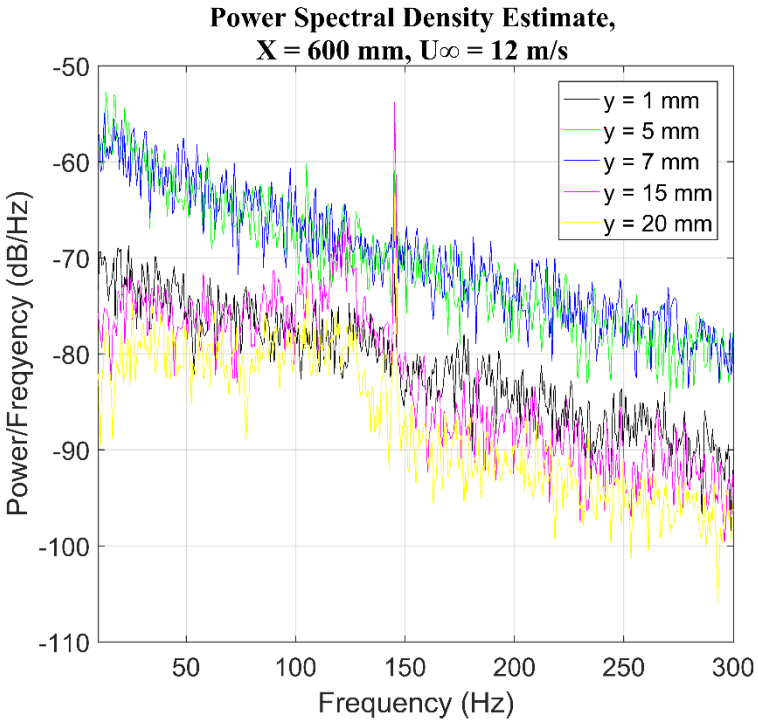

Fig C.12. Power spectral density profiles in and out of the wake region in plane Z = 0 at X = 600mm, $U_\infty = 12\ m/s$.

Appendix D- Additional Particle Image Velocimetry (PIV) Results

Sine Wave, Velocity Ratio of 1.50, Angular Position: $\phi = 5°$

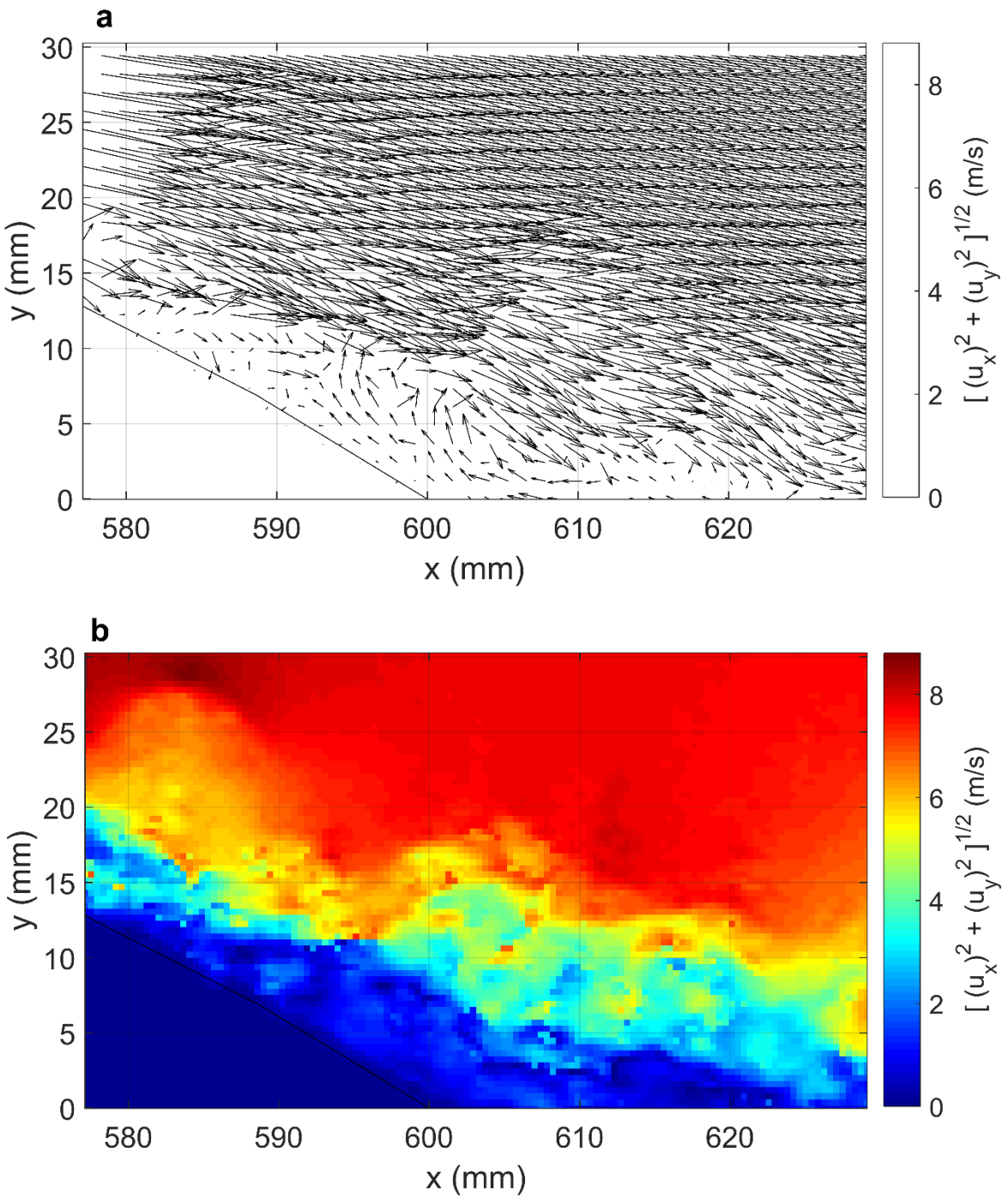

Fig D.1. (a , b) Instantaneous velocity vector and magnitude fields in the wake region- actuated case, Sine wave, VR=1.5, Angular position: $\phi = 5°, U_\infty = 7\ m/s$.

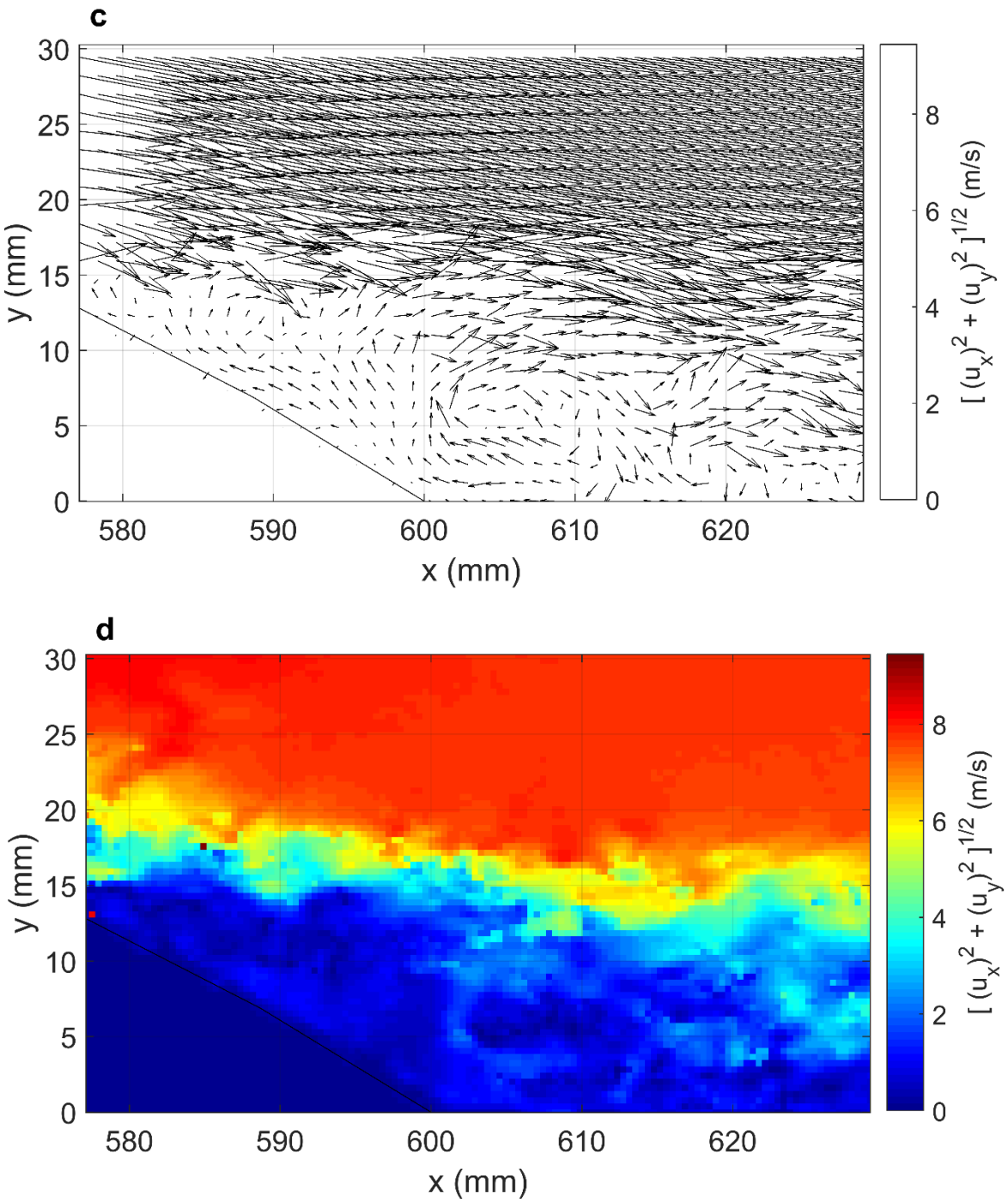

Fig D.1. (c , d) Instantaneous velocity vector and magnitude fields in the wake region- actuated case, Sine wave, VR=1.5, Angular position: $\phi = 5°, U_\infty = 7\ m/s$.

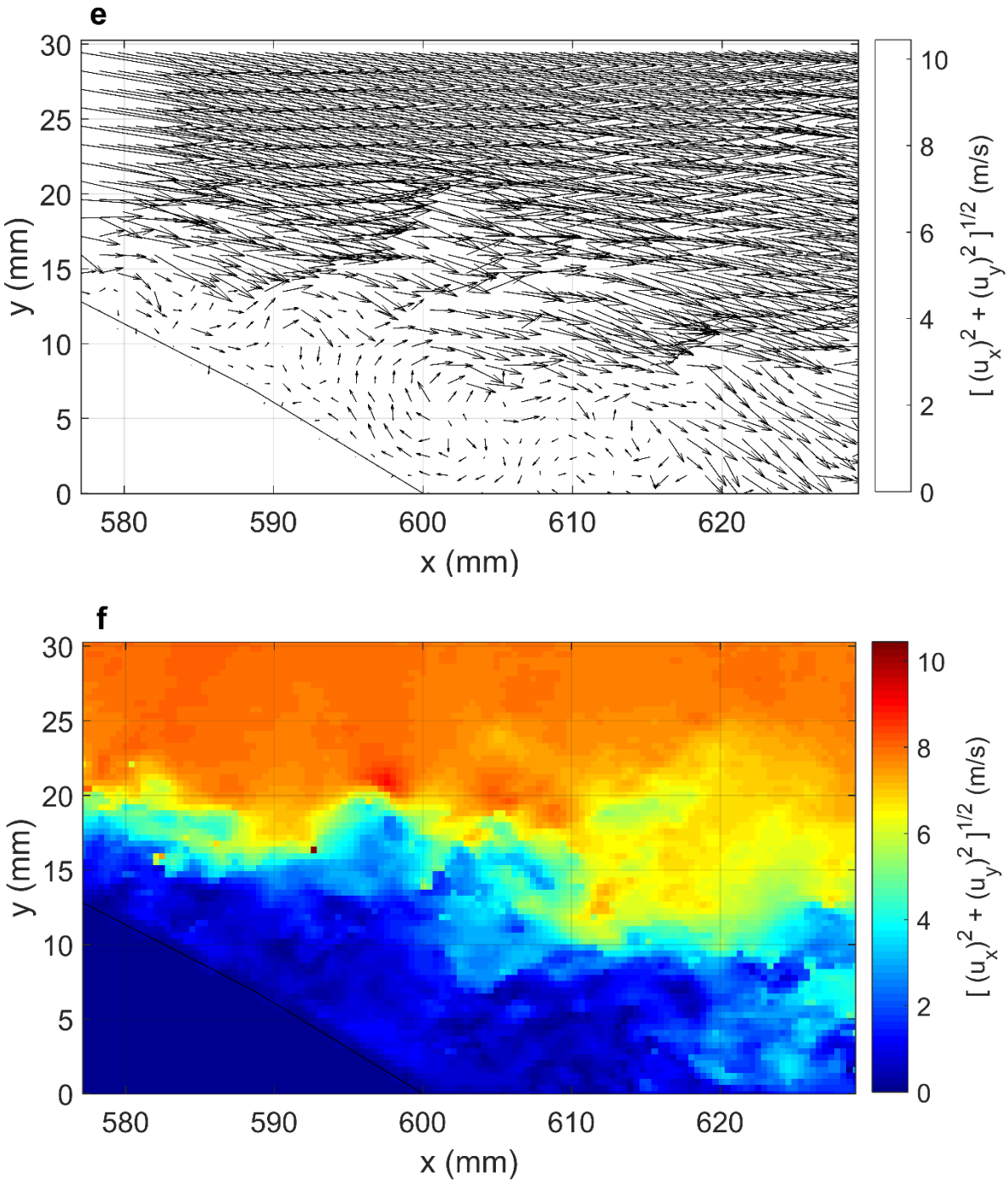

Fig D.1. (e , f) Instantaneous velocity vector and magnitude fields in the wake region- actuated case, Sine wave, VR=1.5, Angular position: $\phi = 5°, U_\infty = 7\ m/s$.

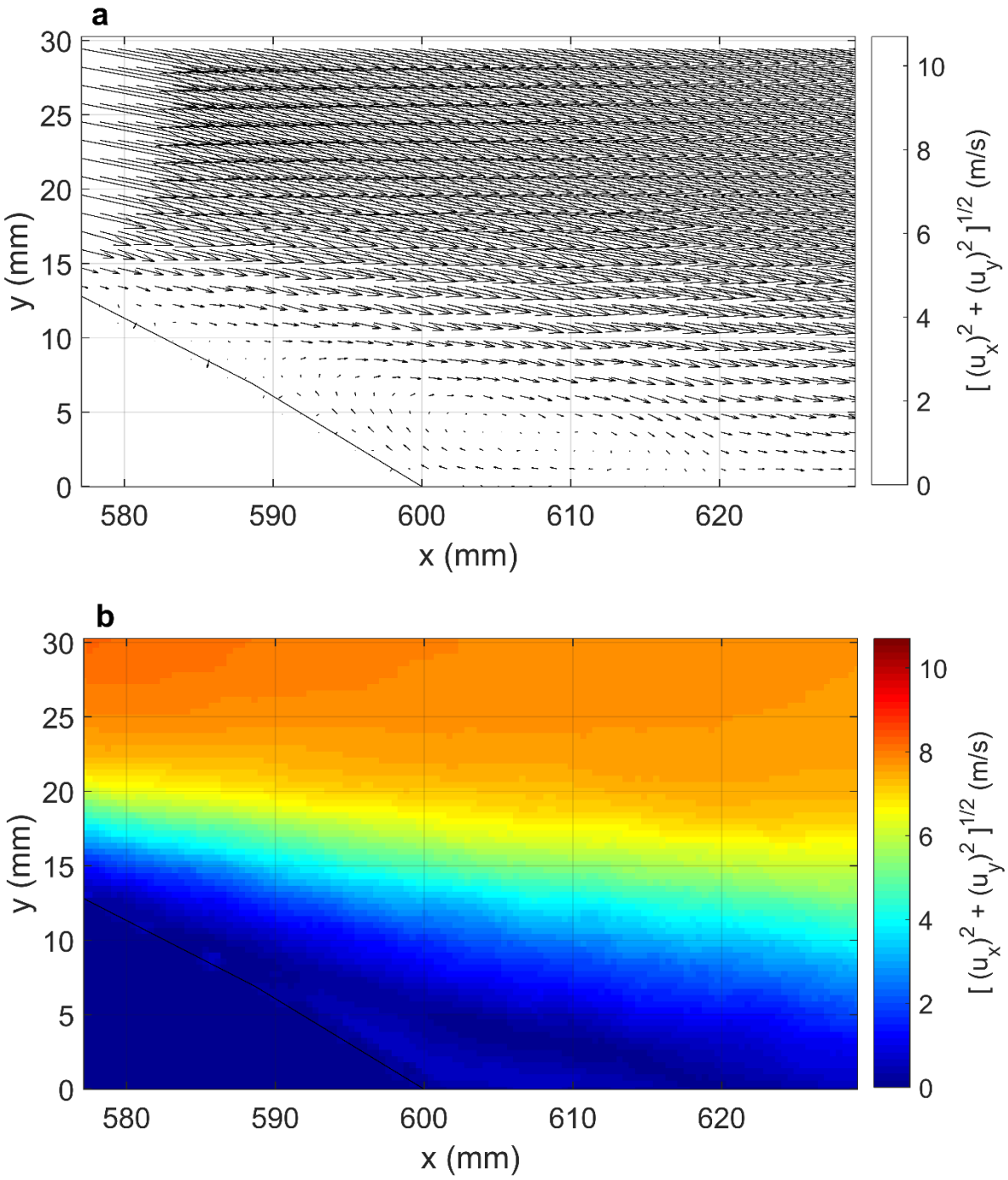

Fig D.2. (a , b) Average velocity vector and magnitude fields in the wake region- actuated case, Sine wave, VR=1.5, Angular position: $\phi = 5°, U_\infty = 7\ m/s$.

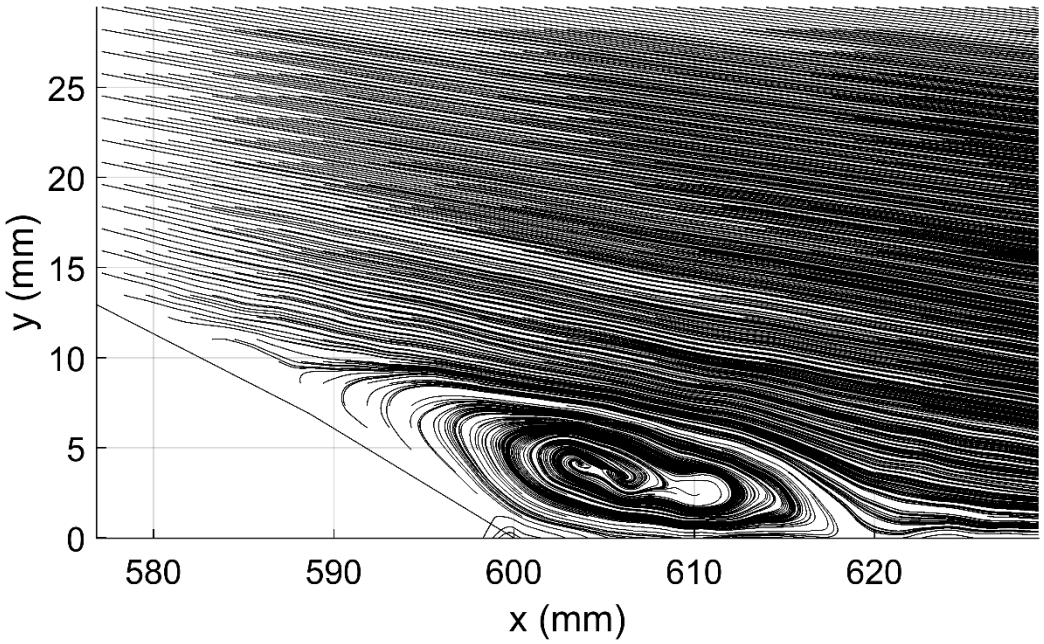

Fig D.3. Streamlines profile, actuated case, Sine wave, VR=1.5, Angular position: $\phi = 5°$, $U_\infty = 7\ m/s$.

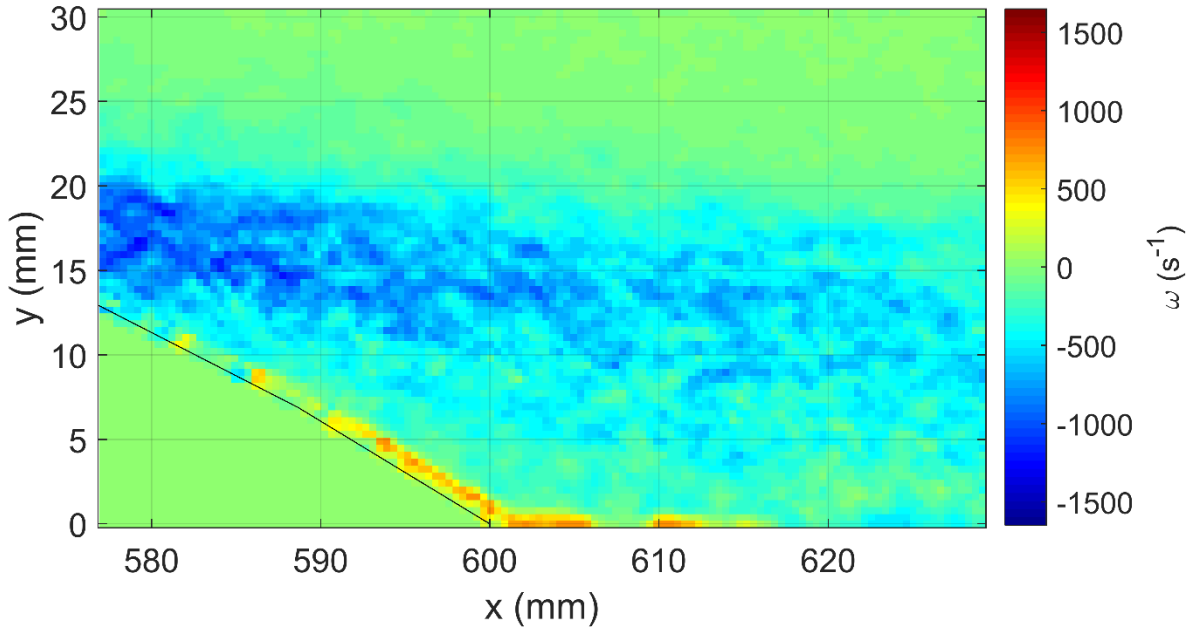

Fig D.4. Vorticity contour, actuated case, Sine wave, VR=1.5, Angular position: $\phi = 5°$, $U_\infty = 7\ m/s$.

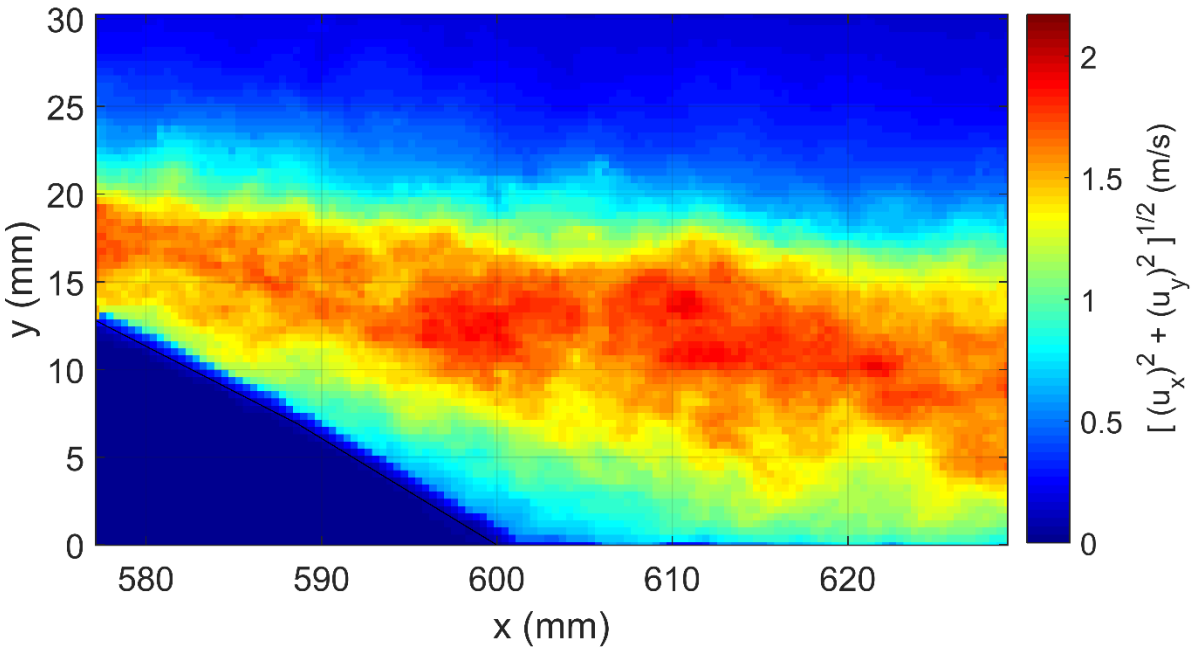

Fig D.5. RMS Velocity contour actuated case, Sine wave, VR=1.5, Angular position: $\phi = 5°$, $U_\infty = 7\ m/s$.

This Space Intentionally Left Blank.

Sine Wave, Velocity Ratio of 1.50, Angular Position: $\phi = 12.5°$

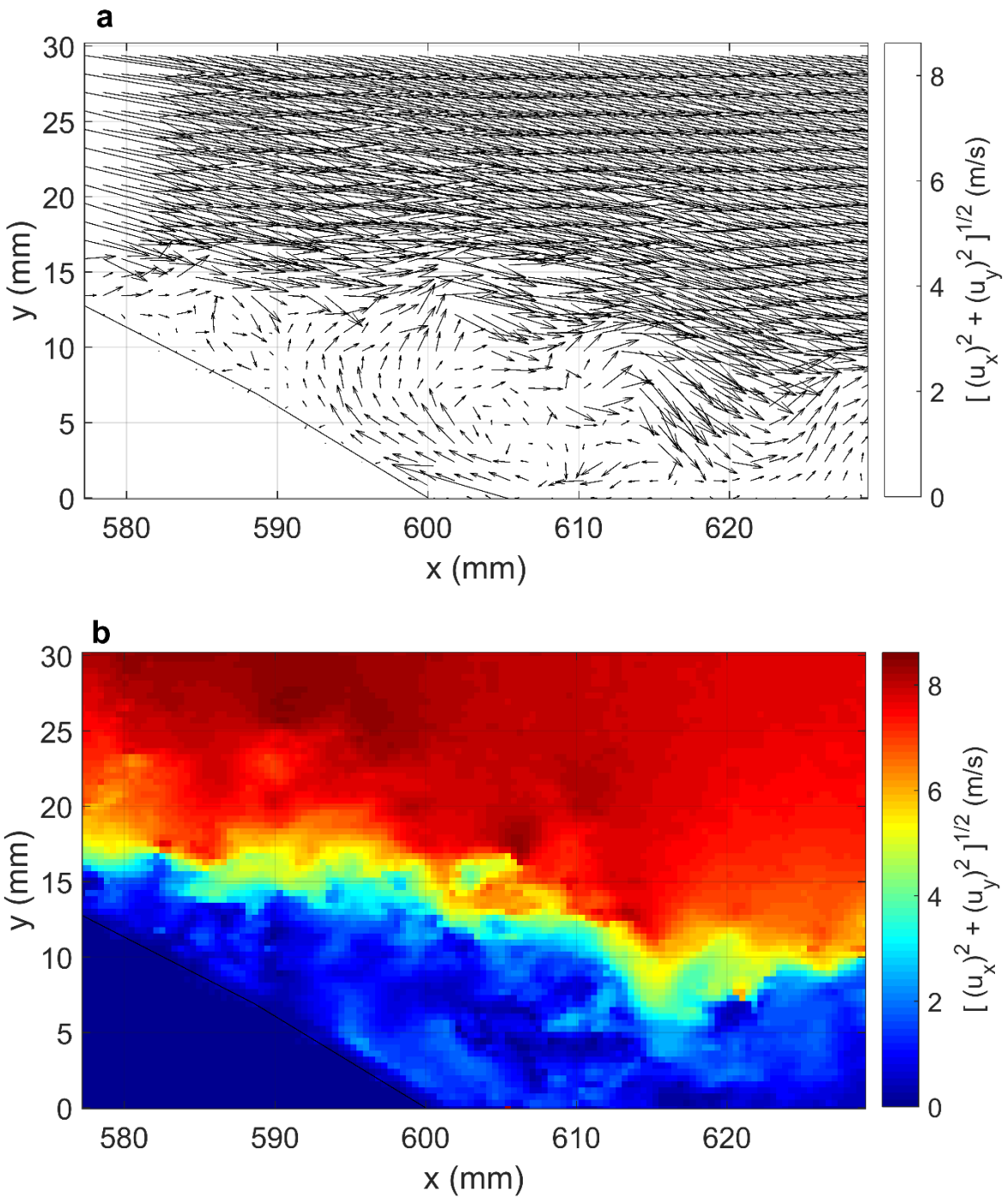

Fig D.6. (a , b) Instantaneous velocity vector and magnitude fields in the wake region- actuated case, Sine wave, VR=1.5, Angular position: $\phi = 12.5°$, $U_\infty = 7\ m/s$.

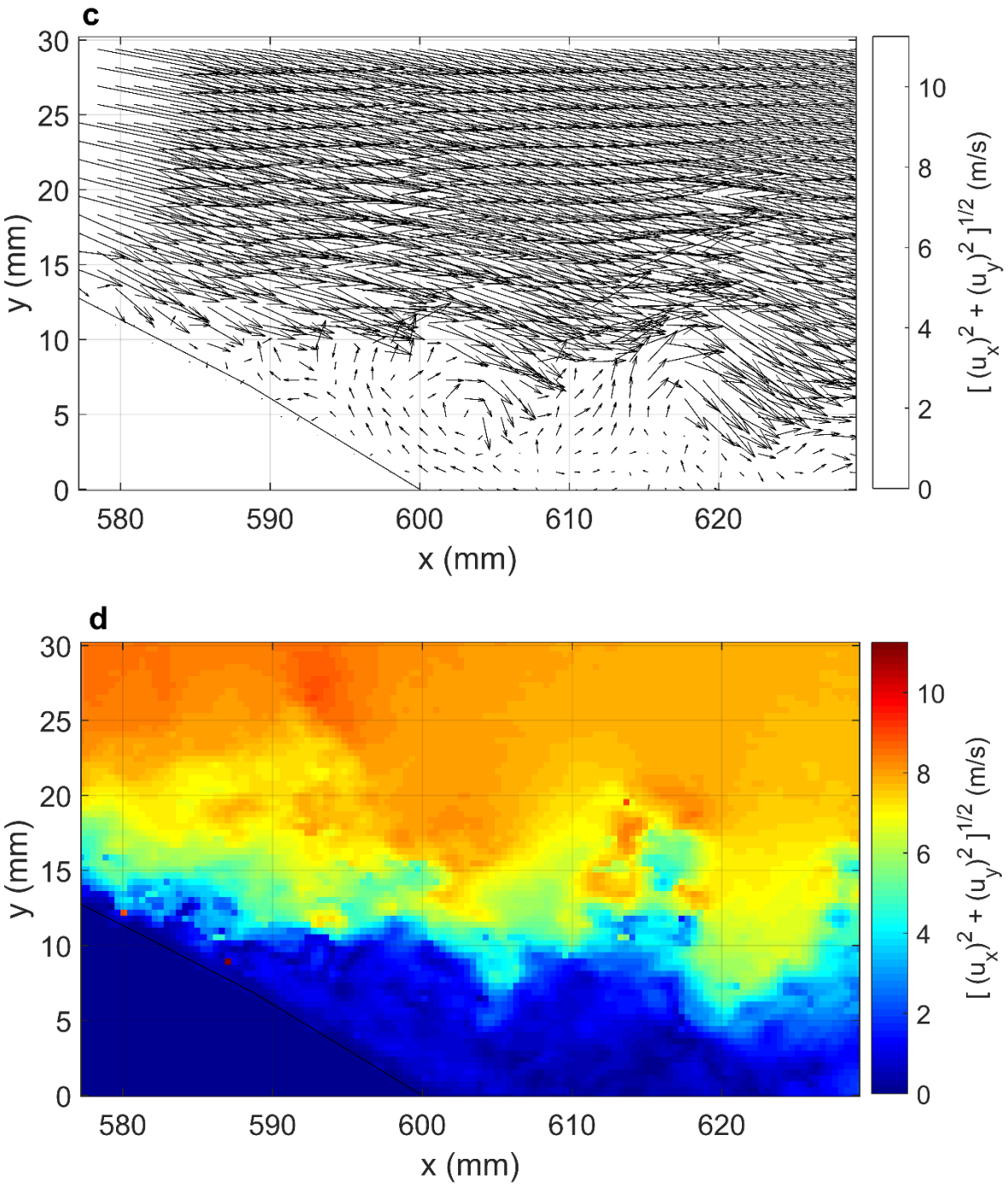

Fig D.6. (c , d) Instantaneous velocity vector and magnitude fields in the wake region- actuated case, Sine wave, VR=1.5, Angular position: $\phi = 12.5°$, $U_\infty = 7\ m/s$.

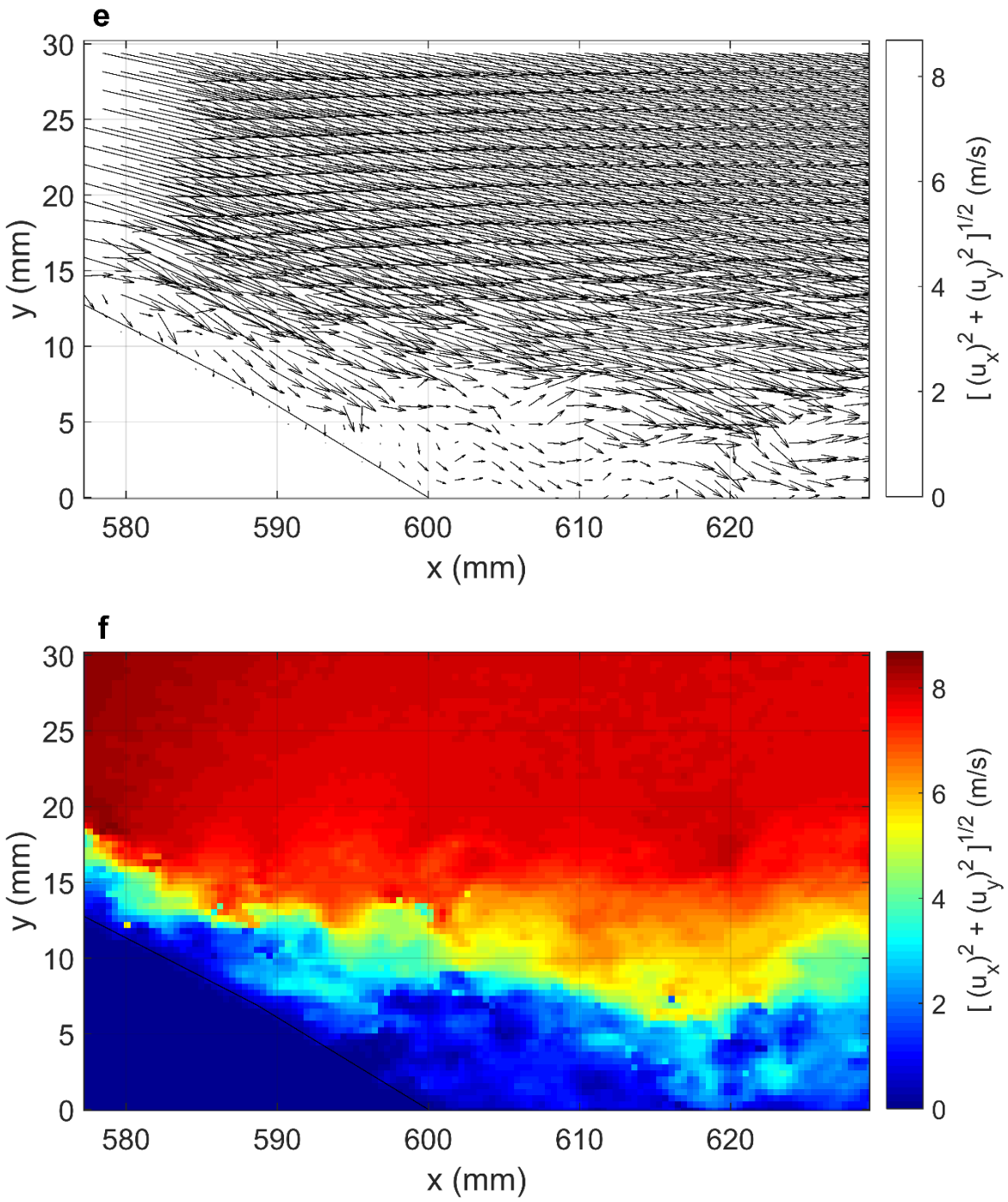

Fig D.6. (e , f) Instantaneous velocity vector and magnitude fields in the wake region- actuated case, Sine wave, VR=1.5, Angular position: $\phi = 12.5°$, $U_\infty = 7\ m/s$.

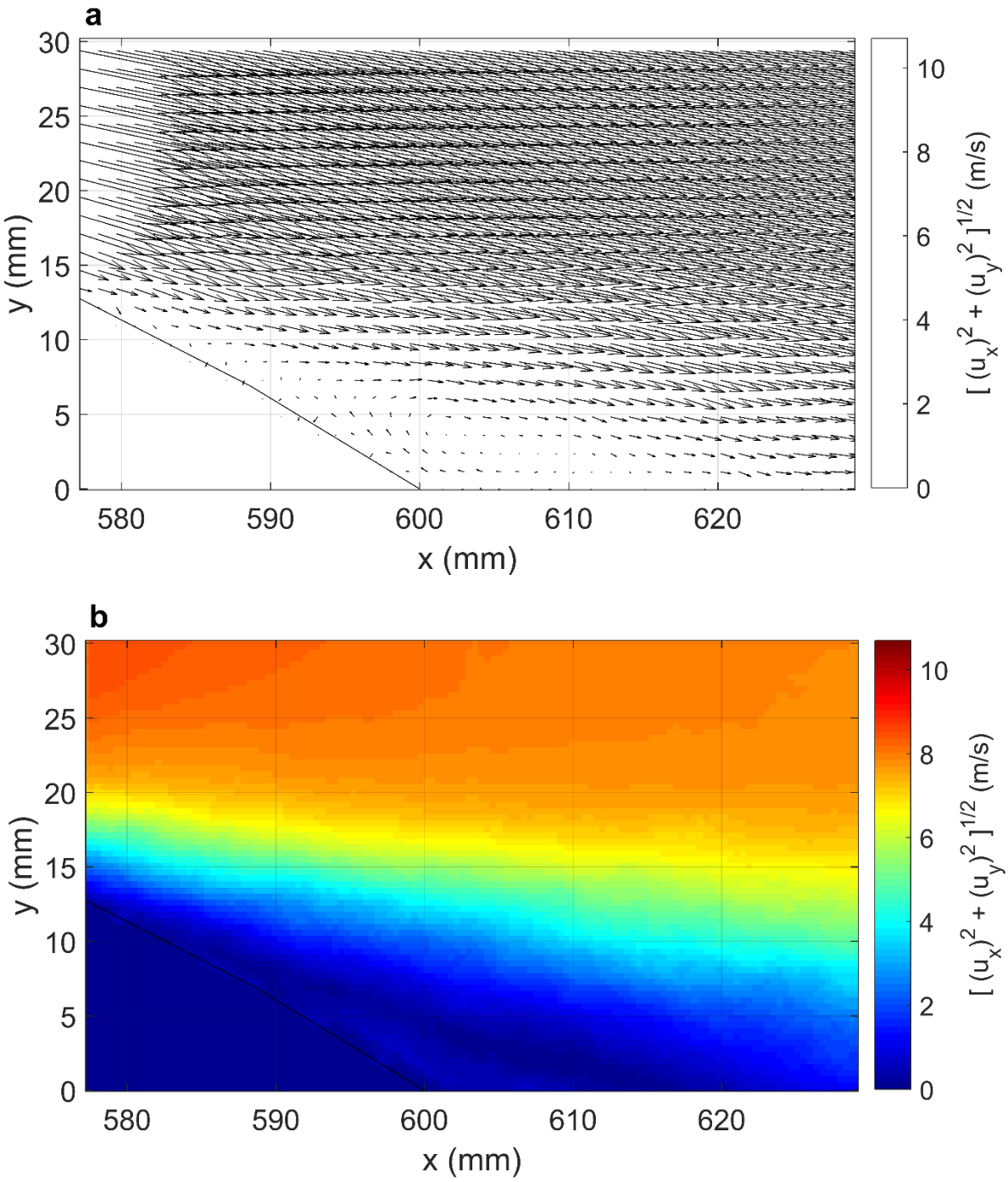

Fig D.7. (a , b) Average velocity vector and magnitude fields in the wake region- actuated case, Sine wave, VR=1.5, Angular position: $\phi = 12.5°$, $U_\infty = 7\ m/s$.

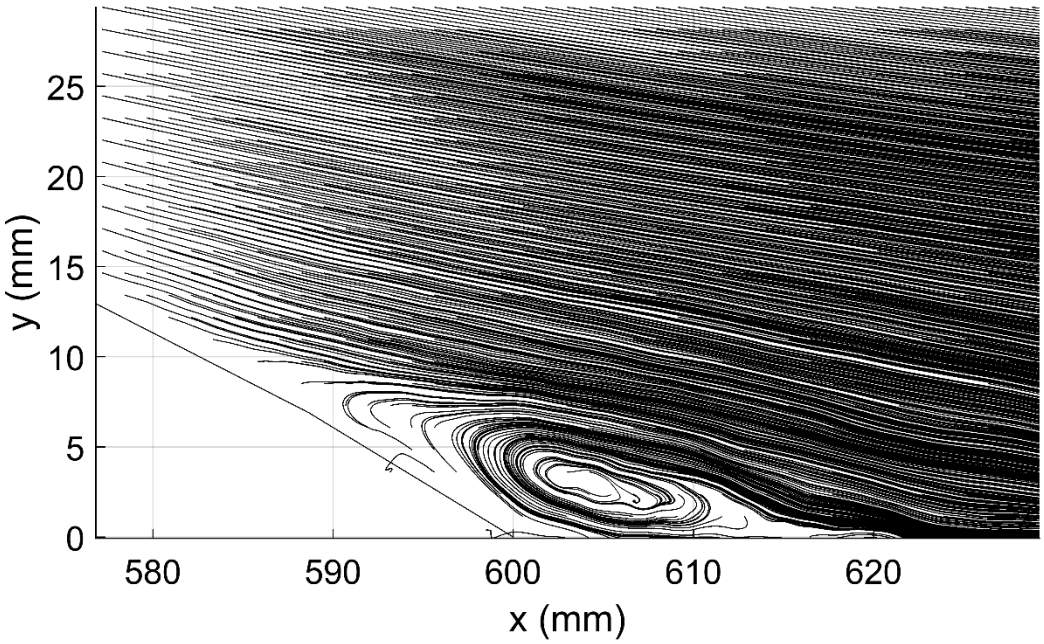

Fig D.8. Streamlines profile, actuated case, Sine wave, VR=1.5, Angular position: $\phi = 12.5°$.

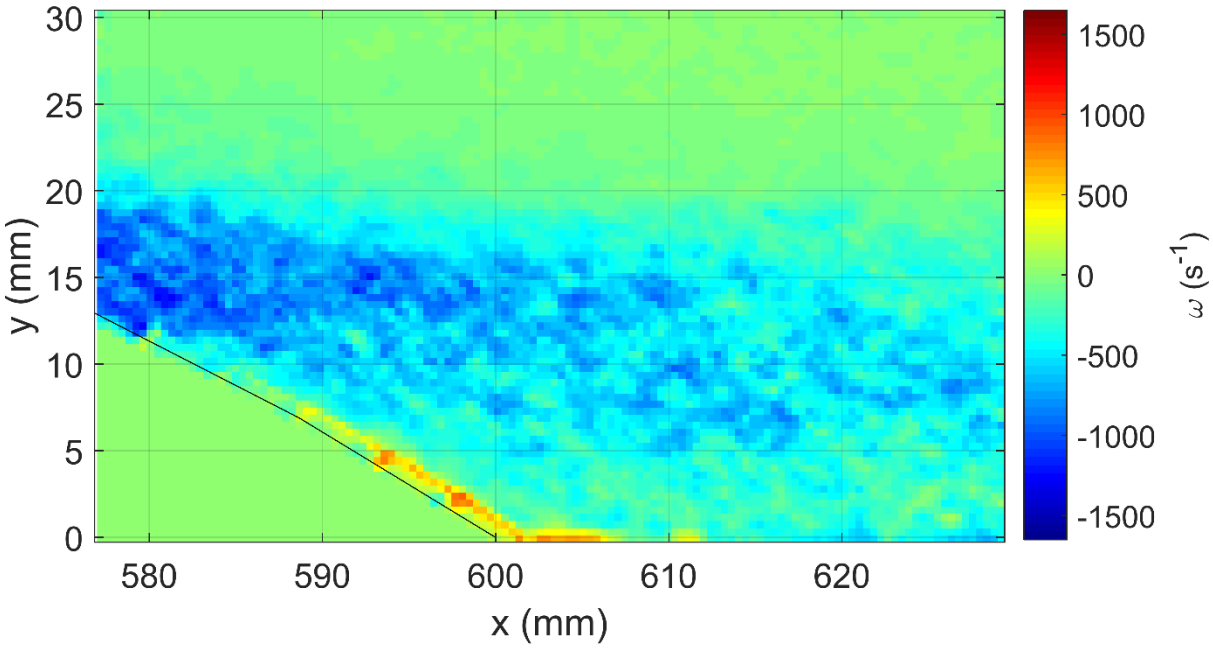

Fig D.9. Vorticity contour, actuated case, Sine wave, VR=1.5, Angular position: $\phi = 12.5°$, $U_\infty = 7\ m/s$.

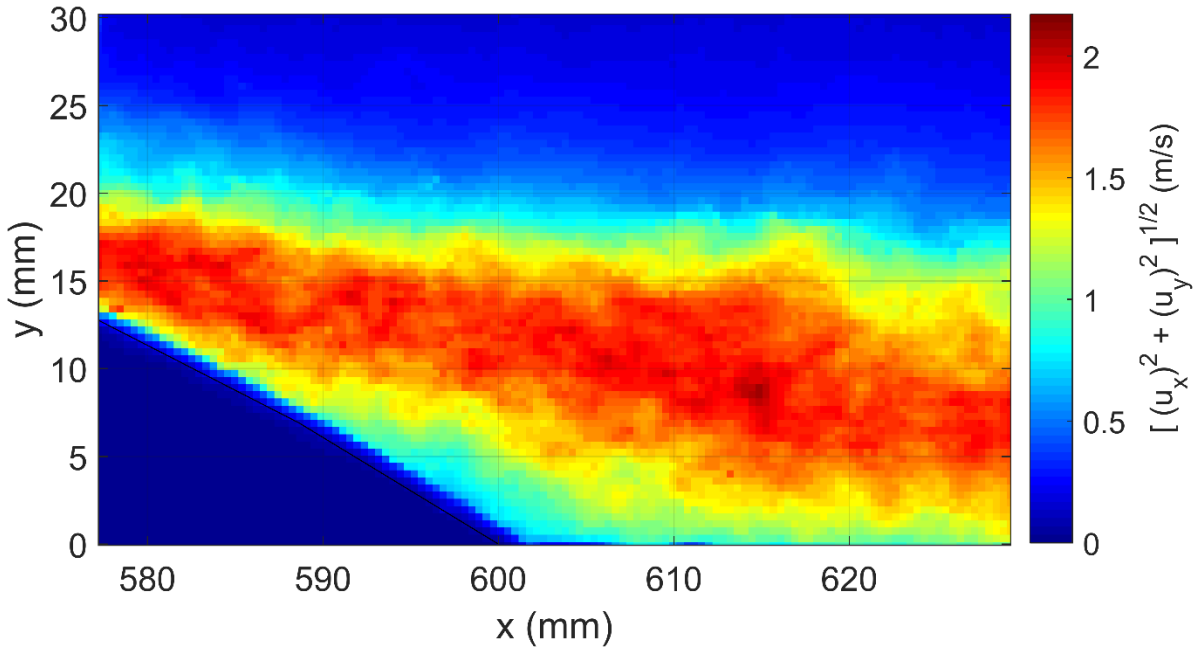

Fig D.10. RMS velocity contour, actuated case, Sine wave, VR=1.5, Angular position: $\phi = 12.5°, U_\infty = 7\ m/s.$

Sine Wave, Velocity Ratio of 1.50, Angular Position: $\phi = 17.5°$

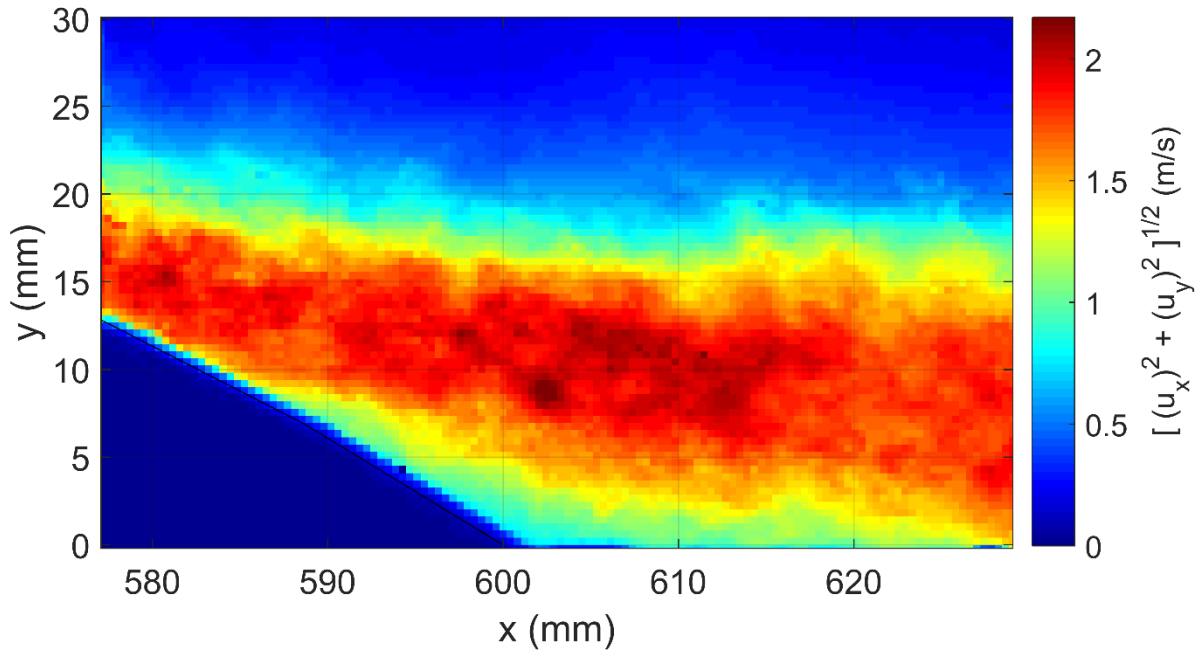

Fig D.11. RMS Vorticity contour, actuated case, Sine wave, VR=1.5, Angular position: $\phi = 17.5°, U_\infty = 7\ m/s.$

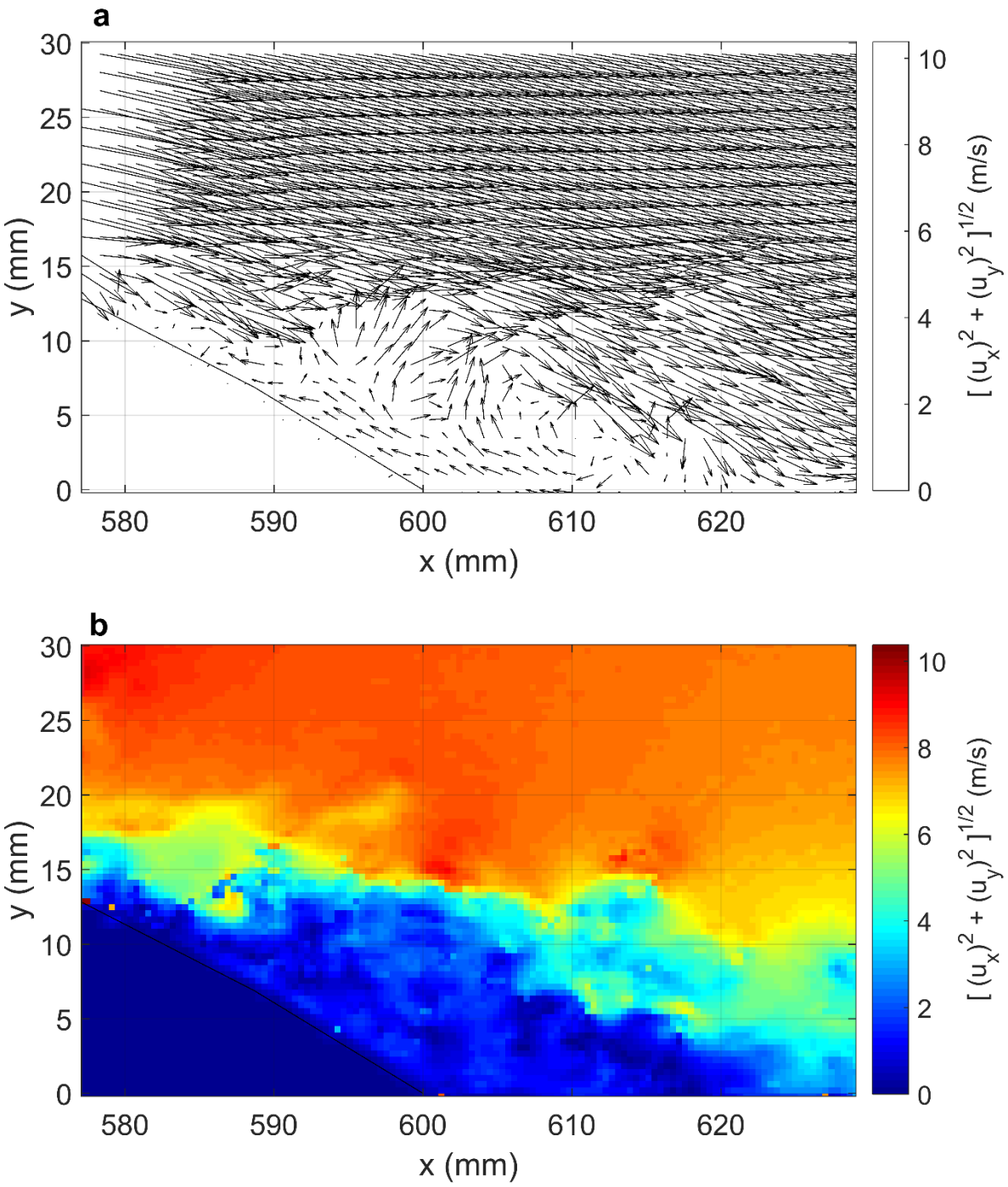

Fig D.12. (a , b) Instantaneous velocity vector and magnitude fields in the wake region- actuated case, Sine wave, VR=1.5, Angular position: $\phi = 17.5°$, $U_\infty = 7\ m/s$.

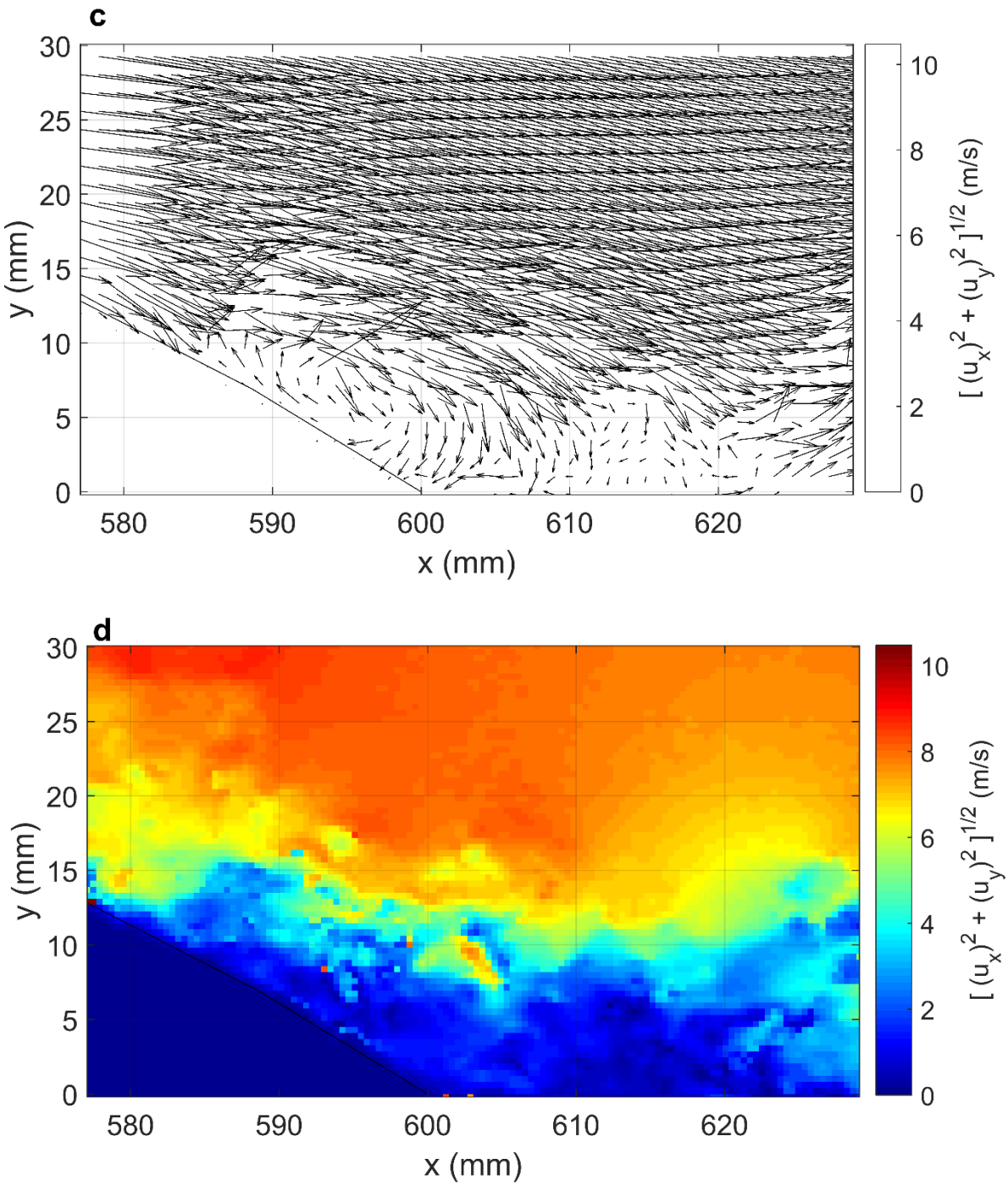

Fig D.12. (c , d) Instantaneous velocity vector and magnitude fields in the wake region- actuated case, Sine wave, VR=1.5, Angular position: $\phi = 17.5°$, $U_\infty = 7\ m/s$.

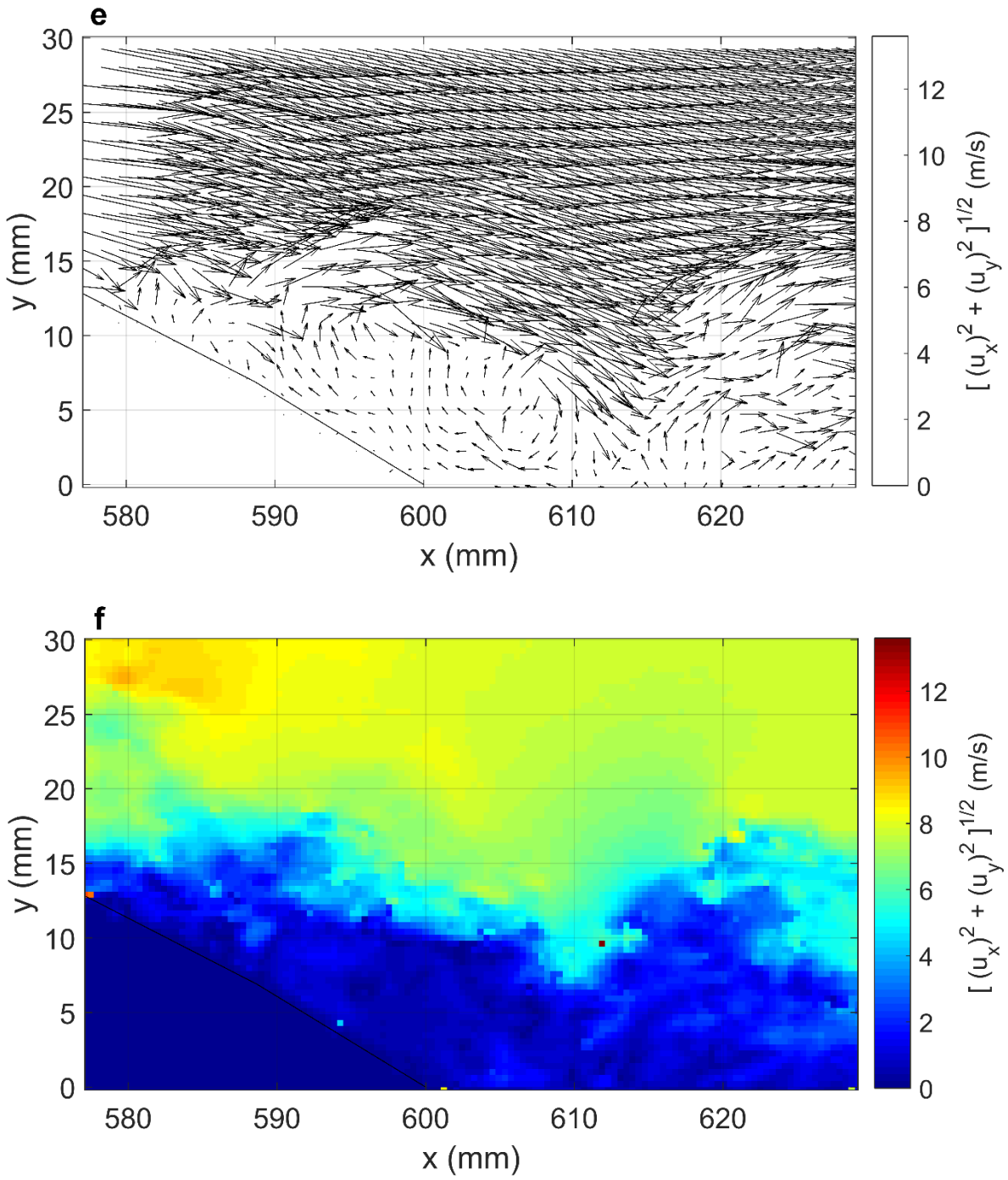

Fig D.12. (e , f) Instantaneous velocity vector and magnitude fields in the wake region- actuated case, Sine wave, VR=1.5, Angular position: $\phi = 17.5°$, $U_\infty = 7\ m/s$.

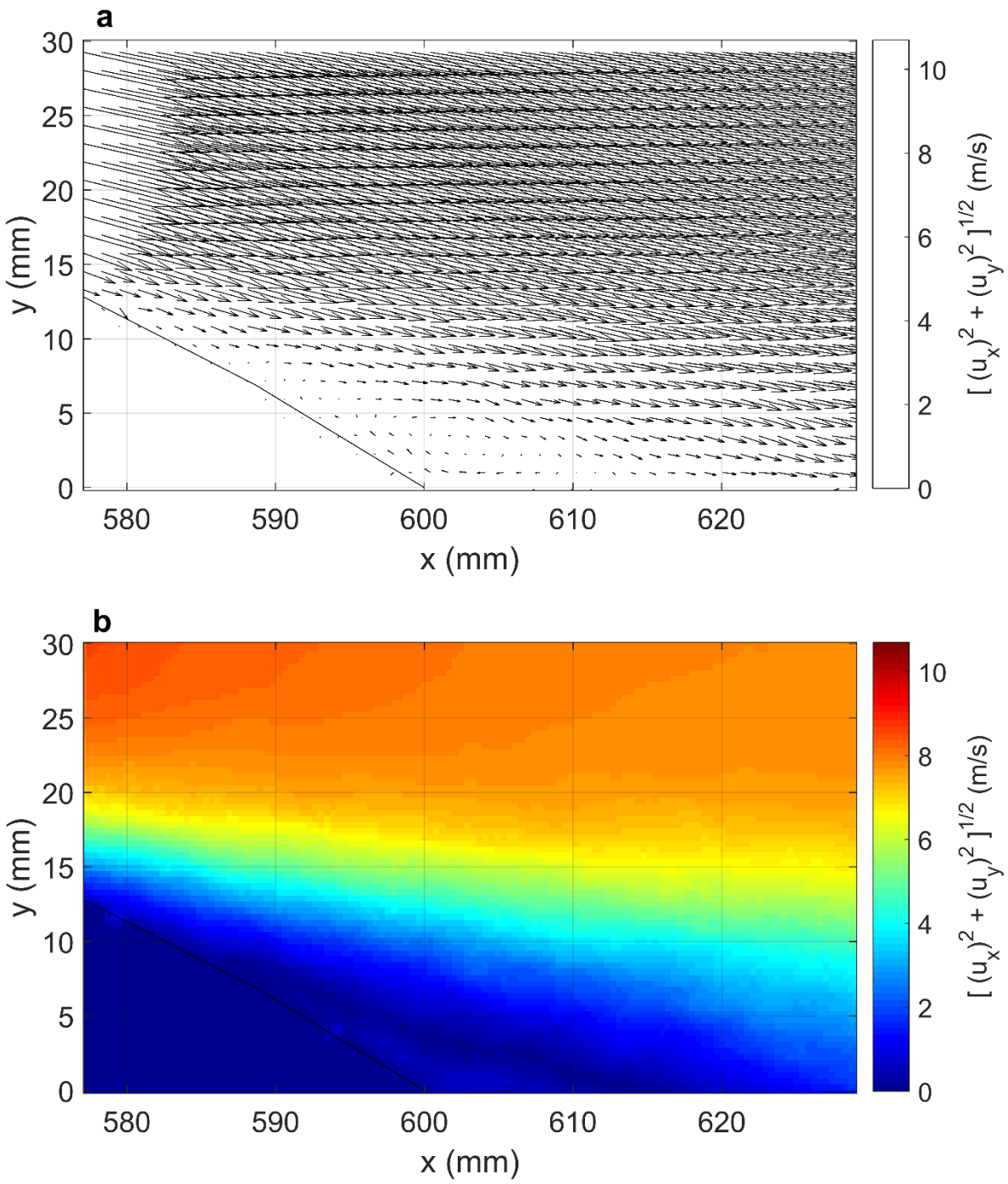

Fig D.13. (a , b) Average velocity vectors and magnitude fields in the wake region- actuated case, Sine wave, VR=1.5, Angular position: $\phi = 17.5°$, $U_\infty = 7\ m/s$.

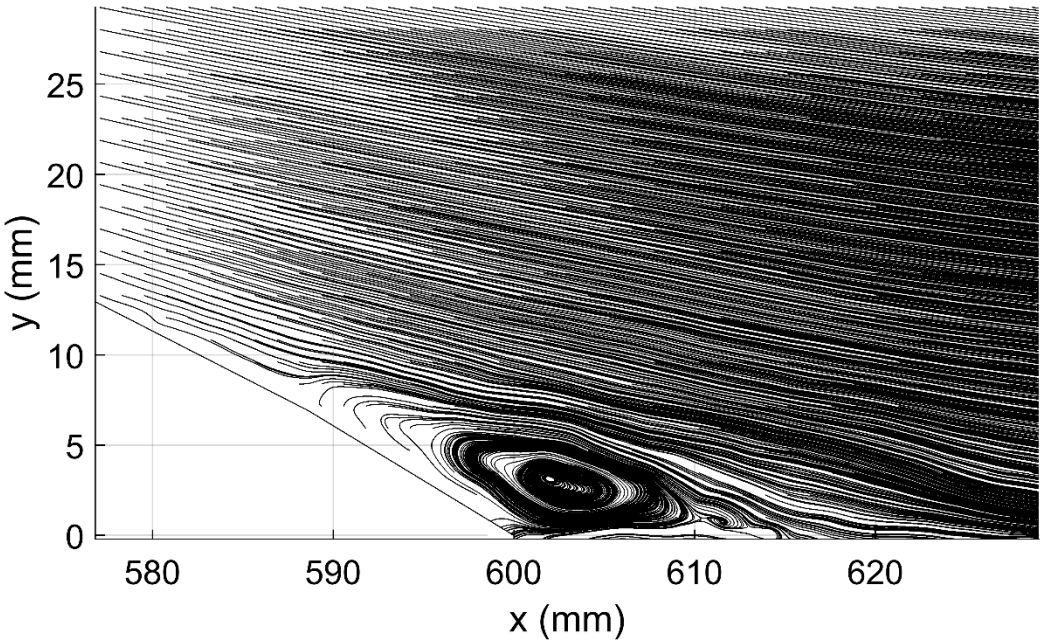

Fig D.14. Streamlines profile, actuated case, Sine wave, VR=1.5, Angular position: $\phi = 17.5°$, $U_\infty = 7\ m/s$.

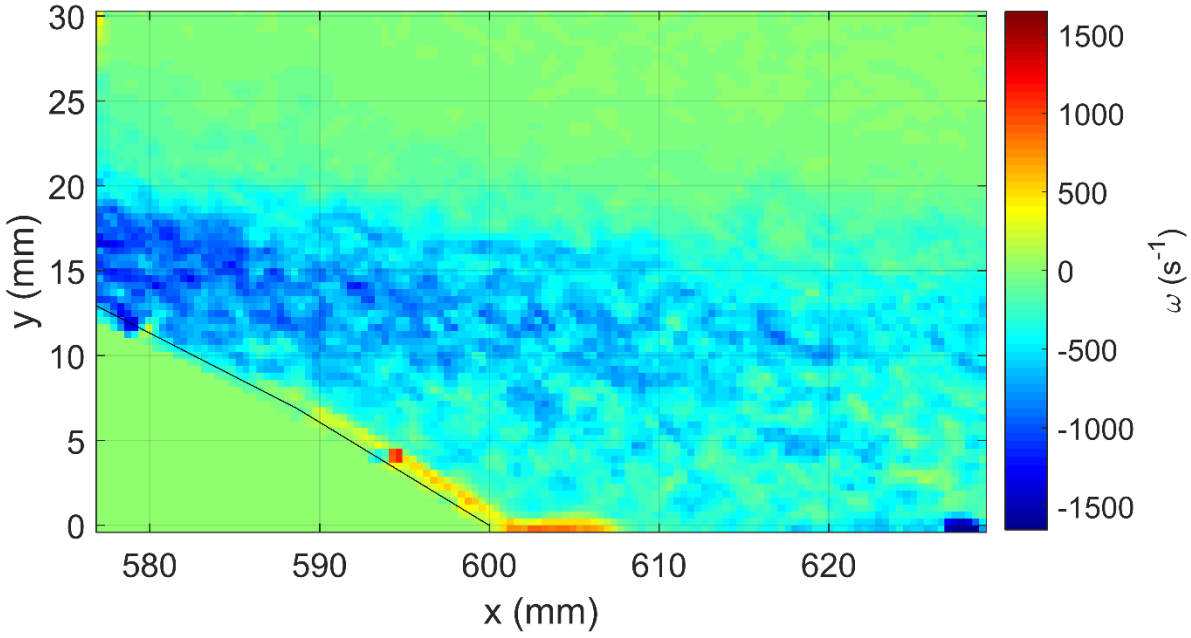

Fig D.15. Vorticity contour, actuated case, Sine wave, VR=1.5, Angular position: $\phi = 17.5°$, $U_\infty = 7\ m/s$.

Sine Wave, Velocity Ratio of 1.50, Angular Position: $\phi = 20°$

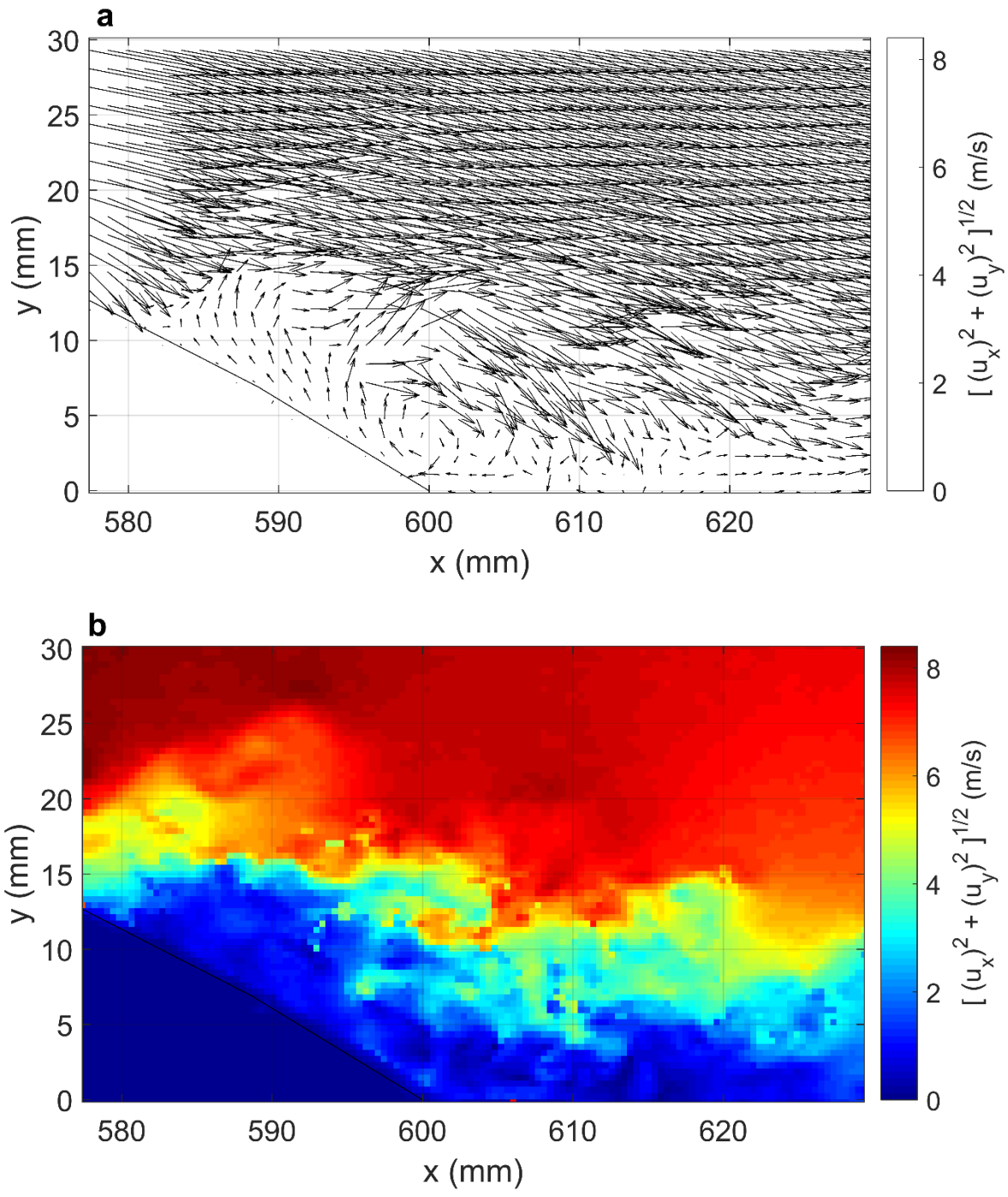

Fig D.16. (a , b) Instantaneous velocity vector and magnitude fields in the wake region- actuated case, Sine wave, VR=1.5, Angular position: $\phi = 20°, U_\infty = 7\ m/s$.

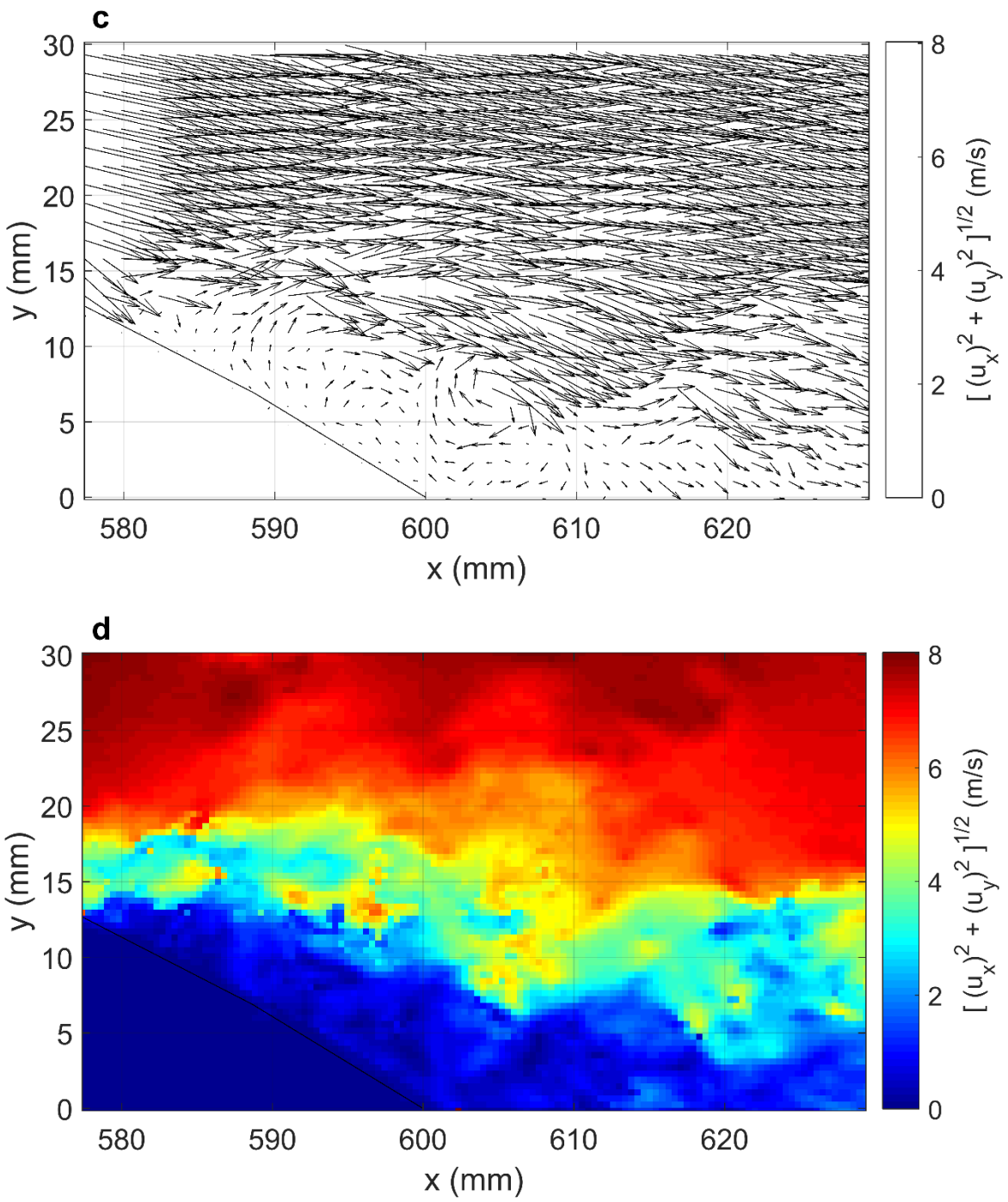

Fig D.16. (c , d) Instantaneous velocity vector and magnitude fields in the wake region- actuated case, Sine wave, VR=1.5, Angular position: $\phi = 20°, U_\infty = 7\ m/s$.

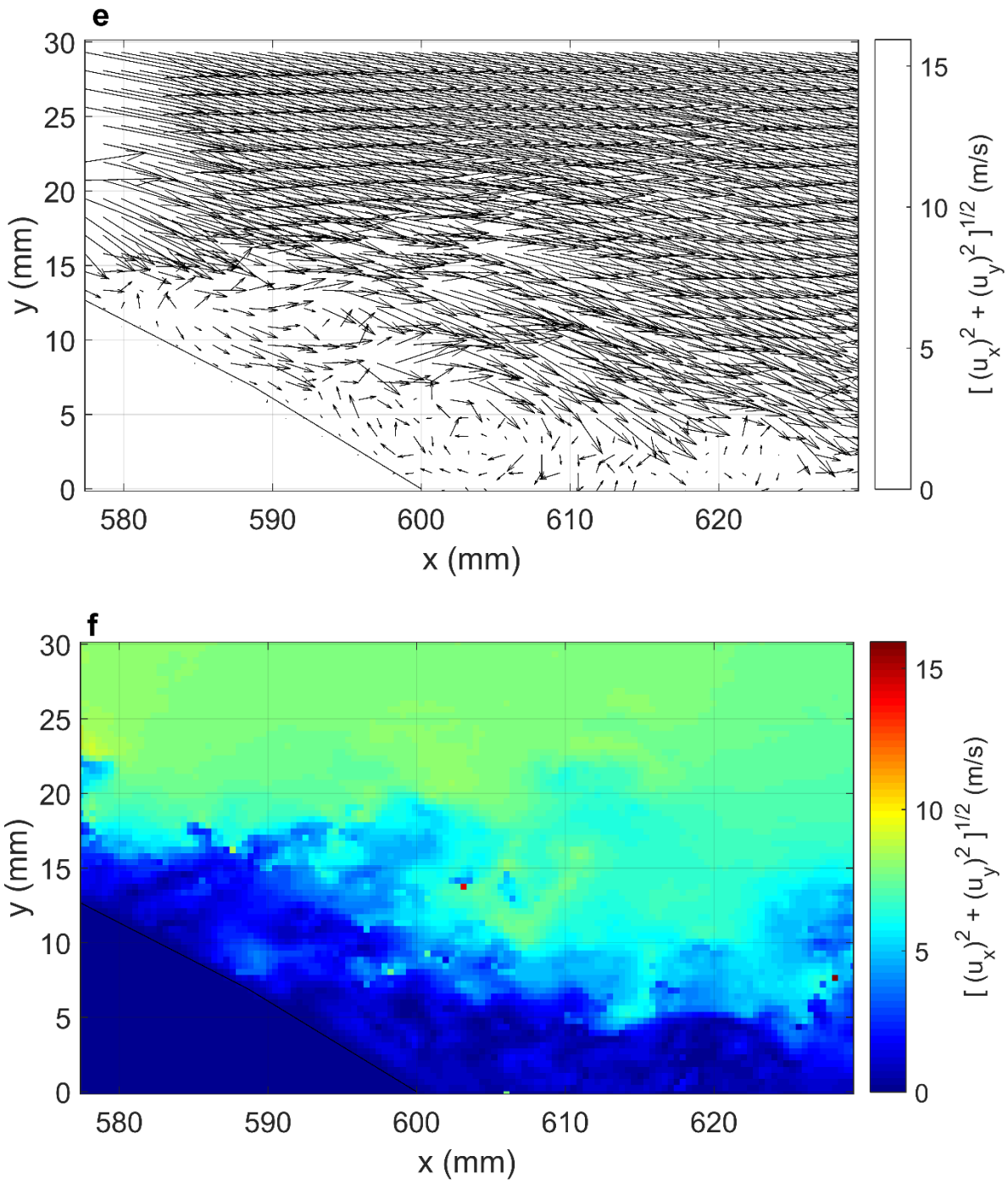

Fig D.16. (e , f) Instantaneous velocity vector and magnitude fields in the wake region- actuated case, Sine wave, VR=1.5, Angular position: $\phi = 20°$, $U_\infty = 7\ m/s$.

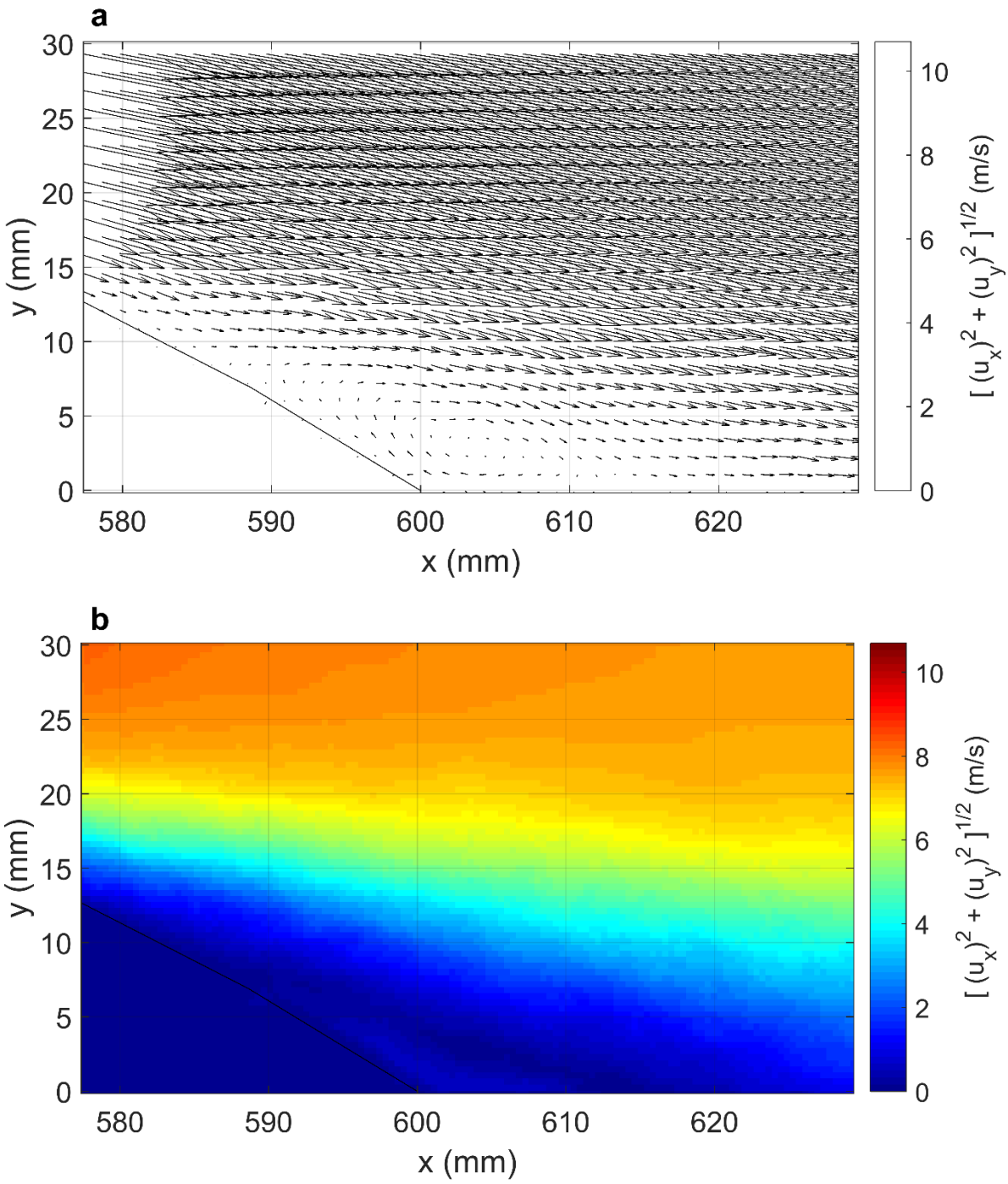

Fig D.17. (a , b) Average velocity vector and magnitude fields in the wake region- actuated case, Sine wave, VR=1.5, Angular position: $\phi = 20°$, $U_\infty = 7\ m/s$.

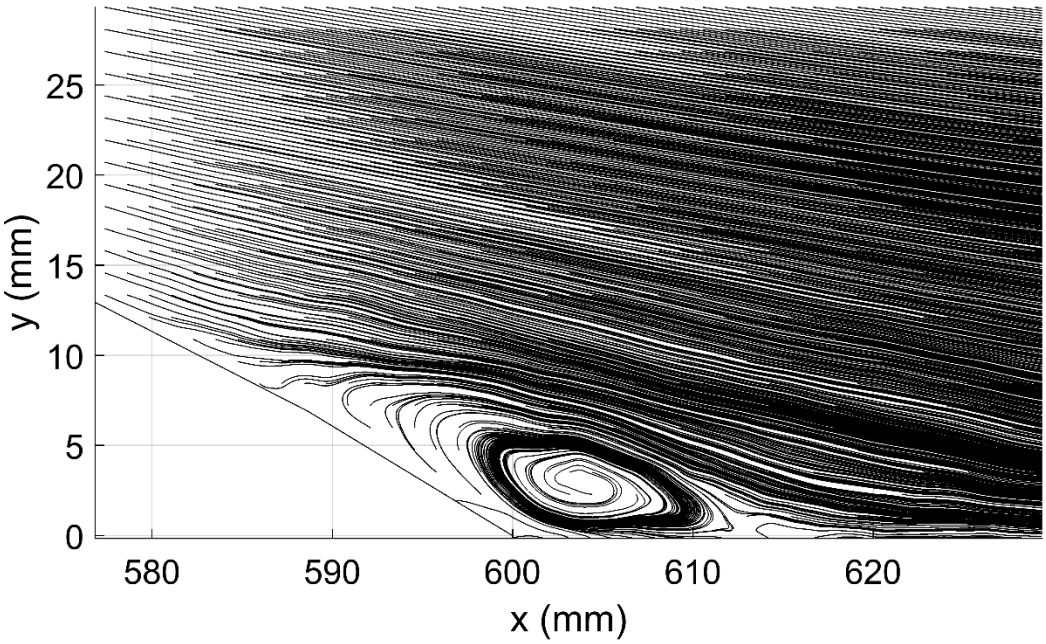

Fig D.18. Streamlines profile, actuated case, Sine wave, VR=1.5, Angular position: $\phi = 20°$, $U_\infty = 7\ m/s$.

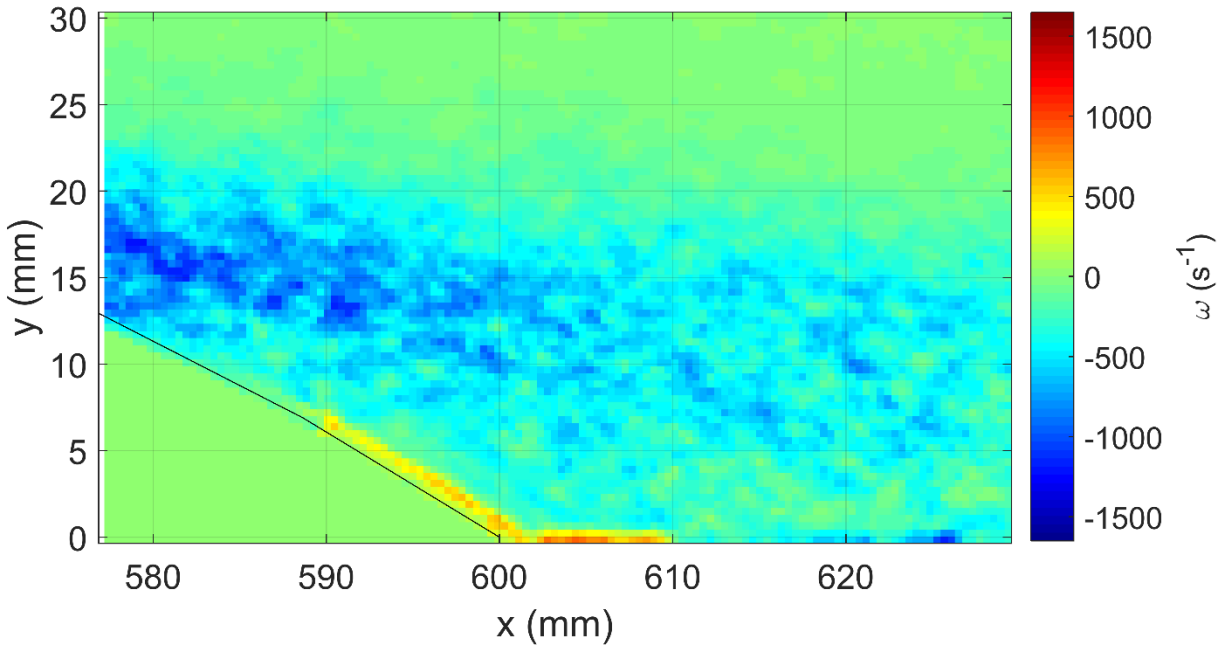

Fig D.19. Vorticity contour, actuated case, Sine wave, VR=1.5, Angular position: $\phi = 20°$, $U_\infty = 7\ m/s$.

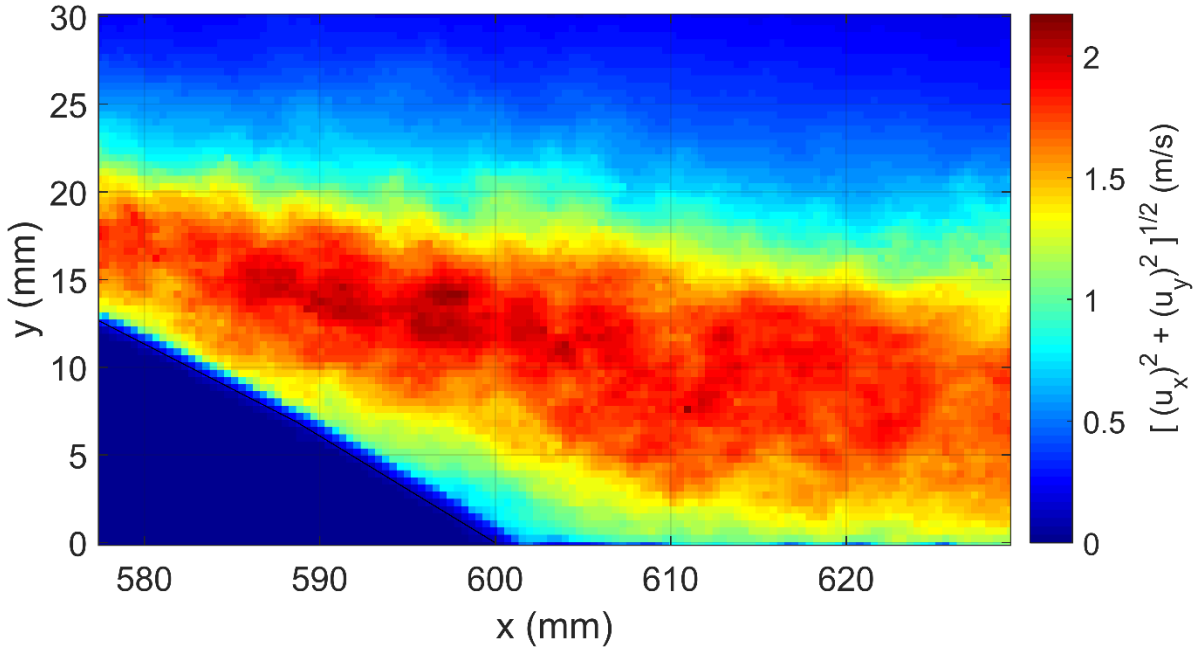

Fig D.20. RMS velocity contour, actuated case, Sine wave, VR=1.5, Angular position: $\phi = 20°, U_\infty = 7\ m/s.$

Sine Wave, Velocity Ratio of 1.50, Angular Position: $\phi = 25°$

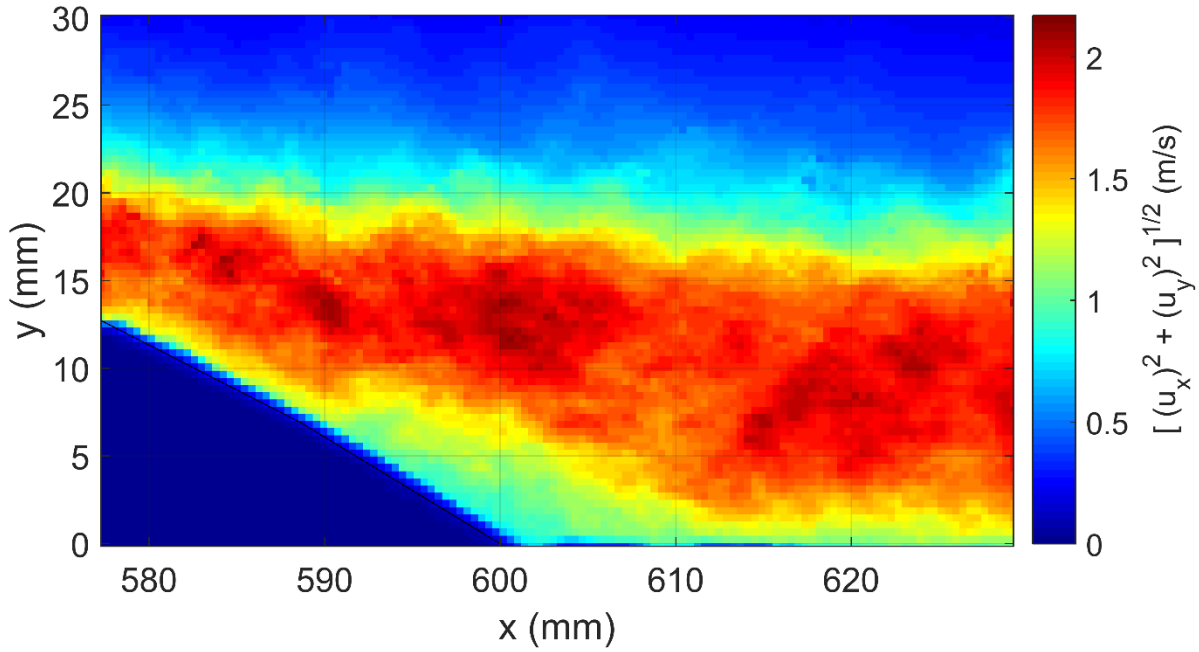

Fig D.21. RMS velocity contour, actuated case, Sine wave, VR=1.5, Angular position: $\phi = 25°, U_\infty = 7\ m/s.$

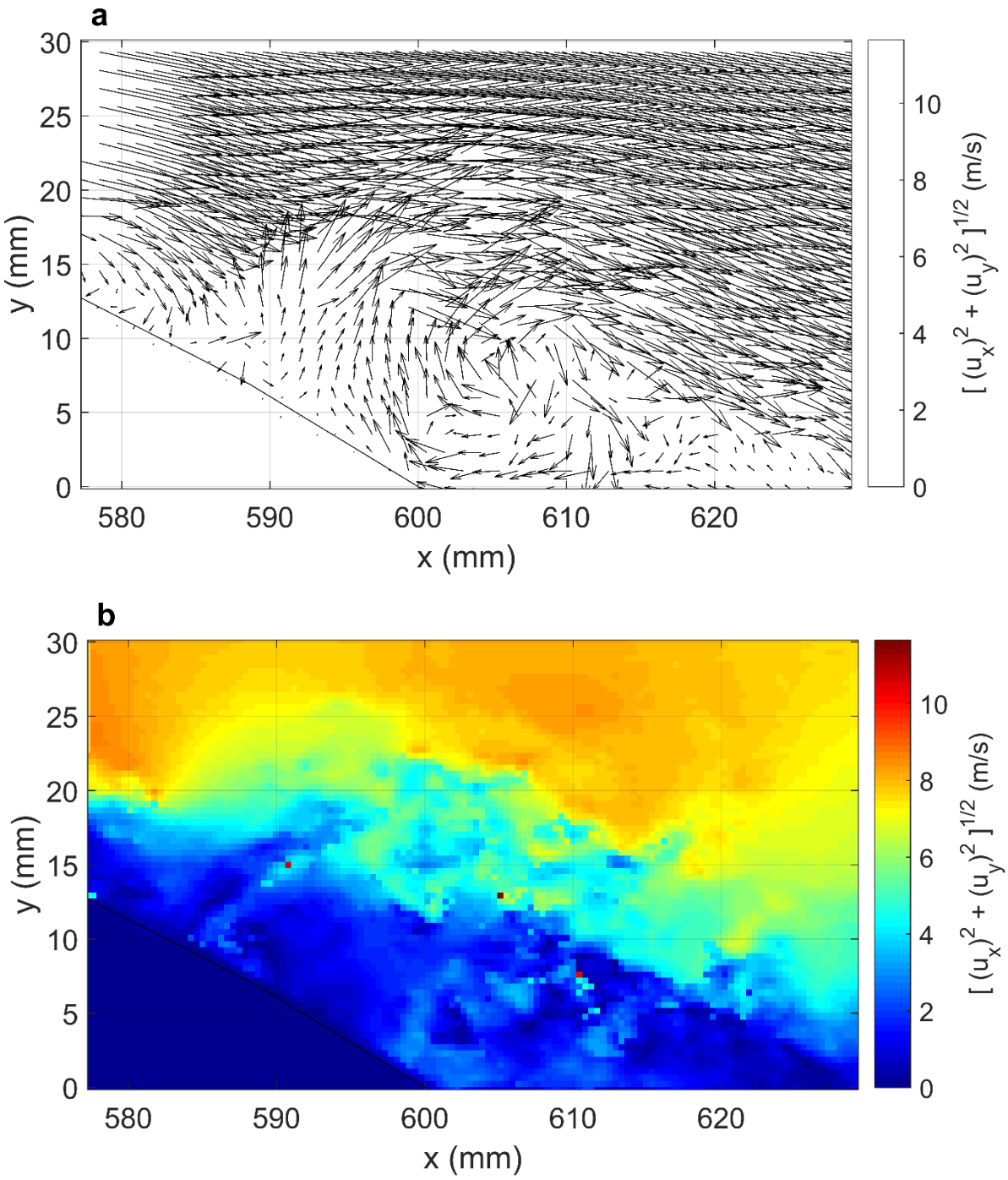

Fig D.22. (a , b) Instantaneous velocity vector and magnitude fields in the wake region- actuated case, Sine wave, VR=1.5, Angular position: $\phi = 25°, U_\infty = 7\ m/s$.

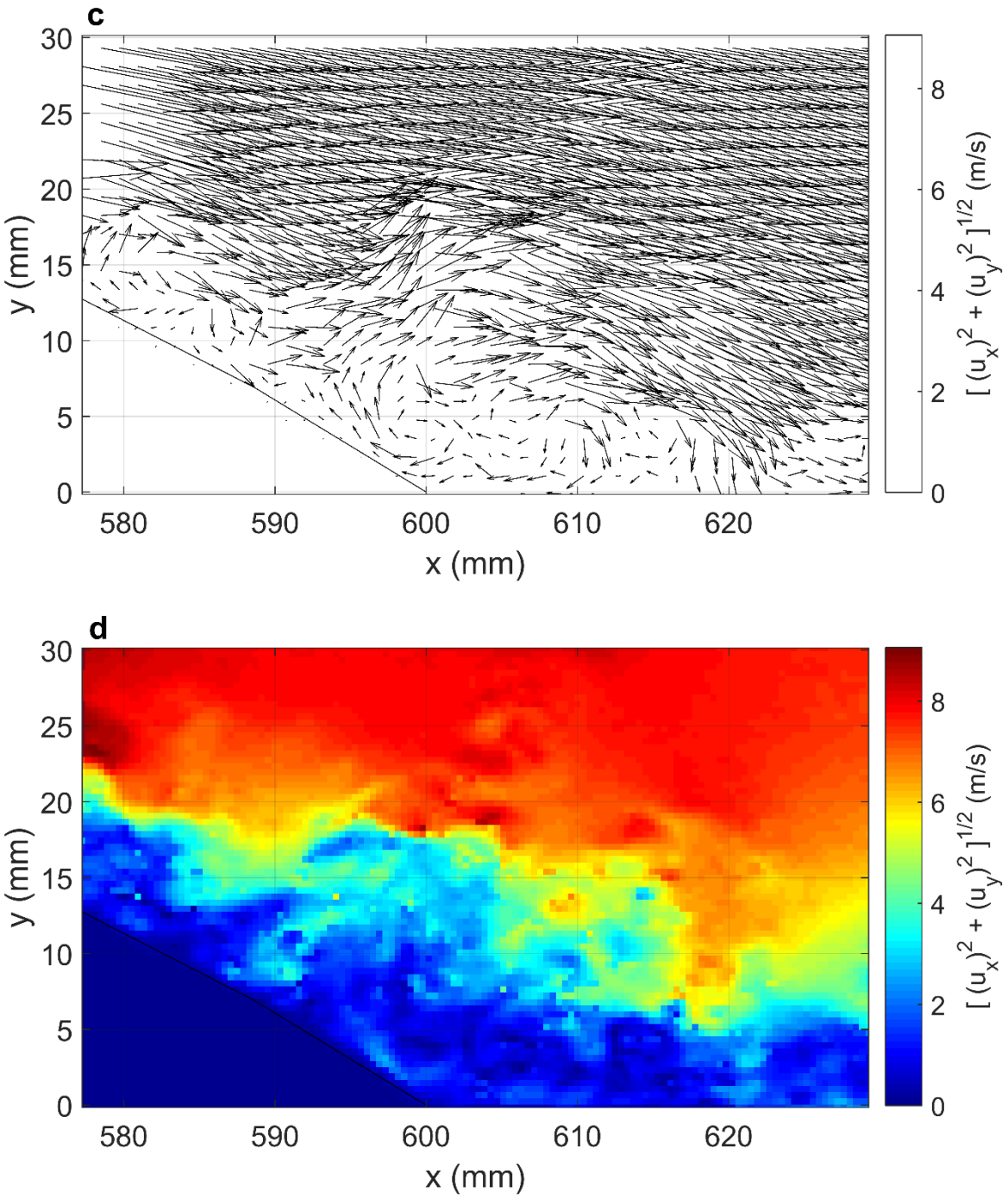

Fig D.22. (c , d) Instantaneous velocity vector and magnitude fields in the wake region- actuated case, Sine wave, VR=1.5, Angular position: $\phi = 25°$, $U_\infty = 7\ m/s$.

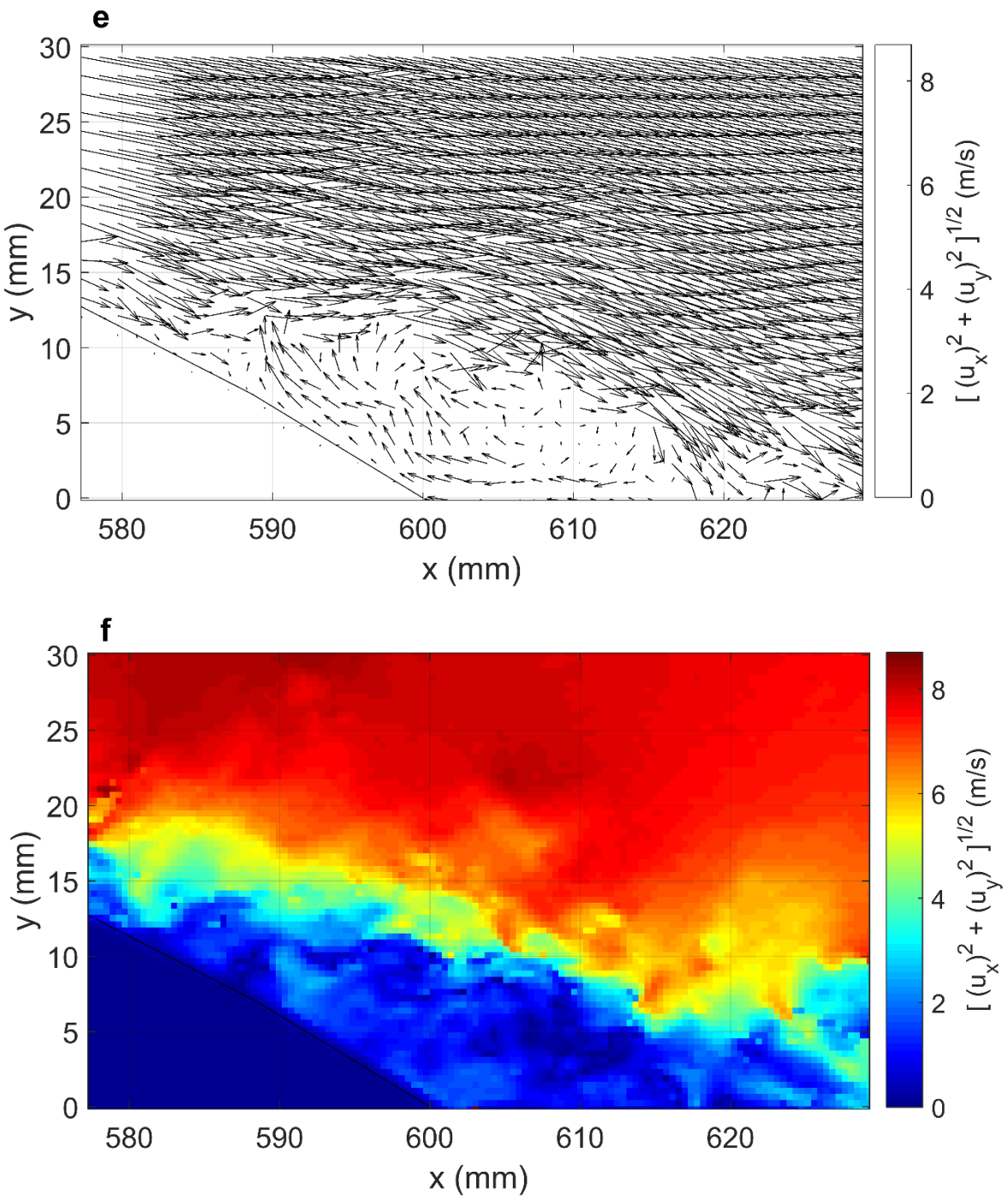

Fig D.22. (e , f) Instantaneous velocity vector and magnitude fields in the wake region- actuated case, Sine wave, VR=1.5, Angular position: $\phi = 25°, U_\infty = 7\ m/s$.

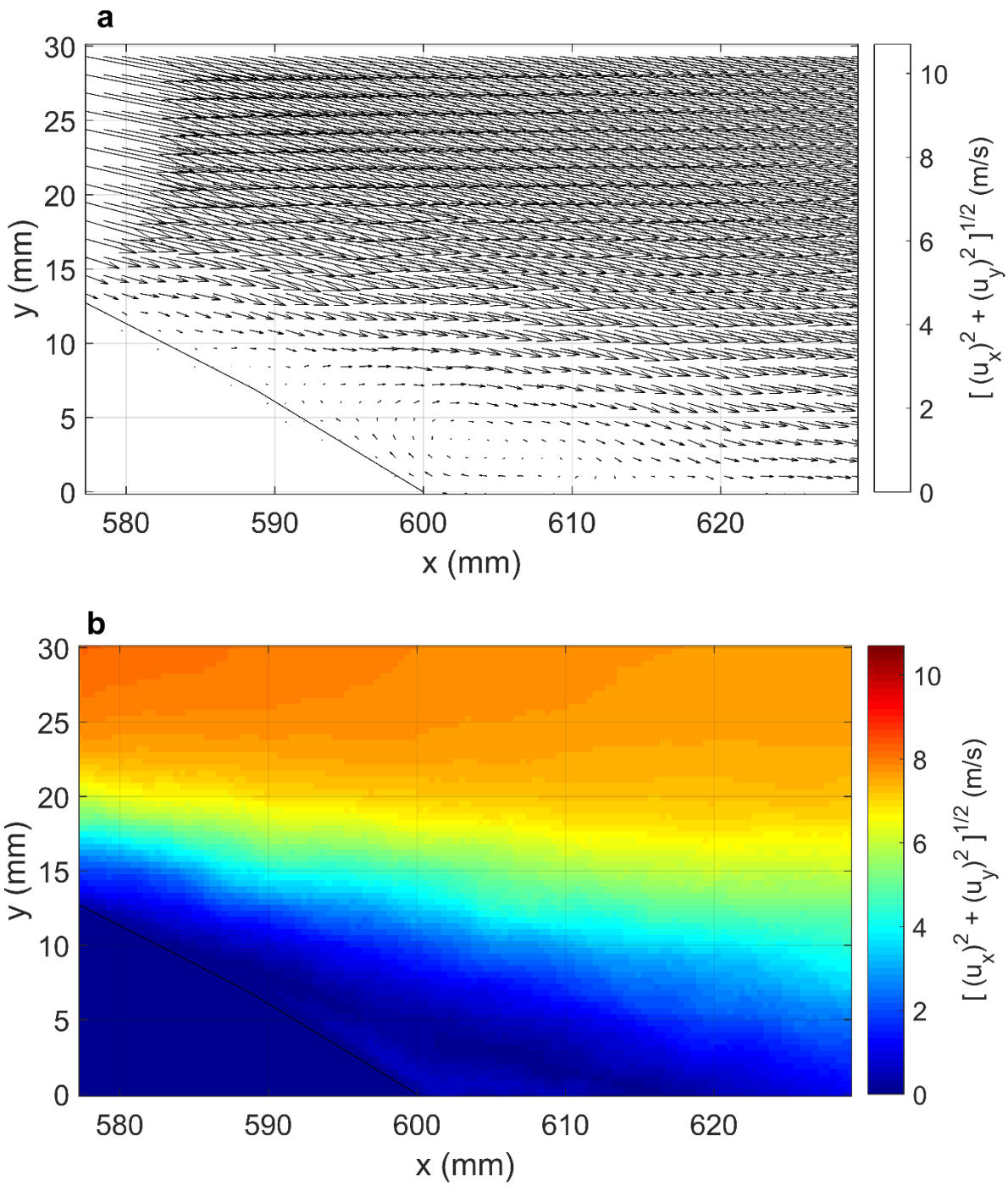

Fig D.23. (a , b) Average velocity vectors and magnitude fields in the wake region- actuated case, Sine wave, VR=1.5, Angular position: $\phi = 25°, U_\infty = 7\ m/s$.

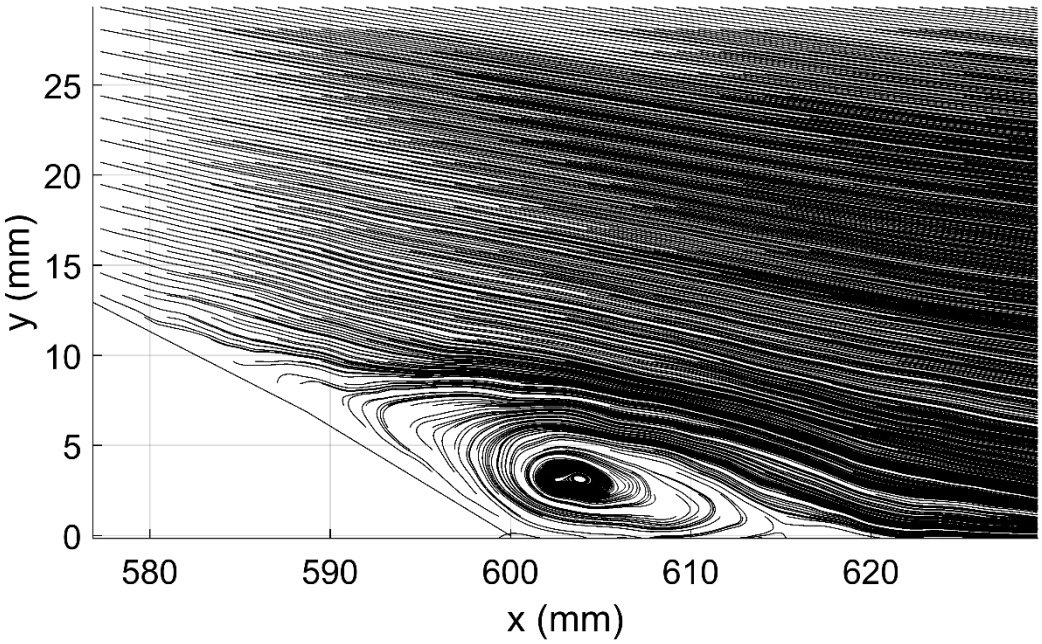

Fig D.24. Streamlines profile, actuated case, Sine wave, VR=1.5, Angular position: $\phi = 25°$, $U_\infty = 7\ m/s$.

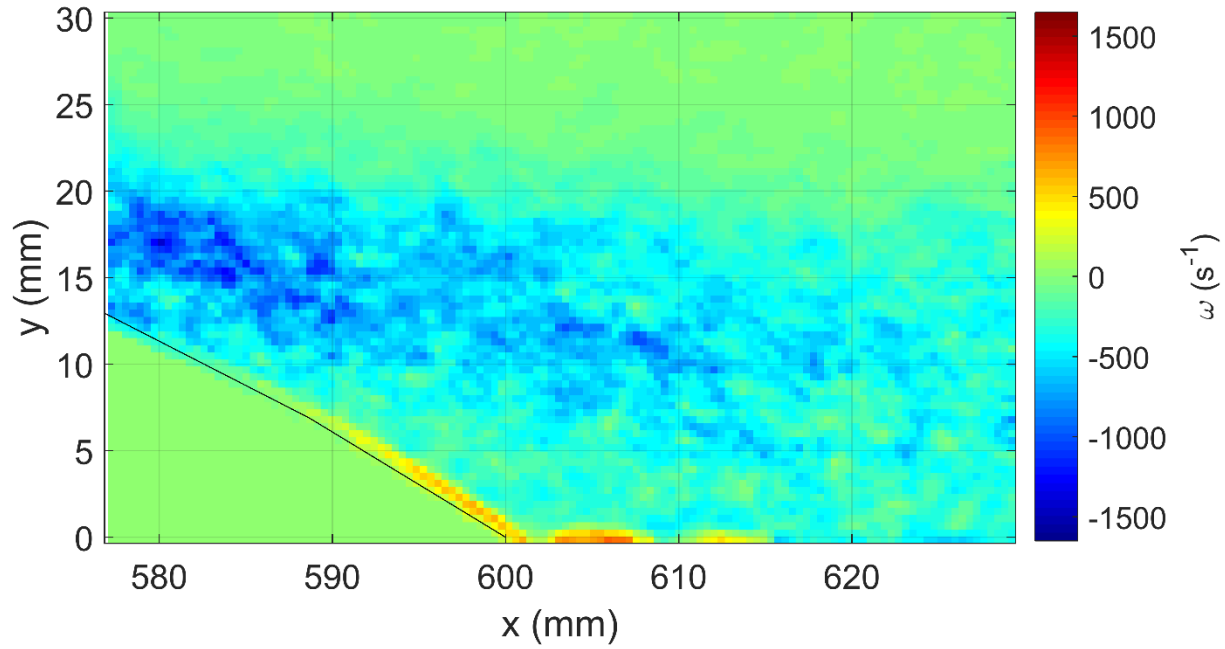

Fig D.25. Vorticity contour, actuated case, Sine wave, VR=1.5, Angular position: $\phi = 25°$, $U_\infty = 7\ m/s$

Square Wave, Velocity Ratio of 1.5, $\phi = 15°$

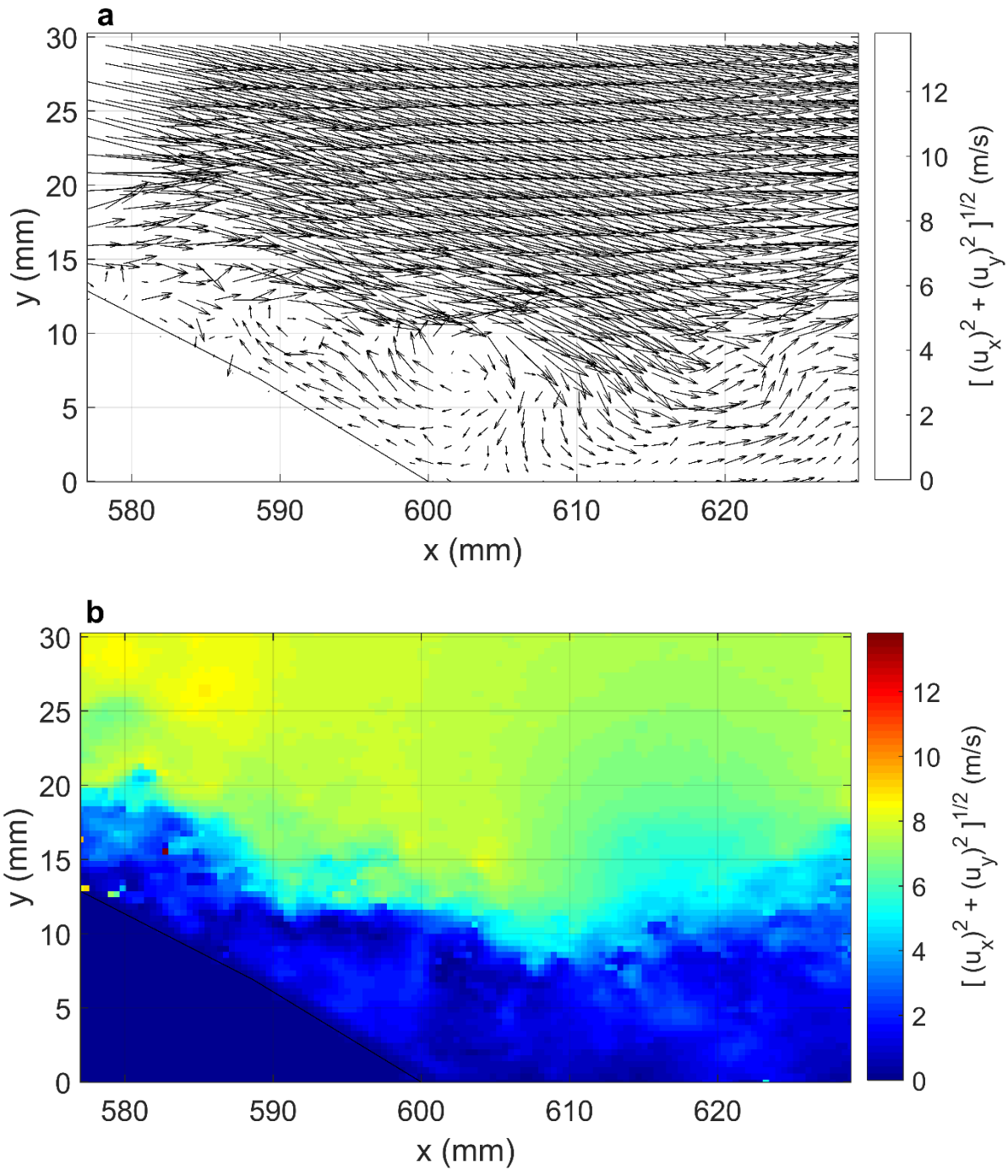

Fig D.26. (a , b) Instantaneous velocity vector and magnitude fields in the wake region-actuated case, Square wave, VR=1.5, Angular position: $\phi = 15°, U_\infty = 7\ m/s$.

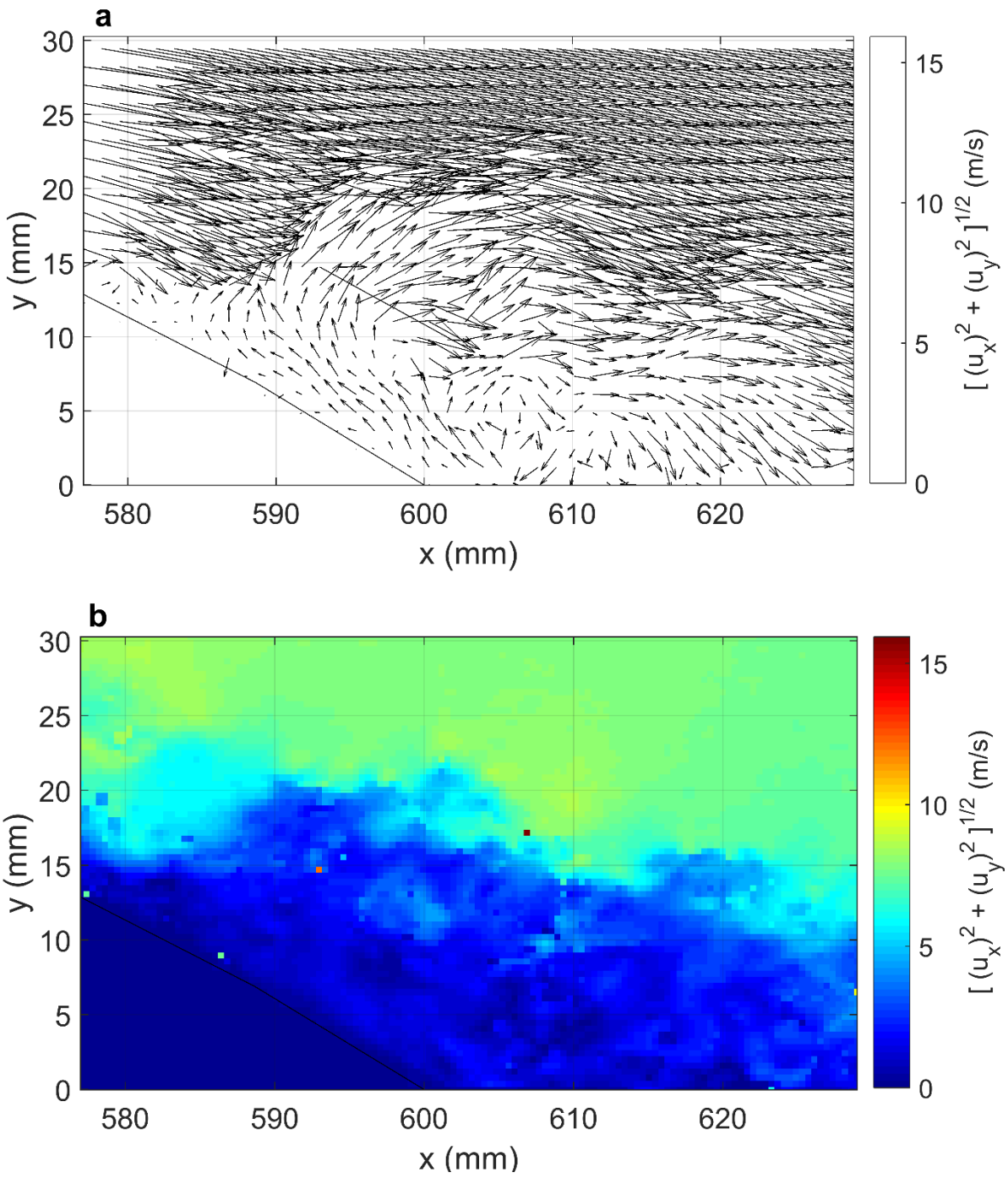

Fig D.26. (c , d) Instantaneous velocity vector and magnitude fields in the wake region-actuated case, Square wave, VR=1.5, Angular position: $\phi = 15°, U_\infty = 7\ m/s$.

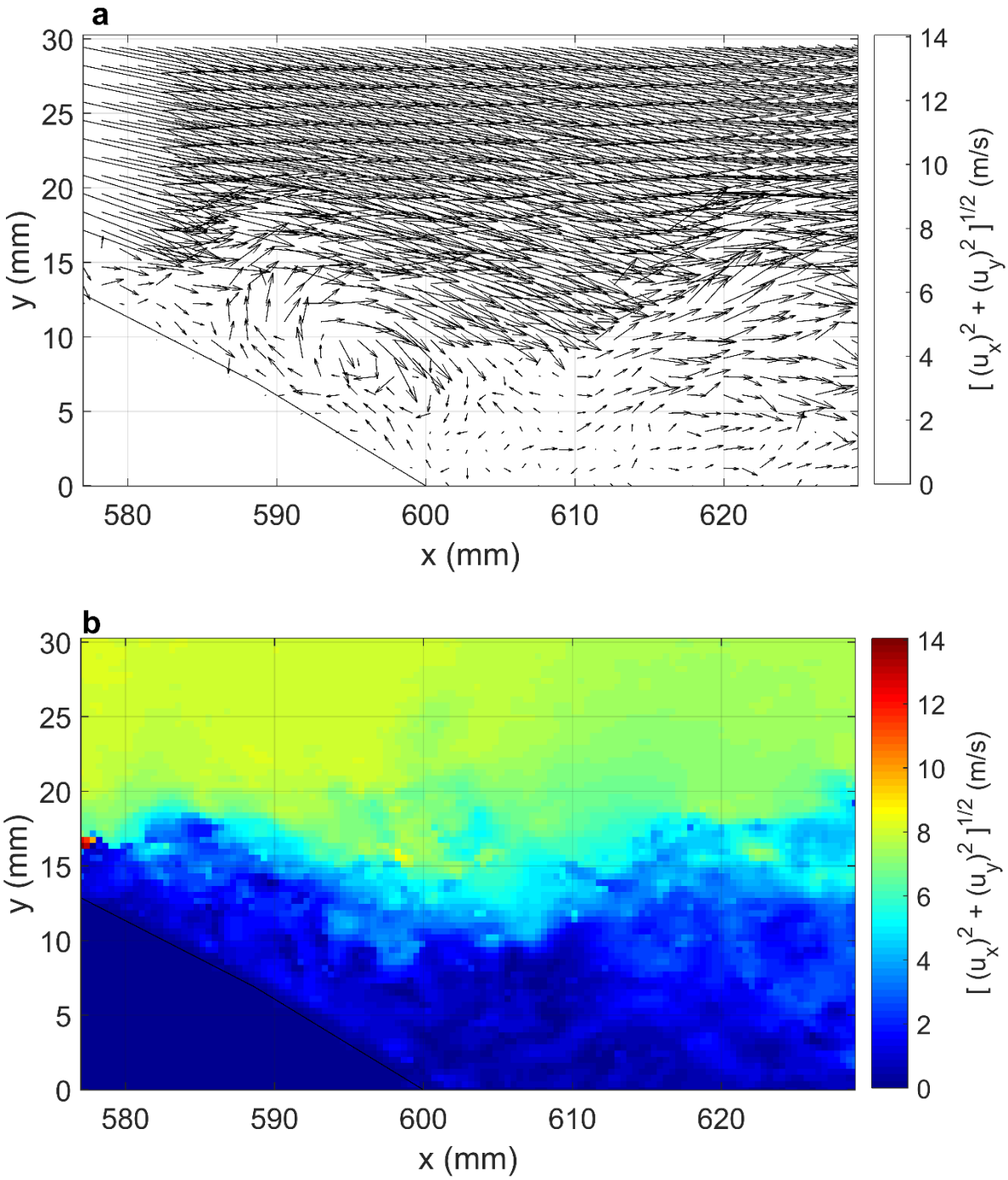

Fig D.26 (e , f) Instantaneous velocity vector and magnitude fields in the wake region-actuated case, Square wave, VR=1.5, Angular position: $\phi = 15°, U_\infty = 7\ m/s$.

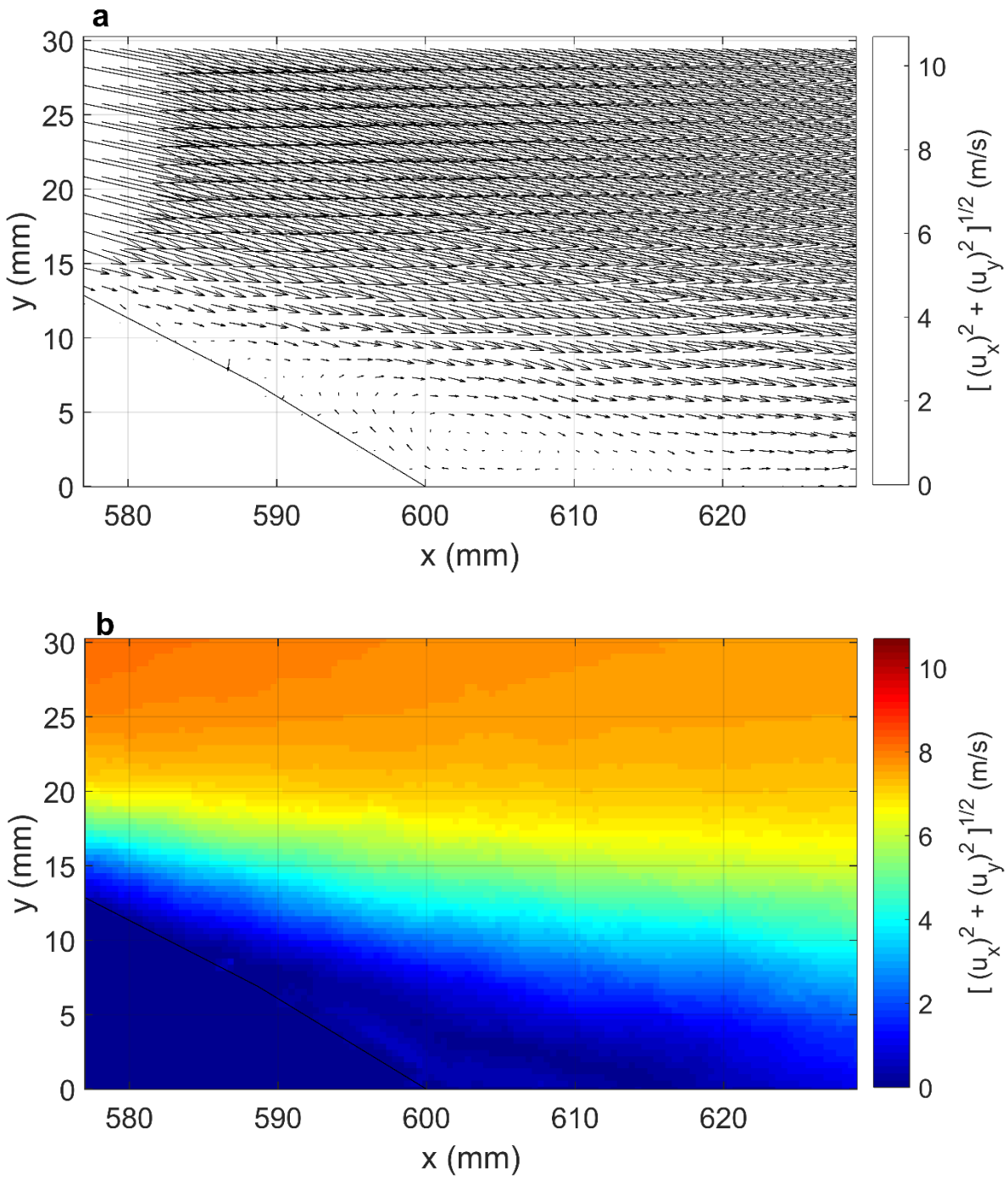

Fig D.27. (a , b) Average velocity vector and magnitude fields in the wake region-actuated case, Square wave, VR=1.5, Angular position: $\phi = 15°, U_\infty = 7\ m/s$.

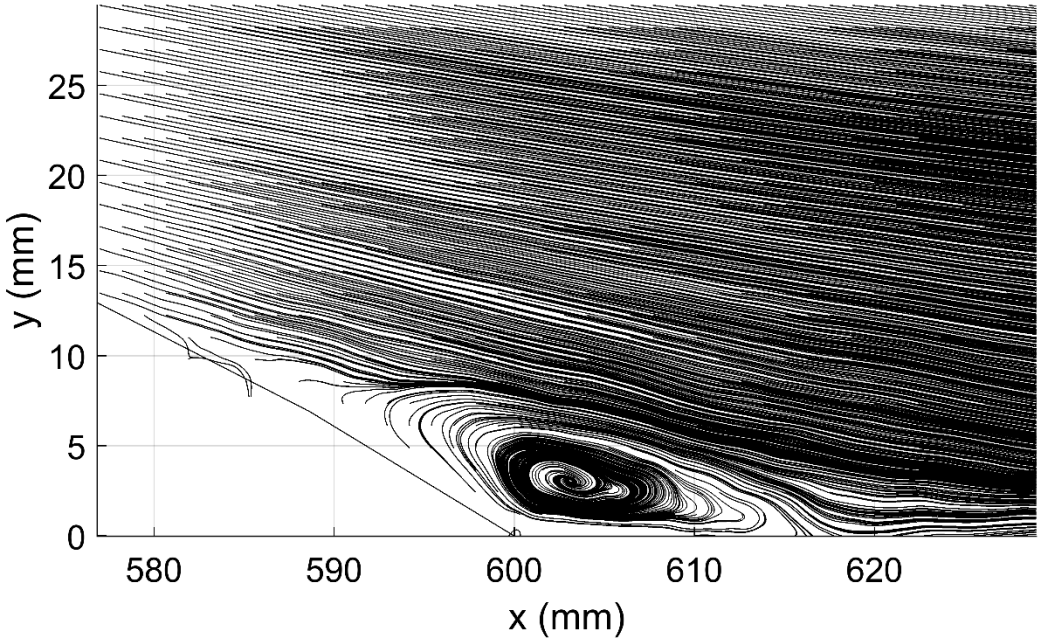

Fig D.28. Streamlines profile, actuated case, Square wave, VR=1.5, Angular position: $\phi = 15°, U_\infty = 7\ m/s$.

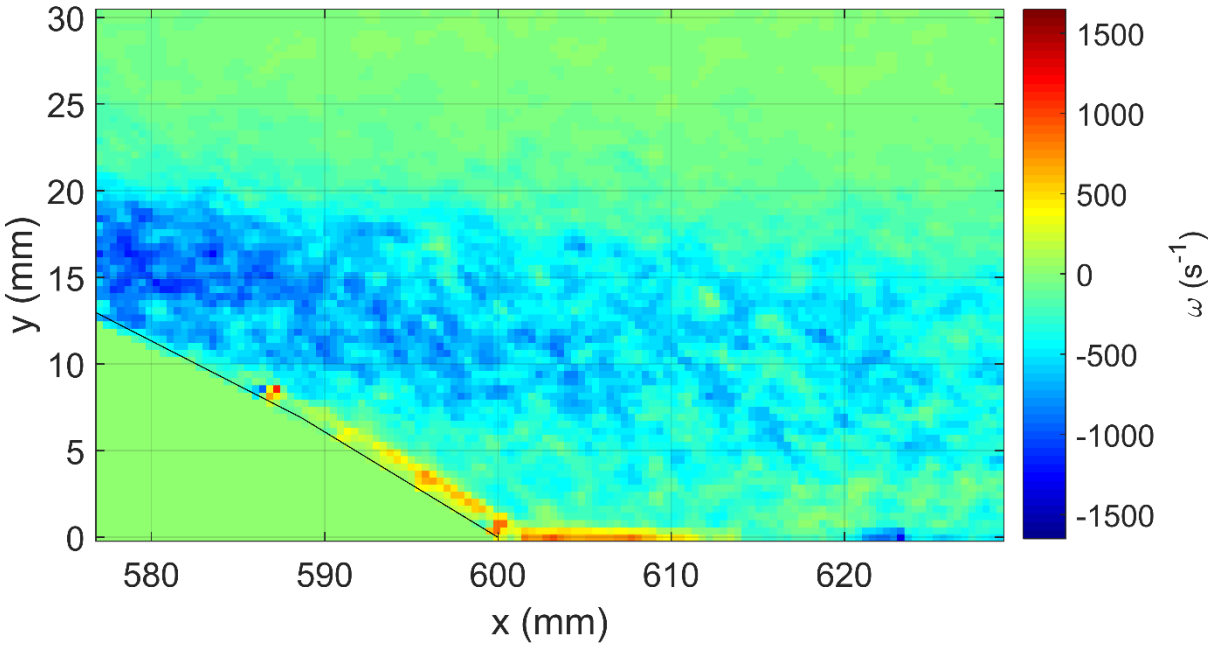

Fig D.29. Vorticity contour, actuated case, Square wave, VR=1.5, Angular position: $\phi = 15°, U_\infty = 7\ m/s$.

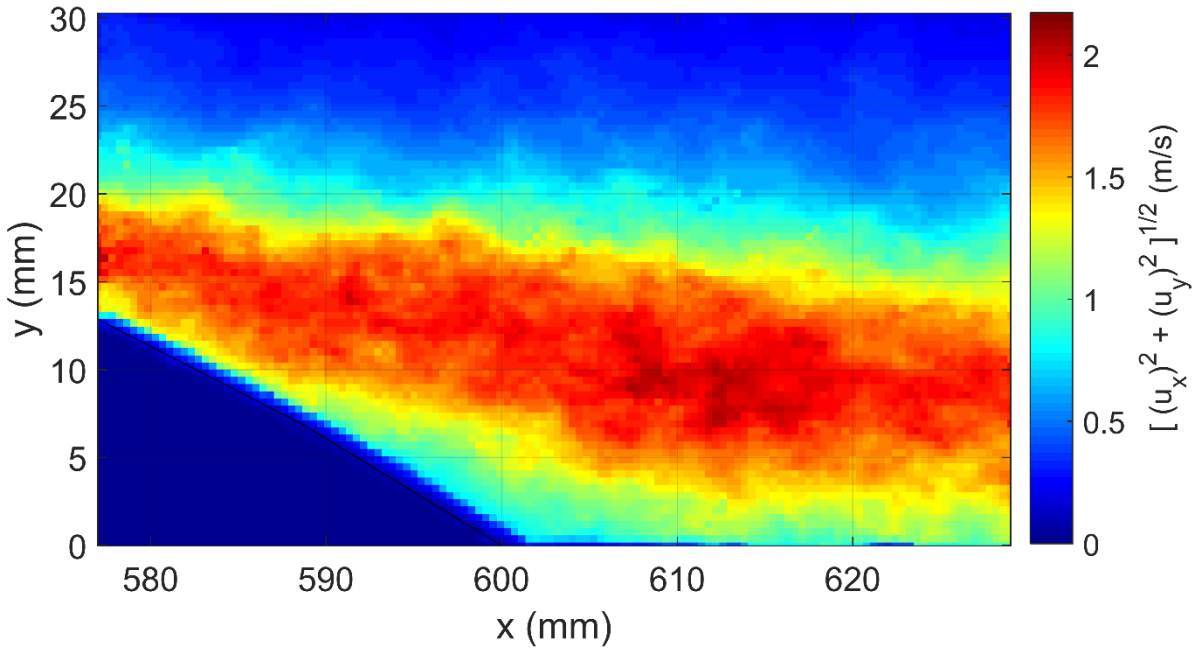

Fig D.30. RMS velocity contour, actuated case, Square wave, VR=1.5, Angular position: $\phi = 15°, U_\infty = 7\ m/s$.